



University of
Nottingham

UK | CHINA | MALAYSIA

A study of microparticle shape and surface chemistry effects on interactions with macrophages

Gordon Bruce

Thesis submitted to the University of Nottingham for
the degree of Doctor of Philosophy

March 2021

Abstract

Internalisation of nano- and microparticles, particularly by macrophages, is a fundamental process impacting the efficacy of particulate delivery systems. A greater understanding of how particle properties such as size, hydrophobicity, surface chemistry, surface charge, and shape influence this process will therefore lead to the design of more effective drug delivery systems and improved clinical outcomes. Recently, there has been a number of studies focussing on how the shape of nanoparticles affects their internalisation, however few studies focus on microparticle delivery systems which are especially useful in the field of inhaled drug delivery. This work aimed to explore the influence of microparticle shape, size, and surface chemistry in order to strengthen the knowledge in this area and assist in the design of microparticle delivery systems.

In this work, microfabrication techniques have been applied to produce a range of microparticles of diverse shape in order to assess their internalisation by RAW 264.7 macrophages. Additionally, surface modification of different sized spherical particles with zwitterionic surface chemistry has been achieved to explore how these properties impact cellular internalisation.

Silicon oxide microparticles of spherical, hexahedral, and truncated pyramid shapes were fluorescently labelled using covalent silane linker chemistry to allow their detection by confocal microscopy and imaging flow cytometry. Each particle shape was shown to be internalised by macrophages and to follow identical uptake pathways resulting in each particle shape residing in the phagolysosome after internalisation. Truncated pyramids were internalised by a lower percentage of macrophages than spherical particles, however in macrophages stimulated with lipopolysaccharide prior to particle administration, no differences in uptake of different shapes were observed.

A wider range of microparticle shapes including hexahedrons, bars, cubes, and circular disks were microfabricated using polycrystalline silicon and a label-free method used to detect

particle uptake by light scattering using imaging flow cytometry. The percentage of cells internalising particles was shown to be dependent on particle shape and in particular, differences in uptake between hexahedral and circular disk shaped particles indicate that points of high curvature may act to increase internalisation. The effect of these polycrystalline silicon microparticle shapes on cellular metabolism, membrane permeability, and release of lysosomal enzymes was then explored revealing no differences in response to different particle shapes across a range of concentrations.

Spherical silicon oxide particles (diameter 0.5, 1, 3 μm) modified either with amine or zwitterionic surface chemistry were applied to cells by equivalent total mass, number, and surface area. Particle uptake was highly dependent on particle dose, dose metric, and particle size, however no difference in particle uptake was seen between the different surface chemistries studied. Additionally, uptake of particles was assessed in the presence of dipalmitoyl phosphorylcholine, a major component of lung surfactant, which resulted in reduced uptake of smaller (0.5, 1 μm) particles but had no effect on the uptake of larger (3 μm) particles.

Acknowledgements

I would like to thank my supervisors, Lluïsa Pérez-García, and Snow Stolnik for their support and motivation throughout this project. Many thanks to my industrial supervisors Richard Kaye and Emanuela Cingolani for their advice and insight and to Frankie Rawson for his constructive feedback over the years. I would like to acknowledge financial support from the EPSRC grant EP/L01646X/1 and GSK through the CDT in Advanced Therapeutics and Nanomedicines.

I would like to thank our collaborators, the group of J. A. Plaza, in particular Marta Duch, who have been so helpful in providing materials which have been essential for the work. I thank Rob Cavanagh for his tutelage and guidance in cell culture, David Onion for his expertise in flow cytometry, and Robert Markus for his skill in microscopy.

I would like to express my gratitude to my office and CDT colleagues, and members of Lluïsa's group for providing an environment in which it has been a pleasure to work.

I would like to thank my parents for their boundless support and encouragement and finally, Rebeca who has both tolerated and encouraged me throughout this process.

Table of Contents

Abstract.....	iii
Acknowledgements.....	v
Table of Contents.....	vi
List of figures	xii
List of tables.....	xvi
List of abbreviations	xvii
1. Introduction	1
1.1 Particulate carriers for drug delivery	1
1.2 Particle entry to the cell: Endocytosis	2
1.2.1 Clathrin-mediated endocytosis	3
1.2.2 Caveolae-mediated endocytosis	4
1.2.3 Clathrin- and caveolin-independent mechanisms of endocytosis.....	5
1.2.4 Macropinocytosis	5
1.2.5 Phagocytosis.....	6
1.2.6 Measures of particle uptake	9
1.3 Particle properties affecting cellular uptake.....	10
1.3.1 The effect of particle size on cellular uptake.....	10
1.3.2 The effect of particle hydrophobicity on particle uptake	12
1.3.3 The effect of particle surface charge on particle uptake.....	13
1.3.4 The effect of particle surface chemistry on cellular uptake	14
1.3.5 Protein corona formation on nano and microparticles.....	15
1.4 Particle shape.....	17

1.4.1 Methods for making nano and microparticles of different shapes	17
1.4.1.1 Bottom-up methods	18
1.4.1.2 Top-down methods	23
1.4.2 The effect of nano and microparticle shape on cellular uptake	29
1.4.2.1 Studies on the effect nanoparticle shape on cellular uptake.....	29
1.4.2.2 Studies on the effect of microparticle shape on cellular uptake	30
1.4.2.3 Other effects of particle shape	32
1.4.2.4 Microparticles for lung delivery	32
1.5 Aims and objectives.....	33
2. Materials and General Methods	36
2.1 Materials.....	36
2.1.1 Plasticware and glassware.....	36
2.1.2 Materials for cells culture.....	36
2.1.3 Chemicals	37
2.2 General Methods	37
2.2.1 Routine cell culture methods	37
2.2.1.1 Culture of RAW 264.7 cells.....	37
2.2.1.2 Cell counting.....	38
2.2.1.3 Cell freezing.....	38
2.2.1.4 Cell revival	39
2.2.1.5 Particokinetics	39
2.2.2 Statistical analysis.....	39

3. Interactions of silicon oxide microparticles of different shape by RAW 264.7 macrophages	40
3.1 Introduction.....	40
3.1.1 Methods of functionalising silicon oxide particles with fluorescent dyes.....	40
3.1.2 Methods of analysing particle internalisation	41
3.1.3 Studies of the uptake of silicon oxide particles of different morphologies	43
3.2 Materials and Methods	44
3.2.1 Materials	44
3.2.2 Methods	44
3.2.2.1 Non-covalent labelling of silicon oxide particles anchored on silicon wafers .	45
3.2.2.2 Covalent labelling of silicon oxide particles anchored on silicon wafers	46
3.2.2.3 Covalent labelling of silicon oxide particles in suspension	47
3.2.2.4 Determination of fluorophore release from particles in PBS at 37°C	48
3.2.2.5 Acquisition of brightfield and fluorescent images	49
3.2.2.6 Water contact angle measurements	49
3.2.2.7 Removal of silicon oxide particles from silicon wafer.....	49
3.2.2.8 Determination of trypan blue quenching efficiency	50
3.2.2.9 Qualitative particle uptake of silicon oxide particles by RAW 264.7 macrophages assessed by confocal microscopy	50
3.2.2.10 Quantitative uptake of silicon oxide particles by RAW 264.7 cells assessed by flow cytometry	52
3.3 Results and Discussion	54
3.3.1 Characterisation of fabricated particles	54
3.3.2 Functionalisation of silicon oxide particles for fluorescent labelling.....	55

3.3.2.1 Non-covalent labelling of silicon oxide particles was achieved using a complexation in solution method	56
3.3.2.2 Covalent labelling using silane linkers	62
3.3.2.3 Comparison of fluorophore release from non-covalent and covalently labelled particles.....	68
3.3.3 Characterisation of fluorescently labelled particles	70
3.3.3.1 Measurement of median fluorescence intensity (MFI) and % coverage of fluorophore	70
3.3.3.2 Measurement of trypan blue quenching efficiency	74
3.3.4 Particle interaction with RAW 264.7 cells	74
3.3.4.1 Qualitative determination of microparticle uptake.....	74
3.3.4.2 Intracellular localisation of Spheres, hexahedrons, and Pyramids.....	77
3.3.4.3 Comparison of image analysis and trypan blue (TB) quenching methods	81
3.3.4.4 Effect of LPS stimulation on particle uptake	84
3.3.4.5 Effect of particle shape on uptake by RAW 264.7 macrophages.....	88
3.4 Conclusions.....	91
4. Interaction of polysilicon microparticles with RAW 264.7 macrophages.....	92
4.1 Introduction.....	92
4.1.1 Polysilicon and silicon microparticles.....	93
4.2 Materials and Methods	97
4.2.1 Materials	97
4.2.2 Methods	97
4.2.2.1 Fabrication and Scanning electron microscopy (SEM) characterisation of polysilicon particles	97

4.2.2.2 Labelling of polysilicon particles with AUTES and RBITC	98
4.2.2.3 Label free detection of polysilicon particles by light scattering	99
4.2.2.4 Quantification of polysilicon particle uptake by RAW 264.7 cells by flow cytometry.....	99
4.2.2.5 MTS, LDH and glucuronidase assays	102
4.3 Results	106
4.3.1 Functionalisation of polysilicon particles with AUTES and RBITC	106
4.3.2 Assessment of particle side scattering	109
4.3.3 Polysilicon particle association with RAW 264.7 macrophages	112
4.3.4 Effect of particle shape on metabolic activity, toxicity, and lysosomal enzyme release	121
4.3.4.1 MTS assay	121
4.3.4.2 LDH assay	124
4.3.4.3 Release of lysosomal enzyme glucuronidase	126
4.4 Discussion	129
4.5 Conclusions	133
5. Effect of silicon oxide particle size and surface modification with zwitterion on interaction with macrophages.....	135
5.1 Introduction.....	135
5.2 Materials and Methods	138
5.2.1 Materials	138
5.2.2 Methods	138
5.2.2.1 Modification of silicon oxide spheres with AUTES, RBITC, and MDSA	138
5.2.2.2 XPS characterisation of modified particles.....	139

5.2.2.3 Zeta potential measurements	140
5.2.2.4 Water contact angle measurements	140
5.2.2.5 Acquisition of brightfield and fluorescent images	140
5.2.2.6 Quantitative uptake of silicon oxide spheres by RAW 264.7 cells	141
5.3 Results and Discussion	143
5.3.1 Characterisation of modified silicon oxide particles	143
5.3.1.1 XPS characterisation	143
5.3.1.2 Zeta potential measurements	147
5.3.1.3 Water contact angle θ (°) measurements.....	149
5.3.1.4 Fluorescence of modified particles.....	151
5.3.2 Uptake of silicon oxide particles by RAW 264.7 macrophages	153
5.3.2.1 Effect of particle size on uptake	153
5.3.2.2 Effect of zwitterion surface chemistry on particle uptake.....	163
5.4 Conclusions.....	170
6. General discussion and Future work	172
7. References	180
Appendix I – Supporting information from chapter 3.....	205
Appendix II - Supporting information for chapter 4	216
Appendix III – Supporting information for chapter 5.....	218

List of figures

Figure 1.1: Schematic representation of the different endocytic mechanisms	3
Figure 1.2: Particle properties affecting cellular uptake	10
Figure 1.3: Gold nanoparticles of different morphology	19
Figure 1.4: Particles fabricated using soft templates	21
Figure 1.5: Hollow silica particles fabricated using a hematite template	21
Figure 1.6: The film stretching method	24
Figure 1.7: Photolithographic production of polysilicon particles.....	24
Figure 1.8: Porous silicon microparticles fabricated using photolithography	25
Figure 1.9: Colloidal alphabet soup	27
Figure 1.10: Particle replication in non-wetting templates (PRINT).....	28
Figure 1.11: Schematic summarising key aspects of the project	35
Figure 3.1 SEM images of fabricated SiO ₂ microparticles.....	55
Figure 3.2: Images of surfaces after functionalisation using the step-by-step method	58
Figure 3.3: Effect of solvent on particle functionalisation	60
Figure 3.4: Particle functionalisation using complexation in solution method.....	61
Figure 3.5: Chemical structures of silanes.....	63
Figure 3.6: Fluorescence of covalently labelled particles.....	67
Figure 3.7 images of particles before and after incubation in PBS 37°C for 2 hours.....	70
Figure 3.8: % reduction in fluorescence intensity after incubation in PBS at 37°C for 2 hours	70
Figure 3.9: Fluorescently labelled particles in suspension	72
Figure 3.10: CLSM images of RAW 264.7 cells with internalised microparticle shapes	76
Figure 3.11: Intracellular localisation of particles after phagocytosis.	80
Figure 3.12: Comparison of image analysis and TB quenching methods for quantifying particle internalisation.....	83
Figure 3.13: Light microscopy images of RAW 264.7 cells.....	85

Figure 3.14: Effect of LPS stimulation on particle uptake	87
Figure 3.15: The effect of LPS stimulation on particle association, internalisation, and surface-binding	88
Figure 3.16: The effect of particle shape on cellular uptake	89
Figure 4.1: SEM images of the polysilicon particles used in this chapter	95
Figure 4.2: Distinction between polysilicon particle-associated and unassociated cells using scattering intensity	101
Figure 4.3: Distinction between cells with internal particles and cells with external particles	102
Figure 4.4: Effect of AUTES deposition solvent on particle labelling with RBITC.....	107
Figure 4.5: Scattering intensity histograms of RAW 264.7 cells and each particle shape ..	110
Figure 4.6: Summary of MSI values for RAW 264.7 cells and each particle shape.....	112
Figure 4.7: Side scattering intensity histograms of RAW 264.7 cells incubated with polysilicon particles	114
Figure 4.8: Cell images from imaging flow cytometry across the range of scattering intensities for cells unassociated and associated with polysilicon particles	115
Figure 4.9: Cellular association, internalisation and surface binding of polysilicon particles with RAW 264.7 cells	117
Figure 4.10: Particle factors affecting cellular association, internalisation, and surface-binding	119
Figure 4.11: Effect of particle shape on number of internalised (A) and surface-bound (B) particles per cell.	120
Figure 4.12: Effect of increasing polysilicon particle dose on RAW 264.7 metabolic activity	123
Figure 4.13: Effect of increasing polysilicon particle dose on RAW 264.7 LDH release	125
Figure 4.14: Effect of increasing polysilicon particle dose on RAW 264.7 lysosomal glucuronidase release	128

Figure 5.1: Widescan XPS spectra of silicon oxide particles with modified surface chemistry.	146
Figure 5.2: Zeta potential measurements of silicon oxide particles with different surface chemistry	148
Figure 5.3: Water contact angle measurements of modified particles	151
Figure 5.4: Representative brightfield and fluorescence images of silicon oxide particles	152
Figure 5.5: Effect of particle size on the percentage of cells with internalised particles	154
Figure 5.6: Effect of DPPC on the % of cells with internalised particles	158
Figure 5.7: Effect of particle size on the number of internalised particles per cell that internalised particles	160
Figure 5.8: Effect of particle size on the % dose internalised	162
Figure 5.9: Effect of zwitterion surface chemistry on the % of cells with internalised particles.	164
Figure 5.10: Effect of zwitterion surface chemistry on the number of internalised particles per cell that internalised particles	167
Figure 5.11: Effect of zwitterion surface chemistry on the % dose internalised	169
Figure S3.1: ^1H NMR of 1-Octadecyl 1H Imidazole	205
Figure S3.2: ^1H NMR of 1.2Br	206
Figure S3.3: Brightfield, fluorescence, and surface plots of surfaces washed with water instead of DMSO after imidazolium treatment in DMSO	206
Figure S3.4: Fluorescence intensity histograms of RBITC labelled particles before and after trypan blue quenching	207
Figure S3.5: Calibration of particle labelling.	208
Figure S3.6: Effect of temperature on phagocytosis	209
Figure S3.7: Gating of single cell population	210
Figure S3.8 Gating of in-focus cell population	211
Figure S3.9: Gating of cells associated with particles	212
Figure S3.10: Cell masks used to identify cells with internal and surface-bound particles	213

Figure S3.11: Histogram of internalisation score defining whether particles are internalised or surface-bound.....	213
Figure S3.12: Distinction between trypan blue stained and unstained cells.....	214
Figure S3.13: Distinction between cells with surface-bound and internalised particles using the trypan blue quenching method	215
Figure S4.1: Cell images from imaging flow cytometry of cells with internal and external particles.	216
Figure S5.1: High resolution XPS spectra of S peaks from MDSA modified particles	218
Figure S5.2: High resolution XPS spectra of Nitrogen peaks for silicon oxide particles	220

List of tables

Table 3.1: Dimensions of fabricated Hexahedrons, Truncated pyramids, and Spheres	55
Table 3.2: Water contact angles θ (°) after treatment with PFP, GOPTS, APTMS, and AUTES	65
Table 3.3: Particle MFI and estimation of surface labelling.....	73
Table 3.4: Quenching efficiency of trypan blue.....	74
Table 4.1: Particle shapes and their dimensions	96
Table 5.1: Surface composition (Atomic %) of silicon oxide particles with modified surface chemistry	147
Table 5.2: Summary of particle characteristics.....	152
Table 5.3: Applied particle doses and equivalent doses by other metrics	153

List of abbreviations

AFM	Atomic force microscopy
APs	Assembly Proteins
APTES	(3-aminopropyl) triethoxysilane
APTMS	(3-aminopropyl) trimethoxysilane
ATP	Adenosine triphosphate
ATPP	5-(4-aminophenyl)-10,15,20-(triphenyl)porphyrin
AUTES	(11-aminoundecyl) triethoxysilane
CNM	Centro Nacional de Microelectrónica
COPD	Chronic obstructive pulmonary disease
CTAB	Cetyltrimethylammonium bromide
DAPI	4',6-diamidine-2'-phenylindole dihydrochloride
DCM	Dichloromethane
DMEM	Dulbecco's Modified Eagle Medium
DMSO	Dimethylsulfoxide
DPI	Dry powder inhaler
DPPC	Dipalmitoylphosphatidylcholine
EBL	Electron beam lithography
EtOH	Ethanol
FBS	Foetal bovine serum
FITC	fluorescein isothiocyanate
GEEC	GPI-AP enriched early endosomal compartments
GOPTS	(3-glycidoxypropyl)trimethoxysilane

GPI	Glycosylphosphatidyl inositol
HBSS	Hank's balanced salt solution
HEPES	4-(2-hydroxyethyl)-1-piperazineethanesulfonic acid
HUVECs	Human umbilical vein endothelial cells
ICP-AES	Inductively coupled plasma atomic emission spectroscopy
ICP-MS	Inductively coupled mass spectrometry
IFN	Interferon
IgG	Immunoglobulin G
IL	Interleukin
LAMP	Lysosome associated membrane glycoprotein
LDH	Lactate dehydrogenase
LDL	Low-density lipoprotein
LPS	Lipopolysaccharide
LSCM	Laser scanning confocal microscopy
MDSA	N-(3-sulfopropyl)-N-methacroyloxyethyl-N,N-dimethylammonium betaine
MFI	Median Fluorescence Intensity
MMPs	Matric metalloproteinases
MSI	Median scattering intensity
MTS	3-(4,5-dimethylthiazol-2-yl)-5-(3-carboxymethoxyphenyl)-2-(4-sulfophenyl)-2H-tetrazolium
MUG	4-methyl umbelliferyl- β -D-glucuronide hydrate
PAMPs	Pathogen-associated molecular patterns
PBS	Phosphate buffered saline
PCL	Polycaprolactone
PDMS	Polydimethyl siloxane

PEG	Poly(ethylene glycol)
PES	Phenazine ethosulphate
PFP	10-(pentafluorophenoxycarbonyl)decyltrimethoxysilane
PFPE	Perfluoropolyether
PLGA	Poly(lactic-co-glycolic) acid
PRINT	Particle replication in non-wetting templates
PVA	Polyvinyl acetate
PVP	Polyvinyl pyrrolidone
RBITC	Rhodamine B isothiocyanate
RES	Reticuloendothelial system
RILP	Rab interacting lysosomal protein
RNS	Reactive nitrogen species
ROS	Reactive oxygen species
SAM	Self-assembled monolayer
SEM	Scanning electron microscopy
TB	Trypan blue
TCPP	5,10,15,20-(tetra-4carboxyphenyl)porphyrin
TEM	Transmission electron microscopy
TEOS	Tetraethyl orthosilicate
TLRs	Toll-like receptors
TNF	Tumour necrosis factor
TX-100	Triton X-100
UFO	Unidentified flying object
WGA	Wheat germ agglutinin
XPS	X-ray photoelectron spectroscopy

1. Introduction

1.1 Particulate carriers for drug delivery

Nano and micro-particulate carriers of therapeutic molecules offer a number of advantages for the purposes of drug delivery. Over recent years the amount of research in this area has risen drastically, although there still remain many hurdles to increasing the number of approved pharmaceutical products ¹. By using particulate drug delivery systems the effectiveness of medicines can be improved through improved drug solubility/stability, passive/active targeting, intracellular delivery, and controlled drug release ². The range of delivery systems studied include micelles, dendrimers, liposomes, polymeric nano/microparticles, lipid nanoparticles, inorganic particles, crystalline particles, and hydrogels ³.

The first major success story in this field was Doxil®, a pegylated liposomal formulation of doxorubicin used for the treatment of a number of cancers including Kaposi's sarcoma, metastatic breast cancer, recurrent ovarian cancer, and multiple myeloma ⁴. By using a liposomal carrier with prolonged circulation time, Doxil® achieves higher tumour accumulation due to passive accumulation and reduced side effects compared to free doxorubicin ⁵.

Since then a number of particle formulations have come on to the market mainly for the treatment of cancer (Abraxane®, Onivyde®, Depocyt®, Daunoxome®, Eligard®) ⁶. However, other therapeutic areas include multiple sclerosis (Copaxone®), analgesia (DepoDur®), macular degeneration (Visudyne®), menopausal therapy (Estrasorb®), and infection (Abelcet®, AmBisome®) ⁶⁻¹¹. In the inhalation field, dry powder inhalers most commonly make use of microparticles with diameters between 0.5 and 5 µm, as these have been shown to be most effective at depositing deep into the lung ¹². Techniques such as spray drying have made possible the control of particle size, density, porosity, and surface energy and have resulted in particles with increased drug loading and higher deposition for example, tobramycin pulmospheres™ for the treatment of pseudomonal infections ¹³.

Most recently, lipid nanoparticle formulations containing RNA have been developed as vaccines against COVID-19 ¹⁴⁻¹⁵. Here the lipid nanoparticle acts to increase efficiency of RNA uptake by cells after intramuscular delivery ^{14, 16}.

When administered particulate carriers come into contact with different cell types, they interact with the cellular membrane and can be internalised by endocytosis ¹⁷. A number of particle factors (size, charge, surface chemistry, hydrophobicity, shape) contribute to this interaction and ultimately, understanding of how each of these factors affect particle-cell interactions will lead to the design of more effective drug delivery systems.

1.2 Particle entry to the cell: Endocytosis

Endocytosis describes the mechanism of internalisation of part of the cells plasma membrane in order to form a distinct intracellular compartment. It is a key cellular process which underlies much of a cells regular function, for example by regulating the sensitivity of the cell to a specific ligand. When a ligand binds to its specific receptor on the plasma membrane, the receptor is endocytosed thereby limiting the cellular response to further stimulation by the ligand ¹⁸. Pathogens such as viruses can exploit routes of endocytosis in order to gain entry into cells and thereby replicate ¹⁹ and it is the goal of many researchers to deliver therapeutic nanoparticles via these same mechanisms. Endocytosis can occur through a number of distinct routes which are normally described by the specific proteins involved and can be subdivided into phagocytosis (occurring only in specialised cell types) and pinocytosis (occurring in all cells) (figure 1.1). Pinocytosis mechanisms are further subdivided to include macropinocytosis, clathrin mediated endocytosis, caveolin-mediated endocytosis, and clathrin/caveolin independent endocytosis ²⁰.

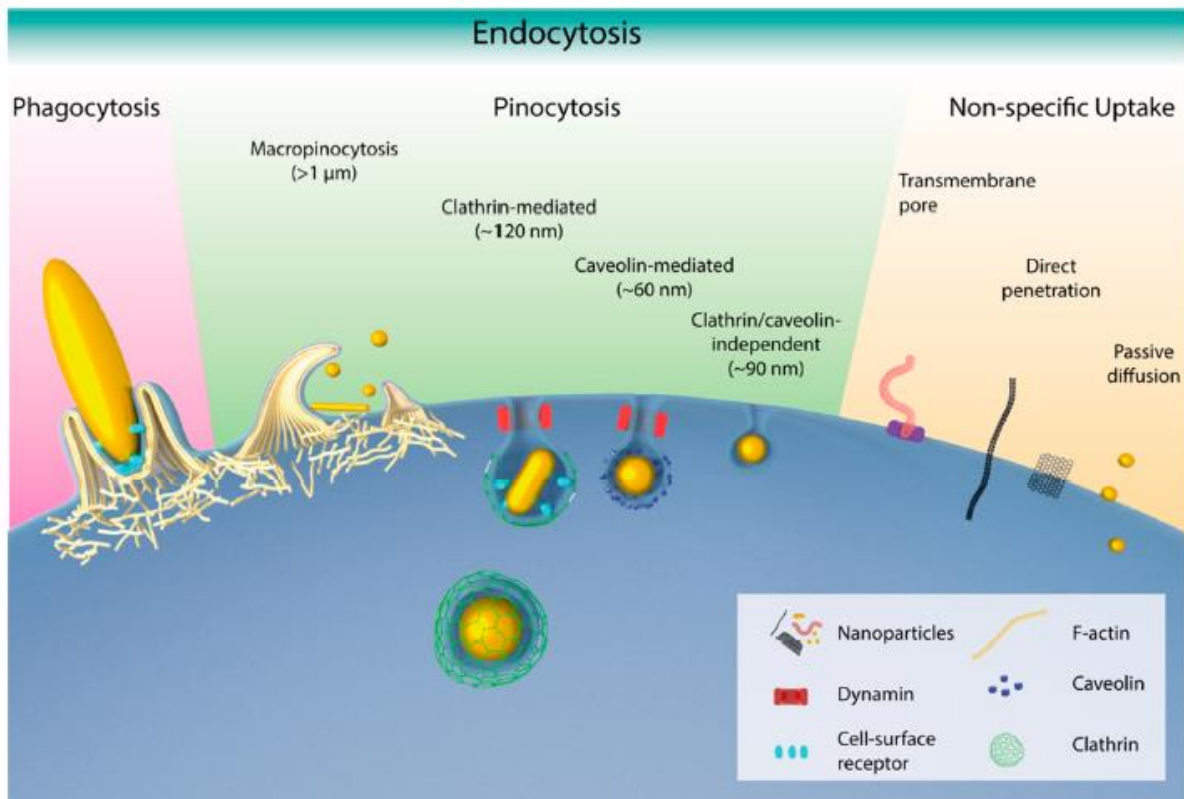


Figure 1.1: Schematic representation of the different endocytic mechanisms from ref ²¹.

1.2.1 Clathrin-mediated endocytosis

Upon binding of certain receptors, for example low-density lipoprotein (LDL) and transferrin receptors ²²⁻²³, clustering of a number of receptors results in the formation of coated pits ²⁴. The coated pits are formed by the assembly of clathrin, a triskelion shaped protein consisting of three heavy and three light chains, into polyhedral lattices ²⁵. Clathrin assembly is mediated by assembly proteins (APs) particularly AP2, and the formation of the polyhedral coat provides the driving force required for membrane invagination ²⁶. Subsequent recruitment of dynamin into helical rings that form a collar at the neck of the invaginated pit, promotes scission of the newly formed vesicle ²⁷. It has also been suggested that the helical structure could act as a spring that pushes the newly formed vesicle towards the cytosol ²⁸. After scission from the membrane, the chaperone protein HSC70 disrupts clathrin-clathrin interaction in the lattice and dephosphorylation of phosphatidylinositol (4,5) bisphosphonate cause depolymerisation

and subsequent disassembly of the clathrin coat ²⁹. The vesicle can then fuse with other internalised uncoated vesicles or be trafficked towards early endosomal compartments ²⁴.

Clathrin-mediated endocytosis has been identified as a route of entry into the cell for a number of nanoparticles including PLGA ³⁰, silica ³¹, and chitosan ³² particles. The internalisation pathway depends on particle properties such as size, surface chemistry, and charge ³³⁻³⁴. It has been shown that positively charged particles are more dependent on clathrin-mediated uptake than negatively charged particles ³⁵, however, the internalization pathway also depends on cell type. Studies have shown an upper size limit for clathrin-mediated endocytosis to be ~ 200 nm ³³ therefore it is important to consider this when designing targeted nanomedicines.

1.2.2 Caveolae-mediated endocytosis

Caveolae were first described as flask shaped invaginations in the cell membrane and later caveolins, membrane proteins that bind directly to cholesterol, ³⁶ were identified as the protein surrounding these invaginations ³⁷. Ligands that bind to folate receptors ³⁸ as well as albumin ³⁹, and cholesterol ⁴⁰ have been shown to trigger internalisation of caveolae and so modifications of nanoparticles with such ligands have been explored ⁴¹⁻⁴³. The caveolae reside at the plasma membrane for extended periods of time ⁴⁴, binding of ligands triggers tyrosine kinase dependent signalling cascades that culminate in the recruitment of dynamin and subsequent budding of vesicles away from the plasma membrane ⁴⁵. After budding, transport is dependent on the type of ligand that is to be internalised, for example, the virus SV-40 is transported to the endoplasmic reticulum, where it resides until transport to the nucleus ⁴⁶ whereas caveolae are responsible for the transcytosis of proteins such as albumin ⁴⁷. The avoidance of fusion with lysosomal compartments mean that internalised material avoids degradation, an attractive property for the delivery of sensitive therapeutics such as RNA.

Typically caveolae are 60-80 nm in diameter ⁴⁸ however, internalisation of nanoparticles up to 100 nm by caveolae-mediated endocytosis has been shown ⁴⁹. In comparison with clathrin-mediated endocytosis, caveolia-mediated endocytosis is slow, however, it plays a much bigger role in transcytosis ⁵⁰ and so is likely to be an important route for the transport of nanoparticles across biological barriers. Indeed, researchers have sought to make use of this to promote transport of nanoparticles across the blood-brain barrier ⁵¹.

1.2.3 Clathrin- and caveolin-independent mechanisms of endocytosis

Glycosylphosphatidyl inositol (GPI) linked proteins can also be internalised through pathways that are independent of clathrin and caveolin ⁵². One mechanism is cholesterol-dependent and gives rise to GPI-AP enriched early endosomal compartments (GEEC) ⁵². Activation of cdc42 on the plasma membrane leads to actin polymerisation and the generation of endosomal invaginations in a dynamin independent manner ⁵³. GEECs are acidic in nature and undergo fusion with sorting endosomes ⁵⁴. Another such endocytic pathway is via flotillins, membrane associated proteins which are thought to have a number of functions including structural, sensing, and endocytic roles ⁵⁵. Flotillins 1 and 2 form microdomains on the cytoplasmic side of the cell membrane ⁵⁶ and have been shown to bud and are thought to be responsible for the internalisation of cholera toxin ⁵⁷. The importance of these pathways as they pertain to nanoparticle delivery is not yet clear as there are no studies that point to them being major uptake pathways compared to clathrin and caveolin dependent mechanisms ¹⁷.

1.2.4 Macropinocytosis

Macropinocytosis is a process, stimulated by growth factor activation of receptor tyrosine kinases, which leads to the engulfment of fluid into inhomogeneous vacuoles with sizes between 0.5 and 10 µm known as macropinosomes ⁵⁸. Actin drives the extension of the plasma membrane as membrane ruffles, which form a cup-like structure that subsequently

seals forming a nascent macropinosome ⁵⁹. After internalisation, the macropinosome interacts with the endosomal pathway, eventually fusing with lysosomes to form an acidic macropinolysosome ⁵⁹. Nano- and microparticles that are in close proximity to the cell can therefore be taken up by this non-specific mechanism, and because macropinocytosis takes place in almost all cell types, it therefore represents a common pathway for nano and microparticle internalisation ⁶⁰. In addition, the rate of macropinocytosis is known to be higher in immune and cancer cells and so this pathway is of particular interest in vaccines and cancer therapy ⁶⁰.

1.2.5 Phagocytosis

Phagocytosis is a process for internalising larger (diameter >500nm) particles and only takes place in specialised cells such as macrophages, neutrophils, monocytes, osteoclasts, eosinophils, and dendritic cells ⁶¹. These cells are responsible for the removal of pathogens, foreign particles, and cellular debris as part of the immune response. The process of phagocytosis can be considered to take place in three main stages; particle recognition, particle internalisation, and phagosome maturation ⁶².

Particle recognition

On the surface of phagocytic cells exist a diverse array of receptors to enable the recognition and binding of foreign particles. Pattern recognition receptors bind pathogen-associated molecular patterns (PAMPs) located on the surface of pathogens, for example bacterial and fungal particles, and are also involved in binding unopsonized particles ⁶³. These include Scavenger receptors (A and B-type) ⁶⁴, and lectins, including mannose and dectin receptors ⁶⁵⁻⁶⁶. On the other hand, opsonic receptors such as Fc receptors ⁶⁷ and complement receptors ⁶⁸ bind particles that have been exposed to opsonins (immunoglobulins and complement components respectively) which adsorb onto the particles, enabling their recognition by macrophages ⁶⁹. Additionally, in response to external stimuli, for example binding of LPS to

toll-like receptor 4 (TLR4), expression of certain receptors ⁷⁰ and their affinity towards specific ligands ⁷¹ is increased thus modulating the macrophage response to different particle types.

Particle internalisation

Particle binding to each receptor type triggers signal transduction pathways unique to the type of receptor bound. Fc and complement receptor signalling pathways have been well studied whereas the exact mechanisms of scavenger receptor-mediated phagocytosis have not yet been fully elucidated due to their structural heterogeneity and functional overlap ⁷².

Upon binding of Fc receptors by a particle opsonised with IgG, tyrosine residues present on the cytoplasmic Fc receptor domains, are phosphorylated by tyrosine kinases which are then able to act as a docking site for the tyrosine kinase SYK ⁷³. SYK phosphorylation drives the activation of LAT and Gab2, which triggers secondary messengers such as phospholipase C to activate protein kinase C triggering calcium release and VAV activation of Rho, RAC, and Cdc42 GTPases. These drive actin polymerisation via WASP and Scar activation of the actin nucleation ARP2/3 complex ⁷³. Actin polymerisation causes the extension of pseudopods surrounding the particle as a cup.

Unlike in the case of Fc receptor mediated phagocytosis, complement receptor mediated phagocytosis does not require tyrosine kinases ⁷⁴. It has been suggested that the formation of pseudopodia surrounding the particle does not occur, instead, the particle appears to sink into the cell membrane ⁷⁵. However, this is disputed, as other studies have reported an internalisation mechanism involving membrane ruffles ⁷⁶. Upon receptor binding, Rho is activated through an as yet undefined mechanism, which leads to Rho kinase and mDia1 activation and actin polymerisation via the Arp2/3 complex ⁷⁷. mDia1 also interacts with CLIP-170 which binds directly to the microtubule cytoskeleton ⁷⁸. Complement receptor mediated phagocytosis therefore proceeds through a cooperation of both actin and microtubules.

The process of sealing the phagocytic cup is less well understood but is known to involve PI3-kinase. When PI3-kinase inhibitors are used, the extension of pseudopods surrounding the

particle proceeds but phagosome closure is inhibited ⁷⁹. Myosin IC has also been implicated in the constriction of the cup in a purse-string-like mechanism that pulls the particle towards the cell ⁸⁰. Recently, it has been demonstrated that dynamin 2 plays a role in the scission of the nascent phagosome from the plasma membrane ⁸¹.

Phagosome maturation

The process of phagosome maturation describes the alteration of the phagosomal membrane and contents towards a phagolysosome which contains an environment designed to breakdown internalised particles. In early phagosome formation, Rab5 promotes fusion of the phagosome with early endosomes, which slightly lowers the luminal pH to 6.1-6.5 ⁸². At the same time recycling of the phagosomal membrane to the plasma membrane and trans-golgi network occurs, so the size of the phagosome remains unaltered. This process continues to occur throughout the maturation process ⁸³. Accumulation of Rab 7 promotes late phagosome formation by recruitment of Rab interacting lysosomal protein (RILP) which mediates centripetal movement of the phagosome to bring it in contact with SNARE proteins such as VAMP 7/8 which promote fusion with endosomes and lysosomes ⁸⁴. During this stage the pH of the lumen is further decreased to pH 5.5-6 due to V-ATPases which, coupled with the presence of newly acquired proteases, increases the degradative capacity of the late phagosome ⁸⁵. Fusion of lysosomes with the late phagosomes marks the final stage of the process by formation of the phagolysosome. LAMP proteins are now present in the membrane and the environment inside the lumen is optimal for the breakdown of internalised protein, in particular by cathepsins ⁸⁶. Reactive oxygen species (ROS) are generated by NADPH-oxidase through generation of O_2^- which can undergo dismutation to H_2O_2 which in turn can generate hydroxyl radicals and singlet oxygen ⁸⁷. Similarly, reactive nitrogen species (RNS) such as NO are generated by nitric oxide synthase and are further converted to species such as NO_2 , $ONOO^-$, N_2O_3 , and HNO ⁸⁸. These highly toxic species serve the purpose of destroying internalised pathogens.

1.2.6 Measures of particle uptake

There are a number of methods that have been used in the literature to determine particle uptake by cells including qualitative and quantitative methods, these are discussed in detail in chapter 3. Particle internalisation is expressed in different ways depending on the method used, for example when using flow cytometry, often the percentage of cells which are above a certain fluorescence threshold is reported ⁸⁹. On the other hand, the amount of material internalised per cell (mass, number of particles etc.) has been determined using methods such as inductively coupled plasma mass spectrometry (ICP-MS) ⁹⁰. Alternatively, the amount of particles not taken up by cells has been used to infer particle uptake ⁹¹. Each is a valid measure of uptake, however, the measure used should be taken into consideration when comparing the results of different studies, as this can affect the interpretation of results. It is also important to ensure that particles that are attached to the cell surface, but not internalised are distinguished from those that have been internalised. This may require extensive washing or trypsinisation to remove the adhered particles, or alternatively quenching of extracellular fluorescence ⁹². This is not always carried out and so what is reported is cellular association rather than particle uptake.

1.3 Particle properties affecting cellular uptake

Properties of particles that have been shown to affect cellular uptake include particle size, shape, surface chemistry, charge, and mechanical properties (figure 1.2). Development of the research in this area provides opportunities to rationally design drug delivery systems based on the desired therapeutic outcome. This section reviews studies investigating the effects of particle properties on cellular uptake.

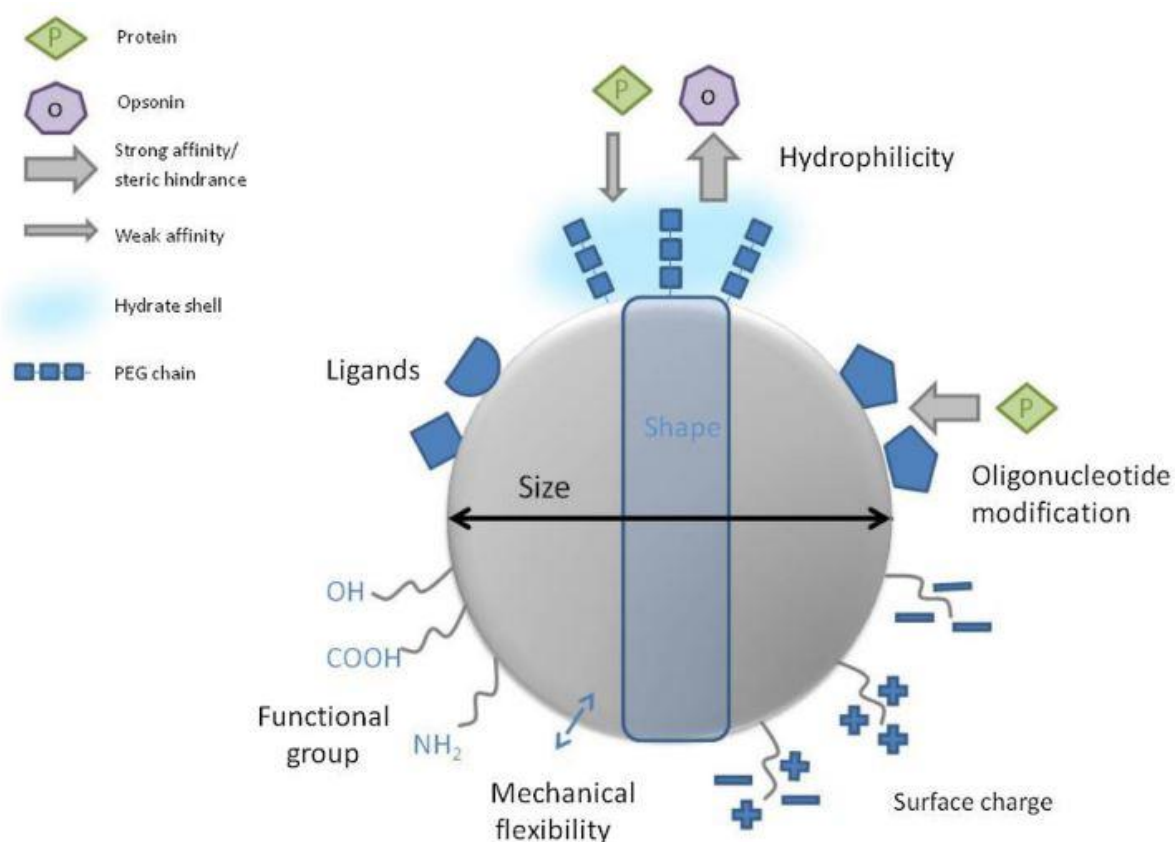


Figure 1.2: Particle properties affecting cellular uptake. Schematic representation depicting modifications that can be made to particulate delivery systems in order to modulate cellular uptake from ref ⁹³

1.3.1 The effect of particle size on cellular uptake

A number of studies have specifically investigated the effects of modulating the size of nano/microparticles on cellular internalisation. Wang *et al.* studied the uptake of gold nanoparticles (diameters 13, 45, 70, 110 nm) into CL1-0 (a lung cancer cell line) and HeLa

cells ⁹⁴. In both cell lines they found that 45 nm particles were internalised to the greatest extent. Differences in internalisation between different sized particles were explained by consideration of a) binding energy between ligands and receptors and b) thermodynamic driving force of membrane wrapping. For nanoparticles <40 nm in diameter, binding of a single particle does not produce sufficient free energy to trigger internalisation and so particles below this size enter cells only when clustered together, this reduces their uptake compared to particles >50 nm in diameter ⁹⁴. For larger particles, >80 nm in diameter, endocytosis occurred rarely. This was attributed to the depletion of free receptors limiting the ligand-receptor binding energy and resulting in partial wrapping of the particles ⁹⁴. In a study by Lu *et al.* the uptake of mesoporous silica nanoparticles (diameters 30, 50, 110, 170, 280 nm) by HeLa cells was assessed ⁹⁵. In agreement with Wang *et al.* it was demonstrated that nanoparticles of 50nm diameter had the highest internalisation. Other studies by Osaki *et al.* (glycosylated quantum dots in HeLa cells) ⁹⁶, Jiang *et al.* ⁹⁷ (gold nanoparticles in SK-BR-3 cells), and Chithrani *et al.* (gold nanoparticles in HeLa cells) ⁹⁸ also concurred that 50 nm particles are taken up most efficiently by cells.

In contrast to the above, Xu *et al.* demonstrated that, in Caco-2 and HT-29 cell lines, particles of diameter 100 nm were taken up to the greatest extent ⁹⁹. Kulkarni and Feng also showed that 100 nm particles were taken up most by Caco-2 and MDCK cells ¹⁰⁰. It is possible that the optimum particle size for uptake is cell-line dependent and so this factor should be taken into consideration when considering particle size modulation for a particular application.

He *et al.* measured the uptake of different sized polymeric nanoparticles across a range of different cell lines including LO2 (hepatocyte), HEK-293 (kidney), 786-O (kidney), HFL-1 (lung fibroblast), A549 (lung epithelial), SMMC-7721 (hepatocarcinoma) as well as freshly harvested murine macrophages ¹⁰¹. It was shown that larger particles (300 and 500 nm) were taken up by the murine macrophages to a greater extent than smaller (150 nm) particles, however in the non-phagocytic cell lines the opposite was the case, with smaller particles being taken up more than larger particles. This suggests that, as a result of their specialised capacity for

engulfing particles, the optimum particle size for internalisation into macrophages may be different from other cell types. This is potentially useful for drug delivery because often it is desirable for an administered particle to avoid macrophage clearance while having enhanced uptake into the desired cell type.

On the other hand, in a study by dos Santos *et al.* which compared the effect of polystyrene particle size on cellular uptake in cell lines including HeLa (epithelial), A549 (lung epithelial), 1321N1 (brain astrocytoma), HCMEC D3 (brain endothelial), and RAW 264.7 (macrophage) cell lines, it was shown that, although differences in the amount of particles taken up by cells did arise, (in the order RAW 264.7 > HCMEC D3 > 1321N1 > A549 > HeLa) the optimum particle size for maximum uptake was the same in all cell lines (40 nm) ¹⁰².

A number of studies comparing effect of particle size on internalisation into macrophages have demonstrated that the optimum particle size for phagocytosis is 1-2 μm ¹⁰³⁻¹⁰⁷. In one such study, an important distinction is made between the number of particles and the total volume of particles ingested per cell ¹⁰⁷. Although there was a higher number of 430 nm particles internalised than 1.9 μm particles, the total volume of particles inside the cells was higher for the larger particles which equates to a higher intracellular dose in the context of drug delivery.

As discussed earlier, the endocytic pathways have varying size limits, so larger particles will be able to make use of fewer endocytic pathways. For example, in cells without phagocytic capacity, the only mechanism through which micron-sized particles may enter the cell is by macropinocytosis, whereas 50 nm particles can make use of each of the clathrin/caveolin-dependent and independent mechanisms.

1.3.2 The effect of particle hydrophobicity on particle uptake

Another factor shown to modulate particle uptake is hydrophobicity. Tabata and Ikada investigated the effect of hydrocarbon chain length on the uptake of cellulose microspheres on uptake by mouse peritoneal macrophages ¹⁰⁸. It was shown that the number of particles

taken up per cell was increased with increasing chain length up to a maximum of 8 carbons. Increasing the chain length further resulted in a decrease of particle uptake. The contact angle of particles with maximum uptake was 50-60°.

In a similar study by Lorenz *et al.* the effect of hydrophobicity on the uptake of poly(methacrylate) nanoparticles by HeLa, Jurkat, Kg1A, and mesenchymal stem cells was examined ¹⁰⁹. In all cell lines, particle uptake increased with increasing hydrophobicity.

Studies generally indicate that more hydrophobic particles tend to elicit higher uptake by cells, although the reason for this is not clear. Hydrophilic polymers have commonly been used in order to decrease particle uptake ¹¹⁰ and so it may be that hydrophobic particles display enhanced interaction with the lipophilic cell membrane. Alternatively, it has been suggested that hydrophobic particles alter the composition of the protein corona, resulting in increased uptake ¹¹¹. The effect of protein corona is discussed in section 1.3.5.

1.3.3 The effect of particle surface charge on particle uptake

It is difficult to study the effect of particle surface charge in isolation owing to the fact that surface chemistry also plays a role in particle uptake, and this must be modified to alter the surface charge. Nonetheless, by studying particle uptake across a range of particle types and surface chemistries, the effect of surface charge on uptake has been elucidated.

He *et al.* studied the uptake of chitosan-based nanoparticles with zeta potential values between -40 and +35 mV by murine macrophages ¹⁰¹. It was shown that regardless of the sign of the charge, a higher magnitude of the zeta potential increased particle uptake. Additionally, positively charged particles appeared to be taken up by a higher percentage of cells than negatively charged particles.

Gratton *et al.* compared the internalization of 1µm microparticles with amines on the particle surface (ζ potential = +23 mV) against the same particles after blocking the amines with acetic anhydride (ζ potential = -19 mV) ¹¹². In each of the cell lines tested (HeLa, 3T3, OVCAR-3,

MCF-7, RAW 264.7) microparticles with positive zeta potential were internalised by a higher percentage of cells with the exception of RAW 264.7 cells.

The majority of studies have shown that positively charged particles are internalised by cells favourably compared to negatively charged particles ^{35, 113-115}. On the other hand, some studies have shown the opposite effect ¹¹⁶. It has been suggested that positively charged particles associated with cells to a higher extent, due to their electrostatic interaction with the negatively charged cell membrane. However, as pointed out by Forest *et al.*, this fails to take into account the protein corona and its effects on the biological identity of the particle and how this affects uptake ¹¹⁷.

1.3.4 The effect of particle surface chemistry on cellular uptake

The effect of particle surface chemistry has been studied with a particular focus on enhancing particle uptake through the use of targeting ligands. The range of targeting ligands is diverse and includes small molecules (e.g. folic acid ¹¹⁸, biotin ¹¹⁹, mannose ¹²⁰, sialic acid ¹²¹), proteins and peptides (e.g. concanavalin A ¹²², wheat germ agglutinin ¹²³, RGD peptides ¹²⁴, transferrin ¹²⁵, endothelial growth factor ¹²⁶) and antibodies (e.g. Herceptin ¹²⁷, rituximab ¹²⁸). On the other hand there is also a need to avoid uptake and subsequent clearance of particles by the reticuloendothelial system (RES) ¹²⁹. Few surface chemistries have been identified that are able to achieve this goal, however poly(ethylene glycol) (PEG) coatings have been used extensively for this purpose ¹³⁰. Other stealth chemistries that have been studied include poly(oxazolines) ¹³¹, betaines ¹³², and polyglycerols ¹³³. A delicate balance of targeting and stealth properties must be struck in order to actively target the site of action and prolong residence time simultaneously ¹³⁴. One way in which this problem has been addressed is by attaching PEG by a linker which degrades in response to a stimulus at the site of action. The active targeting groups can then be exposed in order to enhance particle uptake by the desired cells. Guo *et al.* have employed this strategy in the case of tumours that over express matrix metalloproteinases (MMPs) ¹³⁵.

1.3.5 Protein corona formation on nano and microparticles

When nano and microparticles are exposed to biological fluids, adsorption of proteins takes place, resulting in the formation of the so-called protein corona¹³⁶. The particle is surrounded by a tightly bound layer of adsorbed proteins referred to as the hard corona, which in turn is surrounded by a more loosely bound layer of proteins referred to as the soft corona¹³⁷. Exchange of adsorbed proteins takes place between the protein corona and the biological milieu. The identity of the proteins that adsorb on to the surface of the particle is dependent on particle properties such as size, surface chemistry, hydrophilicity, and charge, and the composition of the biological medium¹³⁸. Upon initial immersion in biological fluids, more abundant proteins adsorb first, these are later exchanged with proteins that have more affinity to the particle surface¹³⁹.

Recently, there has been much interest in the relationship between how particle properties determine the make-up of the protein corona and how the resulting protein corona affects particle-cell interactions.

Tenzer *et al* studied the effect of surface chemistry modifications on protein adsorption using silica nanoparticles with carboxylic acid or amine groups on their surface¹⁴⁰. It was found that, as the incubation time of the particles in human plasma increased, the profiles of protein corona changed depending on the surface chemistry. The same result was observed when comparing bare silica and polystyrene nanoparticles. Silica particles displayed an abundance of apolipoprotein E and A-I which have been associated with enhanced particle uptake into cells¹⁴¹⁻¹⁴². Curiously, negatively charged proteins represented the majority of bound proteins to all particle types irrespective of particle type and surface charge. This indicates that overall protein charge may be less important than the interaction of individual binding domains within the protein structure for corona formation¹⁴⁰.

In another such study, Ashby *et al.* utilized iron oxide nanoparticles with surface modifications of increasing hydrophobicity to study the impact on corona constituents¹⁴³. It was shown that the profile of adsorbing proteins changed with varying surface hydrophobicity and moreover,

a wider variety of proteins adsorbed on to more hydrophobic particles. Proteins with more hydrophobic binding domains were found to bind hydrophobic particles more favourably. The effect of particle size was also examined with larger particles (25 nm) adsorbing higher quantities of protein due to their higher surface area and displaying a different protein profile to smaller particles (15 nm) of the same surface chemistry.

However, another important consideration is the ability of the nanoparticle surface to denature the protein structure upon binding, resulting in a loss of functionality. The effect of gold nanoparticle surface charge on cytochrome C structure has been studied ¹⁴⁴. It was found that particles with a neutral surface charge did not have any significant effect on protein structure. However, when adsorbed onto positively and negatively charged particles, changes in protein structure took place. In the case of positively charged particles, the change in protein structure was significant enough to result in a loss of redox activity.

The orientation of the protein is also a factor in determining its functionality when adsorbed on to the particles surface. Wang *et al.* studied the orientation of transferrin when adsorbing onto gold nanoparticles modified with surface ligands of different chirality ¹⁴⁵. The binding of transferrin to the transferrin receptor was then shown to be dependent on its orientation. This is therefore a key consideration when designing nano/microparticles with targeting ligands, it is not simply enough to display the ligand on the particle surface, but it must also present to the receptor in the correct manner. In a study by Jain *et al.* the orientation and conformation of cytochrome C on the surface of gold nanoparticles was modulated by controlling the underlying surface chemistry ¹⁴⁶. This affected the apoptosis inducing capability of the particles by altering the availability of the heme ring to interact with apoptosis initiating protein (APAF-1).

It is thought that the mechanism through which PEGylation of nanoparticles extends their residence time in the body, is by the reducing the formation of the protein corona which reduces interaction with immune cells ¹⁴⁷. It is not the total prevention of corona formation, but the prevention of binding of certain proteins that promote particle uptake ¹⁴⁸. Recently,

zwitterionic coatings have been explored for their similar ability to reduce protein adsorption and thus offer an alternative coating to pegylation ¹⁴⁹⁻¹⁵⁰.

1.4 Particle shape

The advent of novel methods for fabricating particles of various morphologies has resulted in increased interest in assessing the impact of particle shape on cellular interactions. The majority of studies assessing the effect of particle shape have utilised particles with nano-sized dimensions owing to their potential use in systemic drug delivery as opposed to micron sized particles which tend to be cleared faster from the body ¹⁵¹. Below, methods for manufacturing nano and microparticles as well as studies on the effect nanoparticle and microparticle shapes on cellular uptake are discussed.

1.4.1 Methods for making nano and microparticles of different shapes

There are a wide variety of methods for fabricating nano and microparticles of different shape. These can broadly be divided into bottom-up methods whereby the starting material is on the atomic length scale and is then built up until they are of nano/microscale dimensions and top-down methods whereby bulk material is reduced in size until it is of nano/microscale dimensions ¹⁵². Both methods have their own advantages and disadvantages for example bottom-up approaches are often more easily scaled up, however they can lack the precision in terms of polydispersity of top-down approaches. On the other hand, top-down approaches tend to lose this precision when nanometre-sized (<100 nm) features are required ¹⁵². In the following sections an overview is given of some of the methods used to make nano and microparticles of different morphologies.

1.4.1.1 Bottom-up methods

Synthesis of Gold and Silver nanoparticles

The synthesis of spherical gold nanoparticles occurs via a seed-mediated growth mechanism. Typically a solution of chloroauric acid (HAuCl_4) is mixed with a reducing agent such as sodium citrate or sodium borohydride which converts the gold from an oxidation state of +3 to 0 (atomic gold) ¹⁵³. The aggregation of gold atoms causes the formation of the initial seeds (~1.5nm) and subsequent reaction with AuCl_3 causes the growth of seeds into larger nanoparticles (10-200nm) ¹⁵³. For synthesis of citrate stabilised nanoparticles (known as the Turkevich synthesis) the final size of the gold nanoparticles can be determined by the ratio of gold to citrate ¹⁵⁴. In this case the citric acid acts as both a reducing agent and a stabilising agent preventing aggregation of the nanoparticles ¹⁵⁵. In a method devised by Brust *et al*, a two-phase system is used whereby sodium borohydride is used as the reducing agent, tetraoctylammonium bromide as a phase transfer agent, and dodecanethiol as a stabilising agent ¹⁵⁶. This method allows for the production of highly stable nanoparticles (1-5nm) which can be further functionalised for the desired application.

The synthesis of different shaped gold nanoparticles makes use of the same seed-mediated growth mechanism as spherical particles, however after the initial growth of the gold seeds different reducing agents and surfactants are added to direct the growth of the nanoparticles towards the desired shape ¹⁵⁷. In particular, the addition of silver nitrate along with surfactants to the gold seeds has been shown to aid in the growth of anisotropic particles. It is thought that different amounts of deposition of silver ions onto the different facets of the gold seed crystal helps to slow/inhibit crystal growth along facets with higher coating thus resulting in anisotropic particles ¹⁵⁷.

Lui and Guyott-Sionnest demonstrated that by the addition of cetyltrimethylammonium bromide (CTAB), silver nitrate, and L-ascorbic acid to gold seeds it was possible to form highly uniform populations of nano rods or bipyramidal particles depending on whether the seeds were synthesised using CTAB or sodium citrate ¹⁵⁸. By maintaining the same concentration of

silver nitrate and varying the concentration of gold seeds the aspect ratio of the gold nanorods can be controlled. Using a similar procedure Sau and Murphy were able to synthesise gold cubes, hexagons, triangles, tetrapods and stars by changing the ratio of reactants, some of these are shown in figure 1.3 ¹⁵⁹. It is important to note that due to the use of surfactants during nanoparticle synthesis, the surface chemistry of the different particles produced using these methods is likely to be different and so this should be considered when comparing different shapes for biological applications.

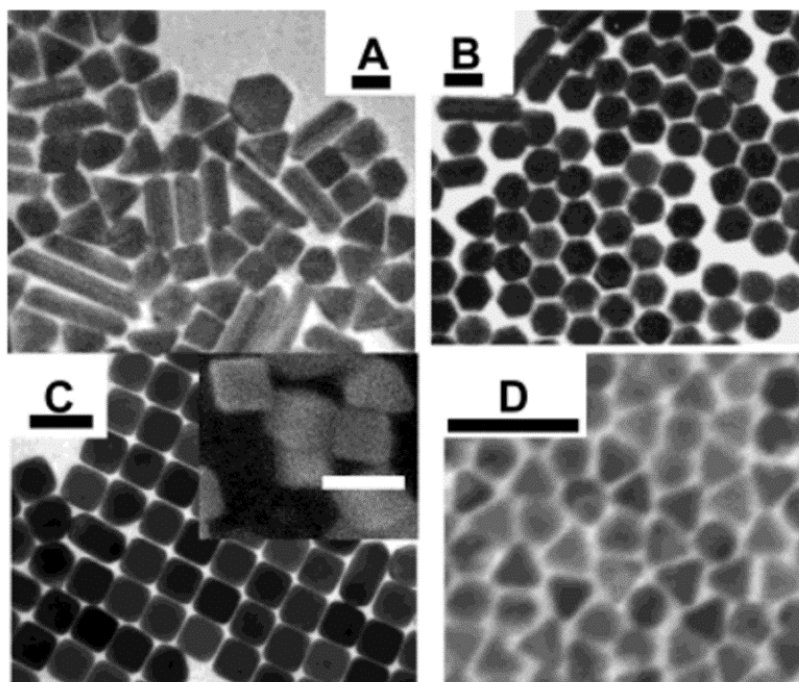


Figure 1.3: Gold nanoparticles of different morphology. TEM images of A) mixture of rods, hexagons and triangles B) hexagonal particles, C) Cubes, D) Triangles. Adapted from reference ¹⁵⁹, Scale bars = 100 nm

In the case of silver nanoparticles, the formation of nanoparticles of different morphology can be achieved using similar methods to those described above ¹⁶⁰. Another common method (which can also be used to form gold nanoparticles of different morphology) is the so called polyol method ¹⁶¹. In this method ethylene glycol or similar compounds are used as the

reducing agent and solvent for silver nitrate and a polymer such as poly(vinyl pyrrolidone) is used as a stabiliser. Shape control is brought about by deposition of the stabiliser on different facets of the seed crystal which can be altered by the addition of various ions ¹⁶². In particular, sulphide ions have proven to enhance the reduction of silver nitrate ions and has been used to aid in scaling up the process ¹⁶³. Due to the high dependence of crystal shape on the ions present in the reaction mixture, it is very important to use starting materials of high purity. Similarly to gold, silver nanoparticles of myriad different shapes including rods, cubes, wires, bars, pyramids, prisms, as well as branched structures have been synthesised ¹⁶⁴⁻¹⁷⁰.

Synthesis of silicon oxide nanoparticles

The most common method for making spherical silicon oxide nanoparticles is the Stöber method ¹⁷¹. The process involves the hydrolysis and condensation of alkoxysilicate precursors such as tetraethyl orthosilicate (TEOS) in alcohol/water solutions under different conditions ¹⁷¹. As the condensation reaction proceeds Si-O-Si bonds are formed and this results in the formation of silicon oxide nanoparticles. Depending on the pH of the solution the particles will aggregate into a gel-like network (low pH) or remain as dispersed nano/microparticles (high pH) ¹⁷². High pH reaction mixtures are obtained by the addition of ammonia (NH₃) and by varying the concentration of NH₃ and other parameters such as temperature and rate of reactant addition, it is possible to control the size of the particles ¹⁷³.

By the addition of surfactants such as cetrimonium bromide into the Stöber process it is possible to synthesise silica nanoparticles that possess pores that are of tailorable size (between 2 and 50nm) and are thus termed mesoporous silica particles ¹⁷⁴. During this process the surfactant acts as a micellar template and is subsequently removed from the particles by heating at high temperatures (>500°C) ¹⁷⁵. This surfactant template method can be used to make rod-shaped silica nanoparticles and can be thought of as a soft-template

method ¹⁷⁶. Other soft templates used, include bacteria, viruses, and lipid nanotubes ¹⁷⁷⁻¹⁷⁹.

Figure 1.4 shows particles that have been fabricated using biological soft templates.



Figure 1.4: Particles fabricated using soft templates. SEM images of g) Cocci templated particles h) *E. coli* templated particles i) Mildew fungus templated particles. Adapted from reference ¹⁷⁸

In contrast to soft templates are hard template methods where a silica shell is grown onto an pre-fabricated solid nanoparticle of the desired morphology, thereafter the template can then be removed by means such as selective etching, resulting in hollow silica particles ¹⁸⁰. Alternatively, the template particle can remain at the core of the silica particle and thus, depending on the core material, the particle will have added properties for example magnetism in the case of an iron core ¹⁸¹. Hard template methods have employed starting materials such as calcium carbonate, aluminium oxide, gold, and haematite ¹⁸²⁻¹⁸⁵. Therefore, the particle morphologies that can be made using this method are those of the template particles including silica rods, cubes, ellipsoids, sheets, octahedrons and dodecahedrons ¹⁸⁶⁻¹⁹⁰. Figure 1.5 shows hollow silica particles fabricated using a hematite template that was subsequently removed.

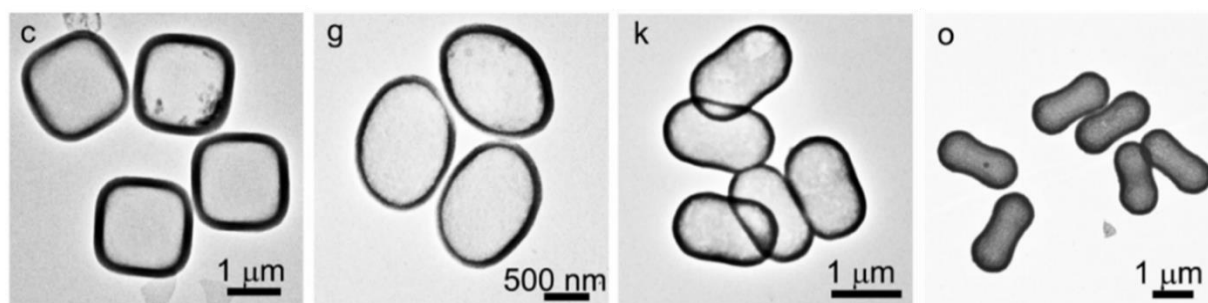


Figure 1.5: Hollow silica particles fabricated using a hematite template. TEM images of c) pseudocubes g) ellipsoids k) capsules o) peanuts ¹⁸⁵.

Curiously, nature has its own way to make silica nano/microparticles with incredibly diverse morphology in the form of diatoms, single-celled algae existing in the oceans and waterways that possess a cell wall made of silica ¹⁹¹. Diatoms themselves have been used as the template for nanoparticle synthesis and for drug delivery applications ¹⁹²⁻¹⁹⁴.

Synthesis of polymeric nanoparticles

Polymeric nanoparticles represent a promising avenue for developing novel therapeutics and as such have been the focus of many researchers. Resulting from this are numerous methods of polymer nanoparticle synthesis including solvent evaporation, nanoprecipitation, emulsification, salting out, dialysis, and spray drying ¹⁹⁵⁻²⁰⁰.

These methods utilise either natural polymers such as chitosan, gelatin, or alginate or synthetic polymers such as poly(lactide co-glycolic acid) (PLGA), poly(ethylene glycol) (PEG) and combinations thereof ²⁰¹⁻²⁰⁴. By using block co-polymers with opposing polarities and different block lengths it is possible to obtain polymers that self-assemble into nanoparticles of different shapes ²⁰⁵. Shapes such as rods (of varying length), vesicles, discs and toroids have been prepared by self-assembly ²⁰⁶⁻²⁰⁸. Self-assembly of polymeric particles tends to result in less uniform particle populations than the inorganic methods detailed above. Additionally, due to their structure being inherently dependent on their environment, the particles shape may be less stable and can change depending upon the conditions. As a tool for drug delivery, this property could be advantageous, for example shape-switching particles developed by Han *et al.* that switch from spherical to rod shape in response to changing pH

²⁰⁹.

1.4.1.2 Top-down methods

Film-stretching method

Originally developed by Nagy and Keller, the film stretching method utilises pre-fabricated polymer spheres which are deposited onto a heated PVA film and stretched ²¹⁰. Polystyrene latex spheres were stretched in this way resulting in a uniform population of ellipsoidal microparticles ²¹¹. The group of Mitragotri developed this method further by stretching in different directions and by altering the heating/stretching sequence to produce microparticles shaped like barrels, bullets, pills, pulleys, ribbons and disks (figure 1.6) ²¹². Other polymers such as PLGA and polycaprolactone (PCL) have been applied to this method with the advantages of being biodegradable and that drugs/fluorophores can be encapsulated into the particles during the initial synthesis steps ²¹³. As with polymeric particles synthesised using bottom-up methods, the stimuli responsive properties of polymers have been utilised to encourage shape switching after fabrication by the film-stretching method.

The film stretching method

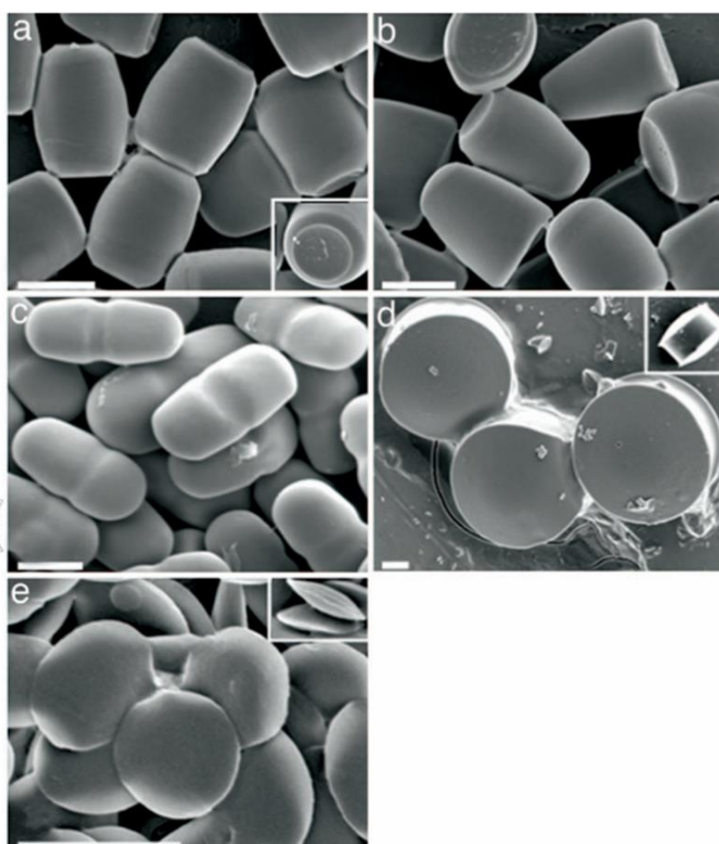
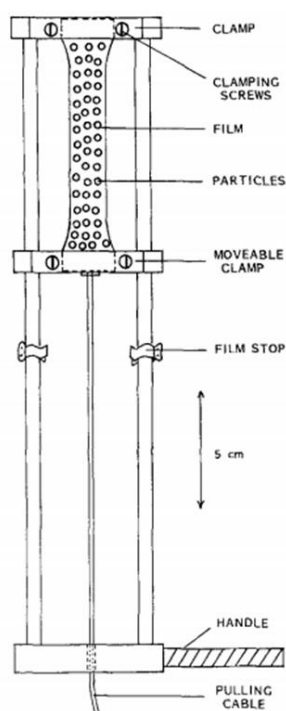


Figure 1.6: The film stretching method. Left: the film stretching method adapted from ²¹¹. Right: SEM images of polystyrene particles fabricated by stretching a) barrels b) bullets c) pills d) pulleys e) biconvex lenses adapted from reference ²¹²

Photolithography

Originally developed for use in the microelectronics industry, photolithography enables the patterning of micro/nanoscale topographies on to silicon wafers ²¹⁴. Computing power is limited by the number of transistors that can fit onto a single chip and over the past 50 years this number has doubled every two years following Moore's law ²¹⁵. This has been enabled by the advancement in photolithographic techniques that have allowed smaller and smaller features to be patterned on to silicon wafers. The technique works by deposition of layers of materials for example gold, copper or silicon oxide onto the silicon wafer and subsequent patterning using a photomask and photoresist (figure 1.7). Through selective etching processes, unwanted elements are removed and the final wafer possesses the micro/nanoscale pattern on its surface.

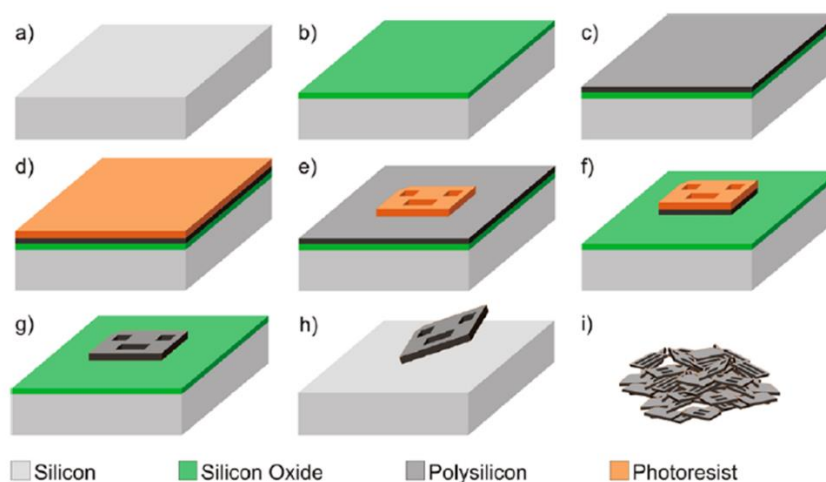


Figure 1.7: Photolithographic production of polysilicon particles a) Silicon wafer b) thermal growth of a sacrificial oxide layer c) deposition of a polysilicon device layer d) spin coating of wafer with photomask e) photolithographic step f) etching of device layer g) removal of photomask h) removal of sacrificial oxide layer i) particles are released into suspension. Adapted from ref ²¹⁶.

In order to fabricate particles using this technique, a sacrificial material layer which is present beneath the particle pattern can be etched away to release the particles from the wafer ²¹⁷. Control of particle shape in the X- and Y- dimensions is achieved by design of the photomask made by electron beam lithography (EBL) with feature sizes which can be in the range of 50-100 nm depending on the wavelength of light and photomask material required during the patterning process ²¹⁸. In the Z-dimension there is no direct control of shape in this way and so particles typically have flat top and bottom surfaces, however thickness of the particles can be controlled by controlling the thickness of the deposited material layer ²¹⁹. There are however, exceptions to this as shown by the group of Ferrari who fabricated bowl-shaped porous silicon microparticles with tailorable pore size by using a series of chemical etchings to form a hemispherical shape (figure 1.8) ²²⁰.

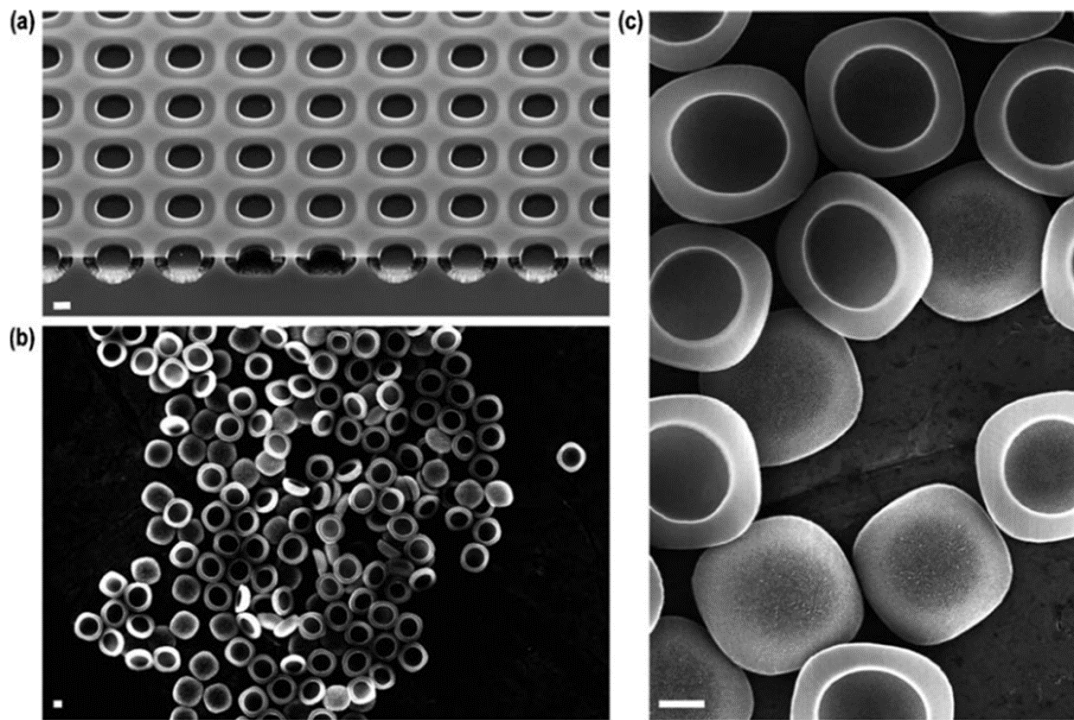


Figure 1.8: Porous silicon microparticles fabricated using photolithography: SEM images of a) bowl-shaped particles still attached to silicon wafer b,c) porous silicon particles after release from the wafer. Adapted from ref ²²⁰.

The group of Jose A. Plaza have fabricated polycrystalline silicon “barcode” particles whereby the morphology of each particle is coded for use in single-cell tracking ²²¹. Additionally the same group fabricated silicon oxide microparticles of varying aspect ratios and branching structures ²²².

Precise control over morphology, resulting in uniform particle populations, is an attractive feature of this technique from a drug delivery perspective, moreover this technique is scalable. However, there are a few limitations to consider. Firstly, the lowest size of the particles that can be produced using this technique is somewhat larger (typically on the order of a few microns) than those produced by bottom up methods which could limit the potential applications. Secondly, the type of materials used are predominately silicon based (silicon, silicon oxide, silicon nitride) the biocompatibility of which requires thorough assessment ²²³. Additionally, due to the specialised nature of this technique and the need for a clean room facility, this technique is not widely available.

Soft lithography

In order to circumnavigate some of the issues pertaining to hard lithography, lithographic methods utilising soft materials such as polymers and hydrogels have been developed. By using the same layer by layer deposition and photomask patterning methods, soft particles of various morphologies have been produced. Patterning can be achieved either by direct patterning of the soft substrate, or by the fabrication of a template using hard lithography and subsequent formation of particles by moulding also known as nanoimprint lithography. Li *et al.* used direct patterning of polyvinyl pyrrolidone (PVP) cross-linked with PEG triacrylate to produce microparticles (<10 µm) of different shapes and sizes incorporating fluorescent dextrans ²²⁴. It was demonstrated that particles could be fabricated comprising multiple polymer layers each incorporating a different fluorescent dextran. Using a similar method Hahgoorie *et al.* fabricated disks, rings, crosses and s-shaped particles all less than 10 µm in size ²²⁵. The diversity of shapes that can be produced is exemplified in a paper by Hernandez

and Mason who fabricated what they termed “colloidal alphabet soup” comprising microparticles $\sim 5\ \mu\text{m}$ in size in the shape of the letters of the alphabet (figure 1.9) ²²⁶.

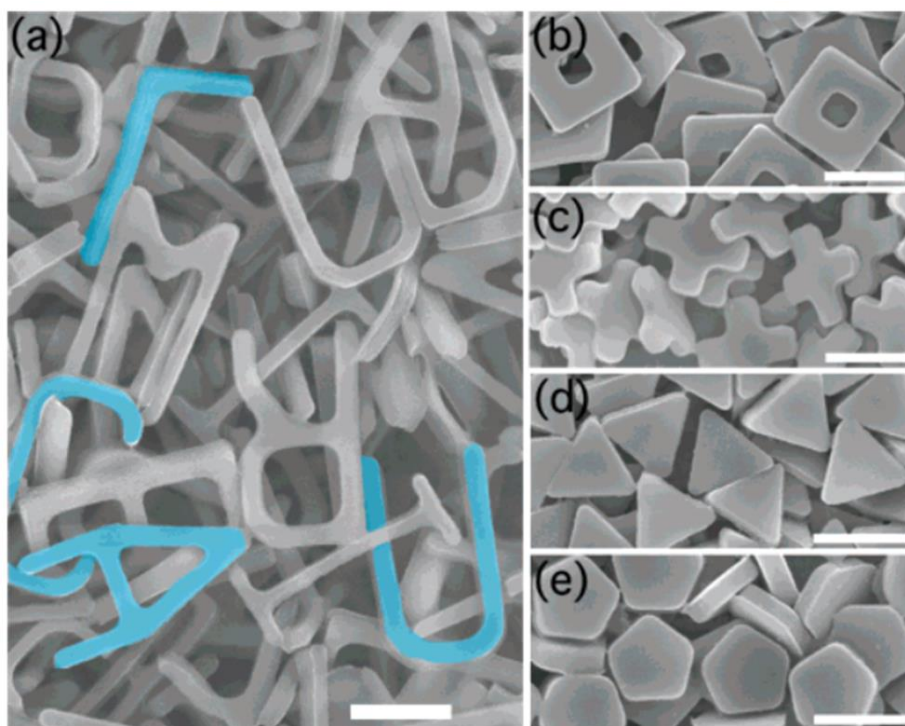


Figure 1.9: Colloidal alphabet soup: SEM images of a) Letters of the alphabet b) square doughnuts c) crosses d) triangular prisms e) pentagonal prisms. Scale bars = $3\ \mu\text{m}$. Adapted from ref ²²⁶.

Nanoimprint lithography can be considered as a more scalable alternative to direct photolithography owing to the fact that many polymer moulds can be fabricated from a single template. One problem is that the technique often results in particles that are stuck together via a residual layer which can be difficult to remove fully ²²⁷. The group of DeSimone overcame this challenge in a methodology they term particle-replication in non-wetting templates (PRINT) (figure 1.10) ²²⁸. By using a non-wetting perfluoropolyether (PFPE) as the material for the mould, an increase in the achieved printing resolution was demonstrated in comparison to polydimethyl siloxane (PDMS) moulds which have been used previously ²²⁹. This is due to the low surface energy of the PFPE mould which prevents the polymer solution from sticking to the non-void parts of the mould ²³⁰. Solidification of the particles can occur via U.V crosslinking or by solvent evaporation and particles are subsequently removed by adherence to a

dissolvable PVP sheet and peeling away of the mould. Using this method, a diverse array of particle shapes have been fabricated with sizes as low as 55x60 nm²³⁰⁻²³².

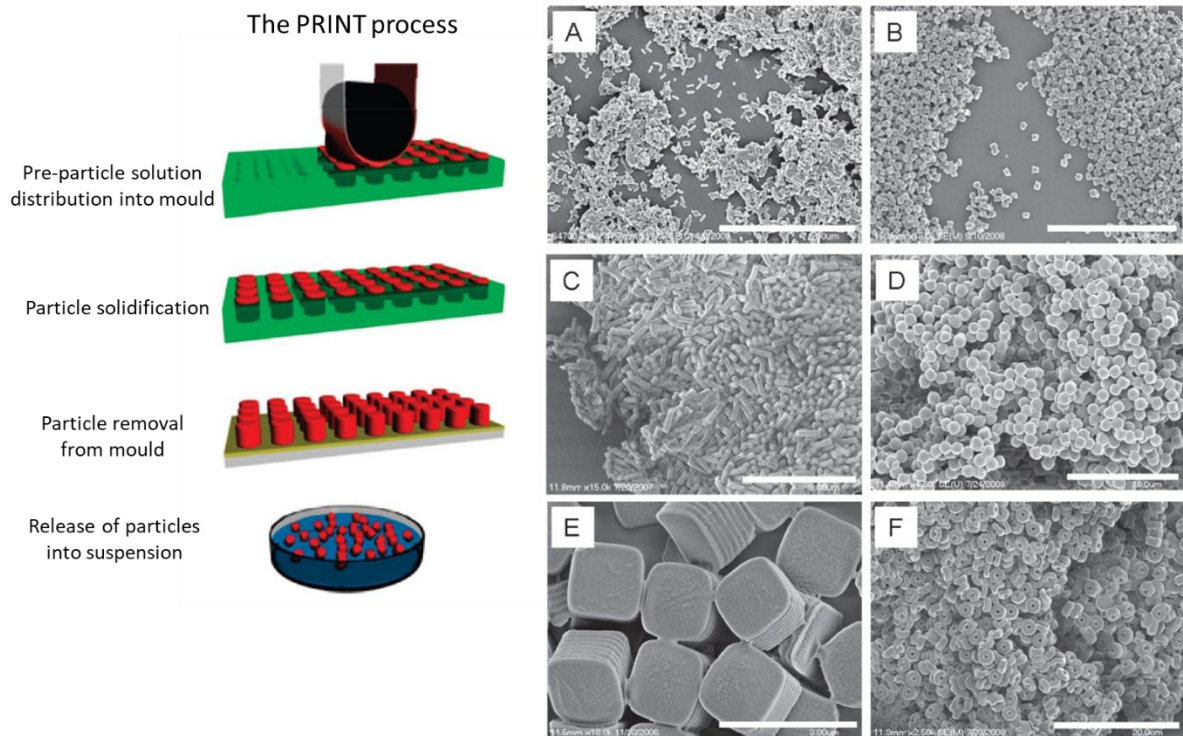


Figure 1.10: Particle replication in non-wetting templates (PRINT) Left: The PRINT process adapted from reference²³². Right: SEM images of PLGA PRINT particles; A) 80 x 320 nm cylinders B) 200 x 200 nm cylinders C) 200 x 600 nm cylinders D) 1 µm "sphere approximates" E) 2 µm cubes F) 3 µm "doughnuts". Adapted from ref²³⁰

A potential issue with these polymerisation methodologies is that monomers left over from the fabrication process are often toxic to cells and so care must be taken to remove these before use in biological systems²³³. Additionally, curing of the polymers using ionising radiation could damage sensitive biological molecules thus potentially limit its use.

1.4.2 The effect of nano and microparticle shape on cellular uptake

1.4.2.1 Studies on the effect nanoparticle shape on cellular uptake

Chithrani *et al.* studied the internalisation of gold nanoparticles of varying aspect ratio by HeLa cells ⁹⁸. Particles were synthesised as either rods (14 x 40 nm, 14 x 74 nm) or spheres (diameter 14 nm or 74 nm) and the number of particles per cell calculated by inductively coupled plasma atomic emission spectroscopy (ICP-AES). It was shown that the administration of particles with an aspect ratio of 1 (spheres), regardless of size, resulted in a higher number of particles per cell. In a further study by Chithrani and Chan spherical gold nanoparticles (diameter 50 nm) displayed increased uptake compared with a range of rod-shaped particles (20x30 nm, 14x50 nm, 7x42 nm) ²³⁴. Uptake of each nanoparticle shape was by clathrin-mediated endocytosis, however the exact mechanism through which rod-shaped particles displayed reduced uptake was not elucidated. Similarly Qiu *et al.* observed that the uptake of gold nanoparticles (diameter 30 nm) by MCF-7 cells decreased with increasing aspect ratio ²³⁵.

Yu *et al.* studied the association of unmodified and amine-modified silicon oxide spheres (diameter 115 nm), mesoporous silica spheres (diameter 120 nm) and mesoporous silica rods of aspect ratio 2, 4, and 8 (diameter ~100 nm) by RAW 264.7 macrophages and A549 epithelial cells. The cellular association of the different particle shapes was assessed using inductively coupled mass spectrometry (ICP-MS). Amine-modified particles exhibited higher association in both cell lines. No difference in cellular association was observed between the different mesoporous particle shapes in RAW 264.7 cells. In A549 cells similar results were seen as in RAW 264.7 cells apart from amine-modified aspect ratio 8 rods which showed significantly higher association than the other amine-modified mesoporous particles ²³⁶.

In a similar study by Herd *et al.* the association of silica “worms” (232 x 1348 nm) and spheres (diameter 178 nm) by RAW 264.7 was examined by flow cytometry and showed that spheres exhibited a higher cellular association than worms ²³⁷. Furthermore, inhibitor studies demonstrated that the primary uptake mechanism was different for worms and spheres. The

uptake of worms was primarily inhibited by colchicine indicating active uptake by phagocytosis as the primary uptake mechanism. In contrast, the uptake of spheres was primarily inhibited by chlorpromazine indicating that clathrin-mediated endocytosis was the major mechanism of uptake ²³⁷. In contrast to the above study, Huang *et al.* found that rod shaped mesoporous silica particles (110 x 240 nm and 110 x 450 nm) had higher association with A375 epithelial cells than spherical particles (d = 100 nm) ²³⁸.

The disparate uptake of nanoparticles of different shapes seems to result from their utilisation of different uptake pathways which is largely dependent on overall particle size, however despite this, particles of different shapes, internalised by the same endocytic mechanism have shown differences in uptake ⁹⁸. Theoretical studies have suggested that differences in the efficiency of membrane wrapping of different shaped particles also plays a significant role ²³⁹.

1.4.2.2 Studies on the effect of microparticle shape on cellular uptake

Champion and Mitragotri used the film stretching method to fabricate a wide array of particle shapes (oblate and prolate ellipsoids, elliptical disks, rectangular disks and UFO-shaped particles) across a range of volumes and assessed whether or not uptake occurred in macrophages by direct observation ²⁴⁰. Whether or not particle internalization occurred was expressed in terms of the particle shape and the angle of particle contact with the cell membrane. Internalisation occurred only when the initial point of contact was with the major axis (the smaller axis of an anisotropic particle) of each particle shape. Although this study gives insight into the reason why particles of different shapes may or may not be internalised in discrete circumstances it did not assess the overall differences in internalisation between particle shapes. Inspired by this study, worm-like particles with high aspect ratio (AR=20) were designed that showed reduced internalisation by macrophages in comparison with spheres of equivalent volume ²⁴¹.

In a study by the same group, comparing the uptake of spheres, prolate ellipsoids and oblate ellipsoids by macrophages, there was no difference observed between particle shapes derived from 3.6 μm diameter spheres ²⁴². However, in particles derived from 0.5 μm and 1 μm spheres, oblate ellipsoids and spheres showed higher uptake than prolate ellipsoids. A further study comparing internalisation of spheres (diameter 5 μm) and disks (0.1x1x3 μm) by human umbilical vein endothelial cells (HUVECS) showed that spherical particles were internalised to a greater extent than disks at earlier time points (0.5-3 hr), however at later time points (5+ hr) the two particle shapes displayed equivalent internalisation ²⁴³.

Lu *et al.* studied the internalisation of CdTe-quantum dot microcomposites of spherical (diameter 1.85 μm), rod (2.5x1.2x1.0 μm), and needle (8.5x0.3 μm) morphologies by RAW 264.7 cells ²⁴⁴. Spheres were internalised by a higher proportion of cells than both rod and needle-shaped particles with needle shaped particles hardly being internalised by any cells.

Kozlovskaya *et al.* compared uptake of hydrogel capsules of spherical (diameter 1.8 μm) and discoidal (3.6x1.2x0.59 μm) microparticles by J774A.1, HMVEC, and 4T1 cells ²⁴⁵. In all cell lines, more spheres were taken up per cell than discoidal particles.

In general, reports on the effects of nano and microparticle shape on cellular uptake are very mixed and the interpretation of published studies is further complicated by the effects of other particle properties and different cell types. For example, the synthesis of nanoparticles of different shapes often involves the use of surfactants which, if not removed before uptake experiments, will have a large impact on the results. It is therefore challenging to study these effects; however, particle shape has been demonstrated to influence uptake and so by extending the current knowledge on how particle shape influences cellular uptake, the design of more effective medicines can be achieved. The majority of studies published thus far compare spherical and rod-shaped particles, therefore the study of a more diverse array of particle shapes is warranted.

1.4.2.3 Other effects of particle shape

Particle shape has also been shown to be an important determinant in the biodistribution of particles after administration to the body. Particular attention has been paid to the movement of micron-sized particles of different shapes in flow ²⁴⁶. The hydrodynamics of non-spherical microparticles in blood often result in their margination towards the blood vessel walls, leading researchers to explore their use in vascular targeting ²⁴⁷⁻²⁴⁸. Differences in biodistribution between spheres, disks, cylinders, and hemispherical particles has been demonstrated by Decuzzi *et al.* ²⁴⁹. This opens another avenue for consideration in the targeting of different areas of the body using different particle shapes.

1.4.2.4 Microparticles for lung delivery

The majority of studies have focused on the effect of particle shape in particles in the nano-size range. However, the use of micron-sized particulate carriers is of particular interest in the field of pulmonary delivery. Particle size has been shown to be a crucial parameter in determining where in the lung the particles are deposited following inhalation. Particles that are too large deposit at the back of the throat and are swallowed, whereas particles that are too small are exhaled ²⁵⁰. Inhaled particles are often between 1 and 5 μm in size as these deposit into the lower airways ²⁵¹. However, disparities between healthy and diseased lungs have been shown whereby higher deposition takes place in the central airways than in peripheral airways in patients with asthma and chronic obstructive pulmonary disease (COPD) ²⁵²⁻²⁵³.

In the small airways, where airflow is low relative to the upper airways, sedimentation by gravity is the predominant mechanism of particle deposition for particles between 0.5-3 μm ²⁵⁴. Below this size, diffusion is the dominant mechanism of deposition and particles that do not deposit are exhaled.

Pulmonary delivery of therapeutics can be useful for both local and systemic delivery. In order for systemic delivery to occur, inhaled particles must reach the alveoli where drug molecules must then dissolve and cross the alveolar epithelium into the blood stream ²⁵⁵.

However, particulate matter in the alveoli is removed by macrophages. Particles are phagocytosed and then macrophages containing particles are cleared either by migration to the lymphatic system or by movement towards the ciliated region in the lung whereby they are transported towards the nasopharynx and swallowed ²⁵⁶. Depending on the clinical scenario it may be beneficial either to enhance or avoid the removal of a therapeutic carrier particle by macrophages in the lung. For example, in the development of COPD, there is often a disturbance in the balance between M1 and M2 phenotypes and so targeting them in order to modulate this balance may be beneficial ²⁵⁷. On the other hand, in cases such as asthma and pulmonary hypertension, a long residence time resulting in prolonged release of the therapeutic could result in less frequent dosing and higher compliance, making avoidance of particle uptake desirable ²⁵⁸. This strategy has been pursued for the sustained systemic release of insulin delivered to the lung ²⁵⁹.

The control of microparticle shape to either reduce or enhance macrophage uptake could therefore be a strategy to enhance the effectiveness of inhaled therapeutics. Although it might be considered that the production of particles with defined shape might be difficult to achieve on an industrial scale, it has been demonstrated that methods such as PRINT are scalable and is being investigated by Liquidia Inc. to produce inhalable microparticles of controlled shape ²⁶⁰.

1.5 Aims and objectives

This work aimed to understand the uptake of polycrystalline silicon (polysilicon) and silicon oxide microparticles with different shapes, size, and surface chemistry by RAW 264.7 macrophages (figure 1.11). A variety of microparticle shapes were microfabricated by collaborators at the Centro Nacional de Microelectrónica (CNM) using lithographic methods. These particles were then functionalised by surface modification with fluorescent molecules

to enable detection of intracellular particles by flow cytometry. Additionally, spherical silicon oxide microparticles of a range of sizes were purchased and functionalised using a zwitterionic surface chemistry and uptake by RAW 264.7 macrophages assessed.

The experimental work is summarised as follows:

- In chapter 3 silicon oxide particles are functionalised with fluorescent molecules using covalent and non-covalent methods and the suitability of each labelling method for use in cellular uptake studies assessed. Uptake of silicon oxide spheres, hexahedrons, and truncated pyramids is then assessed using qualitative and quantitative methods.
- In chapter 4 a label-free method of detecting polysilicon microparticles of hexahedral, cuboidal, bar-shaped and circular disk morphologies is used to assess particle uptake by RAW 264.7 cells. The effect of each particle morphology on cellular metabolism, toxicity, and lysosomal enzyme release is studied.
- In chapter 5 spherical silicon oxide particles (0.5, 1, 3 μm) are functionalised with zwitterionic surface chemistry, and their uptake by RAW 264.7 macrophages measured with emphasis on dosing metric, lipopolysaccharide (LPS) stimulation, and the presence of phospholipid dipalmitoylphosphatidylcholine (DPPC).

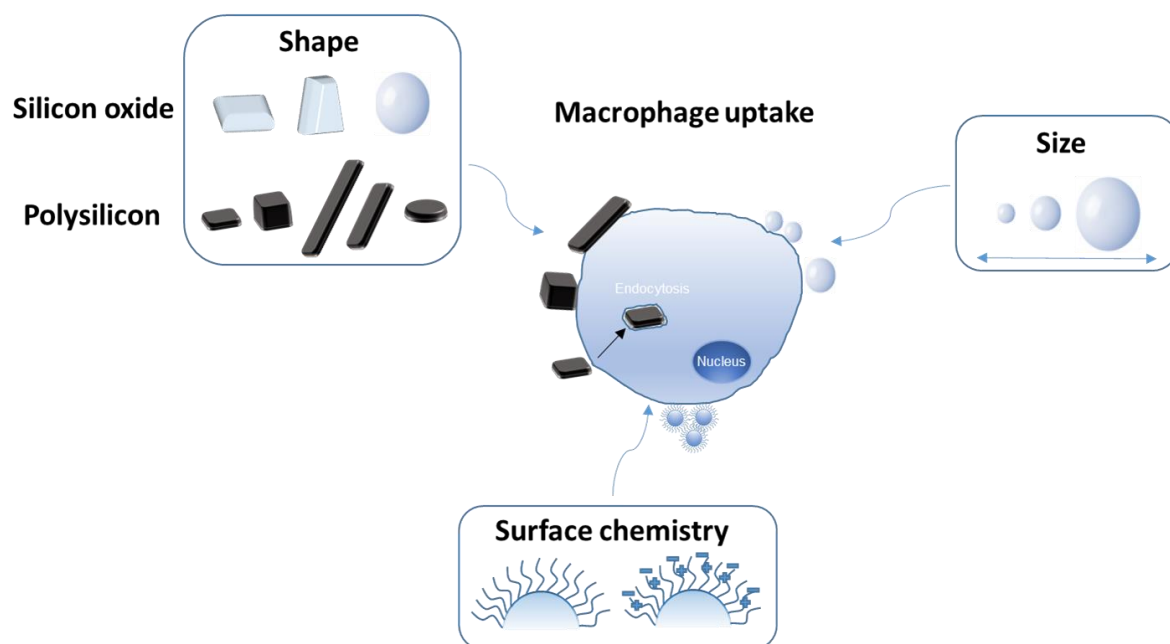


Figure 1.11: Schematic summarising key aspects of the project

2. Materials and General Methods

2.1 Materials

2.1.1 Plasticware and glassware

Tissue culture treated 75 cm² (T-75) cell culture flasks, sterile pipettes, and 12, 24, 96, well polystyrene plates (black/clear) were purchased from Corning life sciences (Holland). 15 mL sterile centrifuge tubes (falcon tubes) were obtained from Greiner (USA). Haemocytometer (Neubauer chamber) for counting of cells and particles was obtained from Scientific Laboratory Supplies (UK).

2.1.2 Materials for cells culture

Dulbecco's Modified Eagle Medium (DMEM, D546), FBS (F7524), L-glutamine (G7513), 4-(2-hydroxyethyl)-1-piperazineethanesulfonic acid (HEPES H0887), Penicillin/Streptomycin, Hank's Balanced Salt Solution (HBSS, H8264), 4',6-diamidine-2'-phenylindole dihydrochloride (DAPI), fluoroshield™ (F6182), LDH assay kit, 4-methyl umbelliferyl-β-D-glucuronide hydrate (MUG) were purchased from Sigma-Aldrich. RAW 264.7 cells were obtained from the American Type Culture Collection, ATCC (USA).

Corning® biocoat™ 20mm collagen coated coverslips 10553322, Lipopolysaccharide (LPS), CD107a (LAMP-1) monoclonal antibody Alexafluor 488, and Accutase were purchased from Fisher Scientific. Phalloidin Ifluor 488 (ab176753) was purchased from Stratech Scientific. Formaldehyde 4% and Dimethylsulfoxide (DMSO) were purchased from VWR. CellTiter 96® AQueous One solution cell proliferation assay (MTS reagent) was purchased from Promega UK. PBS tablets were obtained from Oxoid Ltd (UK).

2.1.3 Chemicals

1H-imidazole, 1-bromooctadecane, Fluoromount™ F4680, Rhodamine B isothiocyanate (RBITC, 283924), 3-aminopropyl trimethoxysilane (APTMS, 281778), Triton X-100 (TX-100), N-(3-sulfopropyl)-N-methacroyloxyethyl-N,N-dimethylammonium betaine (MDSA, 537284), and Silicon oxide spheres (0.5, 1, 3 μm) were purchased from Sigma-Aldrich. H_2SO_4 (98%), NH_4OH (20%) and (3-glycidoxypentyl)trimethoxysilane (GOPTS) 97% were purchased from Fisher Scientific. 5-(4-aminophenyl)-10,15,20-(triphenyl)porphyrin (ATPP) and 5,10,15,20-(tetra-4carboxyphenyl)porphyrin (TCPP) were purchased from Porphychem (France). 10-(pentafluorophenoxycarbonyl)decyltrimethoxysilane (PFP, 15468785) was purchased from Alfa Aesar. 11-aminoundecyltriethoxysilane (AUTES, S25045) was purchased from Fluorochem (UK). 1,3-bis(bromomethyl)benzene, H_2O_2 (35%), and dimethylsulfoxide (DMSO) were purchased from VWR. BDP-630 NHS ester was purchased from Lumiprobe.

2.2 General Methods

2.2.1 Routine cell culture methods

2.2.1.1 Culture of RAW 264.7 cells

RAW 264.7 macrophages were cultured in T-75 cell culture flasks. 15 mL high glucose DMEM supplemented with 10% FBS, 1% L-glutamine, and 1% penicillin/streptomycin was used as the culture media. Cells were incubated at 37°C with 5% CO_2 in 95% humidity. Cell culture media was removed by aspiration and replaced with 15mL pre-warmed fresh media every 48 hours.

Cells were harvested by gentle scraping once they reached 60-80% confluency. Successful detachment of cells by scraping was confirmed by examination under a microscope. Detached cells in media were transferred by pipette into a 15 mL falcon tube. Falcon tubes containing

cells were centrifuged at 1200 RPM (300G) for 5 minutes to cause the cells to form a pellet. The supernatant was removed by aspiration and replaced with 6 mL fresh (pre-warmed at 37°C) media. The cells were suspended in the fresh media by pipetting up and down to disperse the pellet. At this point cells would either be counted for seeding in well plates for experiments or if undergoing routine passaging would be split into new T-75 culture flasks containing 15mL fresh pre-warmed media. Typical passaging ratios from 6 mL cell suspension were 1:3 and 1:6. Cells were passaged between P13 and P30 after which cells were disposed of and fresh P13 cells were revived from storage ²⁶¹.

2.2.1.2 Cell counting

A haemocytometer was used to count the number of cells for each experiment. 10 µL detached cell suspension in fresh pre-warmed media was transferred to a 200 µL microcentrifuge tube. To this, trypan blue solution (0.4%, 10 µL) was added and mixed by pipetting the solution up and down. 10 µL of this mixture was transferred onto the haemocytometer and cells counted under the microscope. Cells were counted from the four corners of the haemocytometer and the sum divided by four to give an average. This result was then multiplied by 2 to account for the dilution by adding the trypan blue solution and then multiplied by 10,000 to give the number of cells per 1 mL.

2.2.1.3 Cell freezing

After detachment of cells and centrifugation following the procedure in section 2.2.1.1 cells were suspended in 1mL cell culture media containing 10% DMSO. This cell suspension was then transferred by pipette to a 1 mL cryovial. Cryovials were labelled with the date, cell type, and passage number and then placed in a Mr Frosty™ (Thermoscientific) freezing container containing isopropanol. The Mr Frosty™ container was placed in a -80°C freezer overnight

after which time cryovials were transferred into liquid nitrogen containers for long-term storage. Each cryovial contained a whole flask of cells.

2.2.1.4 Cell revival

After removal of a cryovial containing cells from liquid nitrogen storage, the cryovial was placed in a water bath at 37°C until partially defrosted. As soon as the cell suspension had partially defrosted it was transferred to a 15 mL falcon tube and 10 mL pre-warmed media added. The suspension was centrifuged at 1200 RPM (300G) for 5 minutes and the supernatant removed. The pellet was suspended in 15 mL fresh pre-warmed media and this cell suspension transferred to a fresh T-75 cell culture flask and stored in an incubator at 37°C, 95% humidity, 5% CO₂.

2.2.1.5 Particokinetics

For all experiments whereby particles were applied to cells, particles were applied as suspensions to wells which contained RAW 264.7 cells adhered to the bottom of the well. The density of silicon oxide (2.20 g/cm³) and polysilicon (2.33 g/cm³) resulted in sedimentation of particles to the bottom of the well to initiate contact with the cells. Stated particle doses are the doses administered to each well.

2.2.2 Statistical analysis

Statistical analysis was performed using GraphPad Prism 7 whereby $P < 0.05$ was considered statistically significant (*). Further statistical significance was denoted as follows $P < 0.01$ (**), $P < 0.001$ (***), $P < 0.0001$ (****). Appropriate statistical tests and *ad hoc* analyses were selected and are detailed in each figure caption. Data is presented as mean \pm SEM for independent experiments and mean \pm standard deviation for dependent experiments. The number of repeats is stated as N for independent experiments and n for dependent experiments.

3. Interactions of silicon oxide microparticles of different shape by RAW 264.7 macrophages

3.1 Introduction

In this chapter, silicon oxide microparticles of hexahedral and truncated pyramid morphologies, fabricated using lithography, are compared with silicon oxide microspheres acquired from a commercial supplier to assess their interactions with RAW 264.7 macrophages. Initially, different methods of functionalising the microparticles with fluorescent molecules are compared and then the interaction of functionalised particles with RAW 264.7 macrophages is assessed.

3.1.1 Methods of functionalising silicon oxide particles with fluorescent dyes

By far the most common method to functionalise the surface of silicon oxide particles is by the use of alkoxysilane molecules. Alkoxy groups hydrolyse in the presence of small amounts of water to form silanols that form hydrogen bonds with the hydroxyl groups on the surface of the silicon oxide. Through loss of water molecules these bonds are made covalent and a self-assembled monolayer (SAM) is formed on the silicon dioxide surface. A wide number of alkoxysilane molecules are available with numerous different functional groups for example amines, epoxides, thiols, azides, and acrylates. Therefore, this method offers a convenient way to impart useful surface chemistries for further functionalisation to silicon oxide particles. Commonly (3-amino-propyl) triethoxysilane (APTES) has been used to modify the surface of silicon oxide particles so that amine-reactive groups such as NHS esters or isothiocyanates can be used to further conjugate the surface with fluorophores, drug molecules or targeting moieties²⁶²⁻²⁶⁶.

Functionalisation of the particle surface with fluorophores allows the visualisation of the silicon oxide particles by fluorescent microscopy. Alternatively, fluorescent dye molecules can be encapsulated into the internal structure of the particles during synthesis, known as fluorescent doping methods. Fluorophores can be linked to the internal structure of the silica either covalently (by alkoxysilanes) or non-covalently by electrostatic interaction²⁶⁷⁻²⁶⁸. This method has the advantage that the dye molecules are encapsulated within the silica rather than present at the surface meaning that the dye has minimal effect on the particle surface properties and additionally does not have the chance to interact with receptors on the cell surface. Non-covalent doping methods can result in dye leakage from the particles²⁶⁹ and so covalent doping methods are typically favoured.

Previously, members of our group have described a novel method for non-covalently immobilising fluorophore onto the surface of polycrystalline silicon microparticles. This method utilises a gemini imidazolium surfactant that physisorbs onto the particle surface. The surfactant serves as a host to immobilise porphyrin dye molecules onto the surface of the particles.

This method could also allow for non-covalent binding of drug molecules and other surface chemistries to the particle surface therefore this methodology is explored here to fluorescently label silicon oxide particles in contrast with covalent methods in order to serve as a proof of concept for further development.

3.1.2 Methods of analysing particle internalisation

There are numerous methods available to researchers to assess the internalisation of particles into cells *in vitro* each with its own advantages and disadvantages. These methods can be divided into quantitative (flow cytometry, plate reader methods, inductively coupled mass spectrometry (ICP-MS) and qualitative (semi-quantitative) methods such as confocal/fluorescence/light microscopy and scanning electron microscopy²⁷⁰.

Qualitative methods rely on high-resolution imaging to allow visualisation of particle internalisation events and are useful in providing descriptive information about the sample. However, often these methods are time-consuming and expensive which therefore leads to a reduction in the number of samples that can be assessed, thus decreasing the reliability of the quantitative information that can be obtained. Furthermore, due to the selection of which cells are imaged by the researcher, these methods can be subject to unconscious sampling bias that can reduce the validity of the obtained results ²⁷¹.

On the other hand, quantitative methods are able to assess high numbers of cells in order to give highly reliable information about the sample, but lack the sensitivity in discriminating between internalised and surface-bound particles ²⁷². For example, assessment of cells by flow cytometry or plate reader methods will give information about the proportion of cells that are associated with fluorescent particles, but not the location of particles with respect to the cells. Further methodological steps can be used, for example by quenching extracellular fluorescence or by staining surface-bound particles with a secondary fluorophore to discriminate between cells with internal and cells with surface-bound particles. However, these methods are very system-specific, requiring efficient quenching/labelling and therefore are not suitable as a general method.

Imaging flow cytometry is a recently developed method that aims to overcome some of these limitations by combining the spatial resolution of microscopy with the high-throughput nature of flow cytometry. It has been used by a number of groups to assess the internalisation of particles. However a study by Fei *et al.* ²⁷³ reported that it is not able to suitably distinguish between internal and surface-bound particles without the addition of a secondary fluorescent label.

In contrast, a study by Vranic *et al* ²⁷⁴ showed similar results between trypan blue quenching of fluorescein isothiocyanate (FITC)-labelled silica nanoparticles and imaging flow cytometry image analysis. Owing to the conflicting reports it is necessary to assess the validity of this

method for the particles used in this chapter, a comparison with a well-established trypan blue quenching method is performed.

3.1.3 Studies of the uptake of silicon oxide particles of different morphologies

Studies of silicon oxide particles of different shapes have primarily been focussed on respirable silica dusts in order to understand how the particle morphology affected toxicity in macrophages²⁷⁵⁻²⁷⁷. Recently, an increased number of studies have begun to examine silicon oxide particle morphology as a tool for enhancing control over drug delivery for example by increasing/decreasing uptake by cells^{236-238, 278-281}.

It is difficult to make clear comparisons between these studies because the effects of particle shape are difficult to study in isolation. Differences in particle size, surface chemistry, and cell type are ever present and have been shown to play important roles in particle internalisation^{93, 95, 282}. Additionally, cellular association is often used as a proxy for internalisation.

The majority of studies examining the effect of silicon oxide particle shape utilise particles that are in the nano size range^{236-238, 278-280, 283}. However, there are few studies that look at silicon oxide particles in the micron size range ($>1\ \mu\text{m}$) and so in this chapter silicon oxide particles with dimensions in the micron range are used to study the effects of particle shape on internalisation. Our group has functionalised hexahedral-shaped silicon oxide microparticles for intracellular pH sensing²⁸⁴ and demonstrated the versatility of particle shapes that can be fabricated using photolithography²²². However, the effect of silicon oxide microparticle shape is yet to be investigated.

3.2 Materials and Methods

3.2.1 Materials

1H-imidazole, 1-bromooctadecane, Fluoromount™ F4680, rhodamine B isothiocyanate (RBITC, 283924), 3-aminopropyl trimethoxysilane (APTMS, 281778), and silicon oxide spheres (diameter 3 μm) were purchased from Sigma-Aldrich. H_2SO_4 (98%), NH_4OH (20%) and (3-glycidoxypentyl)trimethoxysilane (GOPTS) 97% were purchased from Fisher Scientific. 5-(4-aminophenyl)-10,15,20-(triphenyl)porphyrin (ATPP) and 5,10,15,20-(tetra-4carboxyphenyl)porphyrin (TCPP) were purchased from Porphyrchem (France). 10-(pentafluorophenoxycarbonyl)decyltrimethoxysilane (PFP, 15468785) was purchased from Alfa Aesar. 11-aminoundecyltriethoxysilane (AUTES, S25045) was purchased from Fluorochem (UK). 1,3-bis(bromomethyl)benzene and H_2O_2 (35%) were purchased from VWR. BDP-630 NHS ester was purchased from Lumiprobe.

Silicon oxide hexahedrons and truncated pyramids were fabricated by collaborators at the Centro Nacional de Microelectrónica (CNM) in Barcelona according to ref ²²². Briefly, a P-type silicon wafer (100) was wet oxidised (100°C) to produce a 1 μm or 3 μm thick silicon oxide layer. A photoresist (HPR 6512) was spun to produce a 1.2 μm thick layer and subsequently exposed to UV light through a photomask. The photomask was developed by baking at 200°C for 30 minutes and the exposed silicon oxide degraded by dry etching with a $\text{C}_2\text{F}_6/\text{CHF}_3$ mixture in a Drytek quad 484 RIE. Definition of the anchors underneath the particles was achieved by quasi-isotropic etching in $\text{SF}_6/\text{C}_4\text{F}_8$ atmosphere in an A-60E DRIE and photoresist removed by plasma cleaning (TEPLA 300E).

3.2.2 Methods

3.2.2.1 Non-covalent labelling of silicon oxide particles anchored on silicon wafers

Synthesis of imidazolium amphiphile 1.2Br

1-octadecyl-1H-imidazole was synthesised according to reference ²⁸⁵ (3.77 g, 80.05 %) ¹H NMR (400 Hz, CDCl₃, 25°C, TMS): δ 0.9 (t, 3H, CH₃), 1.28 (d, 30H, (CH₂)₁₅), 1.79 (t, 2H, CH₂), 3.94 (t, 2H, CH₂), 6.92 (s, H, Im-H), 7.08 (t, H, Im-H), 7.48 (s, H, Im-H).

1.2Br was synthesised according to reference ²⁸⁵ (1.37 g, 80.20%) ¹H NMR (400 Hz, CDCl₃, 25°C, TMS): δ 0.81 (t, 6H, CH₃), 1.18 (m, 60H, CH₂), 1.83 (t, 4H, CH₂), 4.21 (t, 4H, CH₂), 5.56 (s, 4H, CH₂), 7.11 (s, 2H, Ar-H), 7.2 (s, 2H, Im-H), 7.50 (d, H, Ar-H), 7.98 (m, 1H, Ar-H), 8.04 (m, 2H, Im-H), 10.46 (s, 2H, Im-H).

Surface activation of silicon oxide particles anchored on silicon wafers

Silicon wafers possessing silicon oxide microparticles attached to the surface by supporting anchors were cut using a diamond scribe into ~5x5 mm pieces. Pieces of wafer were transferred to a 10 mL glass vial (4 wafer pieces per vial) with the silicon oxide particle pattern facing up. Acidic piranha solution (1 mL) was prepared by adding H₂O₂ (35%, 300 μ L) dropwise to H₂SO₄ (98%, 700 μ L) and this solution transferred into the vial containing the wafer pieces. This solution was freshly prepared each time to avoid loss of activity. After 1 hour the acidic piranha solution was removed, the surfaces rinsed with MilliQ water (3x 1mL), dried under a nitrogen stream and added to a fresh 10 mL glass vial.

Basic piranha solution was prepared by adding NH₄OH (20%, 150 μ L) to MilliQ water (700 μ L), to this mixture H₂O₂ (35%, 150 μ L) was added dropwise. Basic piranha solution was transferred to the vial containing the wafer pieces for 30 minutes. This solution was freshly prepared each time to avoid loss of activity. The basic piranha solution was removed and the wafer pieces washed with MilliQ water (3x 1 mL) and dried under a stream of nitrogen before being transferred to a fresh 10 mL glass vial.

Step-by step method for non-covalent immobilisation of 1.2Br and labelling with TCPP on silicon oxide particles anchored on silicon wafers

1.2Br solution (2 mM, 2 mL) in either DMSO, DCM, acetone or MeOH was added to the surfaces immediately after surface activation to avoid surfaces being contaminated. After 24 hours the 1.2Br solution was removed and the surfaces washed with milliQ water (3 x 1 mL), dried in a stream of nitrogen and transferred to a fresh 10 mL glass vial. TCPP (sodium salt) (2.5 mM) in milliQ water 1mL was added to the surfaces which were protected from light and left overnight. TCCP solution was removed and the surfaces washed with milliQ water (3x1 mL) and dried in a stream of nitrogen. One wafer piece was used per condition to serve as a proof of concept, multiple areas of each surface were examined for fluorescence.

Solution method for non-covalent labelling with 1.2Br and ATPP

1.2Br solution (2mM) in EtOH (1 mL) was mixed with a solution of ATPP (2 mM) in acetone (1 mL) and 1 mL of the resulting solution added to a 10 mL vial containing freshly activated wafer pieces. The wafer pieces were left submerged in this solution overnight after which time the solution was removed and the surfaces washed with 3 x 1 mL milliQ water and dried with a nitrogen stream.

3.2.2.2 Covalent labelling of silicon oxide particles anchored on silicon wafers

Covalent labelling with PFP/GOPTS and ATPP

Freshly activated wafer pieces were placed in a 10 mL glass vial and submerged in a 2% v/v solution of either PFP or GOPTS in acetone (1 mL) for 30 minutes at room temperature. The silane solutions were removed and the wafer pieces washed with acetone (3x 1mL), dried with a nitrogen air stream and placed in a fresh 10 mL glass vial. ATPP solution (4mM) in acetone (1 mL) was then added to the wafer pieces which were protected from light and left overnight.

The ATPP solution was removed and the wafer pieces washed with acetone (3 x 1mL) before being dried with a nitrogen stream.

Covalent labelling with APTMS/AUTES and RBITC/BDP 630

Freshly activated wafer pieces were placed in a 10 mL glass vial with the silicon oxide particle facing up and submerged in either 2% v/v APTMS solution in acetone (1 mL) for 30 minutes or 0.1% v/v AUTES solution in EtOH (1 mL) for 2 hours. Silane solutions were removed and the wafer pieces washed with 3 x 1mL of the corresponding solvent (acetone for APTMS treated wafer pieces, EtOH for AUTES treated wafer pieces) before being dried with a nitrogen air stream and placed in a fresh 10 mL glass vial. RBITC solution in EtOH (1 mL) was then added to the wafer pieces which were protected from light and left overnight. For experiments in section 3.3.2.2 comparing the covalent labelling methods, a 200 μ M solution of RBITC in EtOH (1 mL) was used, for all subsequent experiments 30 μ M RBITC solution in EtOH (1 mL) was used. Alternatively BDP 630 NHS ester (30 μ M) in $\text{Na}_2\text{HPO}_4/\text{NaH}_2\text{PO}_4$ buffer pH 8 (700 μ L) was added to the wafer pieces, protected from light and left overnight. Wafer pieces were washed with 3x 1 mL EtOH (RBITC labelled wafer pieces) or milliQ water (BDP 630 labelled wafer pieces) and dried with a stream of nitrogen before removal of particles by peeling.

3.2.2.3 Covalent labelling of silicon oxide particles in suspension

Surface activation of silicon oxide particles in suspension

1 mg (20 μ L) silicon oxide spheres as received (stock concentration 5% w/v) were transferred to a 1.5 mL microcentrifuge tube and centrifuged at 5700 RPM (6175 G) for 10 minutes and the supernatant removed. Particles were suspended in acidic piranha solution (700 μ L) for 1 hour with shaking to prevent particles from falling out of suspension. Particles were centrifuged at 5700 rpm (6175 G) for 10 minutes and the acidic piranha solution removed. Particles were washed by resuspension in 700 μ L milliQ water and then centrifuged 5700 rpm (6175 G) for

10 minutes. This washing process was repeated 3x and then the supernatant removed. Particles were suspended in basic piranha solution (700 μ L) and left shaking for 30 minutes. Particles were centrifuged at 5700 rpm (6175 G) for 10 minutes and the basic piranha solution removed. Particles were washed using the same resuspension in 700 μ L milliQ water and centrifugation steps used to wash the particles after removal of the acidic piranha solution.

Covalent labelling with AUTES and RBITC/BDP 630

Freshly activated silicon oxide particles were suspended in 0.1% v/v AUTES in EtOH (700 μ L) and left to shake for 2 hours. Particles were centrifuged at 5700 RPM (6175 G) for 10 minutes and the silane solution removed. Particles were washed by resuspension in 700 μ L EtOH and centrifugation at 5700 RPM (6175 G) for 10 minutes before removal of the supernatant. This washing process was repeated 3x and then the supernatant removed. Particles were suspended in RBITC (30 μ M) in EtOH (700 μ L) or BDP 630 NHS ester (30 μ M) in Na₂HPO₄/NaH₂PO₄ buffer pH 8 (700 μ L) and left on a shaker overnight while protected from light. Particles were washed with EtOH 3x 700 μ L (RBITC labelled particles) or milliQ water 3x 700 μ L (BDP 630 labelled particles) by repeated suspension and centrifugation as above. Particles were stored in 700 μ L EtOH at 4°C.

3.2.2.4 Determination of fluorophore release from particles in PBS at 37°C

Wafer pieces possessing particles labelled non-covalently using 1.2Br-ATPP or ATPP alone and covalently using AUTES-RBITC were placed in microcentrifuge tubes containing warm PBS (700 μ L) and incubated at 37°C for 2 hours with shaking. The fluorescence intensity of the particles was assessed before and after incubation using fluorescence microscopy. Fluorophore release was measured from 3 wafer pieces per sample by imaging 5 areas of each wafer piece, each containing ~500 particles. Images were analysed with ImageJ®.

3.2.2.5 Acquisition of brightfield and fluorescent images

Brightfield and fluorescence images were acquired using a Nikon Eclipse TiU fluorescence microscope. Images of wafer pieces were acquired by placing the wafer piece on a glass slide with the silicon oxide side face-down. Images of particles in suspension were acquired by pipetting 15 μ L particle suspension onto a glass slide and then covering with a coverslip. For fluorescence imaging of TCPP and ATPP-labelled samples $\lambda_{\text{ex}} = 425$ nm and $\lambda_{\text{em}} > 620$ nm. For fluorescence imaging of RBITC labelled samples $\lambda_{\text{ex}} = 550$ nm and $\lambda_{\text{em}} > 590$ nm. Images were processed using imageJ® to produce fluorescent surface plots. For fluorescence imaging of BDP 630 labelled particles $\lambda_{\text{ex}} = 630$ nm and $\lambda_{\text{em}} > 670$ nm.

3.2.2.6 Water contact angle measurements

Water contact angle measurements were acquired using a KSV CAM 200 optical contact meter. Surfaces were placed with the silicon oxide particle face upwards and the water contact angle measured. Measurements were taken in triplicate (3 wafer pieces per sample).

3.2.2.7 Removal of silicon oxide particles from silicon wafer

A drop of fluoromount™ aqueous mounting medium was placed onto each of the wafer pieces and spread using a micropipette tip to ensure complete coverage. This was then left to air dry (~20 minutes). After drying the mounting medium was peeled away from the wafer piece surface using tweezers and placed in a 1 mL microcentrifuge tube. MilliQ water (1mL) was added and the microcentrifuge tube and sonicated to aid dissolution of the mounting medium. After complete dissolution had occurred the microcentrifuge tube was centrifuged for 10 minutes at 5700 RPM (6175 G) resulting in a pellet forming. The supernatant was removed and the cycle of centrifugation and washing with milliQ water (1 mL) repeated x2 times. Particles were stored in EtOH (700 μ L) at 4°C.

3.2.2.8 Determination of trypan blue quenching efficiency

MFI of particles was measured by imaging flow cytometry using a 50 μ L suspension containing RBITC-labelled particles in 1% HEPES in HBSS. MFI was measured with and without the addition of trypan blue solution (0.4%, 10 μ L) immediately before sample analysis. Flow cytometer settings were kept the same for each sample, details can be found in section 3.2.2.10.

3.2.2.9 Qualitative particle uptake of silicon oxide particles by RAW 264.7 macrophages assessed by confocal microscopy

Preparation of particle suspensions

BDP 630 labelled particles were centrifuged at 5700 RPM (6175 G) for 10 minutes. From this point onwards all work took place inside a sterile cell culture hood to maintain the sterility of the particles. Stock particle suspensions were prepared by removal of the EtOH and the addition of 1 mL buffer comprising 1% HEPES in HBSS. The number of particles per mL was calculated by counting particles on a haemocytometer. A volume of each particle stock solution containing 1,500,000 particles was transferred into fresh microcentrifuge tubes and the volume made up to 1 mL with fresh 1% HEPES in HBSS buffer.

Preparation of RAW 264.7 cells

RAW 264.7 cells grown to 60-80% confluency were harvested by scraping and counted as described in section 2.2.1. 300,000 cells per well in 1 mL culture media were seeded onto collagen coated glass coverslips inside clear polystyrene 6-well plates and incubated at 37°C, 5% CO₂ 95% humidity overnight to allow cell attachment. Culture media was then removed and the cells washed with 1 mL pre-warmed (37°C) PBS. The PBS was removed by aspiration and 1 mL per well pre-warmed particle suspensions each containing 1,500,000 particles

added to each well. Cells were kept in an incubator for 4 hours after which time the particle suspensions were removed by aspiration and the cells washed with 3x 1mL pre-warmed PBS. Cells were fixed by the addition of 1 mL per well of 4% formaldehyde in PBS for 15 minutes and then washed with 3x 1mL PBS. Permeabilisation of cells was achieved by adding 1 mL per well 0.1% Triton X-100 in PBS for 3 minutes. Cells were washed with PBS (3x 1 mL) and the PBS removed.

Immunofluorescence staining and preparation of confocal slides

Actin staining was performed by addition of 1 mL per well pre-warmed Ifluor 488 phalloidin solution in PBS (1 μ L ifluor488 stock solution in 1 mL PBS) for 30 minutes at room temperature while protected from light. Staining solution was then removed and the cells washed with PBS (3x 1 mL). Alternatively, LAMP-1 staining was achieved by the addition of 1 mL per well of alexafluor 488 labelled CD107a antibody (5 μ g per mL in PBS) for 45 minutes while protected from light. Cells were washed with PBS (3x 1 mL). Nuclear staining was achieved by addition of 1 mL per well prewarmed 300 nM DAPI solution in PBS for 5 minutes at room temperature. DAPI solution was then removed by aspiration and the cells washed with PBS (3 x 1 mL).

Coverslips were removed from the well plate and rinsed with deionised water to prevent salt crystal formation and mounted onto glass slides with a drop of fluoroshield™ mounting medium. Slides were sealed using nail varnish and stored protected from light at 4°C. Confocal images were obtained within one week of slide preparation.

Confocal microscopy

Confocal microscopy was performed using a Zeiss Elyra PS 1 LSM780 inverted confocal microscope with a Zeiss 63x water immersion objective. Excitation/emission wavelengths for each fluorophore are as follows: DAPI (λ_{ex} :360 λ_{em} :450) Ifluor 488 (λ_{ex} :480 λ_{em} :520)

Alexafluor 488 (λ_{ex} :480 λ_{em} :520) BDP 630 (λ_{ex} :630 λ_{em} :650) Images were processed using imageJ®.

3.2.2.10 Quantitative uptake of silicon oxide particles by RAW 264.7 cells assessed by flow cytometry

Preparation of particles

RBITC modified particles were centrifuged at 5700 RPM (6175 G) for 10 minutes. From this point forwards all work was performed inside a sterile cell culture hood to maintain sterility. The EtOH supernatant was removed and the particles suspended in 1 mL buffer comprising 1% HEPES in HBSS. Particles were counted using a haemocytometer to give the concentration of particles per mL of the stock suspensions. For each experiment the required volume of particle stock suspension was transferred to a fresh microcentrifuge tube and made up to 1 mL with 1% HEPES in HBSS buffer.

Preparation of cells

RAW 264.7 cells were harvested once they reach 60-80% confluency by scraping as described in chapter 2. 100,000 cells in culture media were seeded per well into a 12 well plate and incubated overnight at 37°C, 5% CO₂, 95% humidity. In experiments where RAW 264.7 cells were stimulated with LPS, culture media was used without 1% penicillin/streptomycin and was supplemented with 100 ng per mL LPS.

Culture media was removed by aspiration and the cells washed with 1 mL pre-warmed (37°C) PBS. PBS was removed and 1 mL pre-warmed particle suspensions applied at ratios of 5 or 10 particles per cell. Cells were incubated for 4 hours after which time the particle suspensions were removed and the cells washed with warm HBSS (3 x 1 mL). Cells were prepared for flow cytometry as either fixed or live cells depending on the analysis method.

Preparation of fixed cells for flow cytometry: Image analysis method

HBSS was removed from each well by aspiration and 250 μ L accutase added to each well and the cells placed in an incubator for 5 minutes to detach cells. 250 μ L HBSS was then added to each well and the total volume of each well transferred to fresh microcentrifuge tubes. Samples were centrifuged at 250 G for 5 minutes and the supernatants removed. The cells were suspended in 250 μ L 4% formaldehyde in PBS for 20 minutes before being centrifuged for 5 minutes (250 G) and the supernatant removed. Fixed cells were suspended in 50 μ L HBSS and stored at 4°C until analysis by flow cytometry. Samples were always analysed within 1 week of sample preparation.

Preparation of cells for flow cytometry: Trypan blue quenching method

HBSS was removed from each well by aspiration and 250 μ L accutase added to each well and the cells placed in an incubator for 5 minutes to detach cells. 250 μ L HBSS was then added to each well and the total volume of each well transferred to fresh microcentrifuge tubes. Samples were centrifuged at 250 G for 5 minutes and the supernatants removed. Cells were suspended in 50 μ L HBSS and kept on ice until analysis by flow cytometry. All samples were analysed within 2 hours of sample preparation. Immediately before analysis of each sample 10 μ L 0.4% trypan blue solution was added to quench surface-bound particle fluorescence.

Flow cytometry

All flow cytometry was performed using an Amnis imagestream^X MKII imaging flow cytometer in standard configuration with 40X magnification. Illumination settings: Brightfield LED 32.01 mW, 561 nm laser 200 mW, 785 nm laser 2 mW. Data was acquired using INSPIRE software with a minimum of 500 cells per sample (typically > 1000 per sample). Data was analysed using IDEAS software. Details of analysis can be found in appendix I.

3.3 Results and Discussion

3.3.1 Characterisation of fabricated particles

Silicon oxide microparticles anchored on to silicon wafers fabricated using photolithography by collaborators at the CNM and were characterised by SEM imaging (figure 3.1). The method involves growing a thermal layer of silicon oxide on top of a silicon wafer, a photomask is then used to selectively etch the particles that have a morphology which is defined by A) the photomask and B) the thickness of the original silicon oxide layer²²². After fabrication, particles remain anchored to the silicon wafer by a thin silicon support, which can subsequently be removed to release the particles into suspension. Particle shapes were selected so as to examine particle morphologies that had not yet been studied in the literature.

The images show highly uniform particle populations for both hexahedrons (figure 3.1Ai-iii) and truncated pyramids (figure 3.1Bi-iii). Figure 3.1 Aiii shows a hexahedral particle removed from its silicon support, a ~200nm piece of the support remains attached to the particle. Uniformity of particle size and shape is essential to ensure that any effects of particle shape on cellular uptake in later experiments are not caused by polydispersity. Particle dimensions were measured using imageJ® and the results are displayed in table 3.1.

Both hexahedrons and pyramids have a wider base than at the top of the particles and some curvature can be observed on the particle edges which is particularly evident in the truncated pyramids. For the calculation of particle volume and surface area this curvature was not taken into account and flat edges assumed. Silicon oxide spheres, acquired from a commercial supplier had a diameter of 3 μm ($\pm 0.25 \mu\text{m}$) according to the manufacturer's analysis.

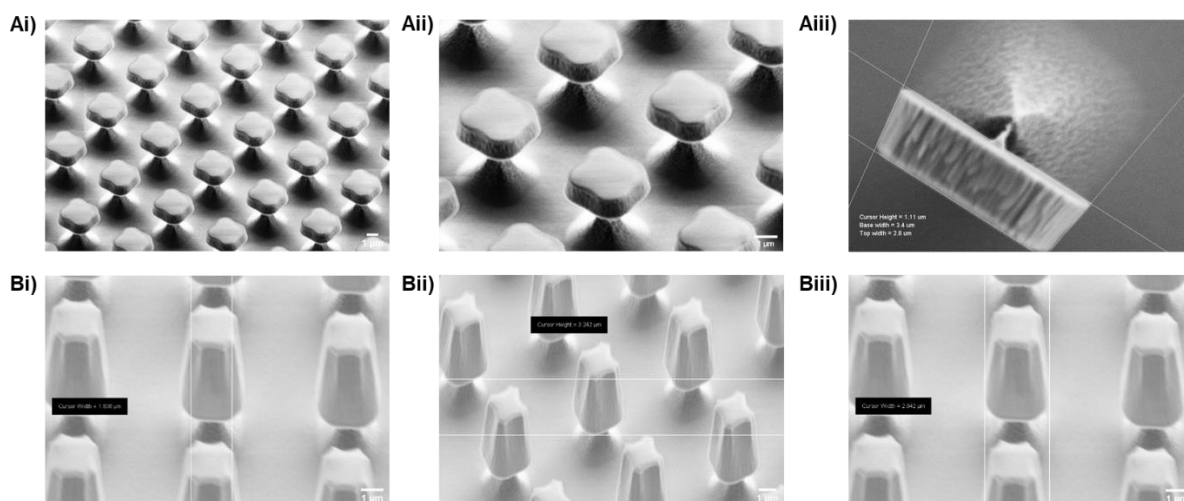


Figure 3.1 SEM images of fabricated SiO₂ microparticles Ai-iii) Hexahedrons Bi-iii) Truncated Pyramids

Table 3.1: Dimensions of fabricated Hexahedrons, Truncated pyramids, and Spheres

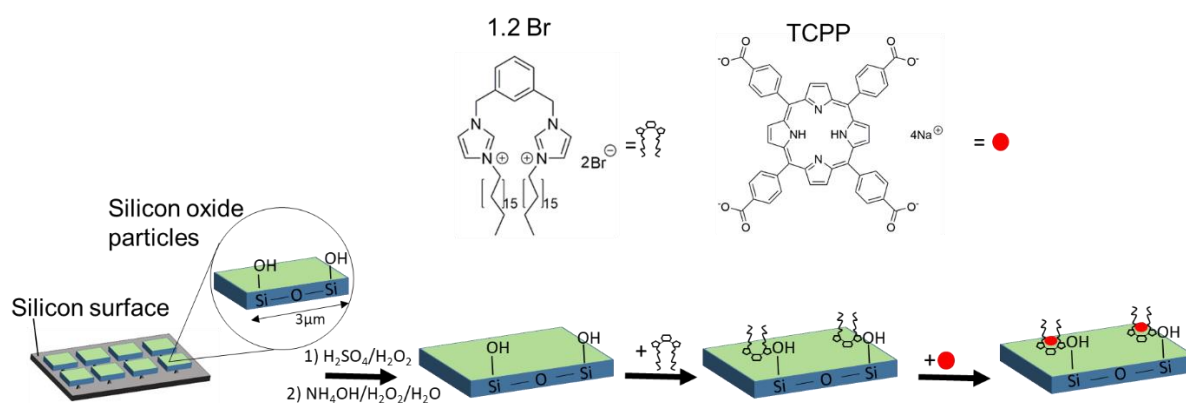
	Height (μm)	Base Width (μm)	Top Width (μm)	Surface Area (μm^2)	Volume (μm^3)
Hexahedrons	1.1	3.4	3.1	35.1	11.6
Truncated pyramids	3.2	2.8	1.8	40.5	17.2
Spheres	-	-	-	28.3	14.1

3.3.2 Functionalisation of silicon oxide particles for fluorescent labelling

As silicon oxide is transparent, in order to detect the microparticles within cells it was first necessary to label them with a fluorescent molecule. To achieve this, different methods were explored to modify silicon oxide hexahedrons while they were still attached to silicon wafer pieces. The functionalised particles could then be removed from their supports into suspension. This section applies a non-covalent functionalisation method previously used in the group to label polycrystalline silicon microparticles and well-established covalent linker methods for this purpose ²⁸⁶.

3.3.2.1 Non-covalent labelling of silicon oxide particles was achieved using a complexation in solution method

Previously, members of the group had used a step-by-step deposition method to first deposit 1.2Br onto polysilicon particle surfaces and subsequently add the salt of a fluorescent porphyrin molecule 5,10,15,20-(tetra-4-carboxyphenyl)porphyrin (TCPP) ²⁸⁶. After activation of the particle surface, 1.2Br is immobilised on the particle surface. TCCP is then introduced which forms a complex with the immobilised 1.2Br (Scheme 3.1).



Scheme 3.1: Step-by-step deposition of 1.2Br on to silicon oxide hexahedrons surface and subsequent complexation with TCPP.

This method was applied to silicon oxide microparticles anchored to a silicon wafer, the results are shown in figure 3.2. Successful activation of surface was confirmed by measuring water contact angle, activated surfaces had a water contact angle $< 10^\circ$ indicating hydrophilic nature due to hydroxyl groups present on the surface.

As can be seen in the fluorescence images and fluorescence surface plot, poor labelling of the particles was achieved using this method (figure 3.2A). The particles can barely be distinguished from the background and there was very little difference in fluorescence compared to the control surface which had been immersed in TCPP solution without prior modification with 1.2Br (figure 3.2B) The presence of 1.2Br did not improve the fluorescent

labelling compared to the control as can be seen from the values in the fluorescence line plots (figure 3.2Aiv/Biv). It was thought that the washing procedure used (washing the surfaces with DMSO) was causing the removal of 1.2Br from the particle surface and so this was further investigated. Changing to washing with water as well as removal of the washing procedure altogether did not result in any increase in labelling (Appendix I -figure S3).

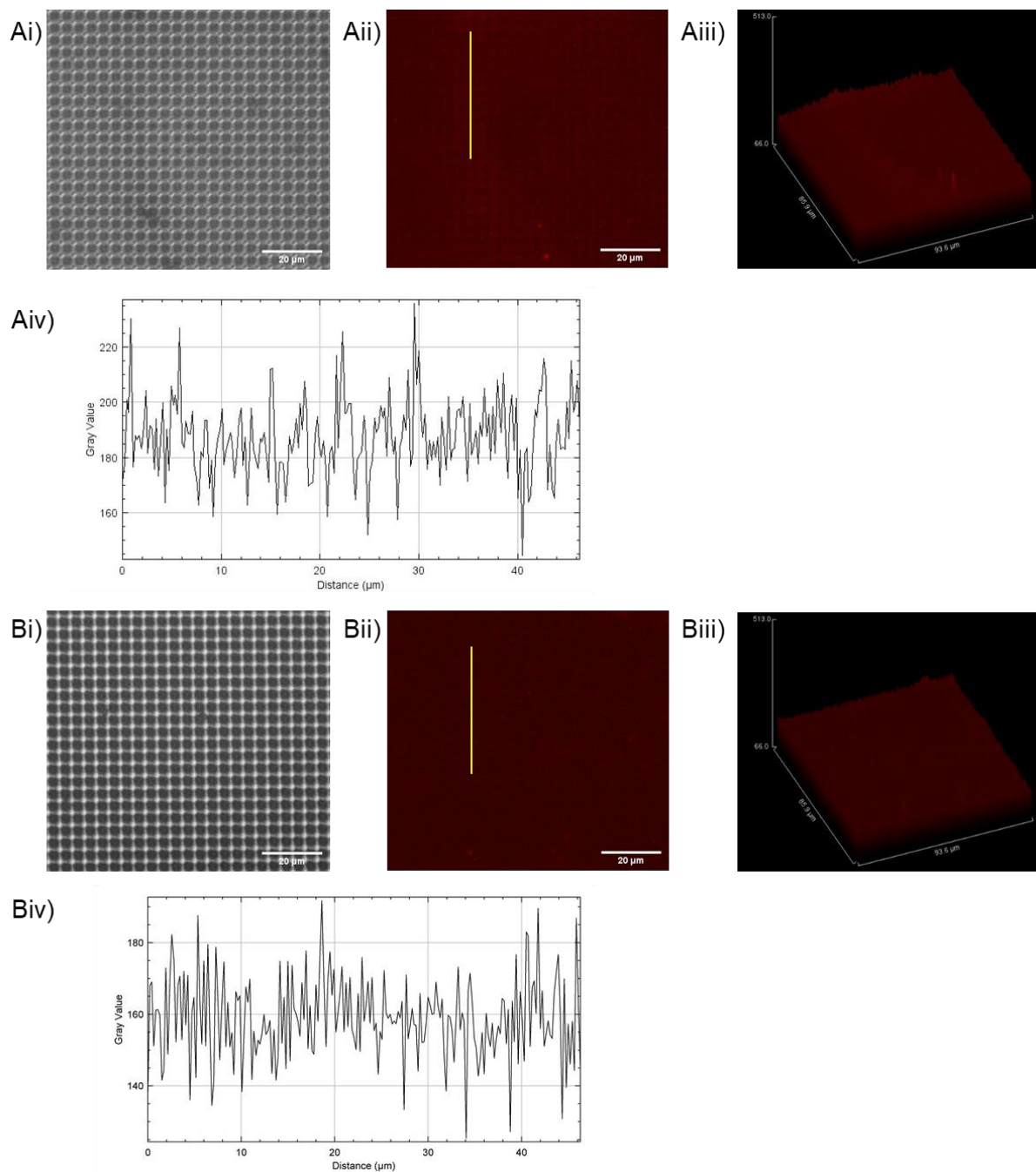


Figure 3.2: Images of surfaces after functionalisation using the step-by-step method. i) brightfield ii) fluorescence iii) fluorescence surface plots iv) fluorescence line plots of surfaces treated with A) 1.2Br and TCPP B) TCPP treatment only (control). Yellow lines represent the location from which fluorescence line plots were taken.

The effect of other solvents used to immobilise 1.2Br (DCM, Acetone, Methanol) was investigated and the corresponding fluorescence images shown in figure 3.3. The fluorescence images and surface plots show that the solvent did affect the immobilisation of 1.2Br on the surface. In the case of DCM the fluorescently labelled particles can be seen on the wafer (figure 3.3A), however the particles are not evenly labelled. Bright spots of fluorescence can be seen unevenly distributed across the surface of the particles. Note also that there are some areas without fluorescent particles. This is a result of accidental particle removal during the handling of the wafer pieces (surface damage).

Likewise, immobilisation in acetone (figure 3.3B) resulted in unevenly labelled particles as well as highly fluorescent patches which are likely aggregates of TCPP. The fluorescence line plot (figure 3.3 Biv) suggests consistent functionalisation of particles, however, the presence of aggregates (which could not be removed by sonication) seemed also to increase the fluorescence of nearby particles, this is most likely an artefact.

When methanol was used there was no evidence of particle labelling (figure 3.3C), only the presence of aggregates.

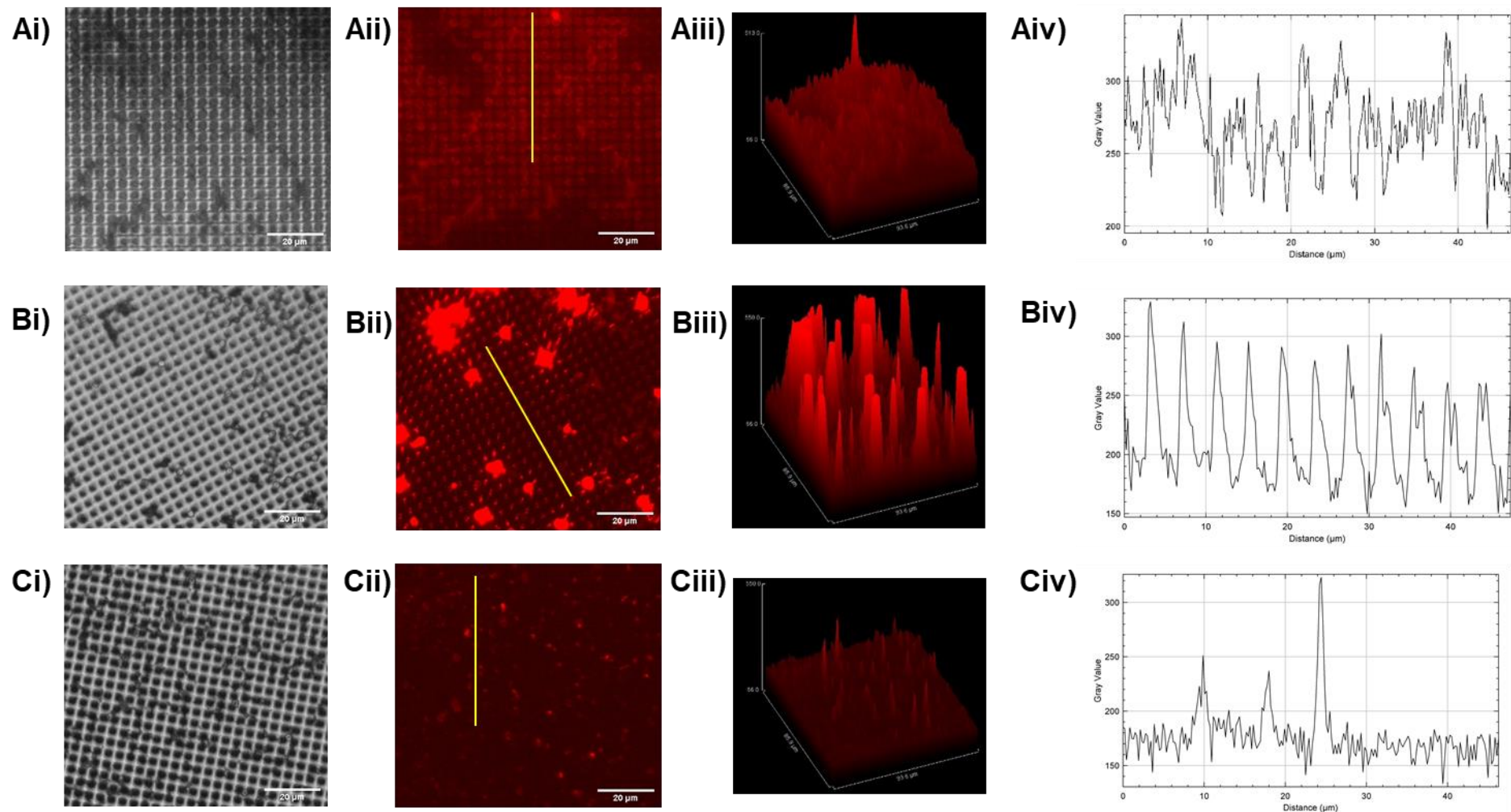


Figure 3.3: Effect of solvent on particle functionalisation. i) Brightfield, ii) fluorescence, iii) fluorescence surface plots, iv) fluorescence line plots showing particle functionalisation after deposition of 1.2 Br in A) DCM, B) Acetone C) Methanol. Yellow lines represent the location from which fluorescence line plots were taken.

None of the functionalised sample met the quality required, in terms of uniformity of labelling for cell studies. A new method was investigated by which the 1.2Br fluorophore complex was formed first in solution before being deposited on the activated particle surface as shown in figure 3.4A. For this method 5-(4-aminophenyl)-10,15,20-(triphenyl)porphyrin (ATPP) dissolved in acetone was used in place of TCPP, 1.2Br was dissolved in ethanol. The results are shown in figure 3.4B-C.

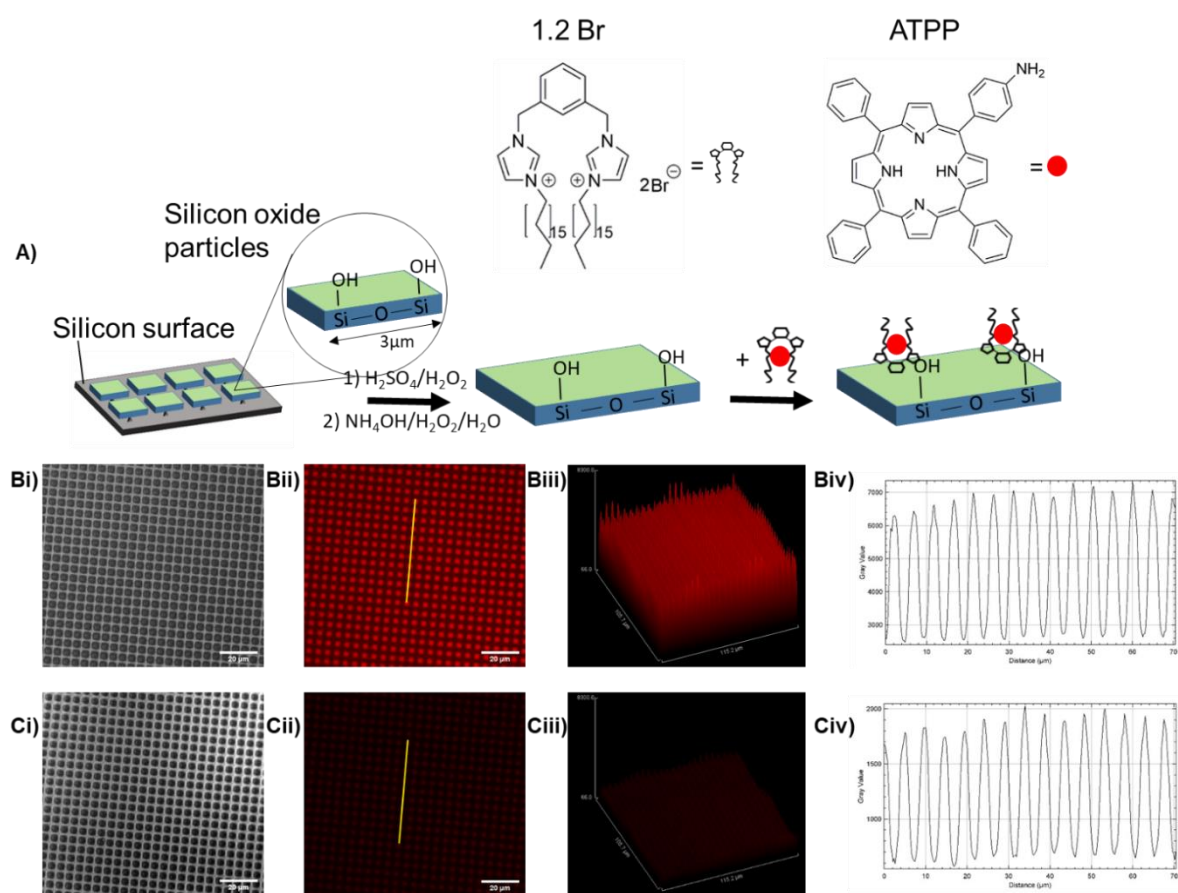


Figure 3.4: Particle functionalisation using complexation in solution method. A) Scheme showing complexation in solution method, B) particles modified using 1.2Br and ATPP C) control particles immersed in ATPP overnight. i) Brightfield images ii) fluorescence images, iii) fluorescence surface plots, iv) fluorescence intensity profiles. Yellow lines represent the location from which fluorescence line plots were taken.

The images show that the particles were fluorescently labelled by ATPP both in the presence of, and in the absence of 1.2Br. This indicates that ATPP adsorbs on to the surface of silicon oxide particles most likely as a result of the electrostatic interaction of the amino groups of the ATPP and the hydroxyl groups of the silicon oxide surface. The particles appear evenly labelled across their surfaces and the fluorescence surface plot shows that the fluorescence values are consistent between different particles. Particles labelled in the presence of 1.2Br had a higher MFI (5757 ± 259 , $n=502$) compared with particles labelled in the absence of 1.2Br (1498 ± 65 , $n=488$) which indicates that the presence 1.2Br increases the amount of ATPP binding to the particles surface.

This method of fluorescent labelling showed much more even functionalisation than using the step-by-step method and so was taken forward to compare with the well-established covalent linking methods.

3.3.2.2 Covalent labelling using silane linkers

Covalent labelling methods have been used by a vast number of groups in order to label silica particles with fluorescent molecules or other molecules of interest²⁸⁷. There are a wide variety of silanes that are available to purchase which have different terminal functional groups for this purpose. The use of four silane linkers were explored, PFP, GOPTS, APTMS, and AUTES, their structures are shown in figure 3.5.

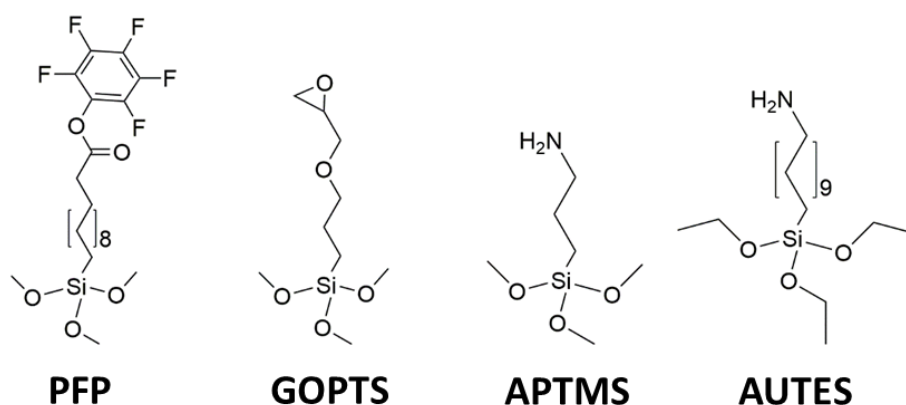
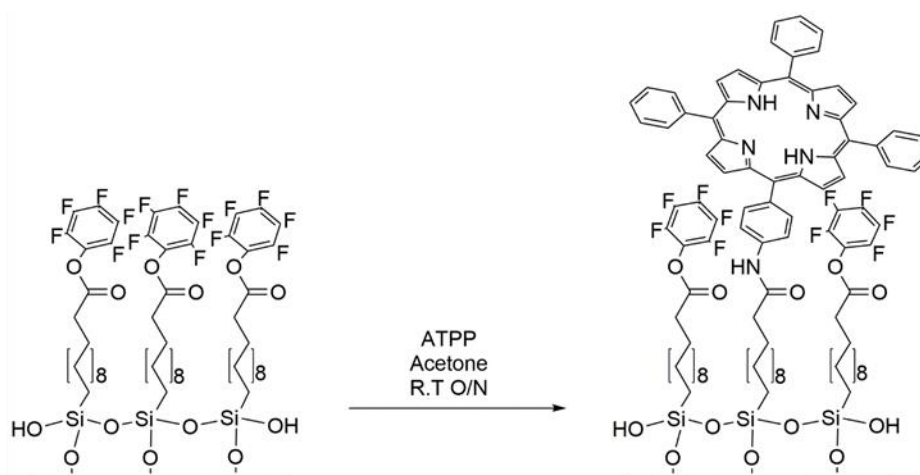


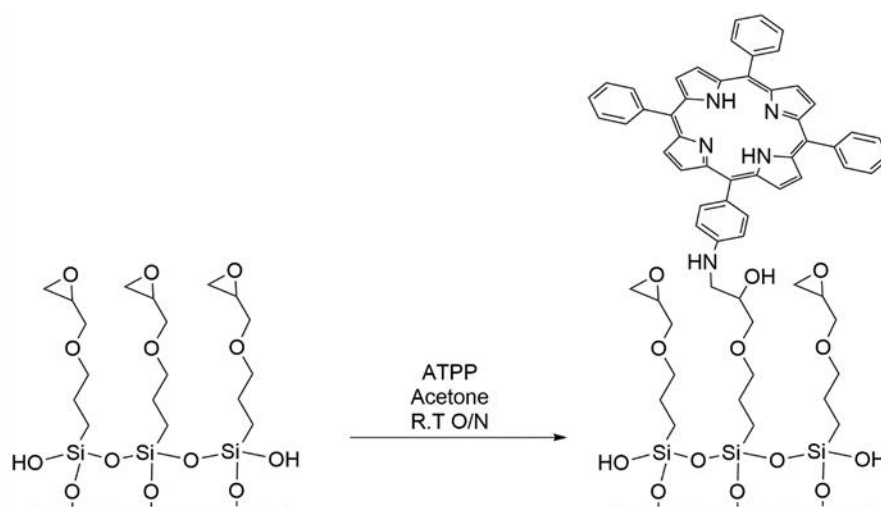
Figure 3.5: Chemical structures of silanes: 10-(pentafluorophenoxycarbonyl)decyltrimethoxysilane (PFP), (3-glycidoxypropyl)trimethoxysilane (GOPTS), 3-aminopropyl trimethoxysilane (APTMS), 11-aminoundecyltriethoxysilane (AUTES).

PFP and GOPTS contain reactive functional groups which undergo nucleophilic substitution/addition reactions (scheme 3.2 A, B) ²⁸⁸. As such, they react with molecules that contain primary amine groups to form amide and amino alcohol groups respectively. On the other hand, APTMS and AUTES are both amine terminated silanes which offer stable terminal groups that can be coupled with amine reactive fluorophores such as rhodamine B isothiocyanate (RBITC) (scheme 3.2 C).

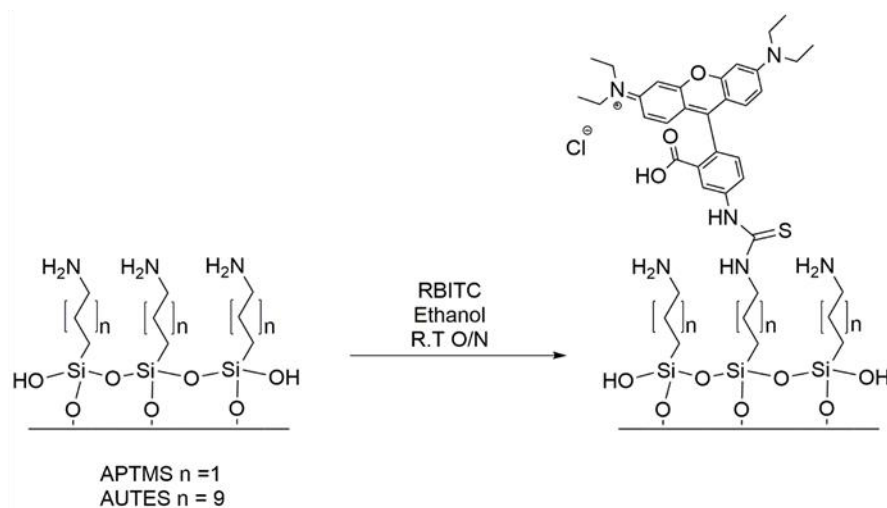
A)



B)



C)



Scheme 3.2: Labelling of particle surfaces functionalised with silane linkers A) PFP and ATPP B) GOPTS and ATPP C) APTMS/AUTES and RBITC.

After activation using acidic and basic piranha treatment, silanes were deposited on particles attached to wafers and their water contact angles measured. The results are shown in table 3.2. The increase in contact angle from hydrophilic ($<10^\circ$) to hydrophobic ($>40^\circ$) is consistent with the presence of hydrocarbon chains of the silanes and thus indicates successful deposition of each of the silanes. GOPTS, APTMS, and AUTES displayed comparable water contact angles to those previously published ²⁸⁹⁻²⁹¹. Only one study has measured the contact angle of a surface after modification with PFP ²⁸⁸. A water contact angle of 88° was measured which is significantly higher than measured in this study, however a different deposition time, solvent, and substrate (polycrystalline silicon) were used.

GOPTS and APTMS exhibit lower contact angles than PFP and AUTES, this is likely due to the length of the hydrocarbon chains. Longer chains are more hydrophobic and so produce higher contact angles ²⁹²⁻²⁹³. It would be expected that PFP would have a higher contact angle than AUTES owing to the highly hydrophobic pentafluorophenyl group, a possible explanation for the lack of difference could be that due to the instability of PFP, some reaction with atmospheric water might have taken place and so the surface is more hydrophilic.

Table 3.2: Water contact angles θ ($^\circ$) after treatment with PFP, GOPTS, APTMS, and AUTES

Surface treatment	Water contact angle \pm s.d
Activation	$< 10^\circ$
PFP	$59.0^\circ \pm 3$
GOPTS	$38.9^\circ \pm 4$
APTMS	$37.7^\circ \pm 11$
AUTES	$61.5^\circ \pm 6$

After immobilisation of each of the silanes on particle surfaces, ATPP solution was added to PFP and GOPTS- modified surfaces and RBITC was added to APTMS and AUTES-modified surfaces as shown in scheme 3.2. Fluorescence microscopy images showed that each of the silanes had been successfully immobilised onto the particle surface and had subsequently been labelled (figure 3.6).

In each case uniformity of labelling on the surface of the particles was very consistent and comparable to the complexation-in-solution method. This is important for cell studies as an uneven distribution of fluorophore on the particle surface will cause a difference in interaction between the particle and cell and thus interfere with the results.

All of the covalent linkers demonstrated suitable labelling in these microparticles to be used for cell work. Although these linkers have been used for labelling silicon oxide particles in the literature, it was necessary to test each of them in these novel microfabricated particles. AUTES was chosen as the linker for subsequent experiments because it has been demonstrated that linkers with longer carbon chains (undecyl) form stable monolayers that are more resistant to hydrolysis than shorter (propyl) chains ²⁹¹.

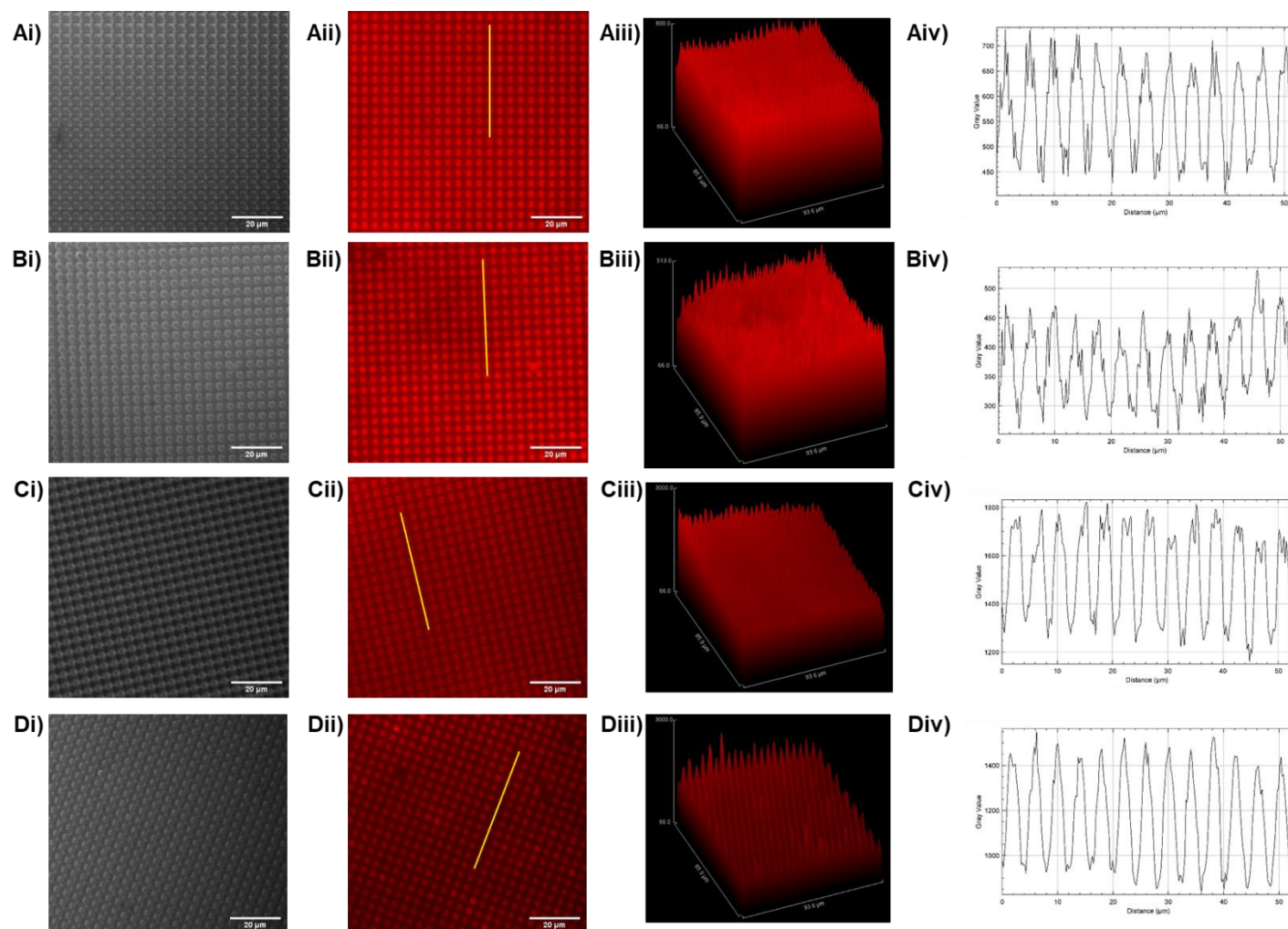


Figure 3.6: Fluorescence of covalently labelled particles. A) PFP and ATPP, B) GOPTS and ATPP, C) APTMS and RBITC, and D) AUTES and RBITC i) Brightfield, ii) fluorescence iii) fluorescence surface plots, and iv) fluorescence intensity profiles. Yellow lines represent the location from which fluorescence line plots were taken.

3.3.2.3 Comparison of fluorophore release from non-covalent and covalently labelled particles

In order to be suitable for uptake experiments, it was necessary to determine that both non-covalently labelled and covalently labelled particles would not release fluorophore in buffer conditions at 37°C. Wafer pieces possessing particles labelled non-covalently using 1.2Br-ATPP or ATPP alone and covalently using AUTES-RBITC were incubated in PBS at 37°C for 2 hours. The fluorescence intensity of the particles was assessed before and after incubation using fluorescence microscopy (figure 3.7). Median fluorescence intensity values were calculated by imaging 5 areas of each wafer piece and measuring the fluorescence intensity of 500 particles per area. After incubation 1.2Br-ATPP labelled particles showed a 19.9% reduction in fluorescence intensity indicating that ATPP was released into the buffer (figure 3.8). This was also the case with particles that were non-covalently labelled with ATPP alone which showed a 53.1% reduction in fluorescence intensity. However, as expected no such decrease was seen with covalently labelled AUTES-RBITC particles which showed no significant change in fluorescence intensity.

The release of ATPP from non-covalently labelled particles could cause erroneous results and so the covalent labelling method using AUTES-RBITC was chosen for subsequent experiments.

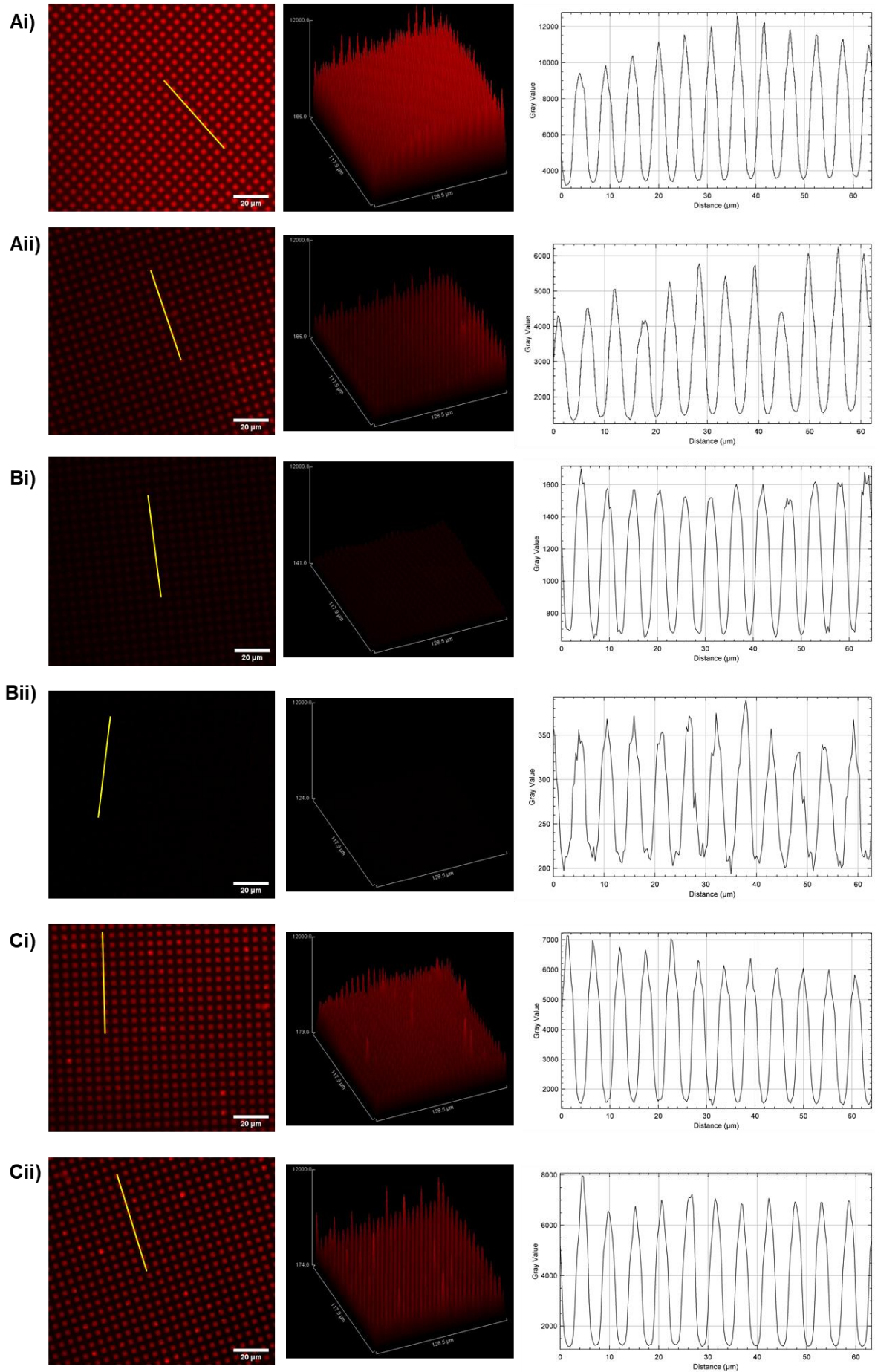


Figure 3.7 images of particles before and after incubation in PBS 37°C for 2 hours. Fluorescence images, fluorescence surface plots, and fluorescence intensity profiles of particles before (i) and after (ii) incubation in PBS for 2 hours at 37°C. A) Particles labelled with ATTP in the presence of 1.2 Br, B) particles labelled with ATPP in absence of 1.2Br, C) Particles labelled with AUTES and RBITC.

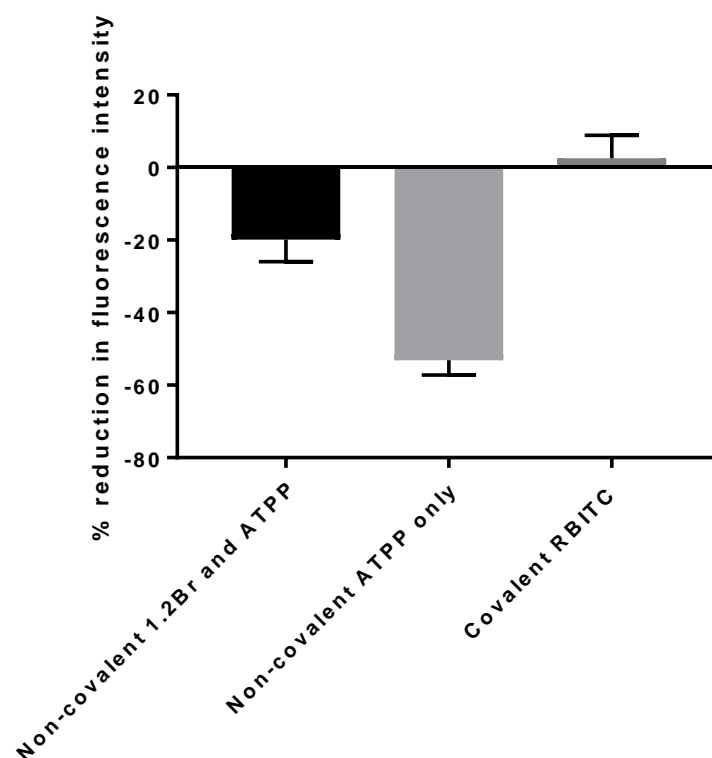


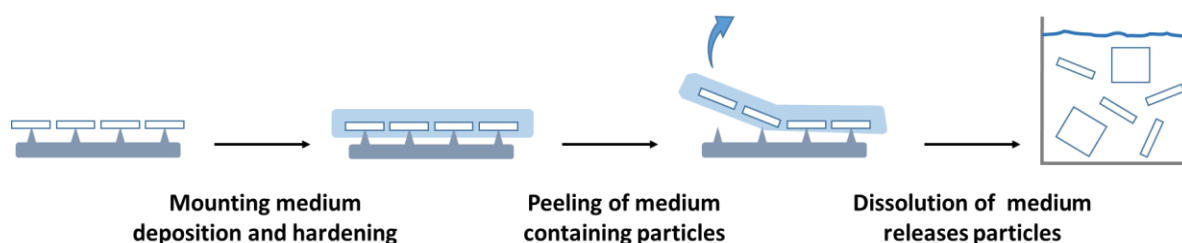
Figure 3.8: % reduction in fluorescence intensity after incubation in PBS at 37°C for 2 hours

3.3.3 Characterisation of fluorescently labelled particles

3.3.3.1 Measurement of median fluorescence intensity (MFI) and % coverage of fluorophore

Silicon oxide spheres, hexahedrons, and pyramids were fluorescently labelled using AUTES and RBITC. For the spheres this process was performed while the spheres were in suspension whereas the hexahedrons and pyramids were fluorescently labelled while still attached to

wafers by a supporting anchor. Hexahedrons and pyramids were peeled away from the wafer by using a mounting medium as shown in scheme 3.3. The resulting particles in suspension were imaged using fluorescence microscopy (figure 3.9).



Scheme 3.3: Peeling of microparticles from silicon wafer

As can be seen from the images of the released particles, successful labelling was achieved for each of the particle shapes. Distinct particle shapes can be identified in the fluorescence images which correspond to the brightfield images indicating that RBITC is evenly distributed across the surface of the particles and that the labelling was not affected by the release of the particles from the wafer.

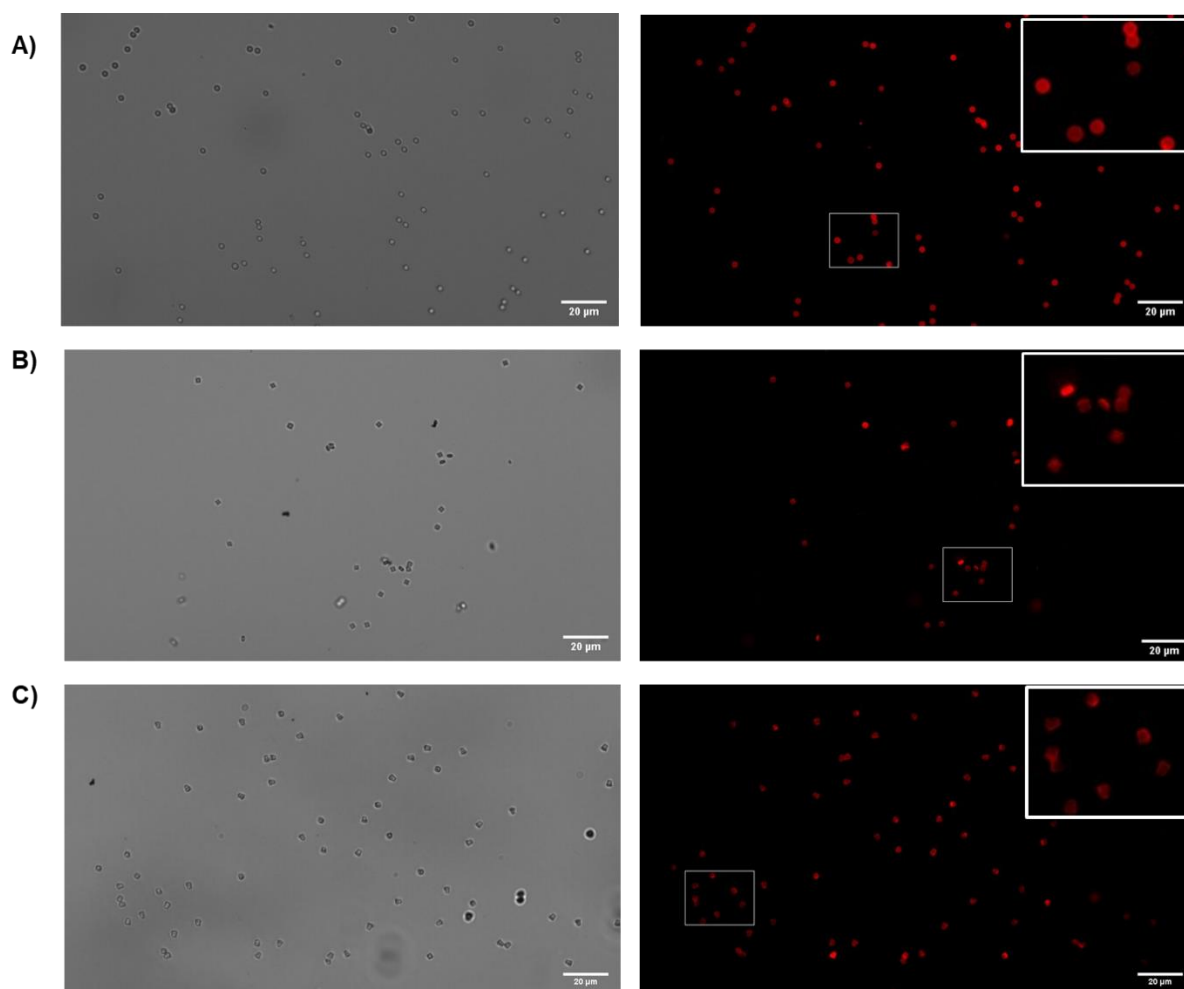


Figure 3.9: Fluorescently labelled particles in suspension. Brightfield and fluorescence images of A) Spheres B) Hexahedrons C) Pyramids after immobilisation of AUTES and labelling with RBITC. Spheres were functionalised in suspension whereas hexahedrons and pyramids were functionalised on wafer pieces and subsequently released into suspension after detachment by peeling.

In order to compare the degree of fluorescent labelling of each particle type, imaging flow cytometry was used to measure the median fluorescence intensity (MFI) ($n > 1000$ particles of each shape). The obtained values are shown in table 3.3 and fluorescence intensity histograms are shown in appendix I S3.4. The values show that each particle type had similar MFI indicating a similar degree of labelling. To confirm this, an estimation of the percentage of labelled surface amines was made. This was done by comparing the MFI values of each particle type with a calibration curve of particles (3µm spheres) that had known percentages

of amines labelled with RBITC (Appendix I S3.5). This was achieved by labelling silane molecules prior to immobilization on the particles. The results displayed in table 3.3 show that all particles had lower than 2% of surface amines labelled with RBITC.

Table 3.3: Particle MFI and estimation of surface labelling

Particle type	Particle MFI	% amines labelled
Spheres	21477.46	1.84
Hexahedrons	22275.59	1.92
Pyramids	18095.48	1.53

It is important to have a similar amount of RBITC on the surface of the particles because rhodamine B is a relatively hydrophobic molecule (logP 1.95)²⁹⁴ and so could therefore can promote uptake into cells¹⁰⁸. Juliano *et al* found that the uptake of dendrimers into HeLa cells was enhanced by their conjugation with Oregon green, a fluorescent dye with a similar chemical structure to rhodamine B, although the exact mechanism was not deduced²⁹⁵. Additionally, it has been shown that rhodamine B interacts with type BI scavenger receptors and so could enhance uptake via specific receptor interactions²⁹⁶. However, by having a low percentage of surface amines labelled with rhodamine, these effects on interaction with the cells will be reduced. In a study looking at the required amount of particle surface functionalisation to enhance cellular uptake, it was found that at least 4% of the surface functional groups (maleimide) needed to be covered with wheat germ agglutinin (WGA) in order to significantly increase uptake of PEG-PLA nanoparticles into Calu-3 cells in comparison with non-functionalised particles²⁹⁷.

3.3.3.2 Measurement of trypan blue quenching efficiency

One of the methods to be used to distinguish internalised particle from surface-bound particles in this chapter requires the use of fluorescence quenching of surface-bound particles. In order for this method to be effective the degree of fluorescence quenching must be known to ensure that surface-bound particles are significantly less fluorescent than internalised particles. In order to calculate this, the MFI of each particle type was measured before and after quenching with trypan blue ($n > 1000$ particles). The results are displayed in table 3.4. In each case the MFI was decreased after trypan blue quenching by over 90%. This indicates particles can be suitably quenched in order to distinguish internal and surface-bound particles ²⁹⁸.

Table 3.4: Quenching efficiency of trypan blue

Particle type	Particle MFI	Quenched particle MFI	Quenching efficiency (%)
Spheres	21477.46	1921.78	91.05
Hexahedrons	22275.59	987.17	95.57
Pyramids	18095.48	1062.05	94.13

3.3.4 Particle interaction with RAW 264.7 cells

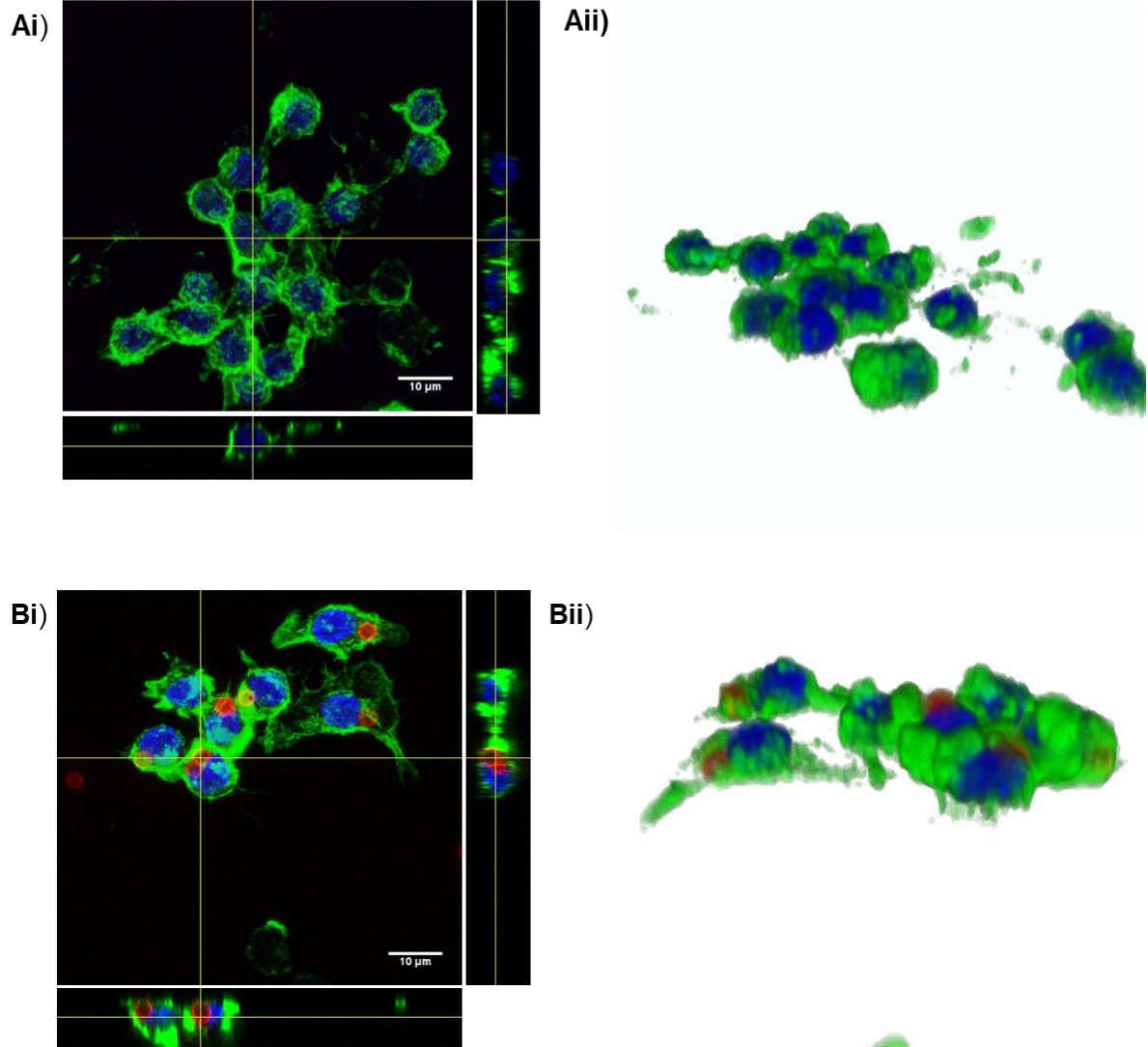
3.3.4.1 Qualitative determination of microparticle uptake

In order to examine if each of the differently shaped microparticles could be internalised by RAW 264.7 macrophages, laser scanning confocal microscopy (LSCM) and immunostaining was used. Macrophages were incubated with fluorescently labelled particles of each shape for 4 hours before being fixed and stained. BDP 630 was used in place of RBITC to fluorescently label the particles for this qualitative examination of particle uptake.

Representative Z-projections are displayed along with their orthogonal views and 3D representations in figure 3.10. Cell nuclei, stained with DAPI are shown in blue, actin filaments stained with ifluor488 phalloidin are shown in green and particles are displayed in red. Actin

staining with phalloidin shows the cell cytoskeleton, with cells appearing either rounded or in some cases spread out with pseudopodia seen protruding from cells.

Particles appear as hollow shapes in the orthogonal views (figure 3.10 Bi-Di), because they are labelled only on their surface and so no fluorescence is seen inside the particles.



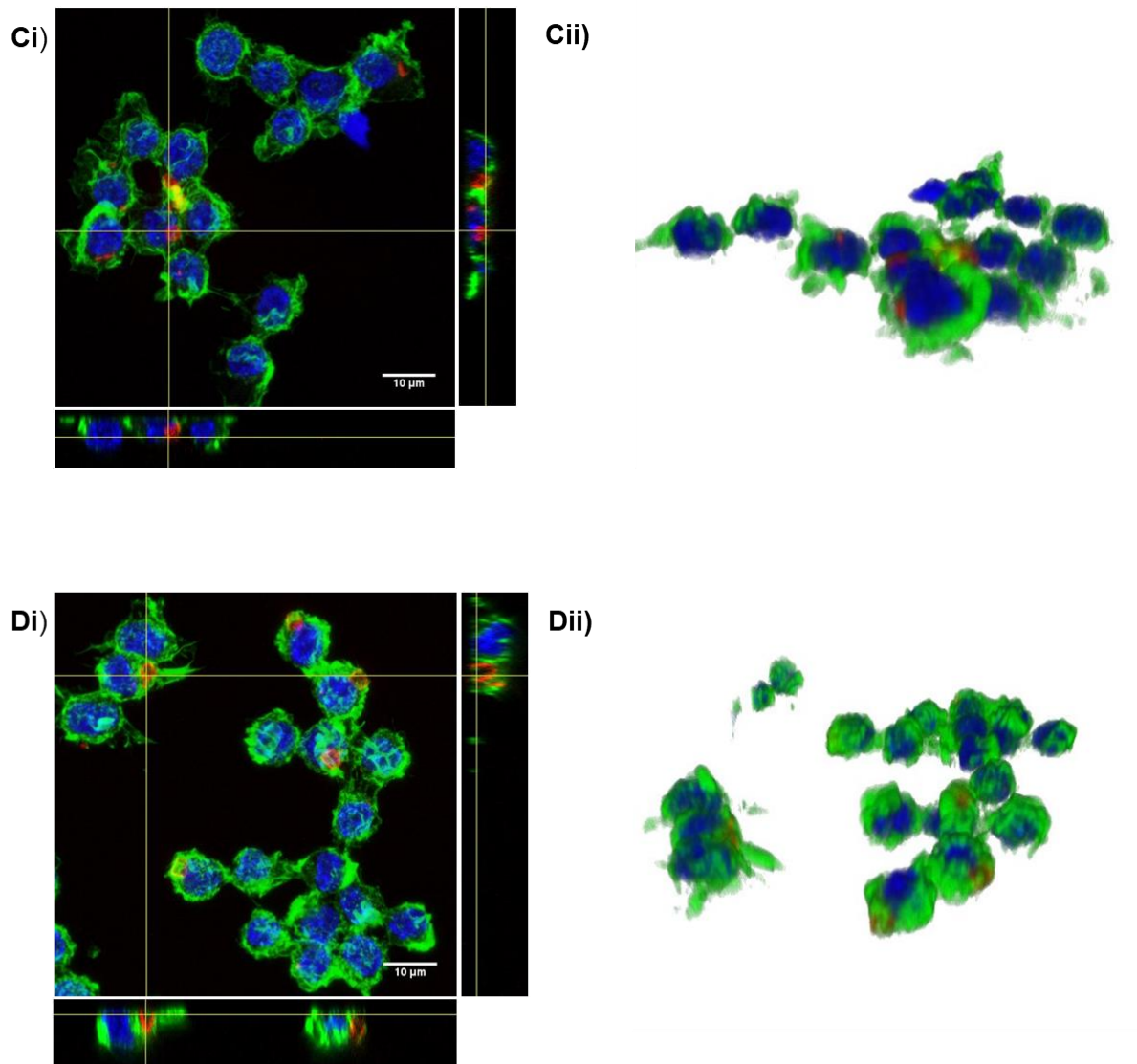


Figure 3.10: CLSM images of RAW 264.7 cells with internalised microparticle shapes. i) Z projections and orthogonal views, ii) 3D reconstructions of cells treated with A) 1% HEPES in HBSS only B) Spheres C) Hexahedrons D) Pyramids. Nuclear staining (BLUE), Actin staining (GREEN), Particles (RED).

In comparison with control cells that had not received any particle treatment, macrophages which had been treated with particles displayed similar morphologies and nuclear shapes. The actin cytoskeleton staining (green) can be used to determine if the particles have been internalised. In the orthogonal views, particles found within the green boundary of the cytoskeleton can be considered to have been internalised. These images show that each of

the particle shapes had been internalised by RAW 264.7 macrophages. Particles were typically found in the perinuclear region of the cell which is in line with the established literature which details that upon phagocytosis particles are contained within the phagosome which is transported towards the nucleus fusing with lysosomes to become a phagolysosome²⁹⁹⁻³⁰².

3.3.4.2 Intracellular localisation of Spheres, hexahedrons, and Pyramids

Immunostaining was used in order to determine the intracellular localisation of the particles after internalisation had taken place. Cells were incubated with particles for 4 hours and then fixed and permeabilised. Cell nuclei were stained blue with DAPI and lysosomal-associated membrane protein 1 (LAMP-1) antibody stain (green) was applied to stain lysosomes/late endosomes. Images of stained cells with each particle shape are displayed in figure 3.11 with particles displayed in red.

In untreated cells (figure 3.11 A) lysosomes/late endosomes were stained and appeared as small green dots inside the cell surrounding the nucleus. Lysosomes/late endosomes were not stained in all cells, this could be because not all cells contained lysosomes/late endosomes or more likely due to a lack of staining, perhaps resulting from a lack of permeabilisation. In cells to which particles had been applied, lysosomes/late endosomes could also be seen as small green dots throughout the cell. However, in cells that had internalised particles a green ring was often observed surrounding the particle. This indicates that LAMP-1 was present in the membrane surrounding the particle.

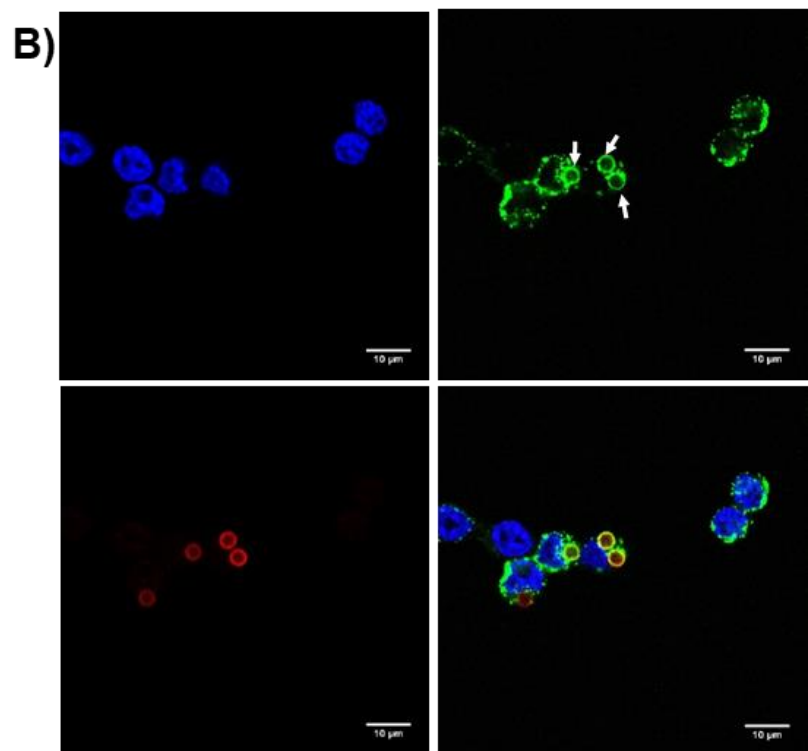
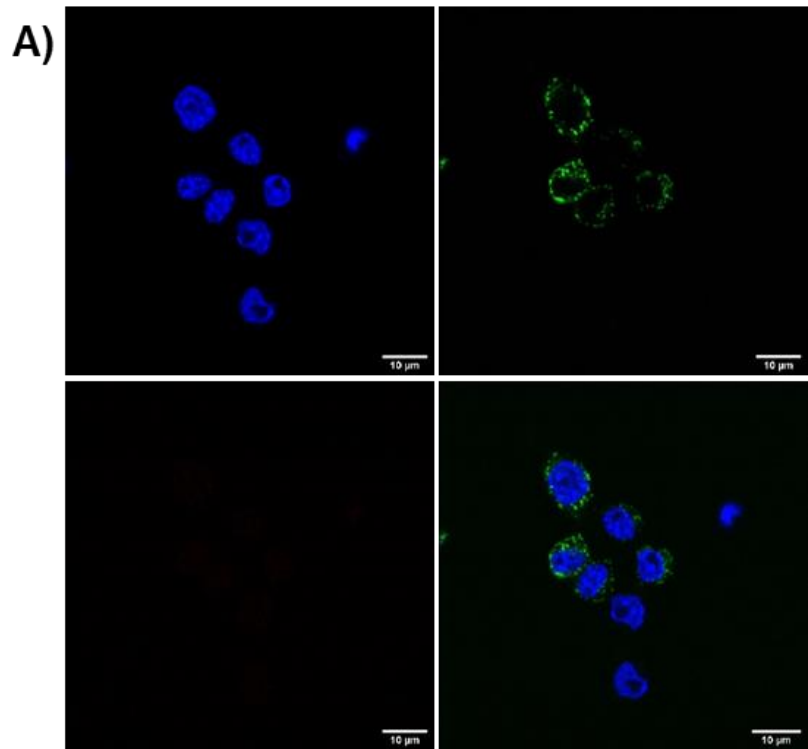
Upon maturation of the phagosome, lysosomes and endosomes fuse with the phagosomal membrane to deposit their contents. A 'Kiss and run' mechanism has been proposed as a major mechanism for this, where complete fusion of the lysosomal/endosomal and phagosomal membranes is prevented by fission after some transfer of luminal contents has taken place³⁰³. Proteins such as LAMP-1 are left behind in the late phagosome/phagolysosome thereby indicating that fusion has taken place³⁰⁴. The white

arrows in figure 3.11 B, C, and D indicate particles that are surrounded by LAMP-1 positive membranes and are therefore contained within the late phagosome/phagolysosome.

Particles that were clearly not internalised by cells displayed no such ring of green fluorescence thus demonstrating that the green fluorescence results from the LAMP-1 positive membrane rather than an artefact of overlapping fluorescent emission or direct binding of the LAMP-1 antibody to the particle. These particles are highlighted with yellow arrows in figure 3.11 C and D.

Also present are particles that had been internalised by cells but that did not display a ring of fluorescence. It is therefore likely that these particles were inside the phagosome and that endosome/lysosome-phagosome fusion had not yet taken place. No difference was seen between the different shapes in terms of localisation. As in the case of the actin staining, the majority of particles were situated in the perinuclear region of the cell.

Images of at least 40 cells from each sample were examined and the percentage of particles surrounded by LAMP-1 positive membranes calculated. The percentage of spheres and pyramids was similar (60.9 and 53.3% respectively), however the percentage of hexahedrons surrounded by LAMP-1 positive membrane was lower (31.0%).



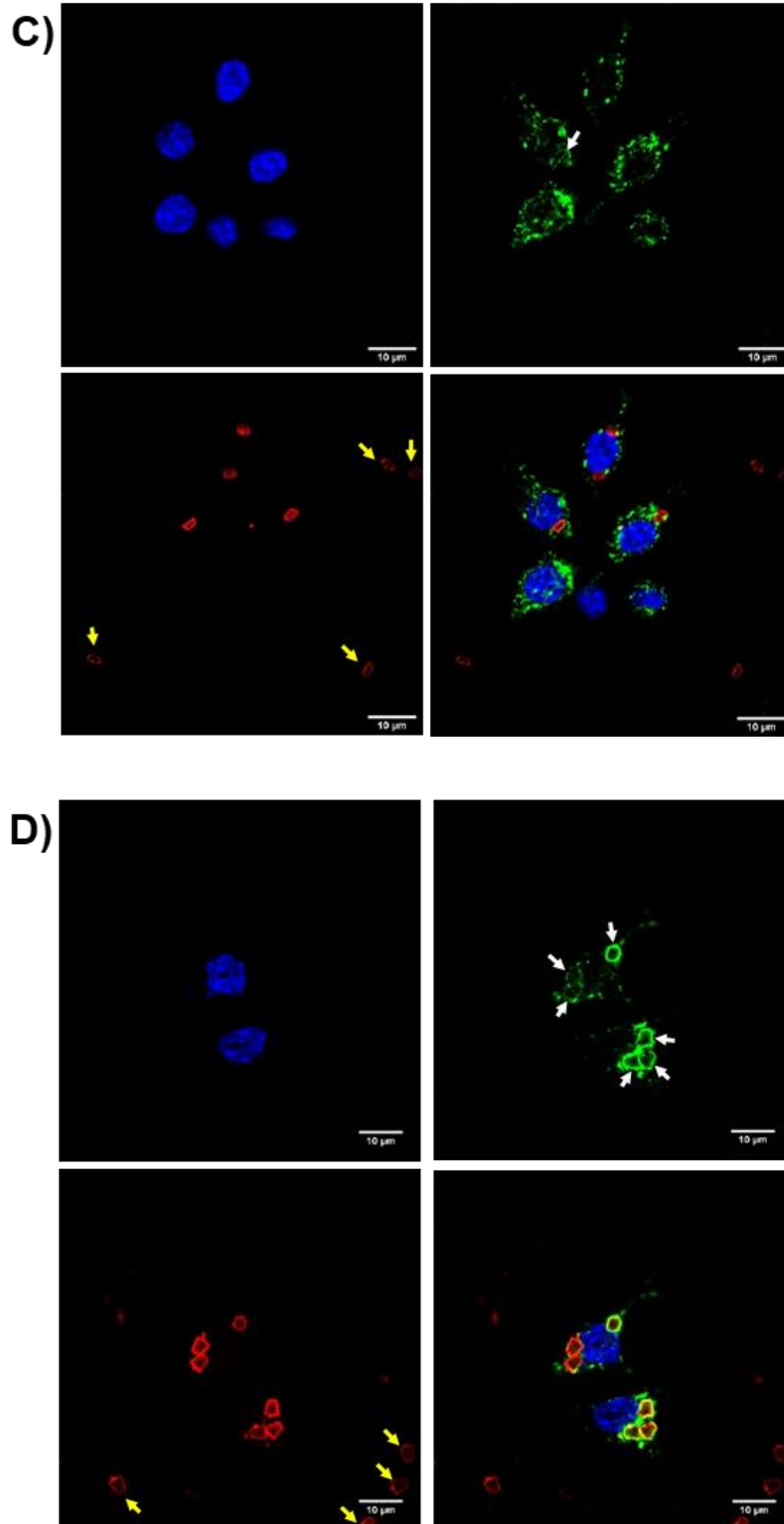


Figure 3.11: Intracellular localisation of particles after phagocytosis. Particles treated with A) 1% HEPES in HBSS only B) Spheres C) Hexahedrons D) Pyramids. DAPI (BLUE), LAMP-1 (GREEN), Particles (RED). White arrows indicate LAMP-1 co-localisation with particles. Yellow arrows indicate particles not associated with cells.

3.3.4.3 Comparison of image analysis and trypan blue (TB) quenching methods

Imaging flow cytometry is a recently developed technique that allows the high-throughput imaging of cells and has been used for applications such as quantifying particle internalisation and localisation³⁰⁵⁻³⁰⁶. However, as image analysis is a relatively new technique to quantify particle internalisation, and as there have been conflicting reports in the literature about its results, it was deemed necessary to compare the results acquired using this method with TB quenching, a more established method²⁷³⁻²⁷⁴.

RAW 264.7 macrophages were incubated with rhodamine B-labelled particle suspensions at particle:cell ratios of 5:1 and 10:1, with or without prior stimulation with LPS and the results shown in figure 3.12. Determination of particle uptake was calculated in two ways. Firstly, the percentage of cells which had internalised particles was measured by counting the number of cells which had a fluorescent intensity above the intensity of untreated cells and dividing by the total number of cells (figure 3.12A). Secondly, by fluorescent spot counting of cells with internal particles, the mean number of particles internalised per cell was calculated (figure 3.12B).

The data in figure 3.12 A showing the percentage of cells with internal particles indicates that there was no statistical difference between the two methods. Owing to the way in which the image analysis method discriminates internal from external particles (appendix I) it might be expected that an over estimate of the percentage of cells with internal particles is observed. This is because although surface-bound particles can be discriminated in the X- and Y-planes, the depth of field in the Z-plane is not sufficient to distinguish whether particles are internal or surface-bound. The TB method does not suffer this drawback and instead relies on adequate fluorescence quenching to gate surface-bound particles. Despite this, these results agree with the study by Vranic *et al.* that showed equivalent uptake using quenching and image analysis

²⁷⁴. A possible explanation for the lack of difference between the two methods is that the majority of particles are internalised rather than surface-bound and so the overestimation of surface-bound particles by the image analysis method is minimised.

Particle uptake at 4°C was assessed using the image analysis method (figure S3.6) and showed a reduction in particle uptake in comparison to 37°C. As Phagocytosis is an energy-dependent process it is reduced at this temperature, ³⁰⁷ and so this confirmed that the image analysis method was able to measure particle internalisation.

The mean number of particles per cell was calculated and the data presented in figure 3.12 B. In the majority of cases the image analysis method calculated a higher mean number of particles per cell than the trypan blue method. This may result from the fact that surface-bound particles in cells that have both internal and external particles are included in the image analysis spot count but not in the trypan blue spot count (due to quenching).

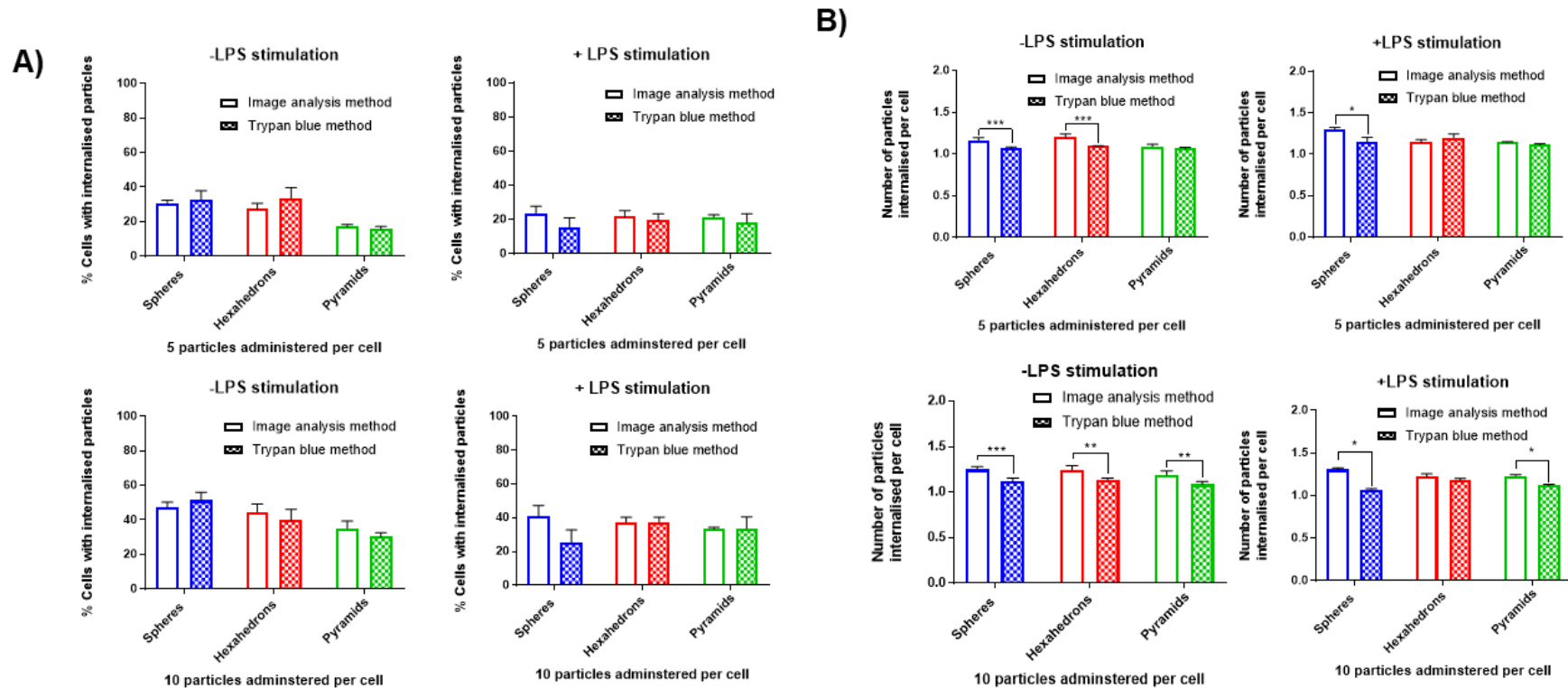


Figure 3.12: Comparison of image analysis and TB quenching methods for quantifying particle internalisation. A) % Cells that had internalised particles. B) Number of particles internalised per cell. *, **, ***, **** indicate statistical significance ($p < 0.05$, 0.01 , 0.001 , 0.0001 respectively) as calculated by multiple unpaired T-tests. Values are representative of three biological repeats \pm SEM ($N=3$).

3.3.4.4 Effect of LPS stimulation on particle uptake

Macrophages are highly dynamic cells that exhibit phenotypic changes in response to environmental cues. Upon stimulation with lipopolysaccharide (LPS), a component of bacterial cell membrane, differentiation occurs towards an M1 phenotype. This is characterised by changes in regulation of membrane receptors, (increase in expression of TLR2, TLR4, CD16, CD32, CD64, CD80, CD86, decrease in expression of Scavenger receptors A/B, CD163, MR, CD14, CD23) and changes in cytokine production (Increase in production of IL-12, IL-23, TNF- α , IL-1, IL-6, Type 1 IFN, decrease in production of IL-10, IL-1 receptor agonist) ⁷⁰. Therefore, the effect of the stimulation of macrophages with LPS on particle uptake was examined.

RAW 264.7 cells were stimulated with LPS for 24 hours prior to dosing in order to encourage differentiation to the M1 phenotype. This was assessed visually by light microscopy as can be seen in figure 3.13. Cells that had undergone stimulation with LPS exhibited morphological changes as can be seen in figure 3.13 B. In general, cells appeared larger and displayed vacuole-like and filopodia structures, indicative of M1-activated macrophages ³⁰⁸⁻³⁰⁹.

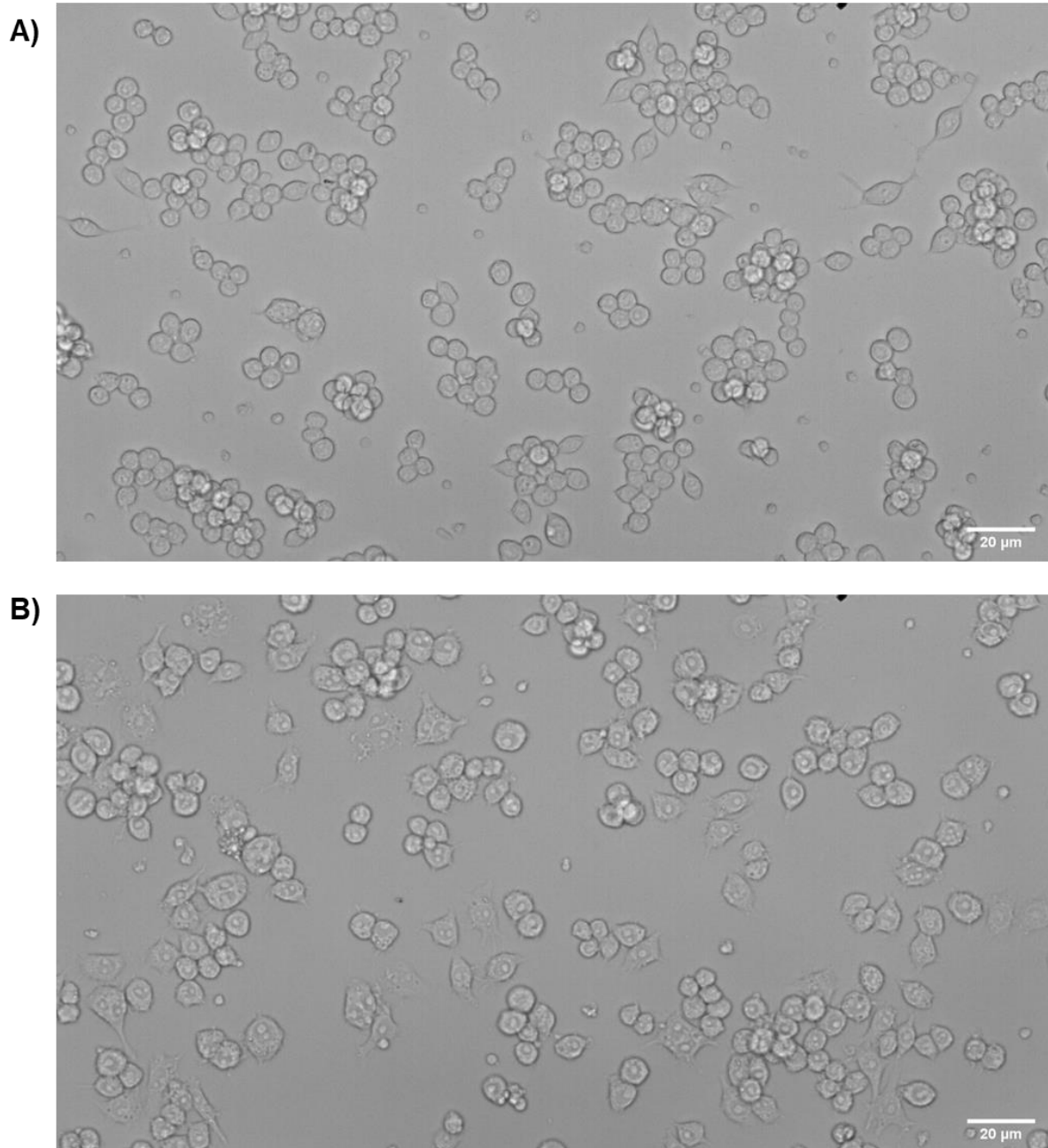


Figure 3.13: Light microscopy images of RAW 264.7 cells incubated for 24 hours in A) Culture media, B) Culture media containing LPS

Particle uptake by cells was analysed using both TB quenching and image analysis, the results are shown in figure 3.14. Figure 3.14 A shows the effect of LPS stimulation on the percentage of cells that had internalised particles. LPS stimulation did not alter significantly the percentage of cells taking up particles. The only significant difference was observed in the case of spheres that were administered at a dose of 10 particles per cell and analysed using the trypan blue quenching method where LPS stimulation resulted in a significantly lower percentage of cells with internal particles.

Similarly, there was very little difference in the average number of particles taken up per cell in LPS stimulated and unstimulated cells (figure 3.14 B). The majority of cells internalised 1 or 2 particles with a much smaller proportion of cells internalising 3 or more particles.

A study by Rieger *et al.* using imaging flow cytometry demonstrated that, upon stimulation with LPS, RAW 264.7 macrophages association with microparticles increased overall, however the cause for the increase in association was not an increase in internalisation but an increase in surface binding of zymosan particles ³¹⁰. If the same was true in the case of the silicon oxide particles used in this study, the increased binding of particles to the cell surface would not be detected by the TB quenching method as these additional particles would be quenched. The image analysis method can quantify this effect by analysing the percentage of cells with surface-bound particles as shown in figure 3.15. Higher surface binding was not observed upon stimulation with LPS, instead no statistically significant difference in overall particle association was observed in LPS-stimulated cells.

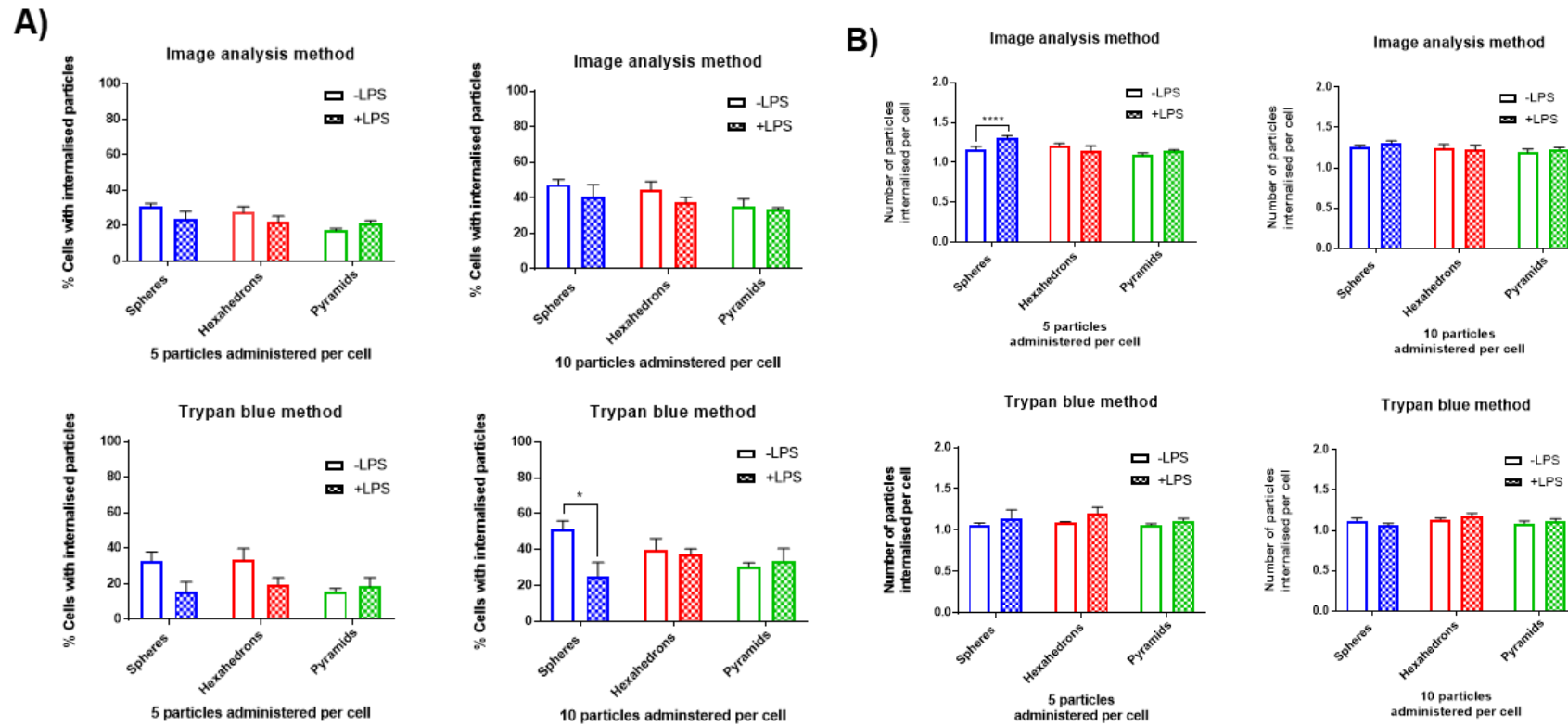


Figure 3.14: Effect of LPS stimulation on particle uptake. The effect of LPS stimulation on A) % cells with internalised particles B) The number of particles internalised per cell. *, **, ***, **** indicate statistical significance ($p < 0.05, 0.01, 0.001, 0.0001$ respectively) as calculated by multiple unpaired T-tests. Values are representative of three biological repeats \pm SEM ($N=3$).

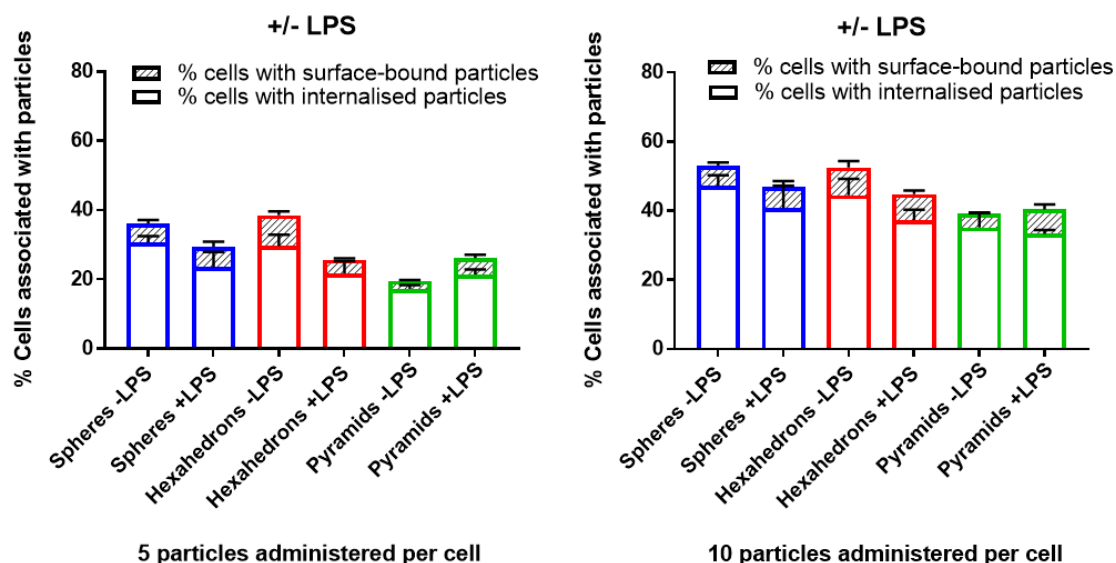


Figure 3.15: The effect of LPS stimulation on particle association, internalisation, and surface-binding. *, **, ***, **** indicate statistical significance ($p < 0.05$, 0.01 , 0.001 , 0.0001 respectively) as calculated by multiple unpaired *T*-tests. Values are representative of three biological repeats \pm SEM ($N=3$).

3.3.4.5 Effect of particle shape on uptake by RAW 264.7 macrophages

Macrophages have previously been shown to display differential uptake of particles depending on the particle morphology. As such, it was expected that differences in the internalisation of spheres, hexahedrons, and truncated pyramids would be observed. The results from analysing differences in internalisation between the different particle shapes using both the image analysis and TB quenching method are shown in figure 3.16. Using both analysis methods there was an increase in the percentage of cells with internal particles upon increasing the dose from 5 to 10 particles per cell figure 3.16 A. This effect was seen in both LPS-stimulated and non-stimulated cells. However the mean number of particles internalised per cell did not change with increasing dose (figure 3.16 B).

Using the image analysis method, the data is presented as the percentage of cells associated with particles and further distinguishes the percentage of cells with internal and surface-bound particles (figure 3.16 Ai-ii).

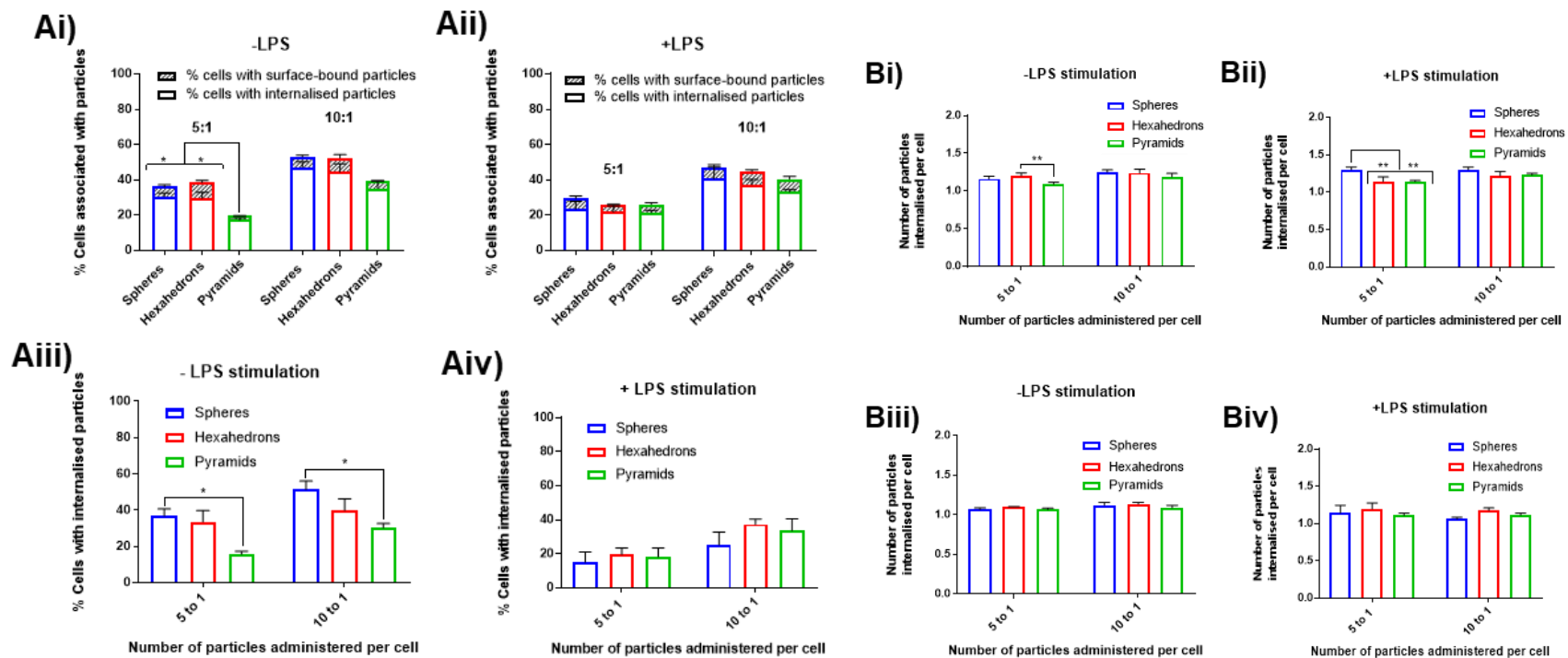


Figure 3.16: The effect of particle shape on cellular uptake. The effect of particle shape on A) % of cells with internal particles, B) Number of particles internalised per cell. i/ii) analysed using image analysis method, iii/iv) analysed using TB quenching method. *, **, ***, **** indicate statistical significance ($p < 0.05$, 0.01 , 0.001 , 0.0001 respectively) as calculated by 2way ANOVA with multiple comparisons. Values are representative of three biological repeats \pm SEM ($N=3$).

Using the image analysis method (figure 3.16Ai-ii) no significant differences between spheres and hexahedrons in terms of the percentage of cells associated with particles, the percentage of cells with internalised particles or the percentage cells with surface-bound particles. This was the case for both LPS-stimulated and non-stimulated cells. This was also the case using the TB quenching method, with no significant differences seen in internalisation of particles between spheres and hexahedrons (figure 3.16 Aiii-iv).

However, significantly fewer cells internalised truncated pyramids compared to spheres indicating that the ability of macrophages to internalise truncated pyramids is lower. This may result from the anisotropic nature of these particles which can present to cells in multiple orientations as opposed to spherical particles which can only make contact with the cell in one orientation. Actin polymerisation must then occur in order to wrap the plasma membrane around the particle ³¹¹. Differences in the capacity of membrane wrapping, depending on particle orientation, could therefore result in reduced uptake.

Curiously this effect was seen only in cells that had not been stimulated with LPS. There were no differences between any of the shapes in LPS-stimulated cells. Filopodia and membrane ruffles on the surface of macrophages are dynamic structures which have been shown to contribute to macropinocytosis and phagocytosis ³¹². Upon stimulation with LPS, actin polymerisation is increased resulting in more filopodia and membrane ruffles ³¹³⁻³¹⁵. This change in the macrophage skeletal structure could therefore explain the reduced the effect of particle shape seen in LPS-stimulated cells.

No differences were seen in the number of particles internalised per cell for any particle shape (figure 3.16 Bi-iv). The majority of cells that internalised particles only internalised one particle regardless of particle shape and this was consistent for both particles doses.

In a similar study by Sharma *et al.* which looked at the internalisation of polystyrene spheres, oblate ellipsoids, and prolate ellipsoids by RAW 264.7 macrophages, there was no difference in internalisation seen between the different shapes with volumes above 24 μm^3 (particles

stretched from a 3.6 μm sphere) ²⁴². There were, however, significant differences seen between the shapes that had volumes up to 0.69 μm^3 . The volumes of the particles used in this chapter were 14.14 μm^3 (spheres), 11.6 μm^3 (hexahedrons), and 17.2 μm^3 (truncated pyramids) and so are in-between the volumes of particle groups used by Sharma *et al.*

On the other hand, shape effects on internalisation of larger microparticles by macrophages has been reported by Doshi *et al.* who found that hyaluronic acid-coated disk-like microparticles ($d = 6 \mu\text{m}$) were able to avoid uptake by J774 macrophages compared with spherical particles (6 μm) of the same surface composition which exhibited high uptake ³¹⁶. Additionally, Champion and Mitragotri have shown that worm-like particles (aspect ratio >20 , length $\sim 10 \mu\text{m}$) are internalised significantly less than spheres of equivalent volume ²⁴¹.

3.4 Conclusions

Silicon oxide have been fluorescently labelled on the surface in order to be used for cell studies. Non-covalent and covalent labelling methods were explored with covalent methods proving to result in a more uniform and stable labelling.

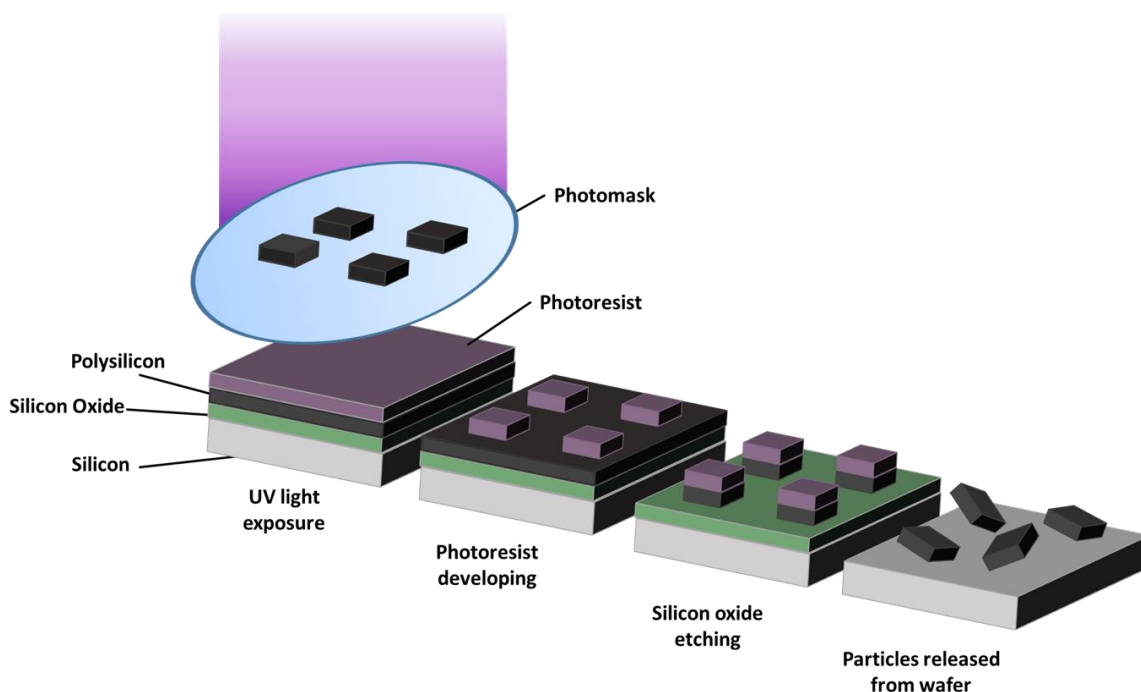
Image analysis as a method for quantifying particle uptake was compared with the trypan blue quenching method and proved to give similar results demonstrating its usefulness as a technique which does not rely on specific quenching of fluorophores.

The effect of particle shape on cellular uptake was evaluated. RAW 264.7 cells could phagocytose all particle shapes which were shown to follow the established phagosomal maturation pathway. The uptake of particles increased with increasing dose and was not significantly altered upon stimulation of macrophages with LPS. Very little difference in particle uptake was observed between spheres and hexahedrons both in terms of the percentage of cells with internalised particles and the number of particles internalised per cell. However, truncated pyramids displayed reduced uptake in comparison with spheres.

4. Interaction of polysilicon microparticles with RAW 264.7 macrophages

4.1 Introduction

Polycrystalline silicon (polysilicon) microfabrication (Scheme 4.1) offered more versatility in terms of varying the size and shape of microparticles than the method for producing the silicon oxide particles used in the previous chapter. A wider range of microparticle shapes was fabricated with varying lengths, thicknesses and curvatures. The effect of particle shape on cellular uptake, metabolic activity, membrane permeability, and lysosomal enzyme release was then assessed.



Scheme 4.1: Fabrication of polysilicon microparticles by photolithography.

4.1.1 Polysilicon and silicon microparticles

Polysilicon microparticles, manufactured by photolithography, have been used by the group of Jose A. Plaza for a number of purposes^{216, 221-222, 284, 288, 317-322}. Their main focus has been to fabricate polysilicon barcodes which can be used for the purpose of cellular tracking throughout the assisted reproductive process^{216, 318-319, 321}. More recently, polysilicon micro-devices were fabricated in order to measure changes in intracellular pressure and to measure intracellular mechanical forces^{320, 322}. These measurements are made possible by the high precision with which polysilicon particles can be fabricated. This property is advantageous for studies looking at the impact of particle shape on internalisation however, few such studies have been undertaken.

The internalisation of polysilicon particles in THP-1 cells was assessed by Fernandez-Rosas *et al.*³¹⁷. Disk-shaped particles with a diameter of 3 μm and a thickness of either 1.5 or 0.5 μm were used. SEM imaging showed that both particle types were taken up by the THP-1 monocytes, however a quantitative examination of particle uptake was not performed.

In a study by Duran *et al.* hexahedral polysilicon particles (3x3x0.5 μm) were fabricated with and without silicon nano wires grown on the top surface and their internalisation into Hela cells compared by SEM. The number of particle internalised per cell did not differ between the different types of particles, however nanowire coated particles were found to have their nanowire face in contact with the cell membrane more frequently than their flat face³²³.

The above studies highlight a difficulty of working with polysilicon particles which is that it is very expensive and time-consuming to fabricate the large numbers of particles that are required for quantitative uptake studies. As such these studies have used mainly qualitative/semi-quantitative techniques such as SEM to assess internalisation into low numbers of cells.

Similarly to polysilicon microparticles, monocrystalline silicon particles fabricated by a similar lithographic process have been assessed for their potential use as a drug delivery system in a number of studies by the group of Mauro Ferrari ²²⁰. Discoidal silicon microparticles have been used as a carrier for nanoparticles which in turn are carriers for the delivery of RNA, and chemotherapeutics ³²⁴⁻³²⁶. Uptake of discoidal particles with diameters of 1.6 and 3.2 μm by HUVECs demonstrated higher uptake of the smaller particles ²⁴⁸. In a study comparing the biodistribution of disk-shaped and cylindrical silicon particles in tumour-bearing mice, cylindrical particles were more accumulated more in the lungs than disk-shaped particles. Additionally, more disk-shaped particles were found in the tumour than cylindrical particles ³²⁷.

The effect of polysilicon microparticle shape on internalisation by macrophages has not been studied. In this chapter, polysilicon microparticles serve as a model particle to investigate the effect of microparticle shape on interactions with macrophages. Polysilicon particles were fabricated and characterised by collaborators at the CNM (figure 4.1). A summary of their dimensions is shown in table 4.1. Shapes were designed so that all had at least one dimension of 3 μm (with the exception of 4 μm circular disks) as it is was shown in chapter 3 that RAW 264.7 cells were able to internalise microparticles within these dimensions. The chosen particle shapes allow for the effect of factors such as particle length, thickness, and curvature on macrophage interaction to be examined. This could provide insight into particle shapes that are advantageous as carriers for drug delivery. The crystal habits of active pharmaceutical ingredients (APIs) describe their particle shape depending on their crystalline form ³²⁸. APIs can form bar, needle, plate, or cuboid shapes and so the particle shapes chosen here are relevant to those that are formed in the processing of API material ³²⁹.

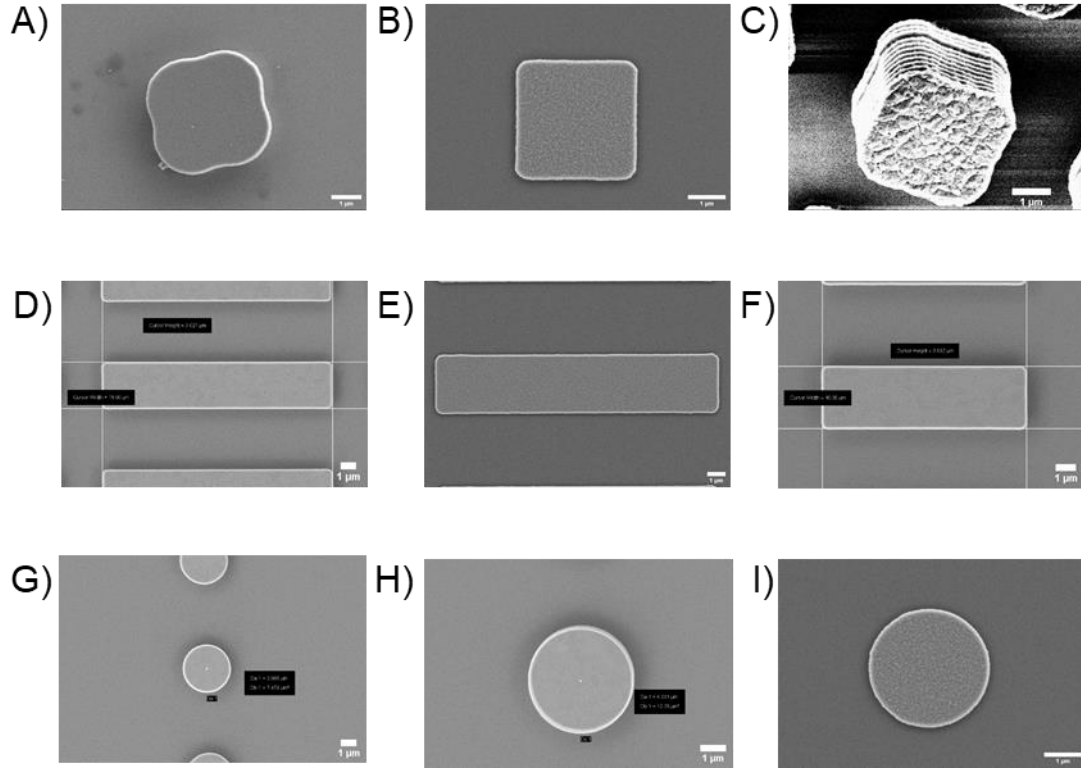











Figure 4.1: SEM images of the polysilicon particles used in this chapter. A) $3 \times 3 \times 0.5 \mu\text{m}$ hexahedrons, B) $3 \times 3 \times 0.05 \mu\text{m}$ hexahedrons, C) $3 \times 3 \times 3 \mu\text{m}$ cubes, D) $3 \times 15 \times 0.5 \mu\text{m}$ bars, E) $3 \times 15 \times 0.05 \mu\text{m}$ bars, F) $3 \times 10 \times 0.5 \mu\text{m}$ bars, G) Circular disks diameter $3 \mu\text{m}$, thickness $0.5 \mu\text{m}$, H) Circular disks diameter $4 \mu\text{m}$, thickness $0.5 \mu\text{m}$, I) Circular disks diameter $3 \mu\text{m}$, thickness $0.05 \mu\text{m}$, Scale bars = $1 \mu\text{m}$.

Table 4.1: Particle shapes and their dimensions

Particle shape	Length/ diameter (μm)	Width (μm)	Height (μm)	Surface area (μm^2)	Volume (μm^3)	Curvature at corner (1/r)	Schematic representation
Hexahedrons	3	3	0.5	24.0	4.5	1.3	
Hexahedrons	3	3	0.05	18.6	0.45	2.9	
Cubes	3	3	3	54.0	27.0	1.2	
Bars	15	3	0.5	120.0	22.5	2.8	
Bars	15	3	0.05	93.0	2.25	2.3	
Bars	10	3	0.5	80.0	15.0	2.6	
Circular disks	4	-	0.5	31.4	6.3	0.5	
Circular disks	3	-	0.5	18.9	3.5	0.7	
Circular disks	3	-	0.05	14.6	0.4	0.7	

4.2 Materials and Methods

4.2.1 Materials

Rhodamine B isothiocyanate (RBITC, 283924), Triton X-100, Silicon oxide spheres (3 μm), LDH assay kit and 4-methyl umbelliferyl- β -D-glucuronide hydrate (MUG) were purchased from Sigma-Aldrich. AQueous One solution cell proliferation assay (MTS reagent) was purchased from Promega UK. 11-Aminoundecyltriethoxysilane (AUTES, S25045) was purchased from Fluorochem (UK). H_2SO_4 (98%) and NH_4OH (20%) were purchased from Fisher Scientific. Polysilicon particles were provided by Centro Nacional de Microelectrònica (CNM) (Barcelona).

4.2.2 Methods

4.2.2.1 Fabrication and Scanning electron microscopy (SEM) characterisation of polysilicon particles

Particles were fabricated and characterised by collaborators at the Centro Nacional de Microelectrònica (CNM) in Barcelona. Particles were fabricated according to the procedure in ref ³³⁰. Briefly, onto a 4 inch P-type silicon wafer, a 1 μm thick silicon oxide layer was grown by thermal oxidation. Chemical vapour deposition was then used to deposit a polysilicon layer of controlled thickness (3, 0.5, or 0.05 μm). A photoresist layer (HiPR 6512, thickness 1.5 μm) was spun onto the wafer and irradiated through a chromium mask. The irradiated areas were then removed by reactive ion etching using a Bosh process recipe (Alcatel A601). The photoresist was removed by plasma etching using a Tepla 300-E. HF (49%) vapours were used to dissolve the underlying oxide layer and release the particles from the underlying wafer. Particles were rinsed thoroughly with EtOH before being stored in EtOH. SEM images were analysed to measure particle dimensions using imageJ®. Particles were stored and transported in microcentrifuge tubes in EtOH at room temperature.

4.2.2.2 Labelling of polysilicon particles with AUTES and RBITC

Surface activation of polysilicon microparticles in suspension

Polysilicon particles suspended in EtOH (700 μ L) in microcentrifuge tubes were centrifuged at 5700 RPM (6175G) for 10 minutes. Particles were suspended in 700 μ L acidic piranha solution for 1 hour with shaking to prevent particles from falling out of suspension. Particles were centrifuged at 5700 rpm (6175G) for 10 minutes and the acidic piranha solution removed. Particles were washed by suspension in 700 μ L milliQ water and then centrifuged at 5700 rpm (6175G) for 10 minutes. This washing process was repeated 3x and the supernatant removed. Particles were suspended in 700 μ L basic piranha solution and left shaking for 30 minutes. Particles were centrifuged at 5700 rpm (6175G) for 10 minutes and the basic piranha solution removed. Particles were washed using the same suspension in 700 μ L milliQ water and centrifugation steps used to wash the particles after removal of the acidic piranha solution.

Labelling of polysilicon microparticles with AUTES and RBITC

Initially the method used to label silicon oxide spheres was duplicated exactly as follows. Freshly activated polysilicon particles were suspended in 0.1% v/v AUTES in EtOH (700 μ L) and left to shake for 2 hours. Particles were centrifuged at 5700 RPM (6175 G) for 10 minutes and the silane solution removed. Particles were washed by resuspension in 700 μ L EtOH and centrifugation at 5700 RPM (6175 G) for 10 minutes before removal of the supernatant. This washing process was repeated 3x and then the supernatant removed. Particles were suspended in RBITC (30 μ M) in EtOH (700 μ L) and left on a shaker overnight while protected from light. Particles were washed with EtOH 3x 700 μ L by repeated suspension and centrifugation as above.

Alternative conditions for silane addition were surveyed as follows: 0.1% v/v AUTES in Toluene, 0.1% v/v AUTES in Acetone. Reaction with AUTES was carried out for 2 hours and the remaining labelling steps were carried out as before. Control particles were incubated with RBITC (30 μ M) overnight after surface activation but without treatment with AUTES.

Labelling of particles was assessed by fluorescence microscopy. Brightfield and fluorescence images were acquired using a Nikon Eclipse TiU fluorescence microscope. For fluorescence imaging of RBITC labelled samples, exposure time was kept constant (1s) $\lambda_{\text{ex}} = 550 \text{ nm}$ and $\lambda_{\text{em}} > 590 \text{ nm}$. Images were processed using imageJ® to produce fluorescence surface plots and measure median fluorescence intensity values. 6 particles were analysed per sample.

4.2.2.3 Label free detection of polysilicon particles by light scattering

Particles were assessed for their ability to scatter the 642 nm laser in an Amnis imagestream^x MKII imaging flow cytometer. Polysilicon particles were suspended in 1% HEPES in HBSS and scattering intensity histograms of each particle type were compared with the scattering of RAW 264.7 cells to see which particles had a sufficiently high scattering to be able to discriminate cells without particles from cells with particles.

4.2.2.4 Quantification of polysilicon particle uptake by RAW 264.7 cells by flow cytometry

Preparation of particles

Particles stored in EtOH in microcentrifuge tubes were centrifuged at 5700 RPM (6175 G) for ten minutes. From this point on all work was carried out inside a sterile cell culture hood to maintain sterility. The EtOH supernatant was removed and the particles suspended in 1 mL buffer comprising 1% HEPES in HBSS. Particles were counted using a haemocytometer and required volume of each particle stock containing 300,000 particles transferred to fresh microcentrifuge tubes. The volume of each microcentrifuge tube was then made up to 1 mL with the required volume of 1% HEPES in HBSS. Particle suspensions were warmed to 37° C before addition to cells.

Preparation of cells

RAW 264.7 cells were harvested once they reach 60-80% confluency by scraping as described in section 2.2.1. 100,000 cells in culture media were seeded per well into a 12 well plate and incubated overnight at 37°C, 5% CO₂, 95% humidity. Culture media was removed by aspiration and the cells washed with 1 mL pre-warmed (37°C) PBS. PBS was removed and 1 mL pre-warmed particle suspensions applied at a ratio of 3 particles per cell. Cells were incubated for 4 hours after which time the particle suspensions were removed and the cells washed with 3 x 1 mL warm HBSS. Cells were prepared for flow cytometry.

Preparation of cells for flow cytometry

HBSS was removed from each well by aspiration and 250 µL accutase added to each well and the cells placed in an incubator for 5 minutes to detach cells. 250 µL HBSS was added to each well and the total volume of each well transferred to fresh microcentrifuge tubes. Samples were centrifuged at 250 G for 5 minutes and the supernatants removed. The cells were suspended in 250 µL 4% formaldehyde in PBS for 20 minutes before being centrifuged for 5 minutes (250 G) and the supernatant removed. Fixed cells were suspended in 50 µL HBSS and stored at 4°C until analysis by flow cytometry. Samples were always analysed within 1 week of sample preparation.

Flow cytometry

Flow cytometry was performed using an Amnis imagestream^X MKII imaging flow cytometer in standard configuration with 40X magnification. Illumination settings: Brightfield LED 30.75 mW, 642 nm laser 150 mW, 785 nm laser 1.25 mW. Data was acquired using INSPIRE software with a minimum of 500 cells per sample (typically > 1000 per sample). Data was analysed using IDEAS software.

Quantification of particle internalisation by image analysis

Single cell populations were first determined by plotting a scatter plot of area against aspect ratio. Scattering intensity histograms of single cells were plotted to distinguish particle associated and non-associated cells as shown in figure 4.2. Cells with internal particles were distinguished from cells with surface-bound particles using the same image analysis method as in chapter 3 but instead of fluorescence, light scattering was used to identify the location of the particle with respect to the cell (figure 4.3).

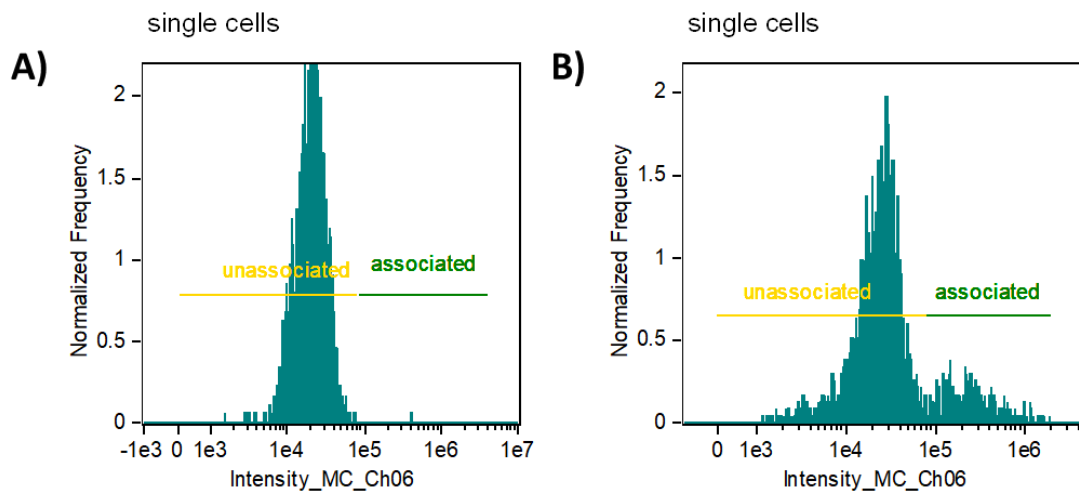


Figure 4.2: Distinction between polysilicon particle-associated and unassociated cells using scattering intensity. A) Scattering of untreated RAW 264.7 macrophages B) Scattering of RAW 264.7 cells treated with polysilicon hexahedrons (3x3x0.5 μm)

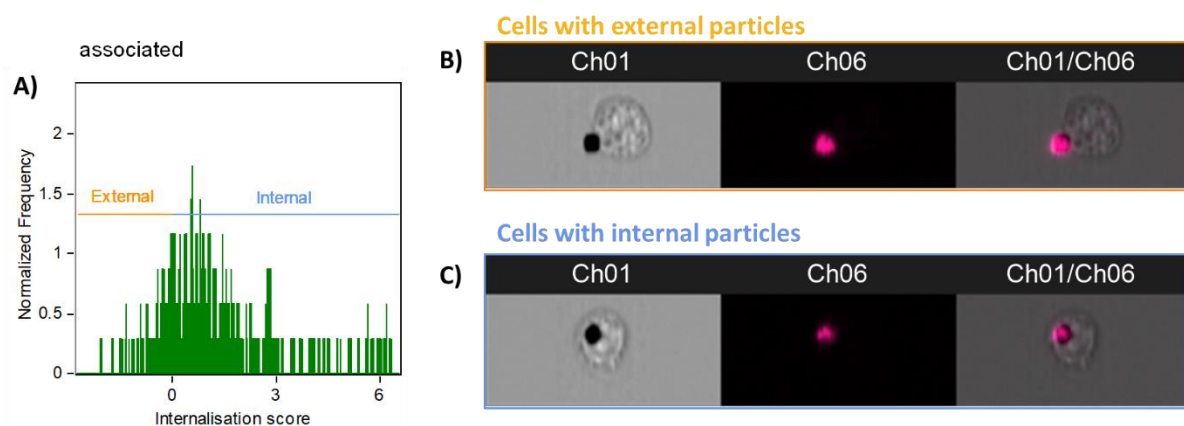


Figure 4.3: Distinction between cells with internal particles and cells with external particles A) Histogram showing internalisation score. Brightfield, scattering and overlay images of B) Cell with external particle C) Cells with internal particle

4.2.2.5 MTS, LDH and glucuronidase assays

Preparation of particles

Particles stored in EtOH in microcentrifuge tubes were centrifuged at 5700 RPM (6175 G) for ten minutes. From this point on all work was carried out inside a sterile cell culture hood to maintain sterility. The EtOH supernatant was removed and the particles suspended in 1 mL buffer comprising 1% HEPES in HBSS. Particles were counted using a haemocytometer and required volume of each particle stock transferred to fresh microcentrifuge tubes. The volume of each microcentrifuge tube was made up to 500 μ L with the required volume of 1% HEPES in HBSS. Particle suspensions were warmed to 37° C before addition to cells.

Preparation of cells

RAW 264.7 cells were harvested once they reach 60-80% confluency by scraping as described in section 2.2.1. 10,000 cells in 150 μ L culture media were seeded per well into a clear 96 well plate and incubated overnight at 37°C, 5% CO₂, 95% humidity. Culture media

was removed by aspiration and the cells washed with 200 μ L pre-warmed (37°C) PBS. PBS was removed and 150 μ L pre-warmed particle suspensions applied to each well. 150 μ L 1% HEPES in HBSS was applied as a negative control, 0.1% Triton X-100 in PBS was applied as a positive control. Cells were incubated for 4 hours after which time 50 μ L per well cell-conditioned buffer was removed and transferred to a fresh clear 96 well plate for LDH assay and 50 μ L per well cell-conditioned buffer transferred to a fresh black 96-well plate for glucuronidase assay. Remaining cell-conditioned buffer was removed by aspiration and the cells washed with 3x 150 μ L pre-warmed PBS.

MTS assay

The MTS assay is a colorimetric assay that measures the metabolic activity of cells. It contains a tetrazolium dye ([3-(4,5-dimethylthiazol-2-yl)-5-(3-carboxymethoxyphenyl)-2-(4-sulfophenyl)-2H-tetrazolium] (MTS)) and an electron coupling reagent, phenazine ethosulphate (PES). The MTS reagent is reduced by metabolically active cells to produce a coloured formazan product. The quantity of formazan produced is directly proportional to the metabolic activity of cells and can be determined by recording the absorbance at 492 nm.

The MTS assay was performed according to the manufacturer's instructions. After removal of the cell-conditioned buffer and washings with 3x 150 μ L PBS, remaining PBS was aspirated and 20 μ L MTS reagent in 100 μ L culture medium was added to each well. Cells were incubated at 37°C, 95% humidity, 5% CO₂ for 2 hours after which time the absorbance at 492 nm of each well was measured using a TECAN spark microplate reader. Relative metabolic activity was calculated with respect to the negative control by using the following equation.

$$\text{Relative metabolic activity (\%)} = ((X - \text{positive control}) / (\text{negative} - \text{positive control})) * 100$$

Where X is the absorbance of the sample well.

LDH assay

The LDH assay is a colorimetric assay that measures the viability of cells by measuring the release of LDH. LDH is an intracellular enzyme located in the cytoplasm that is only released from cells when there is damage to the cellular membrane and therefore can be used as a measure of cell death relative to healthy cells. Released LDH in culture medium reduces NAD to NADH which in turn reduces a tetrazolium reagent to a coloured formazan product. The quantity of formazan which is proportional to membrane damage can be determined by absorbance at 492nm thus relative LDH release can be calculated.

The LDH assay was performed according to the manufacturer's instructions. To the clear 96 well plate containing 50 µL per well cell-conditioned buffer, 100 µL LDH reagent was added and the well plate left for 2 hours at room temperature while protected from light. After this time the absorbance at 492 nm was measured using a TECAN spark microplate reader. Relative LDH release with respect to the positive control was calculated using the following equation.

$$\text{Relative LDH release \%} = ((X - \text{negative control})/(\text{positive} - \text{negative control})) * 100$$

Where X = absorbance of the sample well

Glucuronidase assay

4-Methylumbelliferyl-β-D-glucuronide hydrate (MUG) is a non-fluorescent substrate for β-glucuronidase. Upon cleavage of the O-glycosidic bond, fluorescent 4-methylumbelliferone is produced with excitation maximum at 372 nm and emission at 445 nm. The fluorescent signal is proportional to the amount of enzyme activity and so can be used to measure the release of the lysosomal enzyme β-glucuronidase in to the culture media.

MUG was dissolved in sodium acetate buffer 0.1M pH 4.5 to a final concentration of 100 µM. To the black 96 well plate containing 50 µL per well cell-conditioned buffer, 100 uL per well MUG solution was added. The plate was then protected from light and incubated for 2 hours at 37°C 95% humidity, 5% CO₂. After this time 10 µL per well NH₄OH was added to terminate

the reaction and increase the fluorescent signal. Fluorescence signal at 460 nm was then measured after excitation at 360 nm using a TECAN spark microplate reader. Relative β -glucuronidase release with respect to the positive control was then calculated using the following equation.

$$\text{Relative } \beta\text{-Glucuronidase release \%} = ((X - \text{negative control}) / (\text{positive} - \text{negative control})) * 100$$

Where X = emission of the sample well

4.3 Results

4.3.1 Functionalisation of polysilicon particles with AUTES and RBITC

In order to be able to detect the presence of polysilicon particles after administration to cells by flow cytometry, the particles were labelled using AUTES and RBITC using the same procedures as the silicon oxide particles in chapter 3. The particles were then imaged using fluorescence microscopy and images of the particle analysed to assess their brightness and uniformity of labelling. Hexahedrons of dimensions 3x3x0.5 μm were used to assess particle labelling.

Figure 4.4 shows representative brightfield and fluorescence microscopy images as well as fluorescence surface profiles of fluorescently labelled polysilicon microparticles. Ethanol was used as the solvent for AUTES self-assembled monolayer (SAM) formation on silicon oxide particles in the previous chapter and so it was thought that this would be appropriate to use the same protocol for polysilicon particles. The activation by acidic and basic piranha causes an oxide layer to form on the surface of silicon which then allows for SAM formation³³¹. However, as can be seen in the fluorescence images and fluorescence surface plots (figure 4.4A), poor labelling was achieved as particles could barely be distinguished from the non-fluorescent background and were similar to unmodified control particles (figure 4.4D). Acetone (figure 4.4B) and toluene (figure 4.4C) were assessed as alternative solvents for AUTES deposition as these have been used in the literature for the deposition of aminosilanes to silicon surfaces³³²⁻³³³. A greater degree of labelling was achieved with both acetone and toluene, however labelling was non-uniform. In all cases particles displayed patches of higher fluorescence, indicating areas where more RBITC labelling had occurred. .

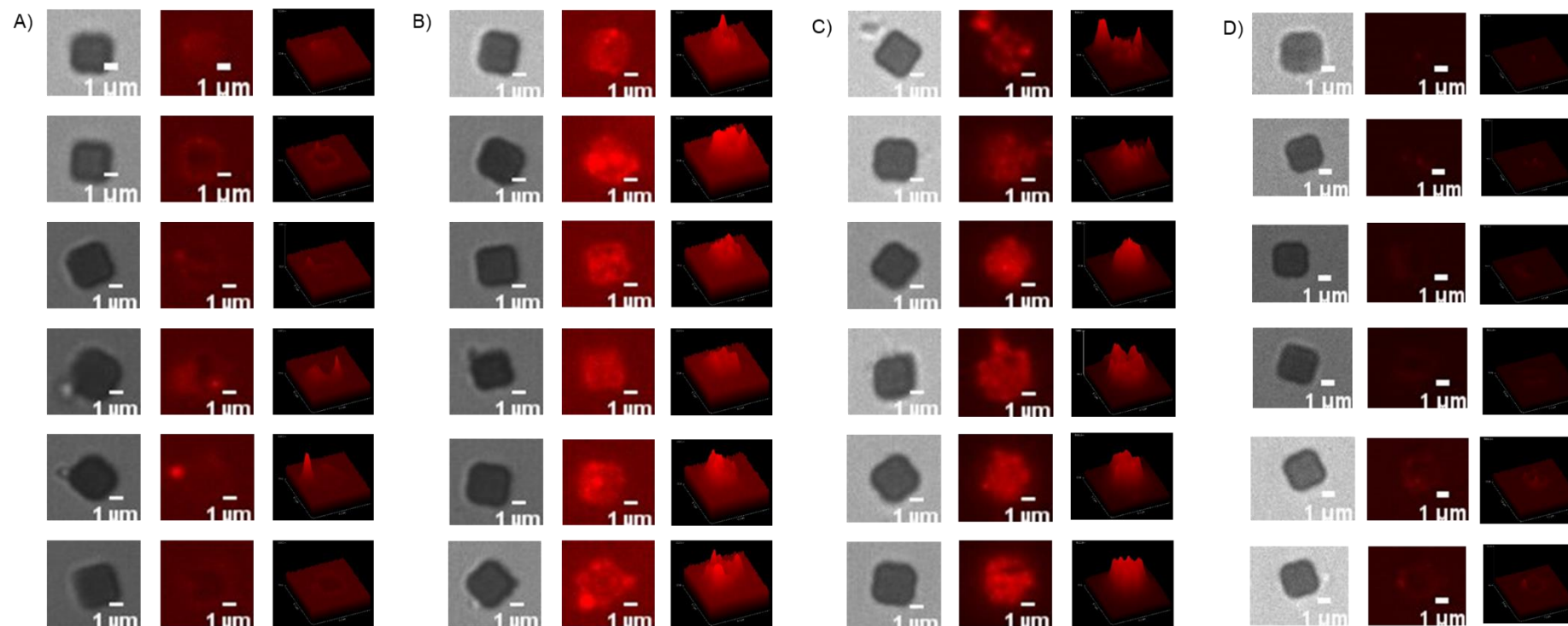


Figure 4.4: Effect of AUTES deposition solvent on particle labelling with RBITC. Brightfield images, fluorescence images, and fluorescence surface plots of $3 \times 3 \times 0.5 \mu\text{m}$ polysilicon hexahedrons after labelling with AUTES and RBITC. A) AUTES deposition in Ethanol, B) AUTES deposition in acetone, C) AUTES deposition in toluene, D) Control particles with no AUTES.

Deposition of silanes onto silicon wafers has been shown to occur faster and result in higher silane surface concentration in toluene than ethanol ³³⁴. Using polysilicon particles, Penon *et al.* showed that silane layers of the same chain length to those used in this chapter were deposited faster in toluene (within 30 minutes) than those in ethanol (overnight) ²⁸⁸. Given this, it seems that polysilicon particles may require a longer silanisation step than silicon oxide particles used in chapter 3, potentially due to their crystalline nature. This may account for the lack of labelling when ethanol was used as the deposition solvent. The lack of labelling uniformity could result from partial deposition of the silanes due to insufficient silanisation time. Alternatively it could be due to the arrangement of the silanes as they form on the rough polycrystalline silicon surface. For example, if the conformation of the silanes is such that the amine is not sufficiently exposed to react with the RBITC then a lack of labelling will result. In order to determine the molecular arrangement of silanes as they deposit on to the polysilicon surface, angle resolved XPS could be used ³³⁵. Atomic force microscopy (AFM) would typically be used to characterise monolayers on surfaces ³³⁶, however this is not possible with polysilicon due to its inherent rough surface.

Additionally, loss of particles (3x3x0.5µm hexahedrons) over the course of the functionalisation procedure (loss during the washing steps) was assessed by counting with a haemocytometer. The number of particles was measured at the beginning and end of the functionalisation process. On average microcentrifuge tubes contained 1,583,750 particles (± 65,407) before the functionalisation (as received) and 162,500 particles (± 7071) after functionalisation (89.7% of particles lost). Due to the high loss of particles during the functionalisation process, further optimisation of particle labelling was not performed. Instead, a label-free method of detecting polysilicon particles was pursued which reduces the need for high numbers of washing steps and subsequent loss of particles. In addition, it ensures that, as all particles have the same surface chemistry, the effect of surface chemistry on cellular interaction between the different particle shapes is negligible

4.3.2 Assessment of particle side scattering

As methods to uniformly fluorescently label polysilicon particles were not successful, it was necessary to find an alternative method to distinguish cells associated with particles from unassociated cells. Particle side scattering has been used by a number of groups to detect high refractive index inorganic particles in cells³³⁷. This approach has been used to detect the association of cells with Stainless steel, TiO₂, ZnO, CuO, Fe₃O₄, Ag, and Au nanoparticles as well as carbon nanotubes³³⁸⁻³⁴³. Additionally, Mauro Ferrari and colleagues have used side scattering to detect porous silicon microparticles in human umbilical vein endothelial cells (HUVECS)³⁴⁴. Side scatter is heavily dependent on both refractive index and particle shape and so each particle shape was assessed and compared with cellular side scatter to ensure that the two could be distinguished in a mixed population. The scattering intensity histograms of each particle shape are shown in figure 4.5.

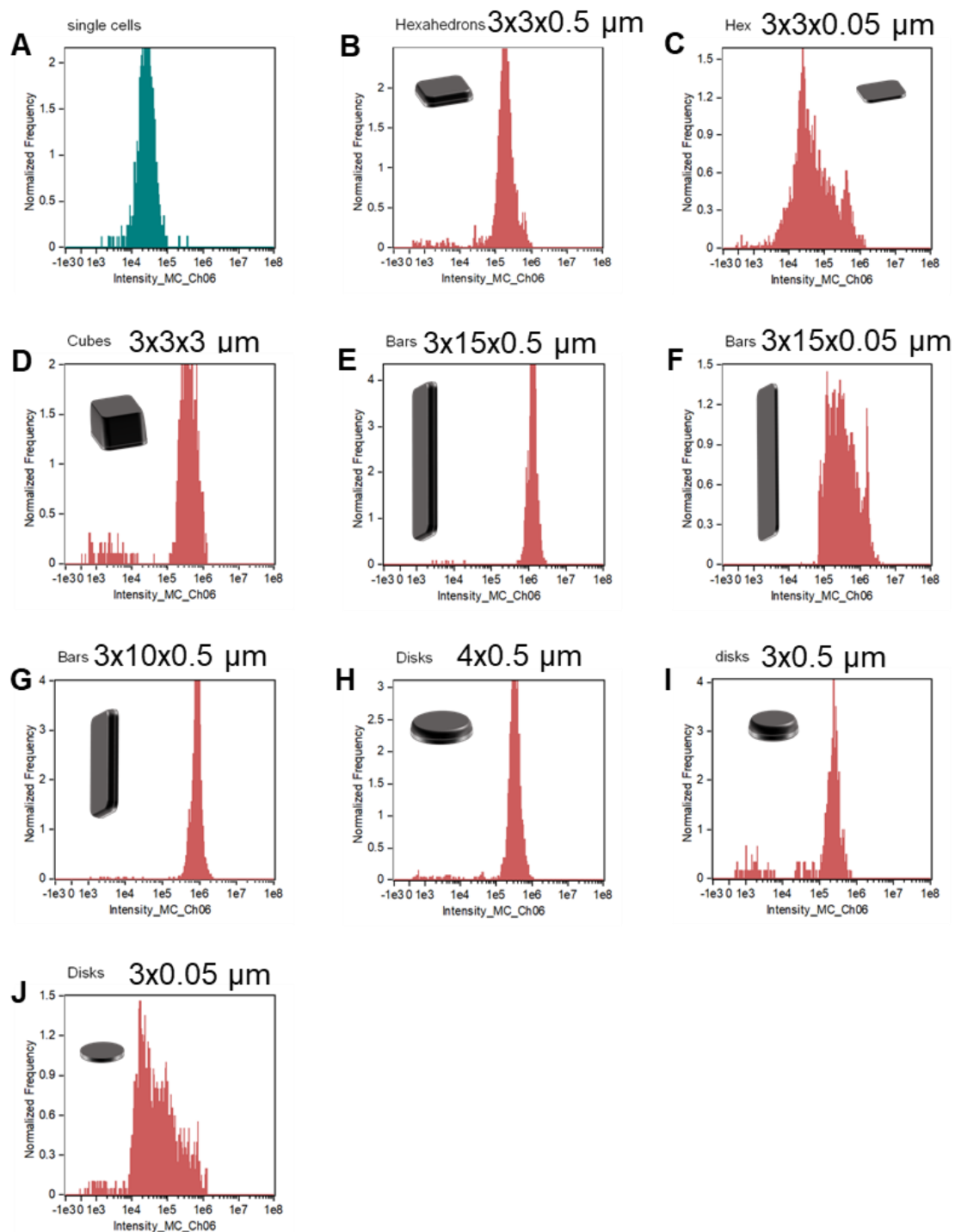


Figure 4.5: Scattering intensity histograms of RAW 264.7 cells and each particle shape. A) RAW 264.7 cells, B) hexahedrons $3 \times 3 \times 0.5 \mu\text{m}$, C) hexahedrons $3 \times 3 \times 0.05 \mu\text{m}$, D) cubes $3 \times 3 \times 3 \mu\text{m}$, E) Bars $3 \times 15 \times 0.5 \mu\text{m}$ F) Bars $3 \times 15 \times 0.05 \mu\text{m}$, G) Bars $3 \times 10 \times 0.5 \mu\text{m}$, H) circular disks $4 \times 0.5 \mu\text{m}$, I) circular disks $3 \times 0.5 \mu\text{m}$, J) circular disks $3 \times 0.05 \mu\text{m}$.

RAW 264.7 cells displayed a median scattering intensity (MSI) of 22382 ± 3575 (figure 4.5A) and so the MSI of particles needed to be significantly higher than these values in order to unambiguously distinguish between particle associated and non-associated cells. Figure 4.6A displays the MSI values of each particle shape. The data shows that for the majority of particle shapes the scattering intensity was significantly higher than that of RAW 264.7 cells, meaning that they could be used in a label-free manner for uptake studies. However, this was not the case for $3 \times 3 \times 0.05 \mu\text{m}$ hexahedrons and $3 \times 0.05 \mu\text{m}$ circular disks which both had similar MSI to that of RAW 264.7 cells. This is likely because of the thickness of the particles ($0.05 \mu\text{m}$) which makes the particles semi-transparent and thus reduces the amount of light scattered. These particles were therefore not suitable for use in cell uptake studies using this method. Despite having the same thickness, bars with dimensions $3 \times 15 \times 0.05 \mu\text{m}$ were able to be distinguished from cells because of their length, although scattering was significantly reduced compared to $3 \times 15 \times 0.5 \mu\text{m}$ bars.

In terms of measuring cellular uptake, this method of detection is advantageous because it avoids a chance of differences in surface labelling affecting the results. Studies have shown that having a higher amount of surface labelling can increase uptake,²⁹⁵ potentially due to the hydrophobicity of the dye molecules and so by maintaining the uniformity of the particle surface chemistry across all particle shapes, the chance of erroneous results relating to this is removed.

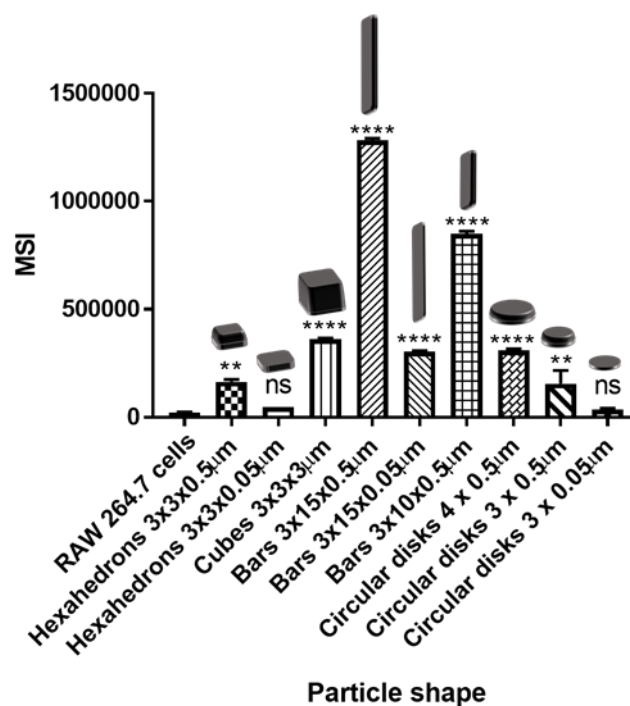


Figure 4.6: Summary of MSI values for RAW 264.7 cells and each particle shape. Particle MSI values compared with RAW 264.7 cells. * indicates statistically significant difference between particle scattering and RAW 264.7 cell scattering as analysed by one-way ANOVA with Dunnet's multiple comparisons (** $p < 0.01$, **** $p < 0.0001$, ns = not significant).

4.3.3 Polysilicon particle association with RAW 264.7 macrophages

Side scattering intensity of RAW 264.7 cells that had been exposed to polysilicon particles for 4 hours was measured by imaging flow cytometry. Representative scattering intensity histograms for each particle type are shown in figure 4.7. In each case, two clear populations of unassociated cells (lower scattering intensity) and cells associated with particles (higher scattering intensity) can be clearly distinguished. This was confirmed by visual examination of the cell images in each population by looking at images across the intensity range of each

population. Cell images from low (minimum), medium (median) and high (maximum) scattering intensity for each population for each sample are shown in figure 4.8. As can be seen from the images of unassociated cells, high scattering intensity relates to having a more granular appearance than those of low scattering. In particle-associated cells, higher scattering was often indicative of more particles associating with the cell.

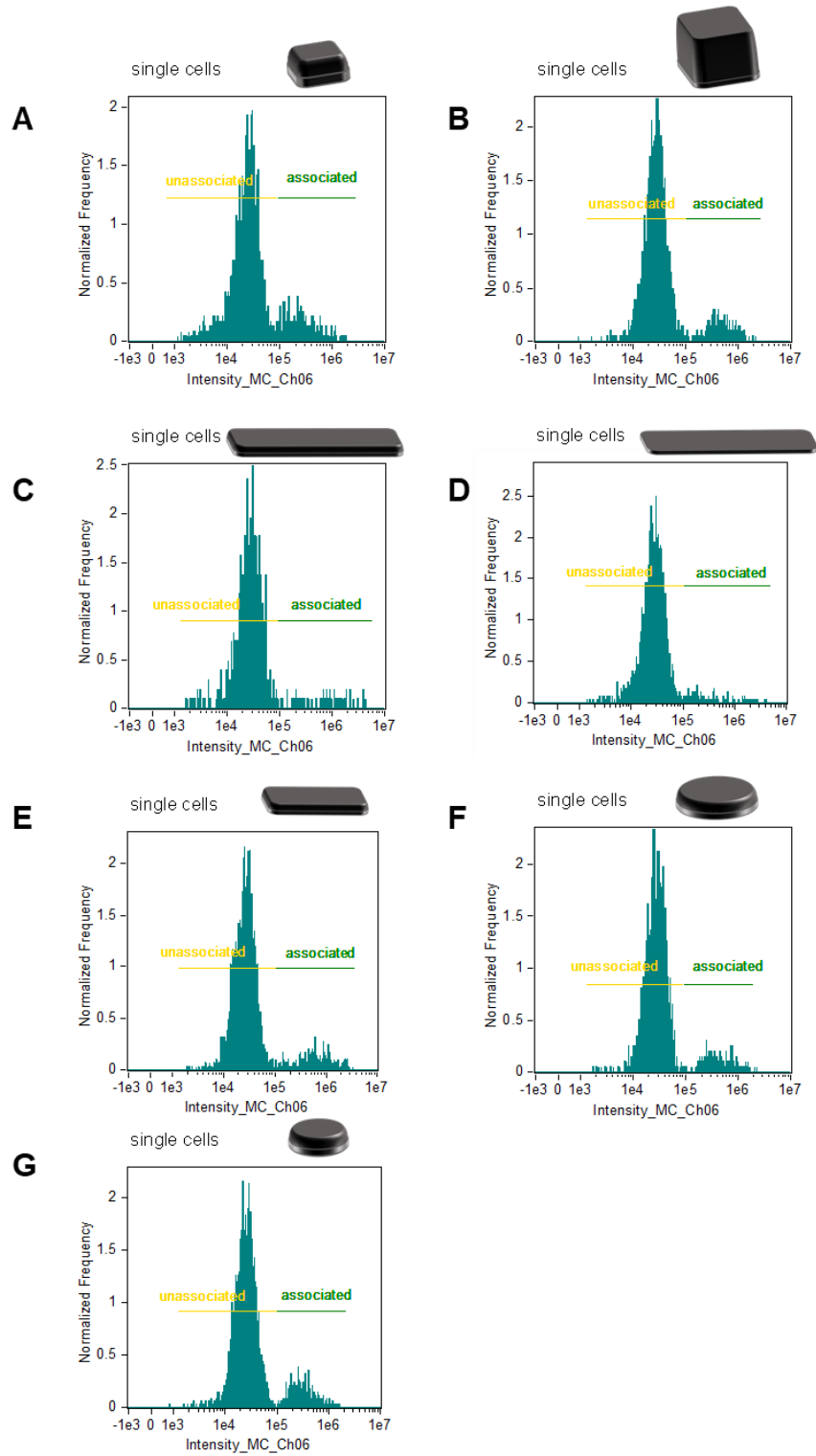


Figure 4.7: Side scattering intensity histograms of RAW 264.7 cells incubated with polysilicon particles. A) Hexahedrons ($3 \times 3 \times 0.5 \mu\text{m}$), B) Cubes ($3 \times 3 \times 3 \mu\text{m}$), C) Bars ($3 \times 15 \times 0.5 \mu\text{m}$), D) Bars ($3 \times 15 \times 0.05 \mu\text{m}$), E) Bars ($3 \times 10 \times 0.5 \mu\text{m}$), F) Circular disks ($d=4 \mu\text{m}$ $h=0.5 \mu\text{m}$), G) Circular disks ($d=3 \mu\text{m}$ $h=0.5 \mu\text{m}$).

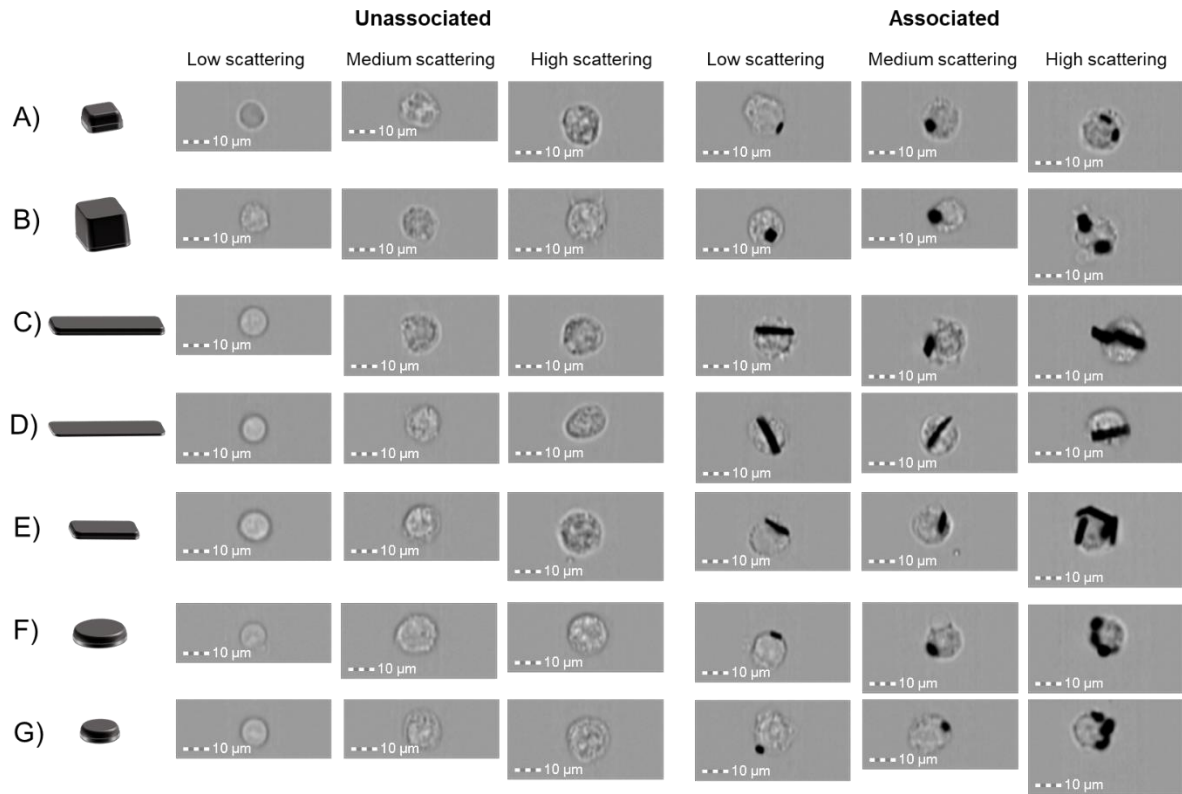


Figure 4.8: Cell images from imaging flow cytometry across the range of scattering intensities for cells unassociated and associated with polysilicon particles. A) Hexahedrons ($3 \times 3 \times 0.5 \mu\text{m}$), B) Cubes ($3 \times 3 \times 3 \mu\text{m}$), C) Bars ($3 \times 15 \times 0.5 \mu\text{m}$), D) Bars ($3 \times 15 \times 0.05 \mu\text{m}$), E) Bars ($3 \times 10 \times 0.5 \mu\text{m}$), F) Circular disks ($d=4 \mu\text{m}$ $h=0.5 \mu\text{m}$), G) Circular disks ($d=3 \mu\text{m}$ $h=0.5 \mu\text{m}$).

The percentage of cells that are associated with particles is shown in figure 4.9A. 3x3x0.5 μm hexahedrons had the highest association (24.6%) and was significantly higher than all other particle shapes apart from 3x3x3 μm cubes (12.9%). There were no significant differences between 3x15x0.5 μm bars (8.1%), 3x15x0.05 μm bars (6.8%), 3x10x0.5 μm bars (10.0%), 4 μm circular disks (11.45%), and 3 μm circular disks (11.3%).

Despite having similar dimensions there is a large difference between the association of 3x3x0.5 μm hexahedrons and 4 and 3 μm circular disks. This may point to a role for particle curvature in influencing cellular association.

Bar-shaped particles showed the lowest association, however as there was no statistical difference between the different bar shapes, no effect of bar thickness (0.5 μm against 0.05 μm) or length (15 μm against 10 μm) was observed.

Due to the large size of these microparticles it was not clear whether the macrophages would internalise the particles or simply spread onto the particle surface in so-called frustrated phagocytosis³⁴⁵. To examine this, the image analysis method used in chapter 3 was applied in order to assess the percentage of particles with internal particles and the percentage of cells with surface-bound particles. After application of the analysis, images of cells were assessed visually to check that internal and surface-bound particles were distinguished (appendix II figure S4.1). For bar-shaped particles there were clear instances of particle internalisation, whereby the shape of the cell is less circular and appears to have stretched to accommodate the presence of the internalised bar. Cells with surface-bound particles could be distinguished from those with internalised particles.

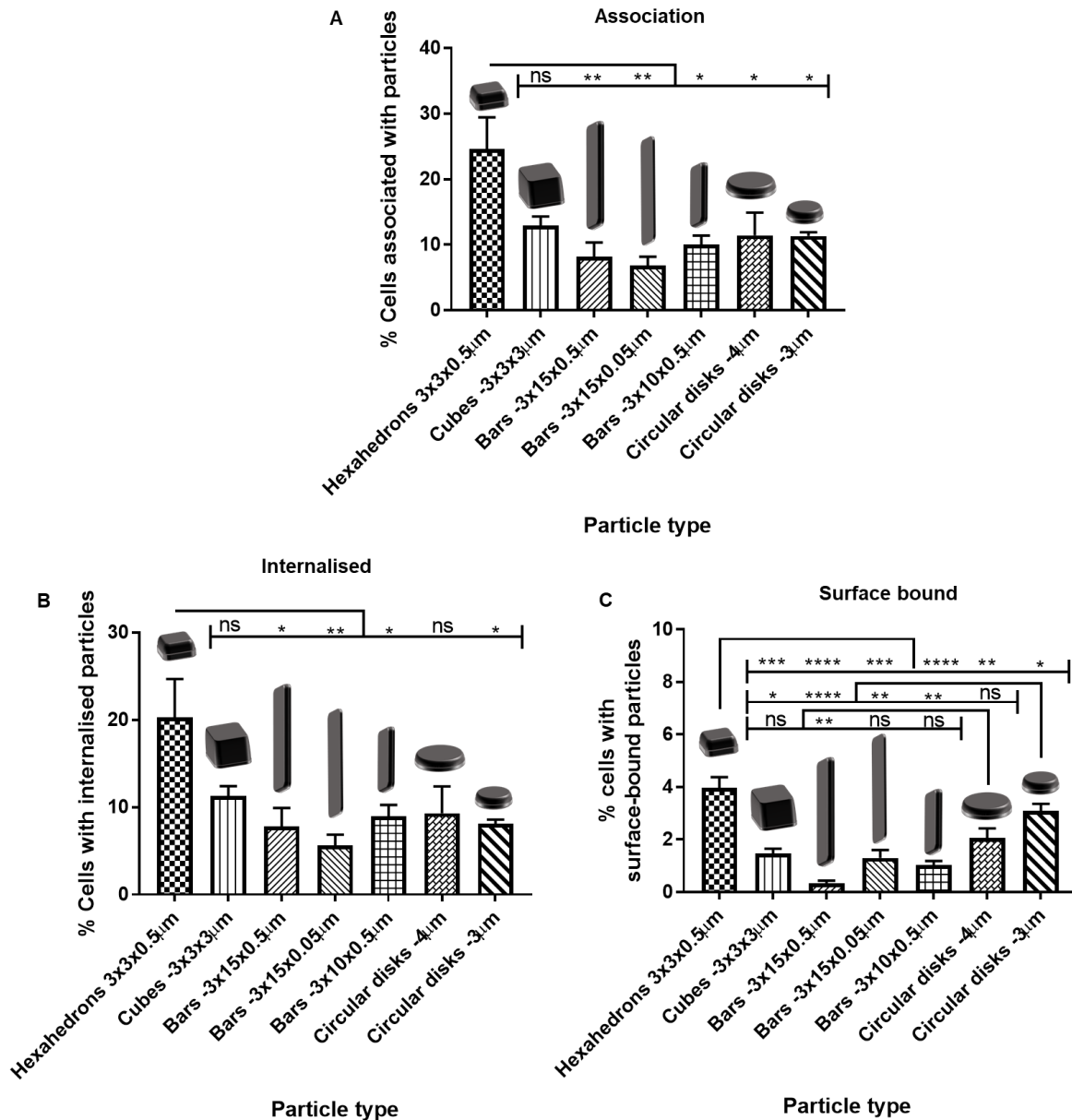


Figure 4.9: Cellular association, internalisation and surface binding of polysilicon particles with RAW 264.7 cells. A) % cells associated with particles, B) % cells with internalised particles, C) % cells with surface-bound particles. Statistical differences analysed by one-way ANOVA with Tukey's multiple comparisons test (* $p < 0.05$, ** $p < 0.01$, *** $p < 0.001$, **** $p < 0.0001$). $n=1$, $N=3 \pm \text{SEM}$

Figure 4.9B shows the percentage of cells that had internal particles. Similarly to the association data, 3x3x0.5 µm hexahedrons showed the highest internalisation (20.3%),

however this was not significantly different from 3x3x3 μm cubes (11.25%) or 4 μm circular disks (9.3%). There were no significant differences in internalisation between 3x15x0.5 μm bars (7.8%), 3x15x0.05 μm bars (5.6%), 3x10x0.5 μm bars (8.95%), and 3 μm circular disks (8.1%).

Figure 4.9C shows the percentage of cells that had surface-bound particles. Here, more significant differences between the different particle shapes were observed. 3x3x0.5 μm hexahedrons showed significantly higher surface binding than all other shapes (3.9%). 3 μm and 4 μm circular disks showed statistically equivalent surface binding (3.1% and 2.1% respectively). 3x3x3 μm cubes, 3x15x0.5 μm bars, 3x15x0.05 μm bars, and 3x10x0.5 μm bars showed the lowest surface binding (1.5%, 0.3%, 1.3%, and 1.0% respectively).

As the first stage of phagocytosis is binding of the cell membrane to the particle, the higher surface binding of hexahedrons tallies well with their increased uptake. Low binding of cells to bar-shaped particles could be the reason for lower internalisation.

The effect of particle volume and surface area on cellular association, internalisation, and surface binding was assessed to see if a correlation was present (figure 4.10). For cellular association (figure 4.10A) and internalisation (figure 4.10B) there was a poor correlation with both particle surface area ($R^2 = 0.28$ and 0.18 respectively) and particle volume ($R^2 = 0.07$ and 0.02 respectively). This indicates that differences in cellular association and internalisation are not dependent on particle surface area or volume when different shapes of particle are administered to cells.

For surface binding (figure 4.10C) there was an inverse correlation with particle surface area ($R^2 = 0.69$). A higher proportion of cells had surface bound particles when the particle surface area was smaller.

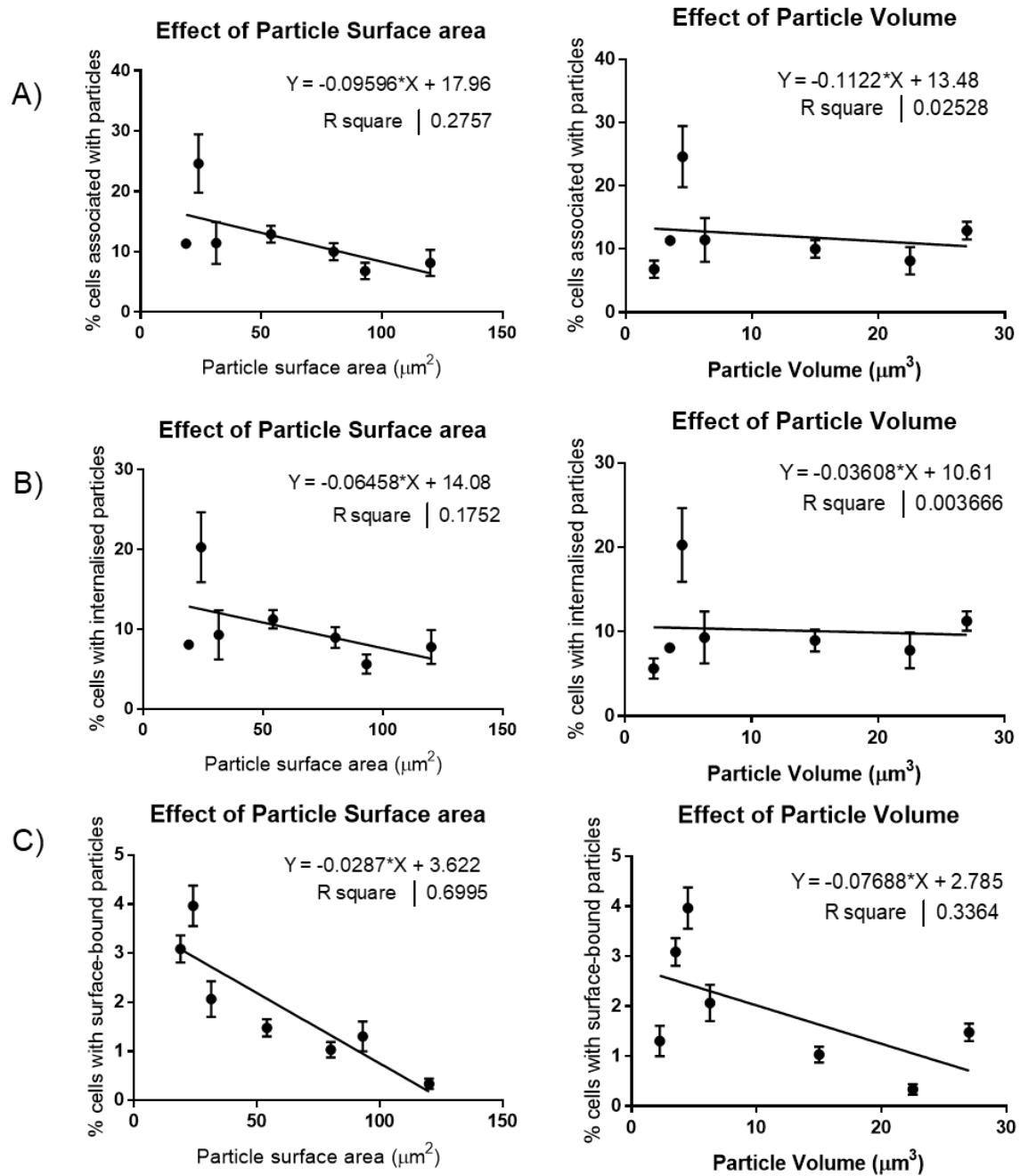


Figure 4.10: Particle factors affecting cellular association, internalisation, and surface-binding. Graphs showing the effect of particle surface area and volume on A) cellular association, B) particle internalisation, and C) particle surface binding.

The number of particles per cell was calculated by dividing the MSI of the cells with internal or surface-bound particles by the MSI of the particles, this data is shown in figure 4.11. On average between 1 and 1.5 particles was internalised per cell for 3x3x0.5 μm hexahedrons (1.34), 3x3x3 μm cubes (1.15), 3x15x0.05 μm bars (1.16), 4 μm circular disks (1.42), and 3 μm circular disks (1.36) (figure 4.10A). For 3x15x0.5 μm bars and 3x10x0.5 μm bars 0.62 and 0.82 particles per cell was calculated respectively.

Similarly for surface-bound particles (figure 4.10B) ~1 surface-bound particle per cell was calculated for 3x3x0.5 μm hexahedrons (1.11), 3x3x3 μm cubes (1.15), 3x15x0.05 μm bars (1.16), 4 μm circular disks (0.99), and 3 μm circular disks (1.15). For 3x15x0.5 μm bars and 3x10x0.5 μm bars 0.22 and 0.47 particles per cell was calculated respectively.

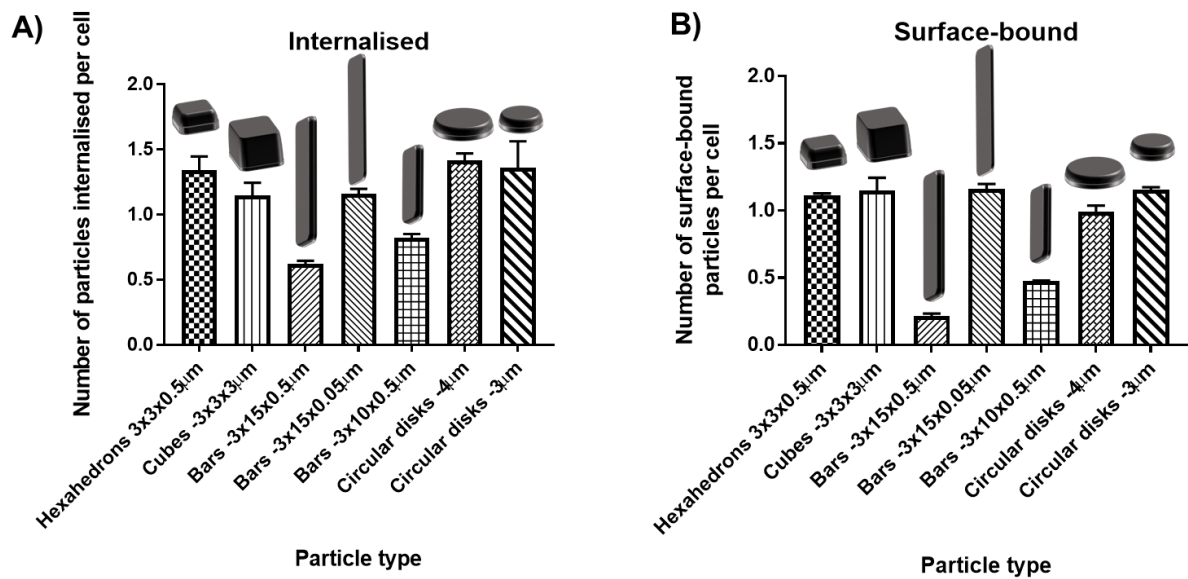


Figure 4.11: Effect of particle shape on number of internalised (A) and surface-bound (B) particles per cell.

The calculated values for 3x15x0.5 μm bars and 3x10x0.5 μm bars are <1 because the scattering intensity values for the cells with particles is lower than the MSI value of the particles

on their own. The reason for this is not clear, however one possible explanation could be the orientation of the particles. When the MSI of the particles alone was measured for 3x15x0.5 μm bars and 3x10x0.5 bars and particles aligned with the flow and so the MSI of the bars was calculated based on a single particle orientation. However, when the bars are present inside or on the surface of cells the orientation is more random with respect to the detector and so there is a disparity between the MSI of particles alone and the particles with cells.

After manually reviewing the images of cells that were exposed to 3x15x0.5 μm bars, 91.4% ($\pm 3.9\%$) of cells that had internalised particles had internalised 1 particle and 100% of cells that had surface-bound particles had 1 particle bound. For 3x10x0.5 μm bars 75.9% ($\pm 8.1\%$) of cells with internal particles had internalised 1 particle and 93.7% ($\pm 5.4\%$) of cells with surface-bound particles had 1 surface-bound particle. These results therefore suggest that, in line with the other particle shapes, the vast majority of cells were associated with 1 particle.

4.3.4 Effect of particle shape on metabolic activity, toxicity, and lysosomal enzyme release

4.3.4.1 MTS assay

MTS assay was used to measure the metabolic activity of RAW 264.7 cells upon exposure to increasing ratios of polysilicon particles. Upon reduction of the assay compound by metabolically active cells producing dehydrogenase, a coloured formazan product is produced which can be detected by absorbance measurements³⁴⁶. As the quantity of formazan produced is related to the metabolic activity of cells, it is often used as a measure of toxicity³⁴⁶. However, as phagocytosis is an energy-dependent process requiring actin polymerisation to rearrange cellular structure, ATP requirement is increased and changes in macrophage metabolism, for example an increase in the rate of glycolysis occurs³⁴⁷⁻³⁴⁸. Changes in cellular metabolic activity in response to phagocytosis of particles were therefore assessed using MTS assay.

Polysilicon hexahedrons (3x3x0.5 μm), cubes (3x3x3 μm), bars (3x15x0.5 μm) and bars (3x10x0.5 μm) were applied to RAW 264.7 macrophages and the effect on cellular metabolic activity studied (figure 4.12). Silicon oxide particles (spheres, diameter 3 μm) were also included as a comparator. Note, due to limited stock of particles, the maximum dose for cubes and bars was 30 particles per cell, while for hexahedrons it was 80 particles per cell. Spheres were applied up to 320 particles per cell.

The metabolic activity followed a similar trend for each particle shape. Cellular metabolism increased compared to that of cells treated with 1% HEPES in HBSS. However, in the case of 3 μm spheres (figure 4.12E) where higher doses of particles were administered, the maximum at 30 particles per cell (46 $\mu\text{g/mL}$) was followed by a steady decline in metabolic activity, likely indicative of toxicity. The highest dose used was equivalent to 500 $\mu\text{g/mL}$ and metabolic activity was ~70% of the control cells, thus the EC_{50} was not reached. This is comparable to dosages found in the literature that elicit toxicity, however, often exposure to particles is allowed to occur for 24 hours rather than the 4 hours used in this study ^{236, 349}.

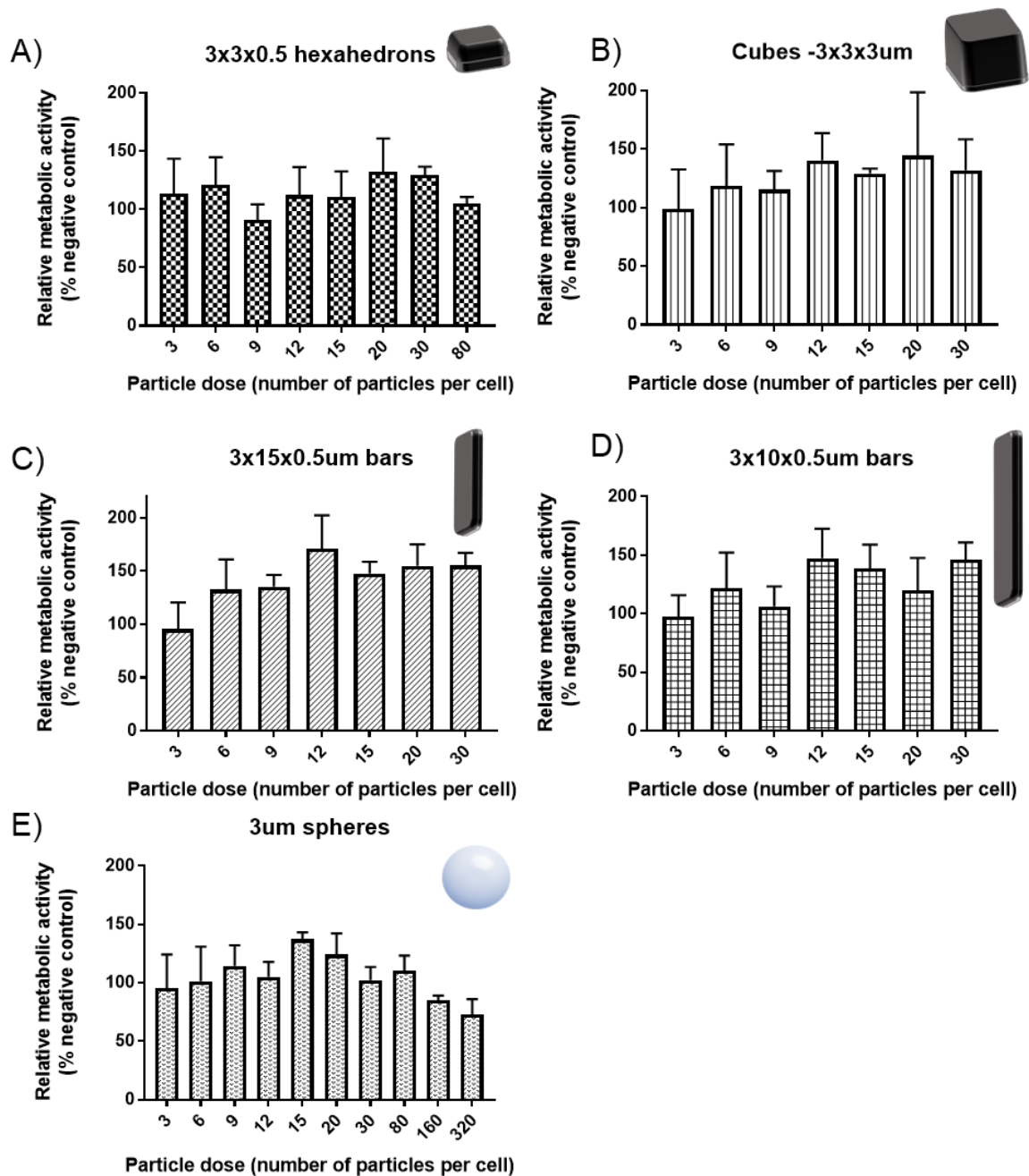


Figure 4.12: Effect of increasing polysilicon particle dose on RAW 264.7 metabolic activity. A) Hexahedrons (3x3x0.5 μm), B) Cubes (3x3x3 μm), C) Bars (3x15x0.5 μm), D) Bars (3x10x0.5 μm), E) Silicon oxide spheres (diameter 3 μm). Relative metabolic activity was calculated with respect to cells treated with 1% HEPES in HBSS (positive control), and cells treated with 0.1% Triton X-100 (negative control). Data is expressed as a mean \pm SD ($n=3$).

Maximum metabolic activity of cells treated with polysilicon particles was around 140-150% of control cells and was achieved at different particle doses. For hexahedrons and cubes this occurred at 20 particles per cell (10 µg/mL and 21 µg/mL respectively), for bar shaped particles 3x15x0.5 µm and 3x10x0.5 µm this occurred at 12 particles per cell (31 µg/mL and 21 µg/mL respectively). The increase in metabolic activity could be indicative of the increased energy requirement of the cells internalising particles. As seen in the uptake data, between 5 and 20% of cells are likely to take up particles, which might explain why the increase in activity is not more pronounced at lower doses. The increases in metabolic activity do not match the uptake data, for example the largest increase was seen with bar shaped particles which also had the lowest uptake. This may indicate that these bar shaped particles required disproportionately large increase in metabolic activity upon internalisation.

4.3.4.2 LDH assay

Lactate dehydrogenase (LDH) is an intracellular enzyme which is present in the cytoplasm of cells and is only released extracellularly when the cellular membrane is damaged³⁵⁰. As such, the LDH assay can be used to measure the toxicity of nano and microparticles³⁵¹. Polysilicon particles were applied at increasing doses and the amount of LDH in the supernatant measured compared with cells that were treated with 1% HEPES in HBSS (negative control, 0%) and cells treated with 0.1% Triton X-100 (positive control, 100%). The data is shown in figure 4.13.

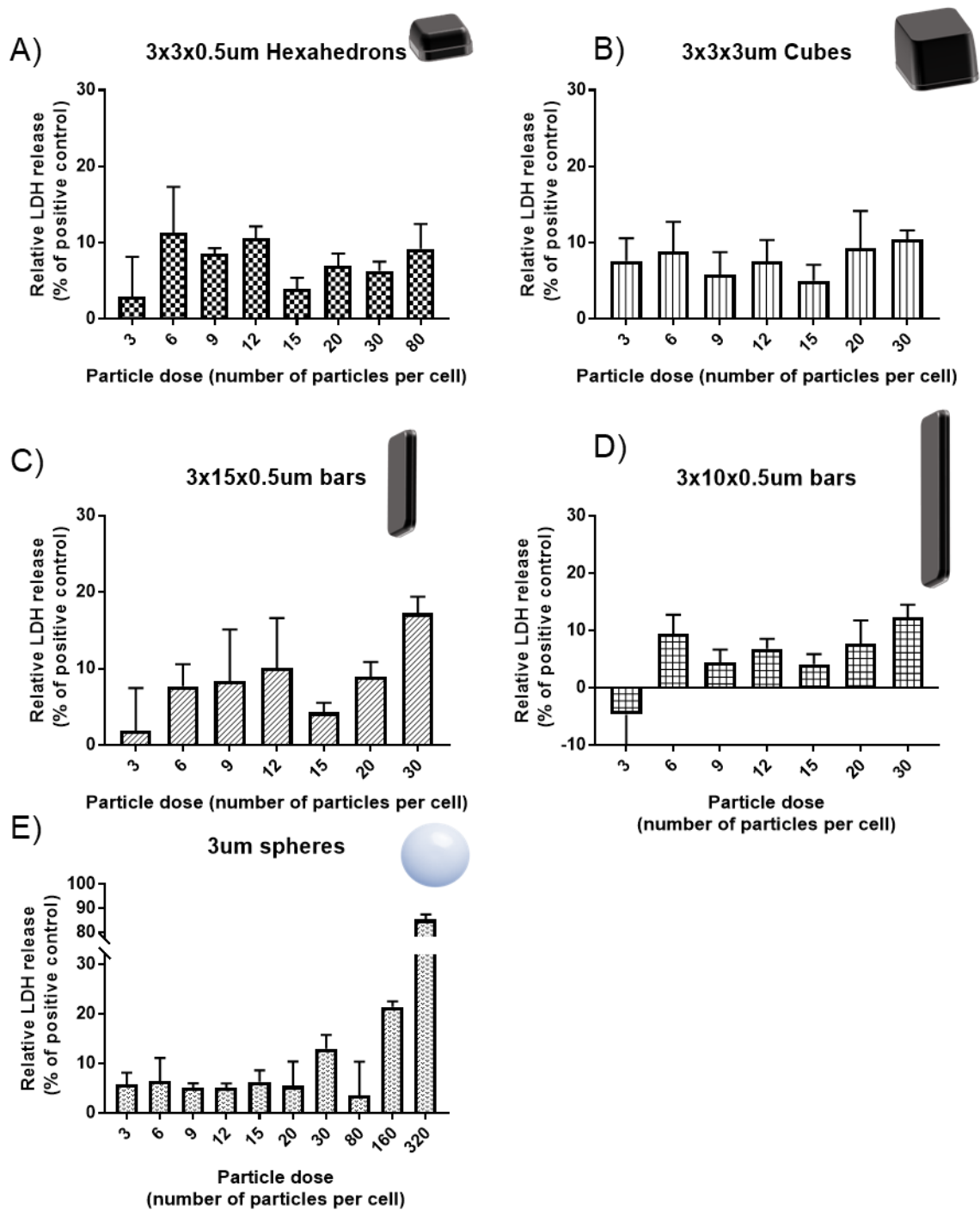


Figure 4.13: Effect of increasing polysilicon particle dose on RAW 264.7 LDH release. A) Hexahedrons (3x3x0.5 μm), B) Cubes (3x3x3 μm), C) Bars (3x15x0.5 μm), D) Bars (3x10x0.5 μm), E) Silicon oxide spheres (diameter 3 μm). Relative LDH release was calculated with respect to cells treated with 1% HEPES in HBSS (negative control), and cells treated with 0.1% Triton X-100 (positive control). Data is expressed as a mean \pm SD (n=3).

Low levels (5-10%) of LDH were released for each particle type for doses between 3-80 particles per cell for hexahedrons, 3-30 for cubes, 3-20 for 3x15x0.5 bars, 3-30 for 3x10x0.5 bars, and 3-80 for spheres. For 3x15x0.5 μm bars this increased to ~17% when the dose was increased to 30 particles per cell (78 $\mu\text{g/mL}$) indicating that at this dose an increasing number of cells were damaged by the particles. As in the case of the MTS assay the EC_{50} value was not obtained for polysilicon particles.

For spherical particles, where higher doses could be applied, LDH release remained fairly constant up to 80 particles per cell (124 $\mu\text{g/mL}$). LDH release then increased and showed an EC_{50} value of ~250 particles per cell (388 $\mu\text{g/mL}$) thus indicating that membrane damage was increasing, causing cell death. This matches fairly well with the MTS data. Although, the EC_{50} was not obtained in that case, this is likely due to the initial increase in metabolic activity upon exposure to particles.

4.3.4.3 Release of lysosomal enzyme glucuronidase

During phagocytosis, actin polymerisation drives the formation of a phagocytic cup surrounding the particle, which is subsequently internalised ³⁵². The internalised phagosome then matures by undergoing fusion with lysosomes containing an array of digestive enzymes ³⁵³. It has been shown however, that during phagocytosis lysosomes can undergo fusion with the cell membrane (exocytosis) in order to contribute to the extra cellular membrane that may be required to engulf larger particles and that this process is increased with increasing particle size ³⁵⁴⁻³⁵⁵.

Additionally, it has been shown that upon damage to the cell membrane, an influx of calcium ions causes intracellular vesicles, including lysosomes, to fuse with the cell membrane in order to regain plasma membrane integrity ³⁵⁶⁻³⁵⁷.

Upon fusion with the cell membrane, the contents of the lysosome are released into the extra cellular medium which can then be detected. It was therefore hypothesised that polysilicon particles of different shapes would differentially trigger release of the lysosomal enzyme glucuronidase. The release of glucuronidase is therefore indicative either of the cells

requirement of additional membrane to engulf larger particles or damage to the cell membrane. The two can be distinguished by comparing glucuronidase release with LDH release which is only indicative of cell membrane permeability ³⁵⁸.

Glucuronidase release was detected using 4-methyl umbelliferyl- β -D-glucuronide hydrate (MUG), a non-fluorescent molecule which becomes fluorescent upon degradation by glucuronidase. The data are shown in figure 4.14.

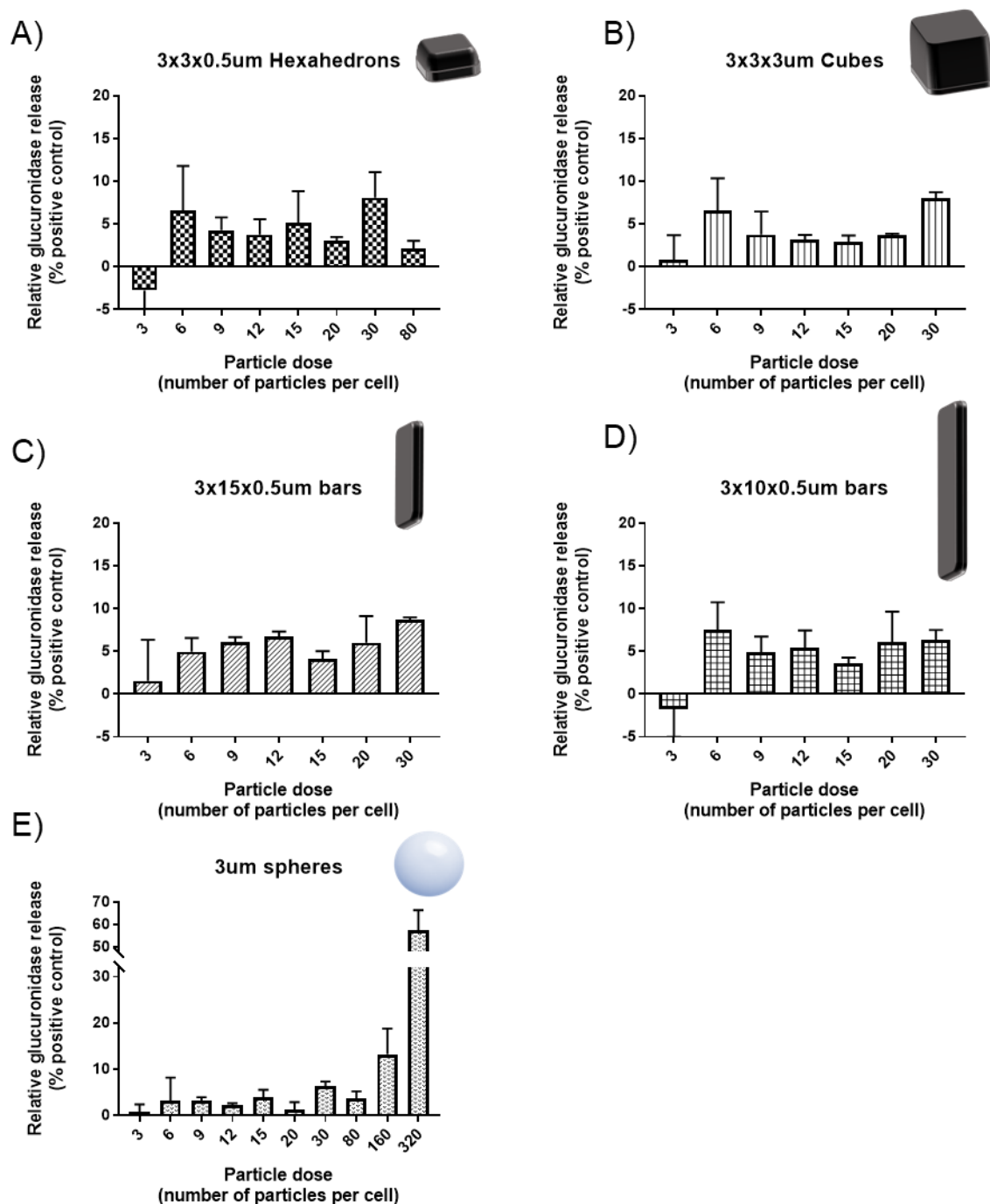


Figure 4.14: Effect of increasing polysilicon particle dose on RAW 264.7 lysosomal glucuronidase release. A) Hexahedrons (3x3x0.5 μm), B) Cubes (3x3x3 μm), C) Bars (3x15x0.5 μm), D) Bars (3x10x0.5 μm), E) Silicon oxide spheres (diameter 3 μm). Relative glucuronidase release was calculated with respect to cells treated with 1% HEPES in HBSS (negative control), and cells treated with 0.1% Triton X-100 (positive control). Data is expressed as a mean \pm SD ($n=3$).

The data for release of lysosomal glucuronidase follows a similar trend to LDH release. Low levels (~5% of total glucuronidase) were released from each particle shape across the administered dose range. It does not appear from this data that a significant different release of lysosomal glucuronidase occurs in response to the different particle shapes used, however, the congruency with the LDH data suggests that particles are causing some degree of cell membrane damage, which causes the release of both LDH and glucuronidase at low levels. In the case of 3 μm spheres, where higher doses were administered, lysosomal glucuronidase release increased with increasing dose rising from 13% to 57% of total lysosomal glucuronidase when particle dose increased from 160 to 320 particles per cell (250 to 500 $\mu\text{g/mL}$).

4.4 Discussion

It is difficult to know if *in vitro* studies assessing the effects of nano and microparticles reflect realistic *in vivo* scenarios. It has been observed that toxicity can be caused by an overload of cells by particles which may not occur *in vivo* due to lower fractions of the applied dose reaching the cells ³⁵⁹. How the doses used in this study relate to realistic, physiological doses of particles to macrophages requires numerous assumptions. For example, considering particle delivery to the lung by a dry powder inhaler (DPI), only a rough estimate can be made. Stone *et al.* calculated the number of macrophages per surface area of alveolar epithelium to be ~1 macrophage per 18000 μm^2 ³⁶⁰ and it has been calculated that the surface area of alveolar epithelium to approximately 140 m^2 ³⁶¹. Using a deposition fraction for 3 μm particles in the alveolar region of 0.4 ³⁶² and assuming 50% of the total emitted dose makes it to the lungs ³⁶³, a 500 μg dose would result in 100 μg particles depositing in the alveolar region. 100 μg particles of density 1.3 g/cm^3 ³⁶⁴ (spherical, diameter 3 μm) is equivalent to 5.4×10^6 particles and thus dividing by the approximate number of macrophages in the alveoli gives a particle per cell ratio of 0.0007. Therefore, realistically a macrophage is unlikely to interact with

more than one microparticle, therefore indicating that the doses used in this study are significantly above what may be delivered in a single inhalation from a DPI. However, removal of particulate material by macrophages is known to take place over a number of weeks, the accumulation of multiple doses of insoluble particles over a number of weeks could reach the levels of doses used in this study ³⁶⁵.

Albrecht *et al.* studied the release of LDH and glucuronidase from alveolar macrophages 90 days after the intra tracheal instillation of quartz particles (0.4-0.8 μm) in rats ³⁶⁶. The dose used (10 mg/kg) was chosen to represent the exposure of a worker to a years' worth of respirable quartz rather than drug delivery, and showed increased release of both LDH and glucuronidase compared to a PBS control. However, in rats treated with quartz, the number of alveolar macrophages increased which likely contributed to the increase in enzyme release.

On the other hand, Van Landuyt *et al.* studied the release of LDH and glucuronidase by NR8383 macrophages *in vitro* after exposure to quartz (of respirable size, but shape not well characterised) and showed similar enzyme release to those found in this study at similar doses. Enzyme release then increased with increasing dose between 22.5 and 180 $\mu\text{g/mL}$ ³⁶⁷. Similarly to quartz particles, the polysilicon particles studied in this chapter are crystalline whereas the 3 μm spheres used are amorphous. Costantini *et al.* showed that amorphous particles are equally toxic to macrophages as crystalline particles ³⁶⁸. Moreover, significant membrane damage was seen after 4 hours incubation suggesting that the duration of experiments in this chapter were sufficient to observe these effects.

In vitro studies utilising microparticles of different shapes have tended to focus on inhaled fibres with macrophage responses studied to assess potential toxicity predominantly by LDH release. For example, the effect of macrophage exposure to glass fibres of different lengths (3, 4, 7, 17, 33 μm , width 0.5 μm) was studied by Blake *et al.* at doses of 50-500 $\mu\text{g/mL}$. In congruence with this study, low levels of LDH release were seen upon exposure to particles at comparable doses, and very few differences were seen in LDH release by the different length particles. The one exception was a marked increase in LDH release by fibres with

length 17 μm which the authors attributed to frustrated phagocytosis of these longer fibres. However, there is no explanation for why this effect was not seen in fibres with length 33 μm . The 3x15x0.5 μm bars used in this study were similar in length, and elicited lower LDH release at the same dose which is not suggestive of frustrated phagocytosis.

Watanabe *et al.* studied the effect of titanium dioxide fibres (5 μm x 0.2 μm) and particles (diameter \sim 2 μm) on LDH release by macrophages between 20 and 60 $\mu\text{g/mL}$ ³⁶⁹. Particles of this size did not exhibit any increase in LDH release upon increasing dose, however the fibres elicited a dose dependent increase in LDH release. It was theorised that the narrow diameter of the fibres caused puncturing of the cell membrane which was the cause of LDH release, however, this was not proven definitively. It is unlikely that the particles used in this chapter would cause a puncturing of the cell membrane in this manner as the dimensions are greater than those used by Watanabe.

The mechanism by which silicon toxicity occurs is not clearly defined. The predominant theory is that of free radical generation leading to DNA damage and subsequent apoptosis ³⁷⁰. On the other hand it has been suggested that toxicity can arise from lysosomal disruption caused by a failure of the lysosomal environment to break down the particle ³⁷¹. The release of cathepsin D and subsequent sphingomyelinase activation leads to mitochondrial membrane depolarisation and the activation of caspase 3 and 9. These two theories are likely not mutually exclusive and what they have in common is the requirement of particles to be internalised before events leading to toxicity take place. In other words, direct disruption of the cellular membrane by contact with particles is not thought to be the cause of toxicity. In this chapter it was shown that \sim 10-20% of cells internalised particles of each shape over the course of the experiment. Thibodeau *et al.* looked at the time course of silica toxicity and showed that \sim 15% cells had lost membrane integrity within 6 hours, which then increased to \sim 60% within 24 hours ³⁷². This may therefore indicate that the assays in this chapter depict the early stages of toxicity due to the increased metabolic activity and the release of low levels of intracellular enzymes within 4 hours.

There are few studies focusing on the shape of microparticles and their uptake by macrophages. Mathaes *et al.* looked at the difference in uptake of PLGA micro particles with spherical (diameter 2 μm) compared with equivalent particles stretched to decrease the aspect ratio to 0.2³⁷³. It was shown that spherical particles were internalised to a greater extent than the stretched particles. Additionally, Champion and Mitragotri demonstrated that macrophages are less able to internalise high aspect ratio microparticles (length $\sim 20\mu\text{m}$) than spherical particles (3 μm particles)²⁴¹. The phenomena was explained by low attachment of macrophages to the major axis of the particles (the tips of the particles). Given the results of these studies it would be anticipated that the bar shaped particles (3x15x0.5 μm , 3x15x0.05 μm and 3x10x0.5 μm) would therefore show drastically reduced uptake relative to particles with a lower aspect ratio. While this was the case compared with hexahedrons it did not hold true for disks and cubes. The above-mentioned studies used polymer particles which are known to have a degree of deformability and indeed macrophages were observed exerting enough mechanical force to bend the particles in the study by Champion and Mitragotri²⁴¹.

A number of studies suggest that macrophages are less capable of internalising soft particles than those that are more rigid³⁷⁴⁻³⁷⁶. Alexander *et al.* studied the effect of both mechanical properties and shape on phagocytosis by J774A.1 macrophages by comparing core-shell and shell only particles of spherical and cubic shape (diameters 2-3 μm)³⁷⁷. There was no effect of particle shape on uptake, however macrophages showed significantly reduced uptake of shell only particles with lower Young's moduli. Young's modulus is affected not only by the material properties but also by the shape of the material³⁷⁸. This is therefore a confounding factor in such particle uptake studies as is difficult to separate from shape alone.

No deformation of the majority of polysilicon particles used in this chapter was observed and so the effect of mechanical stiffness may be low. The exception to this is the 3x15x0.05 μm bars which were observed to bend slightly, most likely due to their thickness. In comparison, the deformation of polymer particles used by Champion and Mitragotri was far more extensive.

Hexahedrons (3x3x0.5 μm) were associated with, and internalised by significantly more macrophages than circular disks (diameter 3 μm). Given the similarity between these two particle sizes, similar binding and uptake characteristics would be expected. No published studies have compared the phagocytosis of these two shapes, however the phagocytosis of circular disk shaped microparticles have been compared with spherical particles ³¹⁶. It was shown that macrophages attached to, but did not internalise circular disk-shaped particles, whereas spherical particles were internalised. Other studies have made use of hitchhiking particles of this disk shape to enable particles to be carried by macrophages to the site of action ^{374, 379-380}. There is therefore a precedent for the reduced uptake of disk-shaped particles but no studies comparing the uptake of hexahedral disks. Because hexahedrons have corners, there are points of high curvature compared to circular disks that may influence macrophage binding and internalisation. Receptor clustering, drives particle internalisation during phagocytosis ³⁸¹. If the initial point of contact between particle and cell is at a point of high curvature receptor clustering could be more efficient and so drive more efficient phagocytosis. Further investigation of this is warranted by monitoring individual particle cell interactions.

4.5 Conclusions

The shape of polysilicon particles had only small effects on their interactions with macrophages. In terms of particle uptake, it was shown that 3x3x0.5 μm hexahedrons displayed the highest cellular association and uptake, therefore this particle shape may have benefits for targeted delivery to macrophages compared to the other shapes used in this study. On the other hand, similarly sized circular disks and bar-shaped particles displayed lower uptake and so may be beneficial for the avoidance of macrophage uptake. Uptake studies could only be done using a single concentration due to limitations on the available number of particles. Therefore, in future it would be beneficial to expand on this work using a range of higher concentrations, longer dosing times and in different conditions including bio-relevant media.

As in the case of particle uptake, polysilicon particles of different shapes did not elicit major changes in cellular metabolism, LDH release, or release of lysosomal glucuronidase. In response to particles, macrophages increased their metabolic activity, and released low levels of intracellular enzymes which could indicate the early stages of toxicity. Increasing the particle dose did appear to increase the metabolic activity of the cells although it had no effect on enzyme release.

5. Effect of silicon oxide particle size and surface modification with zwitterion on interaction with macrophages

5.1 Introduction

Altering particle size and surface chemistry are potential methods for modulating the uptake of particles by macrophages. In a study looking at the effect of microparticle size it has been shown that particle internalisation was highest at a particle size of 1.9 μm when compared against 450 nm and 4.8 μm particles ¹⁰⁷. Another study showed a peak in uptake at a particle size of 2-3 μm when particles of diameter 1-6 μm were compared ¹⁰⁶. A study by Catelas *et al.* found very little difference in uptake in particles sized between 1-5 μm whereas particles <1 μm in size showed significantly less uptake ¹⁰⁵.

Targeting macrophages by altering the surface chemistry of particles has been used for a number of particle types. Liposomes, modified to display mannose on their surface, displayed 3.6 fold increase in uptake by alveolar macrophages compared to those without the modification ³⁸². It has also been shown that folate decorated PLGA nanoparticles exhibit enhanced uptake ³⁸³. On the other hand, a great deal of work has focussed on modifying particle surface chemistry to decrease particle uptake by macrophages. The most studied of these is polyethylene glycol (PEG) which has been used successfully by a number of groups to reduce particle uptake ³⁸⁴⁻³⁸⁷. However, it is important to note that the chemical identity on the surface of the particle after administration is altered by the formation of a biological corona. The underlying surface chemistry (and other factors such as size, charge etc.) will affect the composition of this corona, as well as the components of the biological medium which in turn can modulate uptake by macrophages ³⁸⁸.

Recently, the application of zwitterionic surface chemistries and their effect on cellular uptake has been studied. Zwitterionic molecules contribute to the formation of a hydrophilic surface which has been shown to affect protein adsorption and cellular uptake. For example, Liu *et al.* coated gold nanoparticles with a mixed monolayer containing both quaternary amine (+ve charge) and sulphate groups (-ve charge). The study found that this zwitterionic coating considerably reduced particle uptake by RAW 264.7 macrophages compared with particles that had monolayers of only quaternary amines or only sulphates ³⁸⁹. In another such study, Zhao *et al.* showed that zwitterionic phosphorylcholine-coated micelles exhibited reduced particle uptake by mouse peritoneal macrophages ³⁹⁰.

The majority of studies seem to suggest a reduction in cellular uptake of particles with zwitterionic surface chemistries ³⁹¹⁻³⁹³. However, studies have mainly focused on particles in the nano-size range. As such, it is necessary to see what the effects of zwitterionic coatings on cellular uptake are in micron-sized particles.

In this chapter the effect of particle size and zwitterionic coating on cellular uptake by macrophages is assessed. Three sizes of silicon oxide particles (0.5 μm , 1 μm , and 3 μm) were modified with either AUTES surface chemistry (positively charged) or further modified with zwitterionic *N*-(3-sulfopropyl)-*N*-methacroyloxyethyl-*N,N*-dimethylammonium betaine (MDSA). Modified particles are characterised using X-ray photoelectron spectroscopy (XPS), Zeta potential, water contact angle, and fluorescence microscopy. Particle uptake is assessed using imaging flow cytometry in undifferentiated RAW 264.7 cells, LPS stimulated RAW 264.7 cells, and in the presence of phospholipid dipalmitoylphosphatidylcholine (DPPC). ²⁵⁵

During different stages of respiratory disease states, particularly in infections such as tuberculosis and pneumonia, macrophages have been shown to differentiate towards an M1 phenotype ³⁹⁴⁻³⁹⁵. This phenotype can be replicated *in vitro* by stimulation with LPS and therefore can be used to represent the macrophage activation state in these cases ³⁹⁶.

Furthermore the effect of including DPPC in the media was examined. In the alveoli, lung surfactant is present in order to prevent the alveolar structures from collapsing ³⁹⁷. Phospholipids, including DPPC, form the majority of this surfactant and so are likely to interact with inhaled particles, potentially altering their interactions with macrophages ³⁹⁸.

Particle uptake studies are common in the literature and typical experiments involve the administration of particle suspension to cells in a well plate for a defined period of time, removal of the suspension and subsequent rinsing of the cells ²⁷². The cells are then analysed for fluorescence by flow cytometry or elemental concentrations by ICP-MS. In order to compare, for example, the effect of nanoparticle surface chemistry, typically an equivalent mass of particles is applied to each well, however some studies have included the use of multiple dose metrics ^{35, 107}.

When comparing the uptake of different sized particles it is particularly important to bear in mind the effect of dose metric, as administering an equivalent particle mass results in non-equivalent particle number and surface area applied. In this study, three dose metrics were chosen for the purpose of examining how this affects the uptake of differently sized particles. Particles were administered according to equivalent mass (10 µg per well), number (10 particles per cell), and total surface area (10,000,000 µm²) and quantified in terms of the percentage of cells internalising particles, the number of particles internalised per cell, and the percentage dose internalised.

5.2 Materials and Methods

5.2.1 Materials

Rhodamine B isothiocyanate (RBITC, 283924), N-(3-sulfopropyl)-N-methacroyloxyethyl-N,N-dimethylammonium betaine (MDSA, 537284), NaCl, and Silicon oxide spheres (diameter 0.5, 1, 3 μm) were purchased from Sigma-Aldrich. H_2SO_4 (98%) and NH_4OH (20%) were purchased from Fisher Scientific. 11-aminoundecyltriethoxysilane (AUTES, S25045) was purchased from Fluorochem (UK). H_2O_2 (35%), and dimethylsulfoxide (DMSO) were purchased from VWR. DPPC was purchased from Avanti polar lipids Inc.

5.2.2 Methods

5.2.2.1 Modification of silicon oxide spheres with AUTES, RBITC, and MDSA

Activation of silicon oxide spheres

Silicon oxide spheres 1 mg (20 μL) in suspension (stock concentration 5% w/v) were transferred to a 1.5 mL microcentrifuge tube and centrifuged at 5700 RPM (6175G) for 10 minutes and the supernatant removed. Particles were suspended in 700 μL acidic piranha solution for 1 hour with shaking to prevent particles from falling out of suspension. Particles were centrifuged at 5700 rpm (6175G) for 10 minutes and the acidic piranha solution removed. Particles were washed by resuspension in 700 μL milliQ water and then centrifuged at 5700 rpm (6175G) for 10 minutes. This washing process was repeated 3x and then the supernatant removed. Particles were suspended in 700 μL basic piranha solution and left shaking for 30 minutes. Particles were centrifuged at 5700 rpm (6175G) for 10 minutes and the basic piranha solution removed. Particles were washed using the same resuspension in 700 μL milliQ water and centrifugation steps used to wash the particles after removal of the acidic piranha solution.

Modification of silicon oxide particles surface with AUTES and RBITC

AUTES (5 mg, 0.015 mmol) was mixed with RBITC solution (10 μ M, 15 mL) in EtOH to give a final AUTES concentration of 1mM. The AUTES:RBITC molar ratio was 100:1 so as to result in 1% of the particle surface being labelled. This solution was stirred for 2 hours and then added to microcentrifuge tubes containing 1 mg freshly activated silicon oxide particles (700 μ L per tube). Particles were suspended and left on a shaker for 2 hours while protected from light. Particles were washed 3x by centrifugation at 5700 RPM (6175 G) and replacement of the supernatant with 700 μ L EtOH.

Addition of MDSA to particles

Silicon oxide particles modified as above were suspended in MDSA 1mM in DMSO 700 μ L with triethylamine (30 μ M) and left shaking overnight while protected from light. Particles were washed 3x by centrifugation and rinsing with DMSO 700 μ L. Particles were stored in EtOH 700 μ L at 4°C.

5.2.2.2 XPS characterisation of modified particles

Preparation of XPS samples

1 mg particles were washed by centrifugation and resuspension 3x with 700 μ L MilliQ water and flash frozen by dipping the microcentrifuge tubes in liquid nitrogen. Particles were freeze-dried overnight. Microcentrifuge tubes containing freeze-dried particles were stored at 4°C until analysis by XPS.

XPS analysis

XPS measurements were performed using a Kratos AXIS Ultra DLD instrument. Freeze-dried microparticles were mounted using double-sided tape onto a standard Kratos sample bar which were inserted into the airlock and left overnight until the vacuum reached 3×10^{-7} Torr.

Wide energy survey scans were collected using a pass energy of 80 eV in hybrid slot lens mode with a step size of 0.5 eV. High resolution spectra were obtained at a pass energy of 20 eV over energy ranges suitable for each peak with a step size of 0.1 eV. The charge neutraliser filament was used to prevent sample charging over the irradiated area. The X-ray source was a mono-chromated Al K α emission, run at 10 mA and 12 kV (120 W). The data were captured using Kratos VISIONII software and exported into vms format for data processing with CASAXPS. Three sample positions were set up and data collected for these was quantified from the wide scan data using the standard kratos RSF library. The high-resolution data was charge corrected to C 1s at 285 eV.

5.2.2.3 Zeta potential measurements

Zeta potential measurements were performed using a Malvern zetasizer Nano. Particles were suspended in 10 mM NaCl at a concentration of 0.1 mg/mL. Each sample was then transferred to a DTS 1070 zeta cell for measurement.

5.2.2.4 Water contact angle measurements

30 μ L particle suspension (1 mg/mL) in EtOH was pipetted drop wise onto a glass coverslip and the EtOH allowed to evaporate. After drying the particles were visible as a semi-transparent film on the coverslip. The water contact angle was measured 3 times for each sample using a KSV CAM 200 optical contact meter.

5.2.2.5 Acquisition of brightfield and fluorescent images

Brightfield and fluorescence images were acquired using a Nikon Eclipse TiU fluorescence microscope. Images of particles in suspension were acquired by pipetting 15 μ L particle suspension (0.5 μ g/mL for 0.5 μ m particles, 1 μ g/mL 1 μ m particles, 10 μ g/mL for 3 μ m particles in NaCl 10 mM) onto a glass slide and then covering with a coverslip. For fluorescence imaging of RBITC-labelled samples λ_{ex} = 550 nm and λ_{em} = 590 nm. Images

were processed using imageJ®. The threshold function was used to identify individual particles and create corresponding regions of interest (ROIs). The multi measure tool was then used to acquire the median fluorescence intensity (MFI) of each ROI across multiple images for each sample (~100 particles per sample).

5.2.2.6 Quantitative uptake of silicon oxide spheres by RAW 264.7 cells

Preparation of particles

Modified particles were freeze dried in microcentrifuge tubes of known mass in order to calculate the exact mass of particles in each tube. Particle stock suspensions were prepared in sterile conditions by adding 1% HEPES in HBSS 1 mL to each tube. Stock suspensions were diluted to the desired concentration by removal of the required volume of stock suspension and addition of 1% HEPES in HBSS. Particle suspensions were warmed to 37°C prior to addition to cells. In experiments where particles were administered in the presence of DPPC, the required volume of stock solution was diluted with 1% HEPES in HBSS containing DPPC 0.25 mg/mL freshly prepared on the day of the experiment.

The mass of freeze-dried particles was used to calculate the particle number and surface area using a density of 2.2 g/cm³, particle volumes of 0.065, 0.52, and 14.14 µm³, and particle surface areas of 0.79, 3.14, and 28.27 µm² for 0.5, 1, and 3 µm diameter particles respectively.

Preparation of RAW 264.7 cells

RAW 264.7 cells were harvested once they reach 60-80% confluency by scraping. 100,000 cells in culture media were seeded per well into a 12 well plate and incubated overnight at 37°C, 5% CO₂, 95% humidity. In experiments where RAW 264.7 cells were stimulated with LPS, culture media was used without 1% penicillin/streptomycin and was supplemented with 100 ng per mL LPS.

Culture media was removed by aspiration and the cells washed with 1 mL pre-warmed (37°C) PBS. PBS was removed and 1 mL pre-warmed particle suspensions applied at different concentrations based on particle mass, number, and surface area. Cells were incubated for 4 hours after which time the particle suspensions were removed and the cells washed with 3 x 1 mL warm HBSS. Cells were prepared for flow cytometry.

Preparation of fixed cells for flow cytometry

HBSS was removed from each well by aspiration and 250 µL accutase added to each well and the cells placed in an incubator for 5 minutes to detach cells. 250 µL HBSS was then added to each well and the total volume of each well transferred to fresh microcentrifuge tubes. Samples were centrifuged at 250 G for 5 minutes and the supernatants removed. The cells were suspended in 250 µL 4% formaldehyde in PBS for 20 minutes before being centrifuged for 5 minutes (250 G) and the supernatant removed. Fixed cells were suspended in 50 µL HBSS and stored at 4°C until analysis by flow cytometry. Samples were always analysed within 1 week of sample preparation.

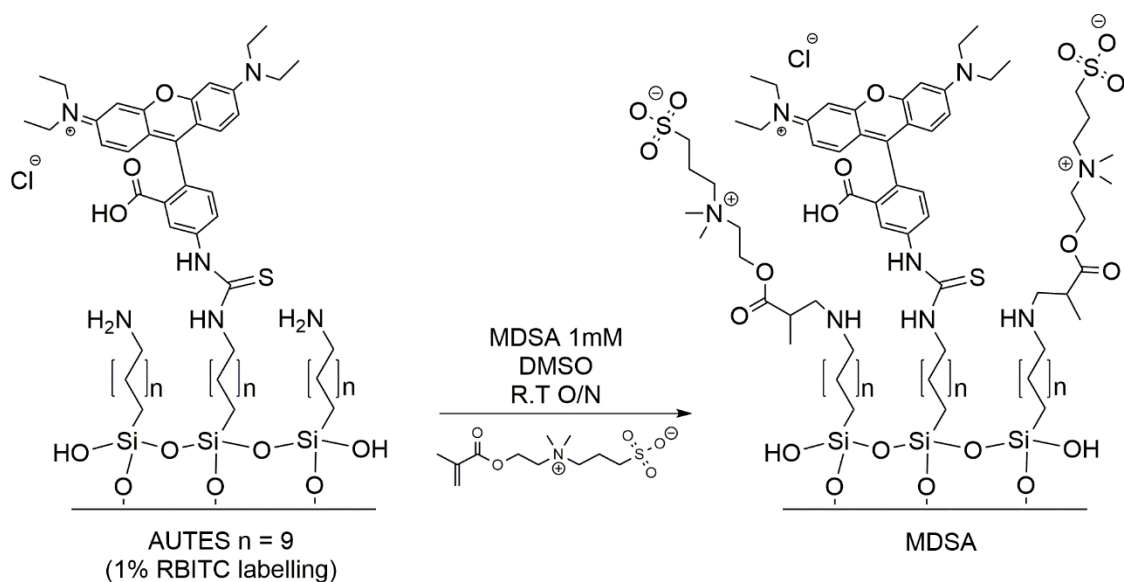
Flow cytometry

Flow cytometry was performed using an Amnis imagestream^X MKII imaging flow cytometer in standard configuration with 40X magnification. Illumination settings: Brightfield LED 32.01 mW, 561 nm laser 200 mW, 785 nm laser 2 mW. Data was acquired using INSPIRE software with a minimum of 500 cells per sample (typically > 1000 cells per sample). Data was analysed using IDEAS software. Gatings for cells with particles were set above the fluorescence of control cells (cells not exposed to particles) for each condition. The percentage of cells internalising particles was determined using IDEAS software's internalisation feature. The number of particles per cell was calculated using the following formula: (MFI of cells internalising particles – MFI of control cells)/ MFI of particles. The % dose internalised was calculated by multiplying the proportion of cells internalising particles by the number of particles per cell and dividing it by the number of particles administered per cell.

5.3 Results and Discussion

5.3.1 Characterisation of modified silicon oxide particles

Spherical silicon oxide particles of 0.5 μm , 1 μm , and 3 μm diameter were purchased and surface chemistry modified with AUTES (labelled with 1% RBITC). Further modification then took place with zwitterionic MDSA (Scheme 5.1) and the particles characterised at each stage by XPS, zeta potential, contact angle, and fluorescence microscopy.



Scheme 5.1: Addition of MDSA zwitterion to silicon oxide particles with AUTES surface chemistry (labelled with 1% RBITC)

5.3.1.1 XPS characterisation

XPS was performed on 0.5 μm , 1 μm , and 3 μm particles without any modification, after modification with AUTES, and after further modification with MDSA, the data is shown in figure 5.1 and table 5.1.

The results obtained for unmodified particles showed the presence of O (533 eV), C (285 eV), and Si (103 eV) at concentrations ~50%, ~20%, and ~30% respectively. The presence of carbon here results from adventitious carbon that results from exposure of the sample to air, this is a ubiquitous phenomenon during XPS analysis ³⁹⁹.

Upon modification with AUTES the results were consistent between each particle size. There was a sharp increase in the % Carbon as determined by the peak at 285 eV which is indicative of the carbon chain in AUTES. A decrease in O (533 eV) and Si (103 eV) peaks resulting from silicon oxide is observed due to the surface being covered by the AUTES layer. Additionally the appearance of a Nitrogen peak at 400 eV resulting from the amine groups in AUTES confirmed deposition of AUTES on the surface of the particles ⁴⁰⁰. Upon further modification with MDSA an appearance of a sulphur peak at 168.9 eV was observed. High resolution scans of MDSA modified particles compared with scans of pure MDSA powder confirmed that this peak comes from the zwitterion on the particle surface (Appendix III figure S5.1). High resolution scans of Nitrogen peaks of AUTES modified particles showed two peaks at 399 and 401 eV representing C-NH₂ and C-NH₃⁺ groups (Appendix III figure S5.2) ⁴⁰¹. Upon modification with MDSA, a third nitrogen peak was found at 402 eV which results from the NR₄⁺ group ⁴⁰² and thus confirmed the presence of the zwitterion.

Table 5.1 shows the relative atomic concentrations for each particle size and modification. Only one other study has examined the deposition of AUTES on silicon oxide, and the results showed a close agreement with those of this chapter for both unmodified silicon oxide and AUTES-modified silicon oxide ⁴⁰³. Specifically, the study showed after deposition of AUTES atomic concentrations of Carbon, Nitrogen, Oxygen, and Silicon to be 62.6 (± 0.3), 2.1% (± 0.8), 21.8, and 13.5 (± 0.3) respectively. The deposition of a similar silane aminopropyl triethoxy silane (APTES) on to silicon oxide surfaces has been more extensively studied and nitrogen concentrations of between 2.0-9.8% after APTES deposition have been reported ^{194, 404-406}. A higher nitrogen concentration is expected than for AUTES because of the relative chain lengths (AUTES has 11 carbons, APTES has 3 carbons).

In order to estimate the % conversion of the AUTES primary amine to secondary amine upon conjugation with MDSA, the ratio of nitrogen:sulphur (N:S) was considered (Table 5.1). Theoretically if a complete conversion of all surface amines were to take place the result would be a N:S ratio of 2:1 with one nitrogen coming from the AUTES and one nitrogen and one sulphur coming from the MDSA molecule. The results showed that the N:S ratio was 3.49, 3.51, and 2.97 for 0.5 μm , 1 μm , and 3 μm particles respectively. This equates to a 40% conversion of the surface amines by MDSA for 0.5 μm and 1 μm particles and 50% conversion of surface amines for 3 μm particles.

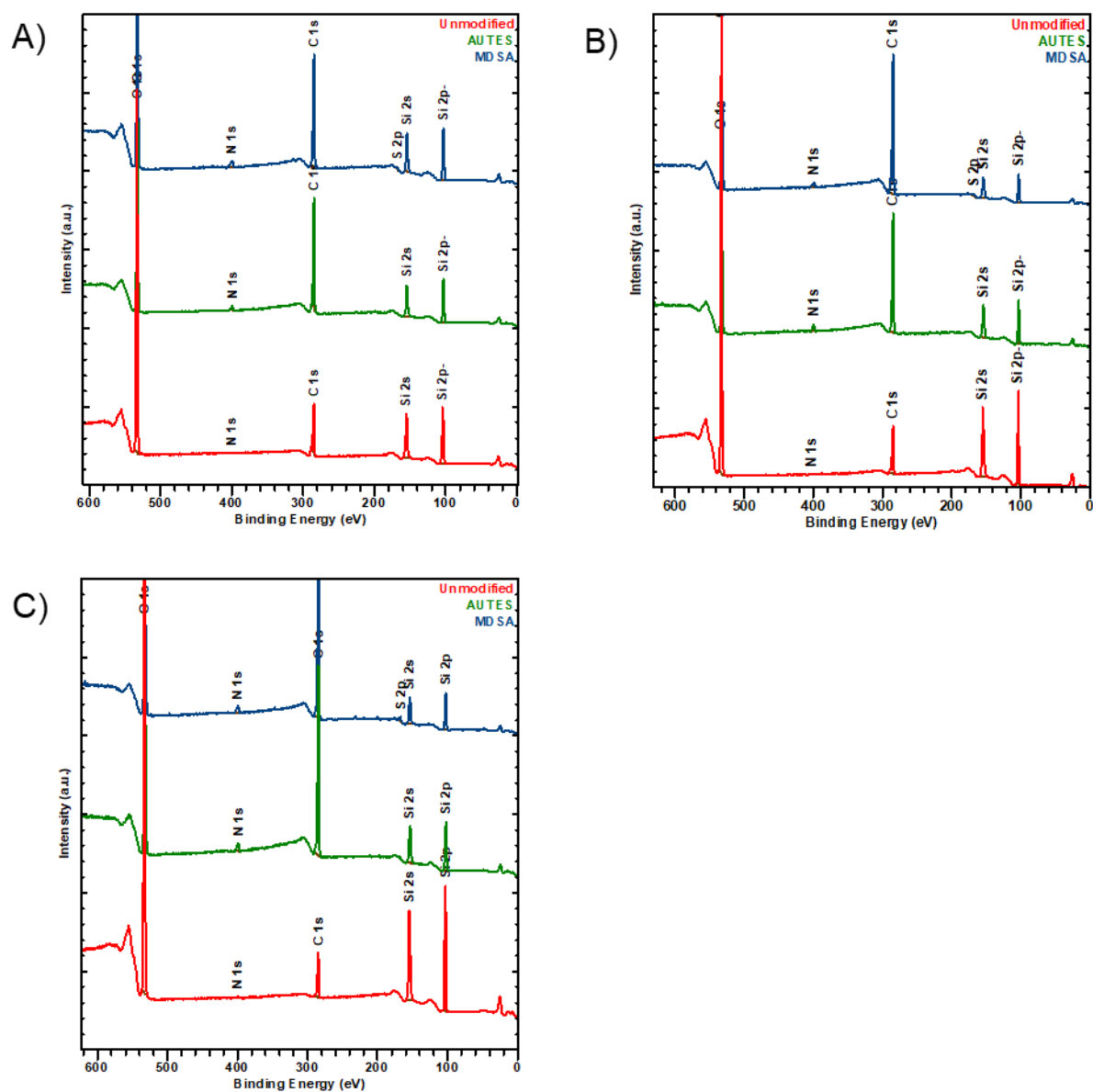


Figure 5.1: Widescan XPS spectra of silicon oxide particles with modified surface chemistry. A) 0.5 μ m, B) 1 μ m, C) 3 μ m. Unmodified particles (red), AUTES-modified particles (green), MDSA-modified particles (Blue).

Table 5.1: Surface composition (Atomic %) of silicon oxide particles with modified surface chemistry

Particle type	Atomic %					
0.5um	O	C	Si	N	S	N/S*
Blank particles	51.10 ± 13.38	18.61 ± 9.45	23.52 ± 5.37	-	-	-
AUTES particles	28.58 ± 2.21	55.14 ± 2.21	15.28 ± 1.84	1.00 ± 0.27	-	-
MDSA particles	32.97 ± 1.41	47.44 ± 3.09	17.83 ± 1.30	1.36 ± 0.25	0.39 ± 0.16	3.49
1um	O	C	Si	N	S	N/S*
Blank particles	54.01 ± 0.66	17.66 ± 0.71	28.1 ± 0.18	-	-	-
AUTES particles	28.11 ± 0.67	52.69 ± 1.73	16.63 ± 1.14	2.43 ± 0.10	-	-
MDSA particles	25.16 ± 1.22	62.12 ± 1.2	10.52 ± 0.02	1.72 ± 0.07	0.49 ± 0.11	3.51
3um	O	C	Si	N	S	N/S*
Blank particles	55.45 ± 1.67	16.64 ± 3.60	27.7 ± 2.14	-	-	-
AUTES particles	21.02 ± 1.61	65.74 ± 4.01	9.72 ± 3.29	1.52 ± 0.82	-	-
MDSA particles	24.16 ± 1.33	60.45 ± 2.47	12.35 ± 0.84	2.29 ± 0.14	0.77 ± 0.16	2.97

* N/S is the ratio of Nitrogen to Sulfur

5.3.1.2 Zeta potential measurements

Zeta potential measurements were taken of each particle size before modification of the particle surface (unmodified), after modification of the surface with AUTES (including 1% labelling with RBITC), and after modification the MDSA in 10mM NaCl. The data is shown in figure 5.2. Unmodified particles showed zeta potential values of -37.3 mV (0.5 µm), -44.4 mV (1 µm), and -25.5 mV (3 µm). Silicon oxide particles have a negative zeta potential at neutral pH owing to surface hydroxyl groups, as pH decreases the zeta potential becomes less negative until it reaches the isoelectric point at pH 2⁴⁰⁷⁻⁴⁰⁸.

Here negative zeta potential values were obtained for all particle sizes, but smaller particles exhibited a more negative zeta potential. From the XPS data it is known that the different

particle sizes have identical surface chemistry and so the reason for the disparity is due to another factor. The measurement of zeta potential is dependent on a number of other factors including pH, ionic strength, applied voltage, particle concentration, and particle size ⁴⁰⁹. The differences could therefore be explained due to particle size differences, particularly as the large size of these particles means that some degree of sedimentation takes place. Additionally, although the mass concentration of particles was kept the same for each sample, this would result in a larger total surface area of smaller particles and could also affect the result.

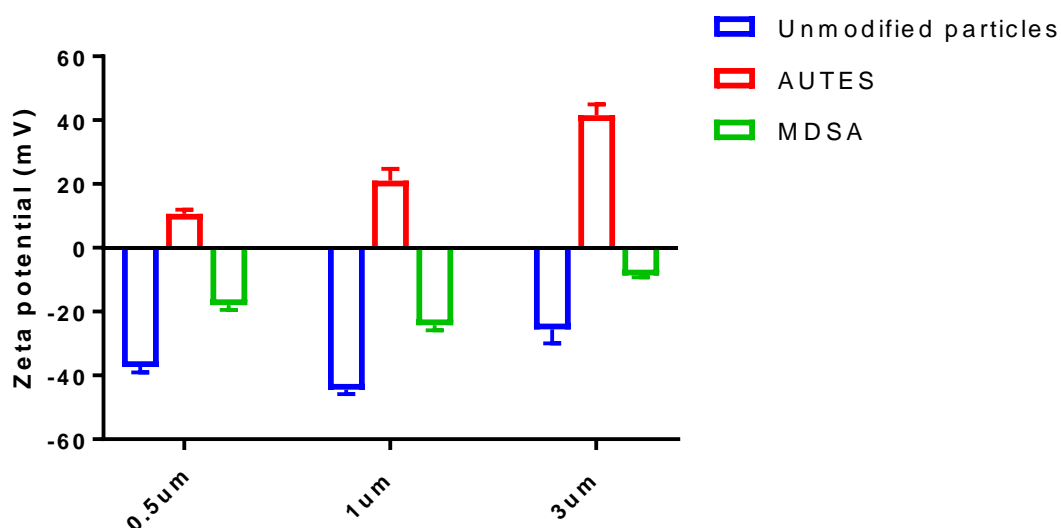


Figure 5.2: Zeta potential measurements of silicon oxide particles with different surface chemistry in 10mM NaCl. Unmodified particles (blue bars), AUTES-modified particles (red bars), MDSA-modified particles (green bars).

After modification with AUTES the zeta potential values were +10.6 mV (0.5 μm), +21.0 mV (1 μm), and +41.5 mV (3 μm) resulting from the primary amines on the particle surface ⁴¹⁰. In aqueous conditions, surface amines are protonated and so a net positive zeta potential results unless the pH is very high ⁴¹¹. Zeta potential values of similarly modified silicon oxide particles have been reported and range between +10 mV and +45 mV ⁴¹²⁻⁴¹⁶.

Upon modification with MDSA the zeta potential values were -17.9 mV (0.5 μm), -24.2 mV (1 μm), and -8.6 mV (3 μm). These results are in agreement with literature values for silicon oxide particles modified with sulfobetaine silanes. Knowles *et al.* reported zeta potential values between -25 mV and -40 mV ⁴¹⁷⁻⁴¹⁸. The results for MDSA particles were slightly less negative than these values, however this can be attributed to the presence of unreacted amines as indicated by the XPS data. Affonso de Oliveira *et al.* reported zeta potential of silicon oxide particles with both amino and sulfobetaine groups on their surface, similar to the particles used in this chapter ⁴¹⁹. They measured the zeta potential of particles with different ratios of amine to sulfobetaine and found that in the absence of sulfobetaine, particles had a positive zeta potential (+10 mV), however when the sulfobetaine was present (amine to sulfobetaine ratios of 3:1, 1:3, and 0:1) the zeta potential was negative (between -20 mV and -40 mV).

The above studies have examined zwitterionic monolayers on silica particles, however Dong *et al.* reported silica particles coated with an MDSA-based polymer which had a zeta potential value of -5mV ⁴²⁰. Other studies utilising the similar polymer coatings have reported zeta potential values of between -30mV and -50mV ⁴²¹⁻⁴²³.

The zeta potential measurements here concur with the XPS results for each step of the functionalisation procedure, however it can also give an indication of colloidal stability. Colloidal particles with zeta potential values of $\pm 0-10$, $\pm 10-20$, $\pm 20-30$, and ± 30 mV are unstable, relatively stable, moderately stable, and highly stable respectively ⁴²⁴. According to this, the majority of particles here fall into the relatively stable category, except for 3 μm MDSA particles which would be unstable. Nonetheless, other factors such as particle hydrophilicity play a role in colloidal stability, and it has been shown that zwitterionic particles with low zeta potential can be stable due to their high hydrophilicity ⁴²⁵⁻⁴²⁶.

5.3.1.3 Water contact angle θ ($^\circ$) measurements

Water contact angle measurements provide a measure of the hydrophilicity of the surface of the particle ⁴²⁷. This is therefore useful in indicating the effects that changes in the surface chemistry have and can be used to compare with values in the literature of particles with similar modifications.

Static water contact angles were measured for particles modified with AUTES and after modification with MDSA, the data is shown in figure 5.3. AUTES modified particles displayed a hydrophobic character in all particles sizes with 0.5 μm , 1 μm , and 3 μm particles displaying water contact angles of 53.9°, 56.2°, and 61.9° respectively. This is to be expected due to the length of the hydrocarbon chain ²⁹³.

After modification with MDSA the particles became more hydrophilic due to the presence of the zwitterion resulting in contact angles of 28.9°, 32.4°, and 22.8° respectively for 0.5 μm , 1 μm , and 3 μm particles. However, it was expected that contact angles for MDSA particles would be lower, as values for sulfobetaine-modified silicon oxide surfaces in the literature can be as low as $<10^\circ$ ⁴²⁸⁻⁴²⁹. The values here are likely higher because of the unreacted AUTES molecules which contribute some hydrophobicity. This is in agreement with the zeta potential measurements and XPS data.

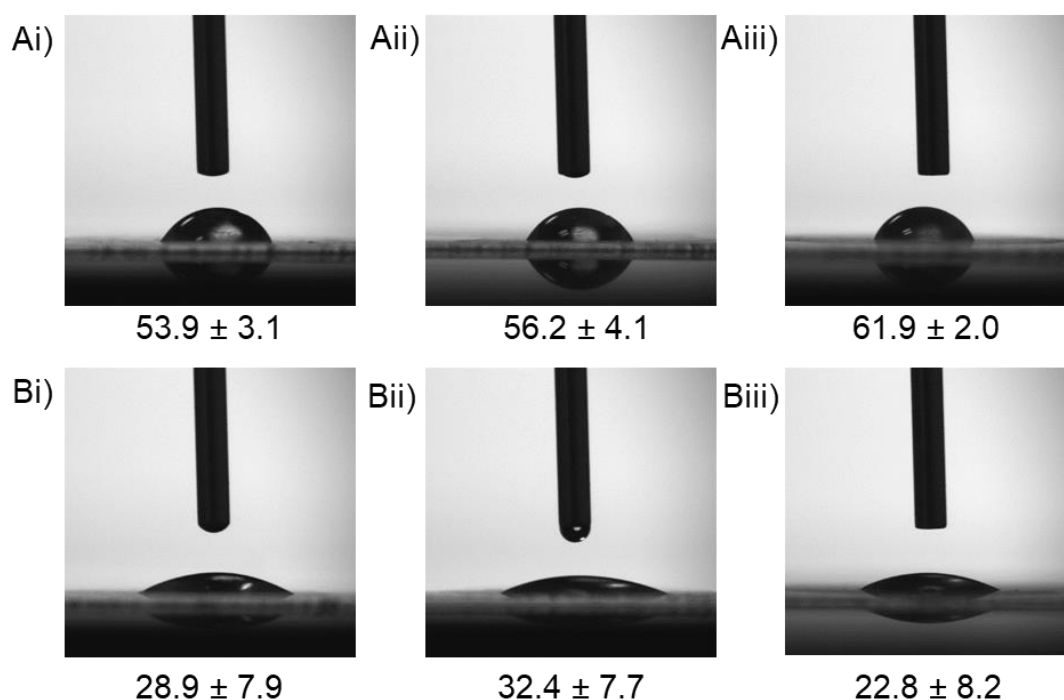


Figure 5.3: Water contact angle measurements of modified particles. A) *AUTES modified particles*, B) *MDSA modified particles*. i) 0.5 μm , ii) 1 μm , iii) 3 μm

5.3.1.4 Fluorescence of modified particles

Brightfield and fluorescence images were acquired of each particle size and representative images are shown in figure 5.4. Images were subsequently analysed using imageJ® to assess the fluorescence intensity values (approx. 100 particles analysed per sample) and are presented in table 5.2 along with a summary of water contact angle and zeta potential measurements. This confirmed fluorescent labelling of the particles and showed increasing particle fluorescence with increasing particle size.

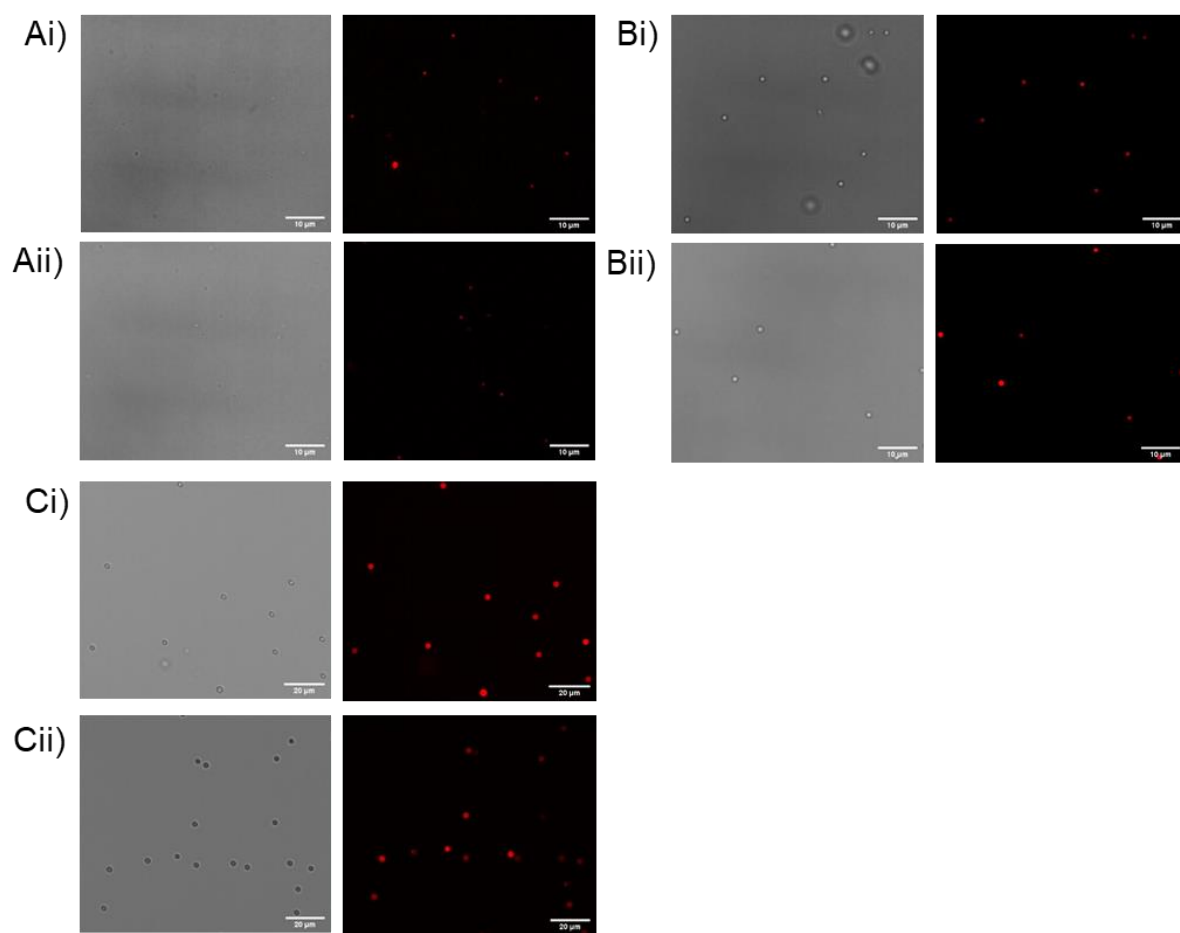


Figure 5.4: Representative brightfield and fluorescence images of silicon oxide particles. A) $0.5\mu\text{m}$ B) $1\mu\text{m}$ C) $3\mu\text{m}$, i) AUTES modified particles, ii) MDSA modified particles. Scale bars are $10\mu\text{m}$ for images A and B, and $20\mu\text{m}$ for images in C.

Table 5.2: Summary of particle characteristics

Particle size (μm)	Surface modification	Water contact angle ($^\circ$)	Zeta potential (mV)	MFI (a.u)
0.5	AUTES	53.9 ± 3	10.7 ± 1.3	257.6 ± 16
0.5	MDSA	28.9 ± 7	-17.9 ± 1.5	235.6 ± 10
1.0	AUTES	56.2 ± 4	21.0 ± 3.7	393.9 ± 59
1.0	MDSA	32.4 ± 7	-24.3 ± 1.6	328.9 ± 51
3.0	AUTES	61.9 ± 2	41.5 ± 3.4	1208.4 ± 279
3.0	MDSA	22.8 ± 8	-8.6 ± 0.6	864.1 ± 331

5.3.2 Uptake of silicon oxide particles by RAW 264.7 macrophages

Particle uptake was examined using imaging flow cytometry with particles being administered to cells based on equivalent mass, number, and surface area. Table 5.3 shows the applied doses and their equivalent doses by other metrics for comparative purposes, for example when an equivalent mass of particles (10 µg) was administered, this equates to 699, 87, and 3 particles per cell for 0.5, 1, and 3 µm particles respectively.

Table 5.3: Applied particle doses and equivalent doses by other metrics

Particle size (µm)	Dose Metric	Mass of particles applied (µg)	Number of particles applied per cell	Total surface area of applied particles (µm ²)
0.5	Mass	10.00	699	55244755
	Number	0.14	10	790000
	Surface area	1.81	127	10000000
1	Mass	10.00	87	2744755
	Number	1.14	10	3140000
	Surface area	3.64	32	10000000
3	Mass	10.00	3	9087694
	Number	31.10	10	28270000
	Surface area	9.98	3	10000000

5.3.2.1 Effect of particle size on uptake

Effect of particle size on the percentage of cells internalising particles

The data for particle uptake, as measured by the percentage of cells that internalised particles, is shown in figure 5.5. When administered according to equivalent mass of particles (figure 5.5 Ai), 0.5 µm and 1 µm particles showed significantly higher uptake than 3 µm particles. The number of 3 µm particles administered in this case (3.21×10^5) was significantly lower than the number of 0.5 µm particles (6.9×10^7) and 1 µm particles (8.7×10^6). It could therefore be

speculated that with an abundance of particles in the medium there was a higher probability of particles coming into contact with, and being internalised by the cells.

However, there was no significant difference between 0.5 μm and 1 μm particles with AUTES surface modification and in the case of particles coated with MDSA, a higher proportion of cells internalised 1 μm particles.

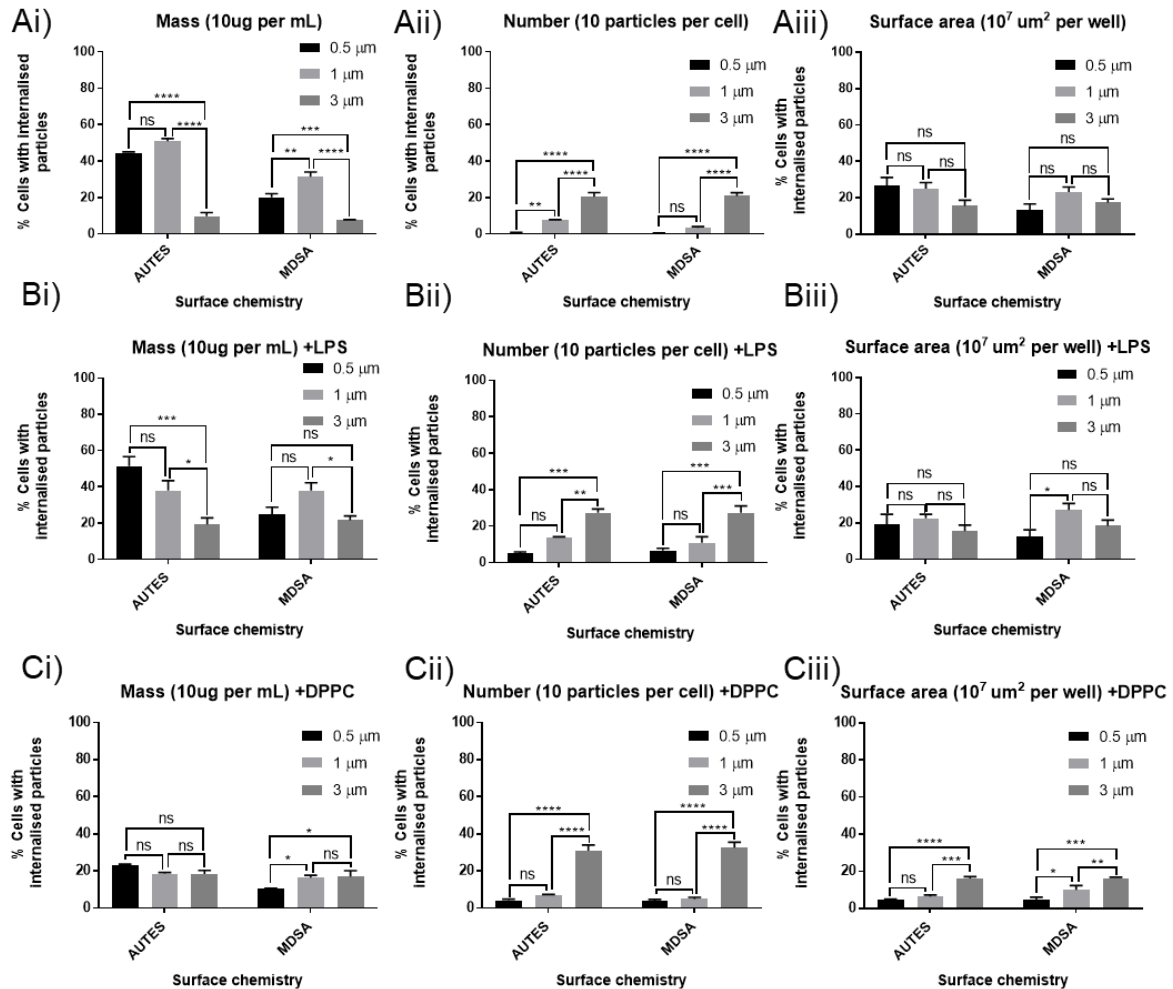


Figure 5.5: Effect of particle size on the percentage of cells with internalised particles. Particles were administered in A) 1% HEPES in HBSS buffer, B) 1% HEPES in HBSS buffer (cells were first stimulated with LPS), C) 1% HEPES in HBSS containing 250 $\mu\text{g}/\text{mL}$ DPPC. Particles were administered according to i) equivalent mass (10ug per well), ii) equivalent number (10^6 particles per well), iii) equivalent surface area ($10^7 \mu\text{m}^2$ per well). Data represent mean \pm SEM (N=3). *, **, ***, **** indicate statistical significance $p < 0.05$, 0.01, 0.001, 0.0001 respectively as calculated by 2 way ANOVA with Tukey's multiple comparisons test.

When particles were administered according to equivalent number (10 particles per cell) the opposite trend was observed, 3 μm particles were taken up by a higher proportion of cells (figure 5.5 Aii). With the same number of particles it would be expected that the cells would have an equal probability of interacting with the particles and therefore resulting differences in the proportion of cells taking up particles are due to differences in the capability of cells to internalise particles. This would indicate that RAW 264.7 macrophages are better able to phagocytose 3 μm particles than 0.5 μm and 1 μm particles. However, it was also considered that the rate of sedimentation of these particles would be different due to their difference in mass. This was examined by assessing the amount of time for each particle size to completely sediment in HBSS (1 mL). It was found that 3 μm particles underwent complete sedimentation within 2 hours, whereas 1 μm and 0.5 μm particles took 19 hours and 64 hours respectively. With 3 μm particles being the only particle size undergoing complete sedimentation within the time course of the experiment (4 hours) it is therefore likely that, as in the case of administration by mass, these results show that having a higher number of particles to interact with was the key driver of the percentage of cells that internalise particles.

In the case of administration by equivalent surface area (figure 5.5 Aiii) there were no significant differences observed between the different particle sizes. Given the higher numbers of 0.5 μm and 1 μm particles used in this experiment (1.27×10^7 and 3.18×10^6 respectively) sedimentation of particles is less likely to play a significant role. It is therefore interesting that despite there being far fewer 3 μm particles (3.5×10^5) available in the media for the cells to interact with, the percentage of cells internalising particles was not significantly less than for smaller particles. This could suggest that the RAW 264.7 macrophages were more able to bind and internalise 3 μm particles.

This data shows a clear relationship between the dose/dose metric used and the effect of particle size on the percentage of cells internalising particles. The highest particle uptake for each particle size was observed using the metric with the highest particle dose (by mass for 0.5 and 1 μm , by number for 3 μm) and the lowest uptake was observed using the metric that

had the lowest particle dose (by number for 0.5 and 1 μm , by mass for 3 μm). In summary, these data showed that comparison of uptake between different particle sizes, using the percentage of cells internalizing particles as a measure, gives different results depending on the dose metric used. Moreover, it is further complicated by differences in sedimentation rate of different size particles. The administration of particles by equivalent surface area resulted in similar levels of uptake across particle sizes and therefore this dose metric may be most appropriate for comparing other effects (e.g. effects of surface chemistry) across different particle sizes.

Upon stimulation with LPS the effect of particle size followed the same pattern as in unstimulated cells (figure 5.5 Bi-iii). This suggests that there is no change in the proportion of macrophages that undergo phagocytosis upon stimulation with LPS. This is in line with published studies which have shown an equivalent ability of macrophages to engulf microparticles regardless of activation state⁴³⁰. It does not rule out that activated macrophages may be internalising more particles however, this is discussed later on.

Particles were administered in the presence of 250 $\mu\text{g/mL}$ DPPC as a simple model to better simulate the environment in the alveoli where pulmonary surfactant is present (figure 5.5 Ci-iii)⁴³¹⁻⁴³². When particles were administered in the presence of DPPC according to equivalent particle mass, there were no significant differences in the number of cells internalising particles for AUTES modified particles and in the case of MDSA modified particles there was more uptake of 1 μm and 3 μm particles than 0.5 μm particles (figure 5.5Ci).

When administered by particle number, the results were consistent with those seen upon administration without DPPC (figure 5.5Cii). 3 μm particles were taken up by a higher percentage of cells than 0.5 μm and 1 μm particles. As previously mentioned, it is likely that sedimentation of particles is the most important factor in determining the percentage of cells taking up particles in this case.

In contrast, particles administered by equivalent surface area showed different results to those administered without DPPC. 3 μm particles were taken up by a higher percentage of cells than both 0.5 μm and 1 μm particles and in the case of MDSA modified particles, 1 μm particles were taken up by a higher percentage of cells than 0.5 μm particles.

Figure 5.6 compares the percentage of cells internalising particles with and without DPPC. For particles administered according to equivalent mass and surface area there is a large reduction in the percentage of cells internalising 0.5 μm and 1 μm particles, however the percentage of cells internalising 3 μm particles increases when administered by equivalent mass and remains the same when administered by equivalent surface area (figure 5.6Ai/ Bi, Aiii/Biii). This result is in agreement with a study published by Vranic *et al.* who studied the uptake of 50 nm and 100 nm silicon oxide particles by murine alveolar macrophages in the presence of lung surfactant substitute Curosurf[®] 433. The reduction in particle uptake was attributed to the reduction in sedimentation of particles due to the presence of lung surfactant, which lead to less interaction of particles with the macrophages. This explanation could account for the results seen in this study for 0.5 μm and 1 μm particles, however 3 μm particles were seemingly unaffected by this due to their mass and even showed a slightly increased percentage of cells internalising particles in some cases.

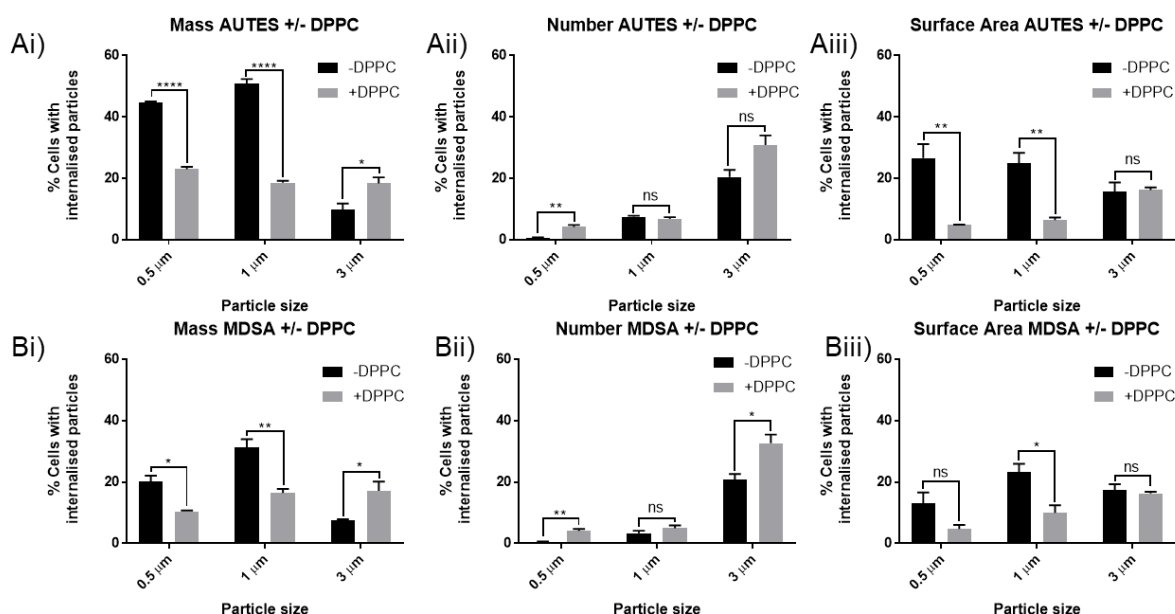


Figure 5.6: Effect of DPPC on the % of cells with internalised particles. A) AUTES-modified particles B) MDSA-modified particles. Particles were administered according to i) equivalent mass (10ug per well), ii) equivalent number (10^6 particles per well), iii) equivalent surface area ($10^7 \mu m^2$ per well). Data represent mean \pm SEM (N=3). *, **, ***, **** indicate statistical significance $p < 0.05$, 0.01, 0.001, 0.0001 respectively as calculated by multiple unpaired T-tests.

Effect of particle size on the number of particles internalised

The second measure of particle uptake used is the number of particles internalised per cell. Here the number of particles internalised per cell has been calculated only for cells that were identified as having internalised particles by the analysis software and as such is independent of the percentage of cells taking up particles. The data is presented in figure 5.7.

When administered by equivalent particle mass (figure 5.7 Ai) the data shows that 4-6 particles were internalised per cell for both 0.5 μm and 1 μm particles whereas for 3 μm particles 1-2 particles was internalised on average. On the other hand, when particles were administered according to equivalent particle number, 3-4 particles were internalised for 0.5 μm and 1 μm particles and 1-2 particles were internalised for 3 μm particles. Upon administration by equivalent particle surface area 2-3 particles per cell was internalised for 0.5 μm and 1 μm

particles and 1-2 particles were internalised for 3 μm particles. Therefore, the number of particles internalised per cell seems to be less sensitive to changes in dose/dose metric than the percentage of cells internalising particles.

Upon stimulation with LPS (Figure 5.7B) the results were similar to unstimulated cells. It would be expected that, after LPS stimulation, the cells would alter receptor density on the plasma membrane. Receptors such as TLR-2/4 are upregulated whereas a decrease in the expression of scavenger receptors is seen⁷⁰. Silicon oxide particles with amines present on their surface are thought to be internalised by scavenger receptors⁴³⁴, and so it is expected that a reduction in the number of particles per cell would be observed. However, this was not the case, possibly because the number of internalised particles per cell was fairly low even in the absence of LPS stimulation. Similarly the number of particles taken up when administered in the presence of DPPC did not change drastically, suggesting there is no change in the behaviour of the cells under these conditions.

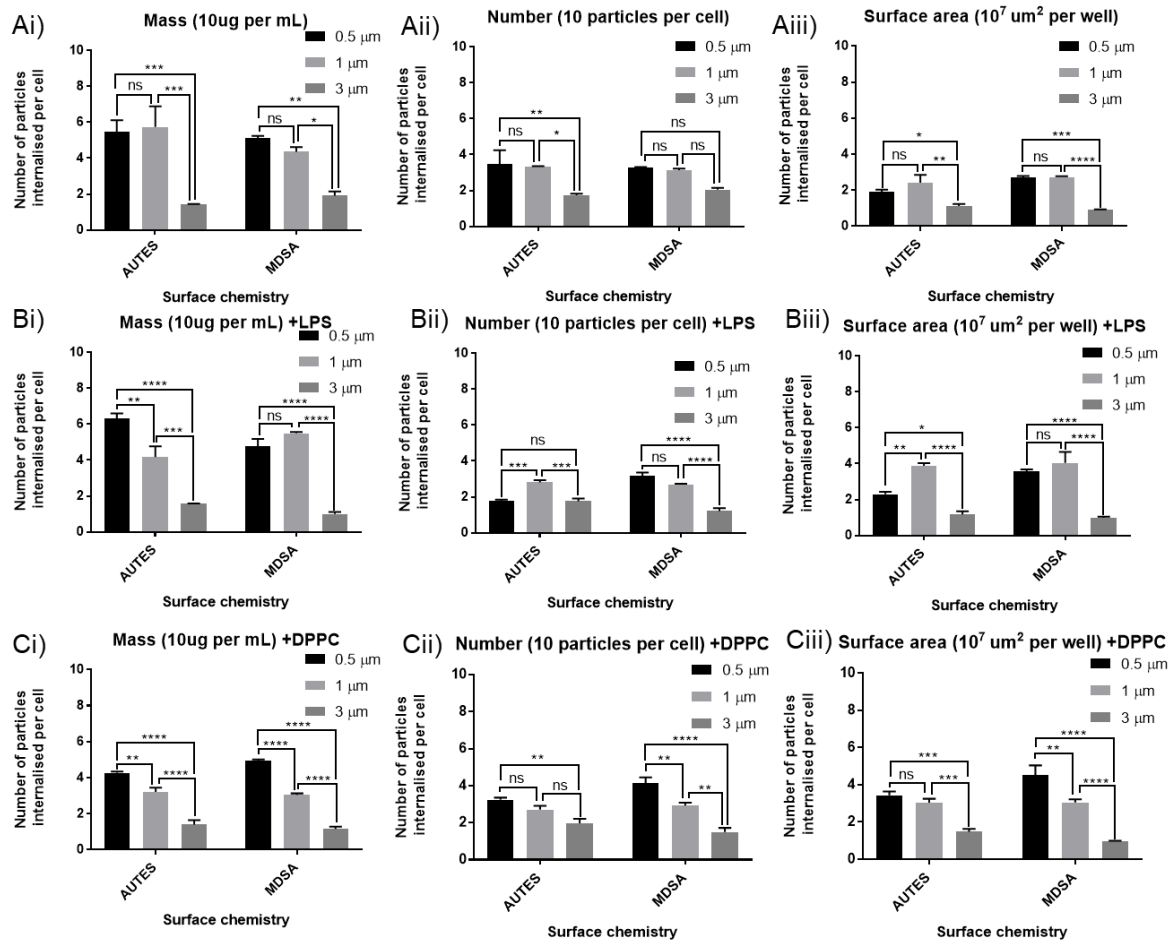


Figure 5.7: Effect of particle size on the number of internalised particles per cell that internalised particles. Particles were administered in A) 1% HEPES in HBSS buffer, B) 1% HEPES in HBSS buffer (cells were first stimulated with LPS), C) 1% HEPES in HBSS containing 250 μg/mL DPPC. Particles were administered according to i) equivalent mass (10 μg per well), ii) equivalent number (10⁶ particles per well), iii) equivalent surface area (10⁷ μm² per well). Data represent mean ± SEM (N=3). *, **, ***, **** indicate statistical significance $p < 0.05$, 0.01, 0.001, 0.0001 respectively as calculated by 2 way ANOVA with Tukey's multiple comparisons test.

Considering these data together, the number of particles internalised per cell taking up particles did not fluctuate a great deal. Only in the presence of a large excess of particles per cell did an increase occur, however in real terms this was only a difference of 1-2 particles per

cell when the number of particles administered per cell was 699.3 and 87.4 for 0.5 μm and 1 μm particles respectively.

From a drug delivery perspective, the mass of particles taken up by each cell is relevant if the majority of the particle mass is comprised of the therapeutic molecule. Given the mass of the particles increases by a factor of n^3 when the particle diameter is increased, the differences in particle size result in large differences in the mass of particles internalised. The mass of one 3 μm particle is equivalent to the mass of twenty seven 1 μm particles and two hundred and sixteen 0.5 μm particles. These results therefore show that in terms of mass, in all cases 3 μm particles were taken up most efficiently.

On the other hand, if the therapeutic molecule does not make up the majority of particle mass but is instead attached to the surface of a carrier particle, the surface area of particles internalised is relevant. The surface area of spherical particles increases by a factor of n^2 when the particle diameter is increased. The surface area of one x 3 μm particle is equivalent to nine 1 μm particles and thirty six 0.5 μm particles. This implies that, in terms of surface area, 3 μm particles were taken up most efficiently. However, this would not apply to porous particles which would have a much higher surface area than a non-porous particle of equivalent size.

Effect of particle size on percentage of dose taken up by cells

Considering the internalisation of particles in terms of the percentage of dose taken up by the cells is useful to understand what particle size is taken up most efficiently as it combines both the percentage of cells internalising particles and the number of particles taken up per cell. These values are presented in figure 5.8. Across each of the conditions tested, the results were mostly consistent. The highest percentage of dose taken up was in the case of 3 μm particles followed by 1 μm and 0.5 μm particles. Similarly to these results, Khanbeigi *et al.* examined the delivered dose of different sized (diameter 0.05, 0.1, 0.2, 0.7, 1 μm) polystyrene particles to J774A.1 macrophages and found 1 μm particles exhibited the most efficient delivery ⁴³⁵. The effect of particle sedimentation was also considered to be a contributing factor, with larger particles exhibiting more sedimentation. It seems therefore, that larger

particles are more efficiently delivered to macrophages in part due to their higher sedimentation, however, this effect will reach a limit at 2-3 μm above which macrophages are less able to internalise particles ¹⁰³.

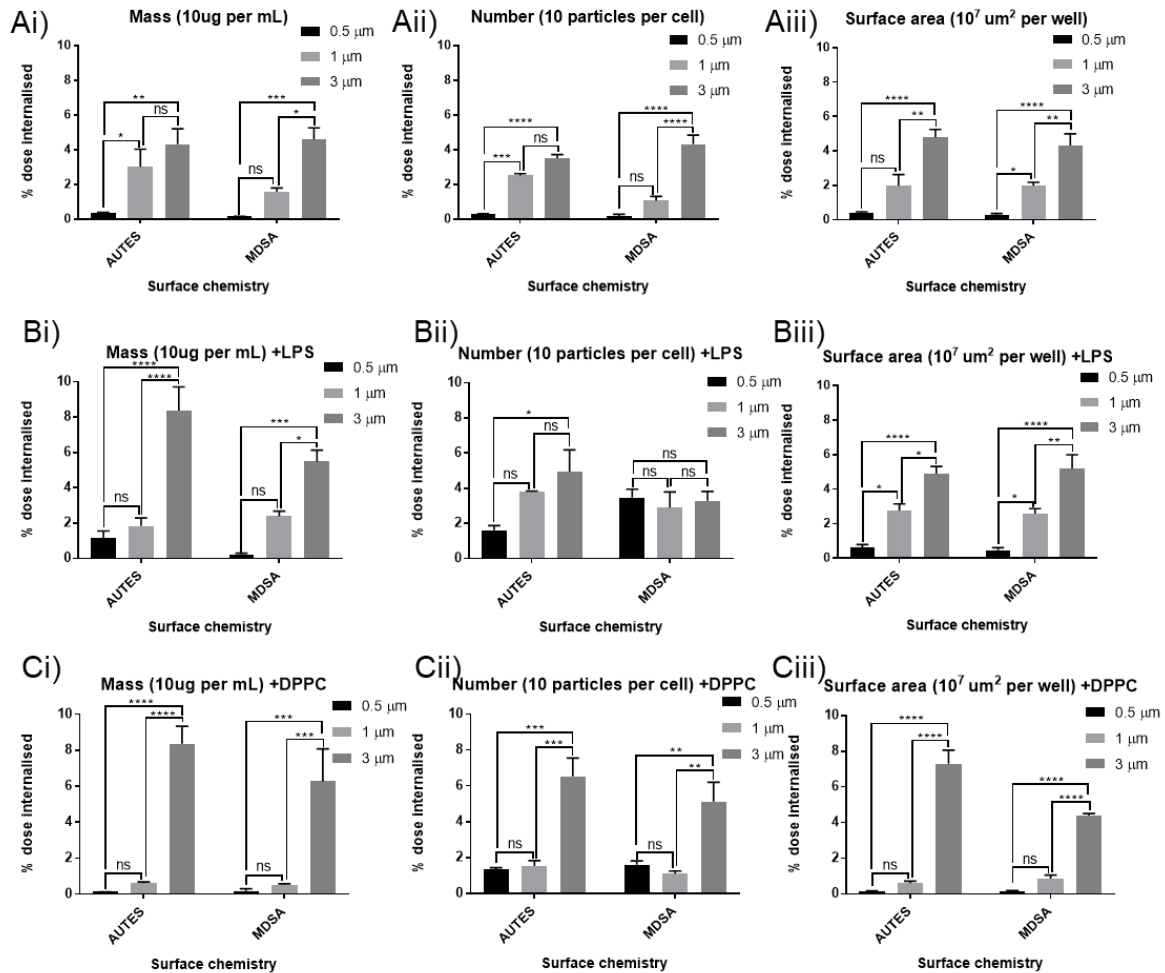


Figure 5.8: Effect of particle size on the % dose internalised. Particles were administered in A) 1% HEPES in HBSS buffer, B) 1% HEPES in HBSS buffer (cells were first stimulated with LPS), C) 1% HEPES in HBSS containing 250 $\mu\text{g/mL}$ DPPC. Particles were administered according to i) equivalent mass (10ug per well), ii) equivalent number (10^6 particles per well), iii) equivalent surface area ($10^7 \mu\text{m}^2$ per well). Data represent mean \pm SEM (N=3). *, **, ***, **** indicate statistical significance $p < 0.05, 0.01, 0.001, 0.0001$ respectively as calculated by 2 way ANOVA with Tukey's multiple comparisons test.

5.3.2.2 Effect of zwitterion surface chemistry on particle uptake

Effect of zwitterion surface chemistry on percentage of cells internalising particles

The data for the percentage of cells internalising particles is shown in figure 5.9. For all particle sizes, the percentage of cells internalising particles showed a clear dependence on the dose applied. In the case of 0.5 μm particles (figure 5.9 Ai) it was only at the highest concentration (10 μg , 699 particles per cell) that there was a difference in uptake between the two surface chemistries, whereby MDSA modified particles were internalised by ~50 % fewer cells. This was also the case when administered to LPS activated cells (figure 5.9 Bi) and in the presence of DPPC (figure 5.9 Ci).

For 1 μm particles (figure 5.9 Bi), as in the case of 0.5 μm particles, there was a significant difference between uptake of the two particle surface chemistries at the highest dose (10 μg , 87 particles per cell). However, there was also a difference seen at the lowest dose (1.14 μg , 10 particles per cell). In contrast, there was no difference in uptake between the two surface chemistries at any particle dose when administered to LPS activated cells (figure 5.9 Bii) or in the presence of DPPC (figure 5.9 Cii).

In the case of 3 μm particles (figure 5.9 Ci-iii) there were no differences seen in uptake between the two surface chemistries at either dose (10 μg , 3.21 particles per cell or 31.1 μg , 10 particles per cell). This result was consistent across all the conditions tested.

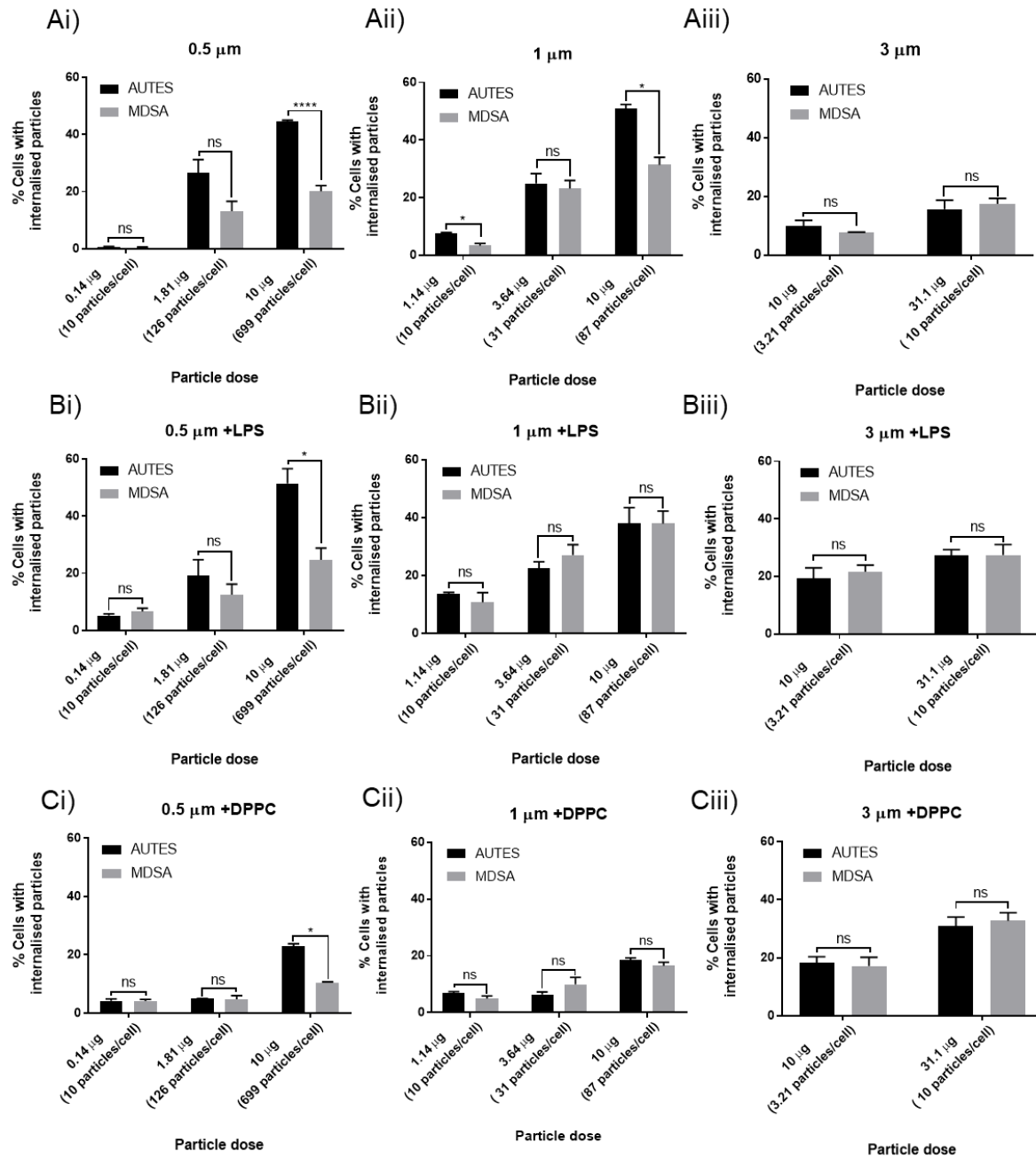


Figure 5.9: Effect of zwitterion surface chemistry on the % of cells with internalised particles. Particles were administered in A) 1% HEPES in HBSS buffer, B) 1% HEPES in HBSS buffer (cells were first stimulated with LPS), C) 1% HEPES in HBSS containing 250 µg/mL DPPC. i) 0.5 µm ii) 1 µm iii) 3 µm. Data represent mean ± SEM (N=3). *, **, ***, **** indicate statistical significance $p < 0.05$, 0.01, 0.001, 0.0001 respectively as calculated by multiple unpaired T-tests.

In section 5.3.1, it was demonstrated that MDSA modified particles had a hydrophilic surface and negative zeta potential in comparison with AUTES modified particles which had a more hydrophobic surface with a positive zeta potential. As such, it would be expected that differences in particle uptake would be observed^{108, 436}. However, this was only observed in a few cases, and only in 0.5 μm and 1 μm particles. In a recent study that looked at the effect of PEGylation of polystyrene particles of different sizes, it was shown that PEGylation only reduced the uptake of particles in particles $<0.5 \mu\text{m}$ and that the effect of PEGylation decreased with increasing particle size. Particles of 2.6 μm showed no difference in internalisation despite having the same surface charge and density of PEG molecules on the surface as smaller particles⁴³⁷. The results presented here are consistent with this finding, but also suggests that a high dose of particles might be necessary to see these effects. On the other hand, PEGylation of PLGA microparticles (diameter 5 μm) has been shown to reduce macrophage uptake,⁴³⁸ which indicates that a reduction in uptake as a result of surface chemistry modifications can take place in larger particles.

In the presence of DPPC, it is expected that adsorption of DPPC could take place onto the particle surface and thereby the underlying surface chemistry is masked by the cells⁴³⁹. Despite this however, a reduction in uptake of MDSA modified particles was seen for 0.5 μm particles at the highest dose (10 μg , 699 particles per cell), however, in all other cases there was no difference in uptake between the two surface chemistries.

Effect of zwitterion surface chemistry on number of particles internalised

Data in figure 5.10 shows the effect of zwitterion surface chemistry on the number of particles internalised per cell that internalised particles. For 0.5 μm and 1 μm particles the number of

particles internalised increased with the highest particle dose (figure 5.10 Ai/Aii). However, this was not the case for 3 μm particles (figure 5.10 Aiii).

MDSA surface chemistry had very little effect on the number of particles internalised in each case. Although in the case of 0.5 μm particles, a slight increase was observed for lower doses in cells stimulated by LPS, this effect is small (figure 5.10 Bi).

Previous studies looking at the effect of zwitterionic surface chemistries on uptake by macrophages have mostly used comparisons of median fluorescence intensity (MFI) as a measure of uptake^{391-392, 440}. This is influenced both by the number of particles per cell, and the percentage of cells taking up particles and so it is difficult to compare these data. It is not clear if reductions in uptake of zwitterion modified particles in the literature result from fewer cells internalising particles, individual cells internalising fewer particles, or both.

It is thought that a reduction of recognition of zwitterionic particles by macrophages could stem from their hydrophilicity which influences the interaction with proteins in the biological milieu⁴⁴¹. As the present work did not include protein in the media, this potentially explains the reason for the lack of difference in uptake.

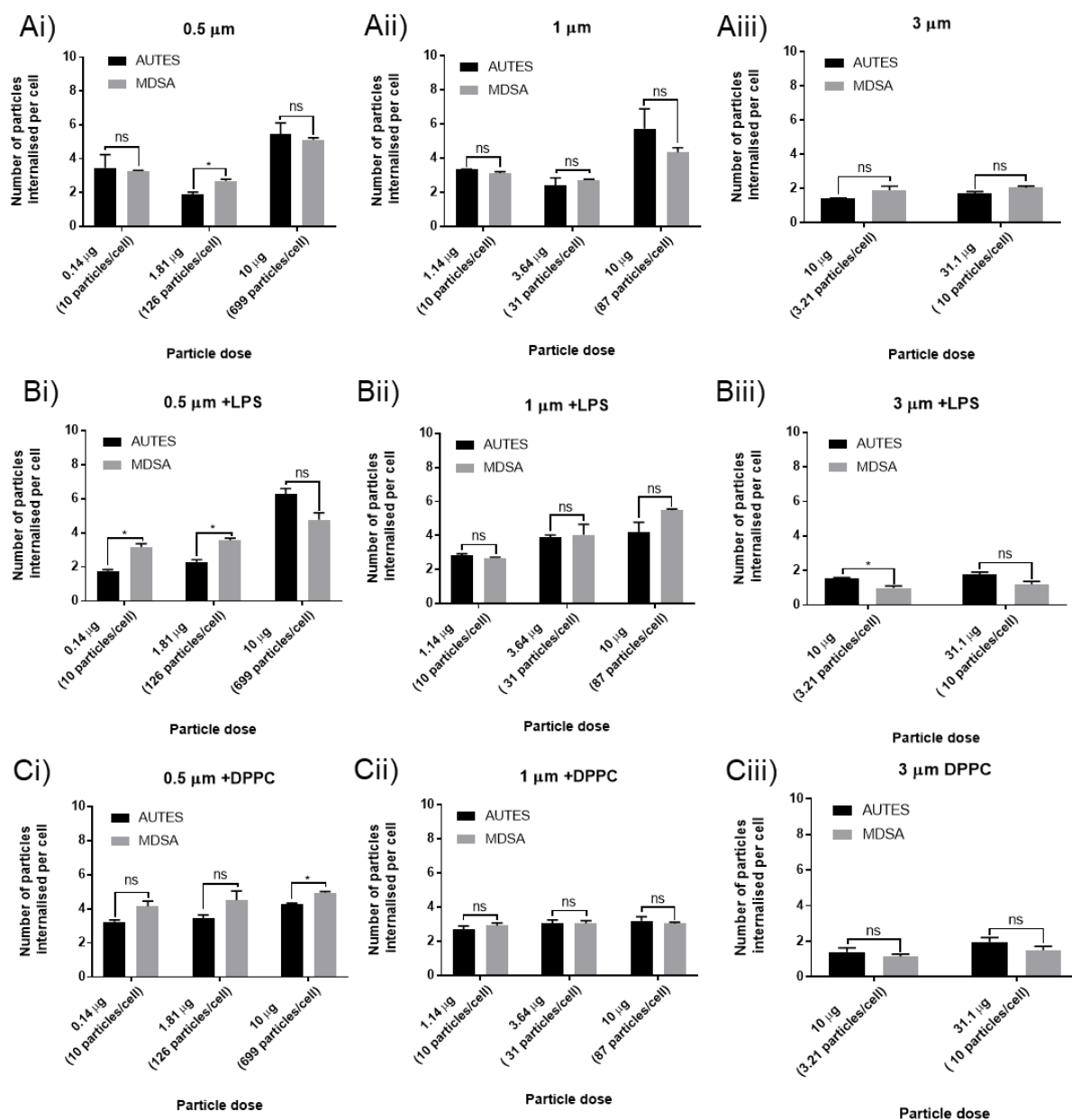


Figure 5.10: Effect of zwitterion surface chemistry on the number of internalised particles per cell that internalised particles. Particles were administered in A) 1% HEPES in HBSS buffer, B) 1% HEPES in HBSS buffer (cells were first stimulated with LPS), C) 1% HEPES in HBSS containing 250 µg/mL DPPC. i) 0.5 µm ii) 1 µm iii) 3 µm. Data represent mean \pm SEM (N=3). *, **, ***, **** indicate statistical significance $p < 0.05$, 0.01, 0.001, 0.0001 respectively as calculated by multiple unpaired T-tests.

In the previous section it was shown that in some cases, zwitterion modified particles showed reduced uptake compared with AUTES modified particles. This did not translate to fewer particles being internalised per cell which suggests that a smaller proportion of cells was able to bind and internalise particles, but the cells that came into contact with MDSA particles did so to the same extent as cells that came into contact with AUTES modified particles.

Effect of zwitterion surface chemistry on the percentage dose internalised

The data for percentage dose internalised is shown in figure 5.11 and shows very little effect of surface modification on the percentage dose internalised in all cases. This is reflective of the lack difference in uptake seen between the two surface chemistries as measured by percentage of cells internalising particles and the number of particles internalised per cell. This data shows that the zwitterionic surface chemistry used here is not effective in modulating particle uptake. As mentioned previously this may result from the size of these particles being large enough so that the effect of surface chemistry on uptake is negligible or alternatively, the lack of protein in the media.

A third explanation could be, as the characterisation of the particles showed, unreacted amines are present on the surface of MDSA-modified particles which could be triggering internalisation by macrophages ⁴³⁴. Although particles were more hydrophilic and showed a negative zeta potential, the amine groups may still be able to interact with the scavenger receptors and thus facilitate particle internalisation. More studies are needed, whereby the amines are blocked to confirm this.

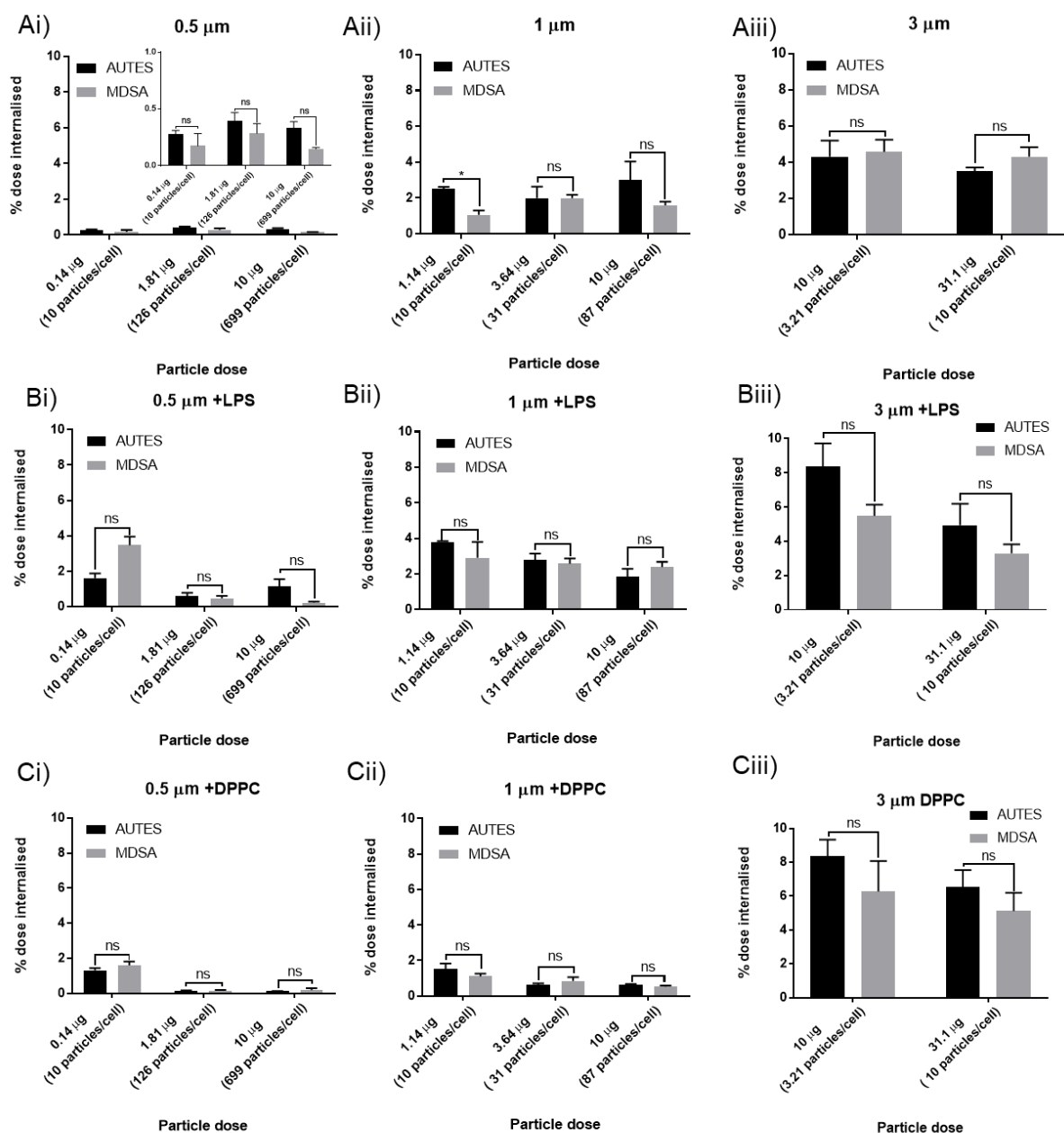


Figure 5.11: Effect of zwitterion surface chemistry on the % dose internalised. Particles were administered in A) 1% HEPES in HBSS buffer, B) 1% HEPES in HBSS buffer (cells were first stimulated with LPS), C) 1% HEPES in HBSS containing 250 µg/mL DPPC. i) 0.5 µm ii) 1 µm iii) 3 µm. Data represent mean ± SEM (N=3). *, **, ***, **** indicate statistical significance $p < 0.05$, 0.01, 0.001, 0.0001 respectively as calculated by multiple T-tests.

5.4 Conclusions

The work described in this chapter has examined the effect of particle size and zwitterionic surface chemistry on particle uptake by macrophages. Three measures of particle uptake were used, percentage of cells internalising particles, the number of particles per cell, and percentage of dose internalised. Also studied, was the impact of the dose metric used when comparing particles of different sizes.

By examining the percentage of cells internalising particles, it was clear that this measure of uptake was heavily influenced by the particle dose. For all particle sizes, the more particles that were present in the medium, the higher the probability of an interaction with a cell, which leads to a higher probability of uptake. In this regard, considering a scenario in which macrophage uptake is to be desired, it would be advantageous to make use of a larger number of smaller particles. This would allow for an equivalent mass of drug to be administered and result in more interactions with macrophages and therefore more uptake. However, in the presence of DPPC, likely due to a lack of sedimentation, the percentage of cells internalising 0.5 μm and 1 μm particles reduces to the point where larger particles are more likely to come into contact with cells and be taken up. Therefore, where lung surfactant is present, it may be beneficial to use larger particles to increase sedimentation and macrophage uptake.

The number of particles internalised per cell was less sensitive to changes in dose compared with percentage of cells internalising particles. As a measure, it is most relevant when considering the particle mass and surface area that each cell takes up. The data showed that more particle mass and surface area is taken up per cell when larger particles are administered. Therefore, where the highest particle dose per cell is required it is advantageous to use larger particles.

The percentage of dose internalised combines the above two measures and considers the efficiency of uptake overall. This data showed that if particle uptake by macrophages is desired, 3 μm particles were most efficient as the highest percentage of dose was internalised. 0.5 μm and 1 μm particles were taken up least efficiently and so, for avoidance of uptake, would be advantageous over 3 μm particles.

Comparing the effect of zwitterionic surface chemistry, it was demonstrated that this had far less significant effect on particle uptake across all three measures than particle size. For 3 μm particles there was virtually no difference in uptake between zwitterionic and positively charged particles. For 0.5 μm and 1 μm particles a reduction in particle uptake was observed in a few circumstances but this effect was not seen consistently. Further study is needed to ascertain the reasons for the lack of difference in particle uptake between the two surface chemistries, however, from this study, it can be concluded that altering particle size was a more effective method of modulating particle uptake than using this zwitterionic surface chemistry.

6. General discussion and Future work

This project sought to investigate the effect of several key particle properties on interaction with macrophages with a particular emphasis on the role of particle shape. Polysilicon and silicon oxide microparticles were selected for this work owing to a collaboration with the CNM who have expertise in fabricating highly uniform populations of microparticles of different morphologies. In addition, silicon-based particles have been widely explored for their use in drug delivery ⁴⁴², with drug molecules either being physically entrapped or covalently bound through modification of particle surface chemistry. This meant that, as well as being a model particle, there exists potential for real-world applications of these particles for drug delivery to the lung.

Particle uptake by the RES, in particular macrophages, is thought to be one of the main challenges to particulate delivery for both systemic and pulmonary routes of administration ⁴⁴³. On the other hand, targeting of macrophages is particularly desirable in certain disease states, for example in the case of infection, where infected macrophages serve as a reservoir for microorganisms leading to persistent reinfection ⁴⁴⁴⁻⁴⁴⁶. Therefore an *in vitro* macrophage cell line, RAW 264.7, which has been used as a model for alveolar macrophages was chosen ⁴⁴⁷⁻⁴⁴⁹. The RAW 264.7 cell line is derived from BALB/c mice and has been used as a macrophage model owing to their ability to perform phagocytosis and to undergo phenotypic changes in response to LPS stimulation e.g. increased nitric oxide production ²⁶¹. Indeed, RAW 264.7 cells have been used by a number of groups to study the uptake of different particle shapes and accordingly have shown to be sensitive to different particle shapes ^{237, 242, 450}.

Particular attention was paid to ensuring that particle uptake was measured, rather than cellular association. Imaging flow cytometry was used for this purpose and, as it is a relatively new technique, this was compared with a well-established method that uses trypan blue to quench extracellular fluorescence ^{298, 451-455} in chapter 3. The two methods yielded comparable

results which confirmed the suitability of imaging flow cytometry for the project. This method offers advantages over traditional quenching methods, which require specific fluorescent molecules and their quenchers limiting options for choosing fluorophores and also requires the quencher to be in close proximity to the fluorophore making it tough to achieve efficient quenching with encapsulated dyes. Moreover, in the course of this work it was found that fixed samples (with 4% formaldehyde or 4% paraformaldehyde) became permeable to trypan blue and so the quenching method could only be performed on live cells.

In chapter 3 the functionalisation of silicon oxide particles with an imidazolium surfactant (1.2Br) in order to enable labelling with porphyrins (TCPP and ATPP) was explored. Although the presence of the surfactant did enable the immobilisation of ATPP onto the particle surface, the retention of ATPP on the particle in PBS was inferior to conjugation of RBITC using covalent silane linker AUTES. The release of dye molecule into PBS meant that this non-covalent labelling method was not suitable for cellular uptake work however, there is potential to explore this method to enable the binding and release of drug molecules. For example, Lu *et al.* immobilised the anti-cancer drug camptothecin onto the surface of mesoporous silica nanoparticles using hydrophobic interactions ⁴⁵⁶. On the other hand, electrostatic interactions have been used to enhance the loading of curcumin on to iron oxide nanoparticles ⁴⁵⁷. The use of imidazolium surfactant molecules such as 1.2Br offers the opportunity for both electrostatic and hydrophobic interactions with drug molecules and has recently been explored by our group for the immobilization of piroxicam on gold nanoparticles ⁴⁵⁸.

It was originally thought that the method that was chosen to label silicon oxide particles using the aminosilane AUTES in chapter 3 could be used to label the polysilicon particles used in chapter 4, however this was not found to be the case. It seemed from the results that, with further optimisation, an improvement in the uniformity of particle functionalisation could be achieved for use in other studies. The surface modification of polysilicon with silane linkers has been shown to take place on polysilicon surfaces ⁴⁵⁹, however vertical polycondensation of hydrolysed silanes and deposition of silane aggregates owing to the presence of water can

occur ⁴⁶⁰⁻⁴⁶². Left over water from the activation steps could therefore be the reason for the uneven labelling observed when acetone and toluene were used as solvents and thus a step for removal of left over water from the samples could be implemented to improve uniformity of labelling. The reason why labelling occurred in silicon oxide particles using ethanol as the solvent but not in polysilicon particles is not clear and further investigation is required to ascertain why.

The effect of particle shape on uptake by macrophages was studied in chapters 3 and 4 in terms of percentage of cells taking up particles and the number of particles internalised per cell. The results of both of these chapters suggested that, for the most part, particle shape had an effect on cellular uptake as determined by percentage of cells taking up particles but no effect on the number of particles internalised per cell.

In chapter 3, the uptake of truncated pyramids was reduced in comparison to spherical particles. When the particles first come into contact with the cell, spherical particles are unique in the fact that, regardless of orientation, the presentation of the particle to the cell is the same. In the case of hexahedrons and truncated pyramids, the particles can come into contact with the cell with different sides or at corners which, according to Champion and Mitragotri, will in turn affect whether or not particle internalization occurs ²⁴⁰. In this thesis, individual particle-cell interactions were not studied and so it is not known if a particular orientation dominated for each particle type but it could suggest that truncated pyramids present to cells in a way that is less favourable for uptake.

Actin remodelling is required to cause extension of the plasma membrane in order for particle internalisation to occur ³¹¹. It has been suggested that shapes that require more actin remodelling will require more time and energy for internalisation to occur ²⁴². Therefore, another potential explanation for the lower internalisation of truncated pyramids relative to spheres is that actin remodelling to accommodate truncated pyramids is less efficient and so results in less particle uptake overall. On the other hand, hexahedrons were internalised to

the same extent as spheres which could suggest a similar level of actin modelling is required for internalisation.

A wider range of particle shapes was studied in chapter 4 including hexahedrons, cubes, bars, and circular disks each with one dimension 3 μm in length. Considering their internalisation in terms of actin rearrangement, large bar-shaped particles (length 10 and 15 μm) would require extensively more actin rearrangement than smaller hexahedrons. This is reflected in the internalisation data for these shapes, however, the internalisation of circular disks (diameter 3 μm) was similar to that of bar-shaped particles but would be expected to require similar actin rearrangement to hexahedrons and so differences in actin rearrangement can only partially explain differences between shapes. The effect of particle high local curvature at the contact point between particle and cell has been suggested to result in more efficient phagocytosis⁴⁶³⁻⁴⁶⁴. This could therefore suggest that the high curvature of the corners of hexahedral particles is sufficient to increase their uptake with respect to circular disks. Further work examining these effects over a wider range of doses, longer periods of time and including the study of individual particle:cell interactions, for example by visualising actin rearrangement during uptake, would be beneficial to more fully elucidate the cause of these shape effects.

Published studies examining the effect of microparticle shape on uptake have described differences in internalisation rate and the ability of cells to attach and take up microparticles^{240, 465}. However, the results of these studies that examined individual microparticle-cell interactions, did not necessarily translate to significant differences in overall microparticle uptake when methods such as flow cytometry were used²⁴²⁻²⁴³. According to the results in chapters 3 and 4, microparticle shape did have an effect on overall cellular uptake.

Although differences in the uptake of different shapes were observed, the significance of these results as they pertain to realistic *in vivo* scenarios is difficult to examine. For example, in chapter 3 the truncated pyramids showed ~30-40% reduction in cellular uptake in comparison to spheres with a similar volume. From a theoretical perspective, this reduction in uptake could be particularly advantageous, allowing for a longer residence time in the body for drug release

to occur, and thus reducing dosing frequency. However, further *in vitro* studies should include the effect of microparticle shapes on cytokine production to gauge the effect on inflammatory response. For example, if reduced uptake results from a lower ability to internalise a particle as a result of its shape, it is possible that this will cause frustrated phagocytosis and downstream toxicity resulting from the production of inflammatory mediators such as TNF- α ⁴⁶⁶⁻⁴⁶⁷. In chapter 4 the effect of microparticle shape on metabolic activity, LDH release, and glucuronidase release showed no differences between shapes and suggests that frustrated phagocytosis did not occur. Further work assessing the effect of particle shape on TNF- α , IL-10, and ROS and NOS generation as well as increasing the amount of time cells are exposed to particles would build on this work to confirm if differences in uptake of different particle shapes cause downstream effects which would limit their usefulness in drug delivery.

In chapter 5 the uptake of different sized silicon oxide spheres (diameter 0.5, 1, 3 μm) showed a large dependence on the dose and the dose metric used and agreed with the findings of published studies showing that more cells take up larger particles (3 μm) than smaller particles (0.5, 1 μm) when equivalent particle numbers are administered^{103, 105, 468}. However, because 0.5 and 1 μm diameter particles do not sediment at the same rate as 3 μm particles it was not clear if this is the cause of differences in uptake or if differences in the macrophages ability to phagocytose particles of different sizes is responsible. Champion *et al.* explained the phenomenon of particle internalisation being most efficient for particles with a diameter 2.8 μm in terms of the measured distance between membrane ruffles (1.9 μm)¹⁰⁶. Particles with diameters smaller than this will be able to fit in-between ruffles without contact and this makes their internalisation less likely, while particles with diameters larger than this will make contact with multiple ruffles and are therefore more likely to be internalised. However, in contrast to this, the number of particles internalised per cell when administered at equivalent particle numbers was higher for smaller particles (0.5 and 1 μm).

When particles were administered according to equivalent mass, both a higher percentage of cells taking up particles and a higher number of particles per cell was observed for 0.5 and 1

μm particles than for 3 μm particles. This is reflective of the abundance of 0.5 and 1 μm particles in the media and demonstrates that the probability of particle internalisation is increased when more particles are in the media for the cells to come into contact with.

Administering particles by equivalent surface area showed that similar numbers of cells internalised particles for each particle type and is therefore perhaps the best dose metric to compare the effects of surface chemistry across different particle sizes. The number of particles internalised per cell was higher for 0.5 and 1 μm particles however, 3 μm particles were more efficiently internalised if the volume and surface area of internalised particles is considered.

Irrespective of dose/dose metric the percentage of dose internalised was highest with 3 μm particles. The nominal dose was used to calculate this and so it does not account for the effects of particle sedimentation. The actual dose for 0.5 μm and 1 μm particles (i.e. the particles that came into contact with cells) was likely a lot lower than the nominal dose. In future experiments, it may be worth attempting to measure how much of the particle suspension reaches the cell layer and then using this to calculate the percentage of internalised dose as a proportion of the dose that reaches the cell layer. Khanbeigi *et al.* attempted to predict how sedimentation would affect uptake using a model of *in vitro* sedimentation, diffusion and dosimetry (ISDD), however the model was not a good predictor of the dose that reached cells ⁴³⁵. On the other hand, in some *in vivo* scenarios, for example in pulmonary delivery, particle sedimentation plays a role so correcting for the presence of sedimentation effects may not be desirable.

The modification of silica spheres with zwitterionic surface chemistry did not have a large impact on their uptake by macrophages despite these particles having a negative zeta potential and a more hydrophilic surface than particles coated with AUTES which have a positive zeta potential and a relatively more hydrophobic surface. As discussed in chapter 1 the hydrophilic, negatively charged particles would be expected to exhibit reduced uptake in comparison to hydrophobic, positively charged particles, however this was not found to be the

case. Although the two particle types are different in respect of hydrophobicity and zeta potential, both have free primary amines on their surface which may explain the similarity of their uptake if their presence dominated cell interaction over the presence of the zwitterion. Further work should focus on increasing the amount of zwitterion on the surface of the particles or blocking free amine groups in order to see if this was the case.

In this work, changing particle size seemed to play a more significant role in affecting cellular uptake than altering surface chemistry, however the two parameters also showed some interplay whereby smaller particles (0.5, 1 μm) modified with zwitterion surface chemistry administered at higher doses showed reduced uptake compared to particles with AUTES surface chemistry. This finding is in agreement with a few published studies of the effect of polymeric particle size and surface chemistry on cellular uptake, which suggest that surface chemistry is less important for larger particles ^{437, 469}. The zwitterionic surface chemistry used in this chapter could therefore be further explored in particles of smaller size to ascertain if greater effects on uptake take place. Additionally, this would allow the study of cell types which are not specialised phagocytic cells and the effects of this surface chemistry on endocytic pathways to be established.

The use of the phospholipid DPPC served as a simple model to represent the presence of lung surfactant and showed to reduce uptake of particles in comparison with buffer alone (HBSS). This highlights the importance of using more bio-relevant media for uptake studies. In future, a better model of lung surfactant would include a more complex mixture of lung surfactant components which includes surfactant proteins A-D and other phospholipids such as phosphatidylglycerol and phosphatidylinositol ⁴⁷⁰. Upon exposure of particles to this complex media, adsorption of proteins and surfactants is expected to take place which would be determined both by media composition and particle surface chemistry. This gives the particles a new biological identity which in turn influences its interactions with cells. The composition of this new biological identity should be determined so as to identify the exact nature of cellular interaction.

Comparing data from each of the chapters 3-5, microparticle uptake by macrophages was dependent on applied dose, particle shape, and size, but the dependence on hydrophobicity, surface charge, and surface chemistry presented a more complex picture which requires more work to fully elucidate. Larger and more elongated particle shapes demonstrated the potential for macrophage avoidance whereas particles possessing high curvature features may be useful in promoting particle uptake. This work supports earlier work in this field by Mitragotri and colleagues and provides impetus to further develop understanding of the properties affecting cellular uptake of microparticles. In particular, the study of parameters which govern the internalisation of different microparticle shapes and how they can be manipulated to tune particle uptake, will be beneficial to improve the efficacy of particulate delivery systems.

7. References

1. Venditto, V. J.; Jr., F. C. S., Cancer nanomedicines: So many papers and so few drugs! *Adv. Drug Deliv. Rev.* **2013**, *65*, 80-88.
2. Hua, S.; Matos, M. B. C. d.; Metselaar, J. M.; Storm, G., Current trends and challenges in the clinical translation of nanoparticulate nanomedicines: Pathways for translational development and commercialization. *Front. Pharmacol.* **2018**, *9*, 1-14.
3. Pan, J.; Chan, S. Y.; Lee, W. G.; Kang, L., Microfabricated particulate drug-delivery systems *Biotechnol. J.* **2011**, *6*, 1477-1487.
4. Barenholz, Y. C., Doxil - The first FDA-approved nano-drug: Lessons learned. *J. Control. Release* **2012**, *160*, 117-134.
5. Gabizon, A.; Catane, R.; Uziely, B.; Kaufman, B.; Safra, T.; Cohen, R.; Martin, F.; Huang, A.; Barenholz, Y., Prolonged circulation time and enhanced accumulation in malignant exudates of doxorubicin encapsulated in polyethylene-glycol coated liposomes. *Cancer Res.* **1994**, *54*, 987-992.
6. Bobo, D.; Robinson, K. J.; Islam, J.; Thurecht, K. J.; Corrie, S. R., Nanoparticle-based medicines: A review of FDA-approved materials and clinical trials to date. *Pharm. Res.* **2016**, *33*, 2373-2387.
7. Johnson, K. P.; Brooks, B. R.; Cohen, J. A.; Ford, C. C.; Goldstein, J.; Lisak, R. P.; Myers, L. W.; Pritch, H. S.; Rose, J. W.; Schiffer, R. B.; Vollmer, T.; Weiner, L. P.; Wolinsky, J. S., Extended use of glatiramer acetate (copaxone) is well tolerated and maintains its clinical effect on multiple sclerosis relapse rate and degree of disability. *Neurology* **1998**, *50*, 701-708.
8. Alam, M.; Hartrick, C. T., Extended-release epidural morphine (DepoDur TM): An old drug with a new profile. *Pain Pract.* **2005**, *5*, 349-353.
9. Cruess, A. F.; Zlateva, G.; Pleil, A. M.; Wirostko, B., Photodynamic therapy with verteporfin in age-related macular degeneration: a systematic review of efficacy, safety, treatment modifications and pharmacoeconomic properties. *Acta Ophthalmol.* **2009**, *87*, 118-132.
10. Simon, J., Estradiol in micellar nanoparticles: the efficacy and safety of a novel transdermal drug-delivery technology in the management of moderate to severe vasomotor symptoms. *Menopause* **2006**, *13*, 222-231.
11. Savla, R.; Browne, J.; Plassat, V.; Wasan, K. M.; Wasan, E. K., Review and analysis of FDA approved drugs using lipid-based formulations. *Drug Dev. Ind. Pharm.* **2017**, *43*, 1743-1758.
12. Borghardt, J. M.; Kloft, C.; Sharma, A., Inhaled therapy in respiratory disease: The complex interplay of pulmonary kinetic processes. *Can. Respir. J.* **2018**, *2018*, 1-11.
13. Hickey, A. J., Emerging trends in inhaled drug delivery. *Adv. Drug Deliv. Rev.* **2020**, *157*, 63-70.
14. Mulligan, M. J.; Lyke, K. E.; Kitchen, N.; Absalon, J.; Gurtman, A.; Lockhart, S.; Neuzil, K.; Raabe, V.; Bailey, R.; Swanson, K. A.; Li, P.; Koury, K.; Kalina, W.; Cooper, D.; Fontes-Garfias, C.; Shi, P.-Y.; Tureci, O.; Tompkins, K. R.; Walsh, E. E.; Frenck, R.; Falsey, A. R.; Dormitzer, P. R.; Gruber, W. C.; Sahin, U.; Jansen, K. U., Phase I/II study of COVID-a9 RNA vaccine BNT162b1 in adults. *Nature* **2020**, *586* (589-593).
15. Jackson, L. A.; Anderson, E. J.; Roupheal, N. G.; Roberts, P. C.; Makhene, M.; Coler, R. N.; McCullough, M. P.; Chappell, J. D.; Denison, M. R.; Stevens, L. J.; Puijssers, A. J.; McDermott, A.; Flach, B.; Doria-Rose, N. A.; Corbett, K. S.; Morabito, K. M.; O'Dell, S.; Schmidt, S. D.; Il, P. A. S.; Padilla, M.; Mascola, J. R.; Neuzil, K. M.; Bennet, H.; Sun, W.; Peters, E.; Makowski, M.; Albert, J.; Cross, K.; Buchanan, W.; Pikaart-Tautges, R.; Ledgerwood, J. E.; Graham, B. S.; Beigel, J. H., An mRNA vaccine against SARS-COV-2. *N. Eng. J. Med.* **2020**, *383*, 1920-1931.
16. Pardi, N.; Tuyishime, S.; Muramatsu, H.; Kariko, K.; Mui, B. L.; Tam, Y. K.; Madden, T. D.; Hope, M. J.; Weissman, D., Expression of nucleoside-modified mRNA delivered in lipid nanoparticles to mice by various routes. *J. Control. Release* **2015**, *217*, 345-351.

17. Sahay, G.; Alakhova, D. Y.; Kabanov, A. V., Endocytosis of nanomedicines. *J. Control. Release* **2010**, *145*, 182-195.
18. Doherty, G. J.; McMahon, H. T., Mechanisms of endocytosis. *Annu. Rev. Biochem.* **2009**, *78*, 857-902.
19. Thorely, J. A.; McKeating, J. A.; Rappoport, J. Z., Mechanisms of viral entry: sneaking in the front door. *Protoplasma* **2010**, *244*, 15-24.
20. Conner, S. D.; Schmid, S. L., Regulated portals of entry into the cell. *Nature* **2003**, *422*, 37-44.
21. Kinnear, C.; Moore, T. L.; Rodriguez-Lorenzo, L.; Rothen-Rutishauser, B.; Petri-Fink, A., Form follows function: nanoparticle shape and its implications for nanomedicine. *Chem. Rev.* **2017**, *117*, 11476-11521.
22. Kibbey, R. G.; Rizo, J.; Gierasch, L. M.; Anderson, R. G. W., The LDL receptor clustering motif interacts with the clathrin terminal domain in a reverse turn conformation. *J. Cell Biol.* **1998**, *142*, 59-67.
23. Miller, K.; Shipman, M.; Trowbridge, I. S.; Hopkins, C. R., Transferrin receptors promote the formation of clathrin lattices. *Cell* **1991**, *65*, 621-632.
24. Brodsky, F. M.; Chen, C.-Y.; Knuehl, C.; Towler, M. C.; Wakeham, D. E., Biological basket weaving: Formation and function of clathrin-coated vesicles. *Annu. Rev. Cell Dev. Biol.* **2001**, *17*, 517-568.
25. Brodsky, F. M., Living with Clathrin: Its role in intracellular membrane traffic. *Science* **1988**, *242*, 1396-1402.
26. Cocucci, E.; Aguet, F.; Boulant, S.; Kirchhausen, T., The first five seconds in the life of a clathrin-coated pit. *Cell* **2012**, *150*, 495-507.
27. Hinshaw, J. E.; Schmid, S. L., Dynamin self-assembles into rings suggesting a mechanism for coated vesicle budding. *Nature* **1995**, *374*, 190-192.
28. Stowell, M. H. B.; Marks, B.; Wigge, P.; McMahon, H. T., Nucleotide-dependent conformational changes in dynamin: evidence for a mechanochemical molecular spring. *Nat. Cell. Biol.* **1999**, *1*, 28-32.
29. Ungewickell, E., The 70-kd mammalian heat shock proteins are structurally and functionally related to the uncoating protein that releases clathrin triskelions from coated vesicles. *EMBO J.* **1985**, *4*, 3385-3391.
30. Malinovskaya, Y.; Melnikov, P.; Baklaushev, V.; Gabashvili, A.; Osipova, N.; Mantrov, S.; Ermolenko, Y.; Maksimenko, O.; Gorshkova, M.; Balabanyan, V., Delivery of doxorubicin-loaded PLGA nanoparticles into U87 human glioblastoma cells. *Int. J. Pharm.* **2017**, *524*, 77-90.
31. Chung, T.-H.; Wu, S.-H.; Yao, M.; Lu, C.-W.; Lin, Y.-S.; Hung, Y.; Mou, C.-Y.; Chen, Y.-C.; Huang, D.-M., The effect of surface charge on the uptake and biological function of mesoporous silica nanoparticles in 3T3-L1 cells and human mesenchymal stem cells. *Biomaterials* **2007**, *28*, 2959-2966.
32. Tahara, K.; Sakai, T.; Yamamoto, H.; Takeuchi, H.; Hirashima, N.; Kawashima, Y., Improved cellular uptake of chitosan-modified PLGA nanospheres by A549 cells. *Int. J. Pharm.* **2009**, *382*, 198-204.
33. Rejman, J.; Oberle, V.; Zuhorn, I. S.; Hoekstra, D., Size-dependent internalization of particles via the pathways of clathrin- and caveolae-mediated endocytosis. *Biochem. J.* **2004**, *377*, 159-169.
34. Zhao, F.; Zhao, Y.; Liu, Y.; Chang, X.; Chen, C.; Zhao, Y., Cellular uptake, intracellular trafficking, and cytotoxicity of nanomaterials. *Small* **2011**, *7*, 1322-1337.
35. Bannunah, A. M.; Villasaliu, D.; Lord, J.; Stolnik, S., Mechanisms of nanoparticle internalization and transport across an intestinal epithelial cell model: Effect of size and surface charge. *Mol. Pharm.* **2014**, *11*, 4363-4373.
36. Murata, M.; Peranen, J.; Schreiner, R.; Wieland, F.; Kurzchalia, T. V.; Simons, K., VIP21/caveolin is a cholesterol-binding protein. *Proc. Natl. Acad. Sci.* **1995**, *92*, 10339-10343.
37. Rothberg, K. G.; Heuser, J. E.; Donzell, W. C.; Ying, Y.-S.; Glenney, J. R.; Anderson, R. G. W., Caveolin, a protein component of caveolae membrane coats. *Cell* **1992**, *68*, 673-682.

38. Chang, W.-J.; Rothberg, K. G.; Kamen, B. A.; Anderson, R. G. W., Lowering the cholesterol content of MA104 cells inhibits receptor-mediated transport of folate. *J. Cell Biol.* **1992**, *118*, 63-69.
39. Schubert, W.; Frank, P. G.; Razani, B.; Park, D. S.; Chow, C.-W.; Lisanti, M. P., Caveolae-deficient endothelial cells show defects in the uptake and transport of albumin in vivo. *J. Biol. Chem.* **2001**, *276*, 48619-48622.
40. Fielding, C. J.; Fielding, P. E., Caveolae and intracellular trafficking of cholesterol. *Adv. Drug Deliv. Rev.* **2001**, *49*, 251-264.
41. Dauty, E.; Remy, J.-S.; Zuber, G.; Behr, J.-P., Intracellular delivery of nanometric DNA particles via the folate receptor. *Bioconjugate Chem.* **2002**, *13*, 831-839.
42. Chatterjee, M.; Ben-Josef, E.; Robb, R.; Vedaie, M.; Seum, S.; Thirumoorthy, K.; Palanichamy, K.; Harbrecht, M.; Chakravarti, A.; Williams, T. M., Caveolae-mediated endocytosis is critical for albumin cellular uptake and response to albumin-bound chemotherapy. *Cancer Res.* **2017**, *77*, 5925-5937.
43. Sengupta, P.; Basu, S.; Soni, S.; Pandey, A.; Roy, B.; Oh, M. S.; Chin, K. T.; Paraskar, A. S.; Sarangi, S.; Connor, Y.; Sabbisetti, V. S.; Koppam, J.; Kulkarni, A.; Muto, K.; Amarasiriwardena, C.; Jayawardene, I.; Lupoli, N.; Dinulescu, D. M.; Bonventre, J. V.; Mashelkar, R. A.; Sengupta, S., Cholesterol-tethered platinum II-based supramolecular nanoparticle increases antitumor efficacy and reduces nephrotoxicity. *Proc. Natl. Acad. Sci.* **2012**, *109*, 11294-11299.
44. Kirkham, M.; Fujita, A.; Chadda, R.; Nixon, S. J.; Kurzchalia, T. V.; Sharma, D. K.; Pagano, R. E.; Hancock, J. F.; Mayor, S.; Parton, R. G., Ultrastructural identification of uncoated caveolin-independent early endocytic vehicles. *J. Cell Biol.* **2005**, *168*, 485-476.
45. Nabi, I. R.; Le, P. U., Caveolae/raft-dependent endocytosis. *J. Cell Biol.* **2003**, *161*, 673-677.
46. Kartenbeck, J.; Stukenbrok, H.; Helenius, A., Endocytosis of simian virus 40 into the endoplasmic reticulum. *J. Cell Biol.* **1989**, *109*, 2721-2729.
47. Milici, A. J.; Watrous, N. E.; Stukenbrok, H.; Palade, G. E., Transcytosis of albumin in capillary endothelium. *J. Cell Biol.* **1987**, *105*, 2603-2612.
48. Predescu, S. A.; Predescu, D. N.; Malik, A. B., Molecular determinants of endothelial transcytosis and their role in endothelial permeability. *Am. J. Physiol. Lung Cell Mol. Physiol.* **2007**, *293*, L823-L842.
49. Wang, Z.; Tiruppathi, C.; Minshall, R. D.; Malik, A. B., Size and dynamics of caveolae studied using nanoparticles in living endothelial cells *ACS Nano* **2009**, *3*, 4110-4116.
50. Pelkmans, L.; Kartenbeck, J.; Helenius, A., Caveolar endocytosis of simian virus 40 reveals a new two-step vesicular-transport pathway to the ER. *Nat. Cell. Biol.* **2001**, *3*, 473-483.
51. Chang, J.; Jallouli, Y.; Kroubi, M.; Yuan, X.-b.; Feng, W.; Kang, C.-s.; Pu, P.-y.; Betbeder, D., Characterization of endocytosis of transferrin-coated PLGA nanoparticles by the blood-brain barrier. *Int. J. Pharm.* **2009**, *379*, 285-292.
52. Sabharanjak, S.; Sharma, P.; Parton, R. G.; Mayor, S., GPI-anchored proteins are delivered to recycling endosomes via a distinct cdc42-regulated clathrin-independent pinocytic pathway. *Dev. Cell* **2002**, *2*, 411-423.
53. Chadda, R.; Howes, M. T.; Plowman, S. J.; Hancock, J. F.; Parton, R. G.; Mayor, S., Cholesterol-sensitive Cdc42 activation regulates actin polymerization for endocytosis via the GEEC pathway. *Traffic* **2007**, *8*, 702-717.
54. Kalia, M.; Kumari, S.; Chadda, R.; Hill, M. M.; Parton, R. G.; Mayor, S., Arf6-independent GPI-anchored protein-enriched early endosomal compartments fuse with sorting endosomes via a Rab5/phosphatidylinositol-3'-kinase-dependent machinery. *Mol. Biol. Cell* **2006**, *17*, 3689-3704.
55. Otto, G. P.; Nichols, B. J., The roles of flotillin microdomains - endocytosis and beyond. *J. Cell Sci.* **2011**, *124*, 3933-3939.
56. Stuermer, C. A. O.; Lang, D. M.; Kirsch, F.; Wiechers, M.; Deininger, S.-O.; Plattner, H., Glycosylphosphatidyl inositol-anchored proteins and fyn kinase assemble in noncaveolar

plasma membrane microdomains defined by reggie-1 and -2 *Mol. Biol. Cell* **2001**, 12, 3031-3045.

57. Glebov, O. O.; Bright, N. A.; Nichols, B. J., Flotillin-1 defines a clathrin-independent endocytic pathway in mammalian cells. *Nat. Cell Biol.* **2006**, 8, 46-54.

58. Mercer, J.; Helenius, A., Virus entry by macropinocytosis. *Nat. Cell Biol.* **2009**, 11, 510-520.

59. Swanson, J. A.; Watts, C., Macropinocytosis. *Trends Cell Biol.* **1995**, 5, 424-428.

60. Li, Y.-X.; Pang, H.-B., Macropinocytosis as a cell entry route for peptide-functionalized and bystander nanoparticles. *J. Control. Release* **2020**, article in press.

61. Rabinovitch, M., Professional and non-professional phagocytes: an introduction. *Trends Cell Biol.* **1995**, 5, 85-87.

62. Rosales, C.; Uribe-Querol, E., Phagocytosis: A fundamental process in immunity. *Biomed Res. Int.* **2017**, 7, 1-18.

63. Zhang, X.; Mosser, D. M., Macrophage activation by endogenous danger signals. *J. Pathol* **2008**, 214, 161-178.

64. Kobzik, L., Lung macrophage uptake of unopsonized environmental particulates: Role of scavenger-type receptors. *J. Immunol* **1995**, 155, 367-376.

65. Brown, G. D.; Taylor, P. R.; Reid, D. M.; Willment, J. A.; Williams, D. L.; Martinez-Pomares, L.; Wong, S. Y. C.; Gordon, S., Dectin-1 is a major B-Glucan receptor on macrophages. *J. Exp. Med* **2002**, 196, 407-412.

66. Stahl, P. D.; Ezekowitz, R. A. B., The mannose receptor is a pattern recognition receptor involved in host defense. *Curr. Opin. Immunol.* **1998**, 10, 50-55.

67. Garcia-Garcia, E.; Rosales, C., Signal transduction during Fc receptor-mediated phagocytosis. *J. Leukoc. Biol* **2002**, 72, 1092-1108.

68. Brown, E. J., Complement receptors and phagocytosis. *Curr. Opin. Immunol.* **1991**, 3, 76-82.

69. Gordon, S., Phagocytosis: An Immunobiologic Process. *Immunity* **2016**, 44, 463-475.

70. Mantovani, A.; Sica, A.; Sozzani, S.; Allavena, P.; Vecchi, A.; Locati, M., The chemokine system in diverse forms of macrophage activation and polarization. *Trends Immunol.* **2004**, 25, 677-686.

71. Caron, E.; Self, A. J.; Hall, A., The GTPase Rap1 controls functional activation of macrophage integrin α MB2 by LPS and other inflammatory mediators. *Curr. Biol.* **2000**, 10, 974-978.

72. Canton, J.; Neculai, D.; Grinstein, S., Scavenger receptors in homeostasis and immunity. *Nat. Rev. Immunol* **2013**, 13, 621-634.

73. Cox, D.; Greenberg, S., Phagocytic signaling strategies: Fcy receptor-mediated phagocytosis as a model system. *Immunology* **2001**, 13, 339-345.

74. Allen, L.-A. H.; Aderem, A., Molecular definition of distinct cytoskeletal structures involved in complement- and Fc receptor-mediated phagocytosis in macrophages. *J. Exp. Med* **1996**, 184, 627-637.

75. Kaplan, G., Differences in the mode of phagocytosis with Fc and C3 receptors in macrophages. *Scand. J. Immunol.* **1977**, 6, 797-807.

76. Patel, P. C.; Harrison, R. E., Membrane ruffles capture C3bi-opsonised particles in activated macrophages. *Mol. Biol. Cell* **2008**, 19, 4628-4639.

77. Olazabal, I. M.; Caron, E.; May, R. C.; Schilling, K.; Knecht, D. A.; Machesky, L. M., Rho-kinase and myosin-II control phagocytic cup formation during CR, but not FcyR, phagocytosis. *Curr. Biol.* **2002**, 12, 1413-1418.

78. Lewkowicz, E.; Herit, F.; Clainche, C. L.; Bourdoncle, P.; Perez, F.; Niedergang, F., The microtubule-binding protein CLIP-170 coordinates mDla1 and actin reorganization during CR3-mediated phagocytosis. *J. Cell Biol.* **2008**, 183, 1287-1298.

79. Araki, N.; Johnson, M. T.; Swanson, J. A., A role fo phosphoinositide 3-kinase in the completion of macropinocytosis and phagocytosis. *J. Cell Biol.* **1996**, 135, 1249-1260.

80. Swanson, J. A.; Johnson, M. T.; Beningo, K.; Post, P.; Mooseker, M.; Araki, N., A contractile activity that closes phagosomes in macrophages. *J. Cell Sci.* **1999**, 112, 307-316.

81. Marie-Anais, F.; Mazzolini, J.; Herit, F.; Niedergang, F., Dynamin-Actin Cross talk contributes to phagosome formation and closure. *Traffic* **2016**, *17*, 487-499.
82. Mukherjee, S.; Ghosh, R. N.; Maxfield, F. R., Endocytosis. *Physiol. Rev.* **1997**, *77*, 759-803.
83. Damiani, M. T.; Pavarotti, M.; Leiva, N.; Lindsay, A. J.; McCaffrey, M. W.; Colombo, M. I., Rab coupling protein associates with phagosomes and regulates recycling from the phagosomal compartment. *Traffic* **2004**, *5*, 785-797.
84. Antonin, W.; Holroyd, C.; Fasshauer, D.; Pabst, S.; Mollard, G. F. v.; Jahn, R., A SNARE complex mediating fusion of late endosomes defines conserved properties of SNARE structure and function. *EMBO J.* **2000**, *19*, 6453-6464.
85. Johnson, L. S.; Dunn, K. W.; Pytowski, B.; McGraw, T. E., Endosome acidification and receptor trafficking: Bafilomycin A1 slows receptor externalization by a mechanism involving the receptor's internalization motif. *Mol. Biol. Cell* **1993**, *4*, 1251-1266.
86. Lennon-Dumenil, A.-M.; Bakker, A. H.; Maehr, R.; Fiebiger, E.; Overleef, H. S.; Roseblatt, M.; Ploegh, H. L.; Lagsudriere-Gesbert, C., Analysis of protease activity in live antigen-presenting cells shows regulation of the phagosomal proteolytic contents during dendritic cell activation. *J. exp. Med* **2002**, *196*, 529-539.
87. Quinn, M. T.; Gauss, K. A., Structure and regulation of the neutrophil respiratory burst oxidase: comparison with nonphagocyte oxidases. *J. Leukoc. Biol* **2004**, *76*, 760-781.
88. Fang, F. C., Antimicrobial reactive oxygen species and nitrogen species: concepts and controversies. *Nat. Rev. Microbiol.* **2004**, *2*, 820-832.
89. Semmling, M.; Kreft, O.; Javier, A. M.; Sukhorukov, G. B.; Kas, J.; Parak, W. J., A novel flow-cytometry-based assay for cellular uptake studies of polyelectrolyte microcapsules. *Small* **2008**, *4*, 1763-1768.
90. Ashraf, S.; Park, J.; Bichelberger, M. A.; Kanter, K.; Hartmann, R.; Maffre, P.; Said, A. H.; Feliu, N.; Lee, J.; Lee, D.; Nienhaus, G. U.; Kim, S.; Parak, W. J., Zwitterionic surface coating of quantum dots reduces protein adsorption and cellular uptake. *Nanoscale* **2016**, *8*, 17794-17800.
91. Feliu, N.; Sun, X.; Puebla, R. A. A.; Parak, W. J., Quantitative particle-cell interaction: Some basic physicochemical pitfalls. *Langmuir* **2017**, *33*, 6639-6646.
92. Ashraf, S.; Said, A. H.; Hartmann, R.; Assmann, M.-A.; Feliu, N.; Lenz, P.; Parak, W. J., Quantitative particle uptake by cells as analyzed by different methods. *Angew. Chem. Int. Ed.* **2020**, *59*, 5438-5453.
93. Kettler, K.; Veltman, K.; Meent, D. V. D.; Wezel, A. v.; Hendricks, A. J., Cellular uptake of nanoparticles as determined by particle properties, experimental conditions and cell type. *Environ. Toxicol. Chem.* **2014**, *33*, 481-492.
94. Wang, S.-H.; Lee, C.-W.; Chiou, A.; Wei, P.-K., Size-dependent endocytosis of gold nanoparticles studied by three-dimensional mapping of plasmonic scattering images. *Journal of Nanobiotechnology* **2010**, *8*, 1-13.
95. Lu, F.; Si-Han Wu; Hung, Y.; Mou, C.-Y., Size effect on cell uptake in well-suspended, uniform mesoporous silica nanoparticles. *Small* **2009**, *5*, 1408-1413.
96. Osaki, F.; Kanamori, T.; Sando, S.; Sera, T.; Aoyama, Y., Quantum dot conjugated sugar ball and its cellular uptake. On the size effects of endocytosis in the subviral region. *J. Am. Chem. Soc* **2004**, *126*, 6520-6521.
97. Jiang, W.; Kim, B. Y. S.; Rutka, J. T.; Chan, W. C. W., Nanoparticle-mediated cellular response is size-dependent. *Nature Nanotechnology* **2008**, *3*, 145-150.
98. Chithrani, B. D.; Ghazani, A. A.; Chan, W. C. W., Determining the size and shape dependence of gold nanoparticle uptake into mammalian cells. *Nano letters* **2006**, *6*, 662-668.
99. Xu, A.; Yao, M.; Xu, G.; Ying, J.; Ma, W.; Li, B.; Jin, Y., A physical model for the size-dependent cellular uptake of nanoparticles modified with cationic surfactants *International Journal of Nanomedicine* **2012**, *7*, 3547-3554.
100. Kulkarni, S. A.; Feng, S.-S., Effects of particle size and surface modification on cellular uptake and biodistribution of polymeric nanoparticles for drug delivery. *Pharm Res* **2013**, *30*, 2512-2522.

101. He, C.; Hu, Y.; Yin, L.; Tang, C.; Yin, C., Effects of particle size and surface charge on cellular uptake and biodistribution of polymeric nanoparticles. *Biomaterials* **2010**, *31*, 3657-3666.
102. Santos, T. d.; Varela, J.; Lynch, I.; Salvati, A.; Dawson, K. A., Quantitative assessment of the comparative nanoparticle-uptake efficiency of a range of cell lines. *Small* **2011**, *7*, 3341-3349.
103. Tabata, Y.; Ikada, Y., Effect of the size and surface charge of polymer microspheres on their phagocytosis by macrophage. *Biomaterials* **1987**, *9*, 356-362.
104. Pratten, M. K.; Loyd, J. B., Pinocytosis and Phagocytosis: the effect of size of a particulate substrate on its mode of capture by rat peritoneal macrophages cultures in vitro. *Biochimica et Biophysica Acta* **1986**, *881*, 307-313.
105. Catelas, I.; Huk, O. L.; Petit, A.; ZUkor, D. J.; Marchand, R.; Yahia, L. H., Flow cytometric analysis of macrophage response to ceramic and polyethylene particles: Effects of size, concentration and composition. *Journal of Biomedical Materials Research* **1998**, *41*, 600-607.
106. Champion, J. A.; Walker, A.; Mitragotri, S., Role of particle size in phagocytosis of polymeric microspheres. *Pharm Res* **2008**, *25*, 1815-1820.
107. Yue, H.; Wei, W.; Yue, Z.; Lv, P.; Wang, L.; Ma, G.; Su, Z., Particle size affects the cellular response in macrophages. *European Journal of Pharmaceutical Sciences* **2010**, *41*, 650-657.
108. Tabata, Y.; Ikada, Y., Effect of surface wettability of microspheres on phagocytosis. *J Colloid Interf Sci* **1988**, *127*, 132-140.
109. Lorenz, S.; Hauser, C. P.; Autenrieth, B.; Weiss, C. K.; Landfester, K.; Mailander, V., The softer and more hydrophobic the better: Influence of the side chain of polymethacrylate nanoparticles for cellular uptake. *Macromol. Biosci.* **2010**, *10*, 1034-1042.
110. Suk, J. S.; Xu, Q.; Kim, N.; Hanes, J.; Ensign, L. M., PEGylation as a strategy for improving nanoparticle-based drug and gene delivery. *Adv. Drug Deliv. Rev.* **2016**, *99*, 28-51.
111. Bewersdorff, T.; Gruber, A.; Eravci, M.; Dumbani, M.; Klinger, D.; Haase, A., Amphiphilic nanogels: influence of surface hydrophobicity on protein corona, biocompatibility and cellular uptake. *Int. J. Nanomedicine* **2019**, *14*, 7861-7878.
112. Gratton, S. E. A.; Napier, M. E.; Ropp, P. A.; Tian, S.; DeSimone, J. M., Microfabricated particles for engineered drug therapies: Elucidation into the mechanisms of cellular internalization of PRINT particles. *Pharm Res* **2008**, *25*, 2845-2852.
113. Schweiger, C.; Hartmann, R.; Zhang, F.; Parak, W. J.; Kissel, T. H.; Rivera-Gil, P., Quantification of the internalization patterns of superparamagnetic iron oxide nanoparticles with opposite charge. *J. Nanobiotechnol.* **2012**, *10*, 1-11.
114. Yue, Z.-G.; Wei, W.; Lv, P.-P.; Yue, H.; Wang, L.-Y.; Su, Z.-G.; Ma, G.-H., Surface charge effects cellular uptake and intracellular trafficking of chitosan-based nanoparticles. *Biomacromolecules* **2011**, *12*, 2440-2446.
115. Harush-Frenkel, O.; Debotton, N.; Benita, S.; Altschuler, Y., Targeting of nanoparticles to the clathrin-mediated endocytic pathway. *Biochem. Biophys. Res. Commun.* **2007**, *353*, 26-32.
116. Pradhan, P.; Giri, J.; Banerjee, R.; Bellare, J.; Bahadur, D., Cellular interactions of lauric acid and dextran-coated magnetite nanoparticles. *J. Magn. Magn. Mater.* **2007**, *311*, 282-287.
117. Forest, V.; Cottier, M.; Pourchez, J., Electrostatic interactions favor the binding of positive nanoparticles on cells: A reductive theory. *Nano Today* **2015**, *10*, 677-680.
118. Low, P. S.; Henne, W. A.; Doorneweerd, D. D., Discovery and development of folic-acid-based receptor targeting for imaging and therapy of cancer and inflammatory diseases. *Acc. Chem. Res.* **2007**, *41*, 120-129.
119. Russel-Jones, G.; McTavish, K.; McEwan, J.; Rice, J.; Nowotnik, D., Vitamin-mediated targeting as a potential mechanism to increase drug uptake by tumours. *J. Inorg. biochem.* **2004**, *98*, 1625-1633.

120. White, K. L.; Rades, T.; Furneaux, R. H.; Tyler, P. C.; Hook, S., Mannosylated liposomes as antigen delivery vehicles for targeting to dendritic cells. *J. Pharm. Pharmacol.* **2006**, *58*, 729-737.
121. Kelm, S.; Brossmer, R.; Isecke, R.; Gross, H.-J.; Strenge, K.; Schauer, R., Functional groups of sialic acids involved in binding to siglecs (sialoadhesins) deduced from interactions with synthetic analogues. *Eur. J. Biochem.* **1998**, *255*, 663-672.
122. Hurkat, P.; Jain, A.; Jain, A.; Shilpi, S.; Gulbake, A.; Jain, S. K., Concanavilin A conjugated biodegradable nanoparticles for oral insulin delivery. *J. Nanopart. Res.* **2012**, *14*, 1-14.
123. Wang, C.; Ho, P. C.; Lim, L. Y., Wheat germ agglutinin-conjugated PLGA nanoparticles for enhanced intracellular delivery of paclitaxel to colon cancer cells. *Int. J. Pharm.* **2010**, *400*, 201-210.
124. Li, H.; Zeng, Q.; Zeng, Y.; chen, D.; Pang, L.; Chen, X.; Zhan, Y., Bovel vinyl-modified RGD conjugated silica nanoparticles based on photoclick chemistry for in vivo prostate cancer targeted fluorescence imaging. *RSC Adv.* **2019**, *9*, 25318-25325.
125. Gan, C. W.; Feng, S.-S., Transferrin-conjugated nanoparticles of poly(lactide)-D- α -tocopheryl polyethylene glycol succinate diblock copolymer for targeted drug delivery across the blood-brain barrier. *Biomaterials* **2010**, *31*, 7748-7757.
126. Shimada, T.; Eueda, M.; Jinno, H.; Chiba, N.; Wada, M.; Watanabe, J.; Ishihara, K.; Kitagawa, Y., Development of targeted therapy with paclitaxel incorporated into EGF-conjugated nanoparticles. *Anticancer res* **2009**, *29*, 1009-1014.
127. Peng, J.; Chen, J.; Xie, F.; Bao, W.; Xu, H.; Wang, H.; Xu, Y.; Du, Z., Herceptin-conjugated paclitaxel loaded PCL-PEG worm-like nanocrystal micells for the combinatorial treatment of HER2-positive breast cancer. *Biomaterials* **2019**, *222*, 1-13.
128. Song, L.; Chen, Y.; Ding, J.; Wu, H.; Zhang, W.; Ma, M.; Zang, F.; Wang, Z.; Gu, N.; Zhang, Y., Rituximab conjugated iron oxide nanoparticles for targeted imaging and enhanced treatment against CD20-positive lymphoma. *J. Mater. Chem. B.* **2020**, *8*, 895-907.
129. Nie, S., Understanding and overcoming major barriers in cancer nanomedicine. *Nanomedicine* **2010**, *5*, 523-528.
130. Hussain, Z.; Khan, S.; Imran, m.; Sohail, M.; Shah, S. W. A.; Matas, M. d., PEGylation: a promising strategy to overcome challenges to cancer-targeted nanomedicines: a review of challenges to clinical transition and promising resolution. *Drug Deliv. Transl. Res.* **2019**, *9*, 721-734.
131. Zalipsky, S.; Hansen, C. B.; Oaks, J. M.; Allen, T. M., Evaluation of blood clearance rates and biodistribution of poly(2-oxazoline)-grafted liposomes. *J. Pharm. Sci.* **1995**, *85*, 133-137.
132. Cao, Z.; Yu, Q.; Xue, H.; Cheng, G.; Jiang, S., Nanoparticles for drug delivery prepared from amphiphilic PLGA zwitterionic block copolymers with sharp contrast in polarity between two blocks. *Angew. Chem.* **2010**, *49*, 3771-3776.
133. Maruyama, K.; Okuizumi, S.; Ishida, O.; Yamauchi, H.; Kikuchi, H.; Iwatsuru, M., Phosphatidyl polyglycerols prolong liposome circulation in vivo *Int. J. Pharm.* **1994**, *111*, 103-107.
134. Mitchell, M. J.; Billingsley, M. M.; Haley, R. M.; Wechsler, M. E.; Peppas, N. A.; Langer, R., Engineering precision nanoparticles for drug delivery. *Nat. Rev. Drug Discov.* **2021**, *20*, 101-124.
135. Guo, F.; Fu, Q.; Zhou, K.; Jin, C.; Wu, W.; Ji, X.; Yan, Q.; Yang, Q.; Wu, D.; Li, A.; Yang, G., Matrix metalloprotein-triggered, cell penetrating peptide-modified star-shaped nanoparticles for tumor targeting and cancer therapy. *J. Nanobiotechnol.* **2020**, *18*, 1-16.
136. Casals, E.; Pfaller, T.; Duschl, A.; Oostingh, G. J.; Puentes, V., Time Evolution of the nanoparticle protein corona *ACS Nano* **2010**, *7*, 3623-3632.
137. Lundqvist, M.; Stigler, J.; Elia, G.; Lynch, I.; Cedervall, T.; Dawson, K. A., Nanoparticle size and surface properties determine the protein corona with possible implications for biological impacts. *PNAS* **2008**, *105*, 14265-14270.
138. Lynch, I.; Dawson, K. A., Protein-nanoparticle interactions. *Nano today* **2008**, *3*, 40-47.

139. Hirsh, S. L.; McKenzie, D. R.; Nosworthy, N. J.; Denman, J. A.; Sezerman, O. U.; Bilek, M. M. M., The Vroman effect: Competitive protein exchange with dynamic multilayer protein aggregates. *Colloids Surf. B* **2013**, *103*, 395-404.
140. Tenzer, S.; Docter, D.; Kuharev, J.; Musyanovych, A.; Fetz, V.; Hecht, R.; Schlenk, F.; Fischer, D.; Kiouptsi, K.; Reinhardt, C.; Landfester, K.; Schild, H.; Maskos, M.; Knauer, S. K.; Stauber, R. H., Rapid formation of plasma protein corona critically affects nanoparticle pathophysiology. *Nat. Nanotechnol.* **2013**, *8*, 772-781.
141. Kim, H. R.; Andrieux, K.; Gil, S.; Taverna, M.; Chacun, H.; Desmaele, D.; Taran, F.; Georgin, D.; Couvreur, P., Translocation of poly(ethylene glycol-co-hexadecyl)cyanoacrylate nanoparticles into rat brain endothelial cells: role of apolipoproteins in receptor-mediated endocytosis. *Biomacromolecules* **2007**, *8*, 793-797.
142. Zensi, A.; Begley, D.; Pontikis, C.; Legros, C.; Mihoreanu, L.; Buchel, C.; Kreuter, J., Human serum albumin nanoparticles modified with apolipoprotein A-I cross the blood brain barrier and enter the rodent brain. *J Drug Target* **2010**, *18*, 842-848.
143. Ashby, J.; Pan, S.; Zhong, W., Size and surface functionalization of iron oxide nanoparticles influence the composition and dynamic nature of their protein corona. *ACS Appl. Mater. Interfaces* **2014**, *6*, 15412-15419.
144. Aubin-Tam, M.-E.; Hamad-Schifferli, K., Gold nanoparticle-cytochrome c complexes: the effect of nanoparticle ligand charge on protein structure. *Langmuir* **2005**, *21*, 12080-12084.
145. Wang, X.; Wang, M.; Lei, R.; Zhu, S. F.; Zhao, Y.; Chen, C., Chiral surface of nanoparticles determines the orientation of adsorbed transferrin and its interaction with receptors. *ACS Nano* **2017**, *11*, 4606-4616.
146. Jain, A.; Trindade, G. F.; Hicks, J. M.; Potts, J. C.; Rahman, R.; Hague, R. J. M.; Amabilino, D. B.; Perez-Garcia, L.; Rawson, F. J., Modulating the biological function of protein by tailoring the adsorption orientation on nanoparticles. *J. Colloid Interface Sci.* **2021**, *587*, 150-161.
147. Satulovsky, J.; Carignano, M. A.; Szleifer, I., Kinetic and thermodynamic control of protein adsorption. *PNAS* **2000**, *97*, 9037-9041.
148. Pozzi, D.; Colapicchioni, V.; Caracciolo, G.; Piovesana, S.; Capriotti, A. L.; Palchetti, S.; Grossi, S. D.; Riccioli, A.; Amenitsch, H.; Lagana, A., Effect of polyethyleneglycol (PEG) chain length on the bio-nano-interactions between PEGylated lipid nanoparticles and biological fluids: from nanostructure to uptake in cancer cells. *Nanoscale* **2014**, *6*, 2782-2792.
149. Schlenoff, J. B., Zwitteration: Coating surfaces with zwitterionic functionality to reduce nonspecific adsorption. *Langmuir* **2014**, *30*, 9625-9636.
150. Estephan, Z. G.; Schlenoff, P. S.; Schlenoff, J. B., Zwitteration as an alternative to PEGylation. *Langmuir* **2011**, *27*, 6794-6800.
151. Kohane, D. S., Microparticles and nanoparticles for drug delivery. *Biotechnol. Bioeng.* **2007**, *96*, 203-209.
152. Iqbal, P.; Preece, J. A.; Mendes, P. M., Nanotechnology: The "top-down" and "bottom-up" approaches. In *Supramolecular chemistry: from molecules to nanomaterials*, Steed, J. W.; Gale, P. A., Eds. John Wiley & Sons: Online, 2012.
153. Agunloye, E.; Panariello, L.; Gavrilidis, A.; Mazzei, L., A model for the formation of gold nanoparticles in the citrate synthesis method. *Chemical Engineering Science* **2018**, *191*, 318-331.
154. Frens, G., Controlled nucleation for the regulation of the particle size in monodisperse gold suspensions. *Nature Physical Science* **1973**, *241*, 20-22.
155. Yeh, Y.-C.; Creran, V.; Vincent, M. R., Gold nanoparticles: preparation, properties, and applications in bionanotechnology. *Nanoscale* **2012**, *4*, 1871-1880.
156. Brust, M.; Walker, M.; Bethell, D.; Shiffrin, D. J.; Whyman, R., Synthesis of thiol-derivatised gold nanoparticles in a two-phase liquid-liquid system. *J. Chem. Soc., Chem. Commun.* **1994**, 801-802.
157. Grzelczak, M.; Perez-Juste, J.; Mulvaney, P.; Liz-Marzan, L. M., Shape control in gold nanoparticle synthesis. *Chem. Soc. Rev.* **2008**, *37*, 1783-1791.
158. Lui, M.; Guyot-Sionnest, P., Mechanism of silver(I)-assisted growth of gold nanorods and bipyramids. *J. Phys. Chem. B* **2005**, *109*, 22192-22200.

159. Sau, T. K.; Murphy, C. J., Room temperature, high yield synthesis of multiple shapes of gold nanoparticles in aqueous solution. *J. Am. Chem. Soc* **2004**, *126*, 8648-8649.
160. Khodashenas, B.; Ghorbani, H. R., Synthesis of silver nanoparticles with different shapes. *Arab J. Chem.* **2019**, *12*, 1823-1838.
161. Rycenga, M.; Cobley, C. M.; Zeng, J.; Li, W.; Moran, C. H.; Zhang, Q.; Qin, D.; Xia, Y., Controlling the synthesis and assembly of silver nanostructures for plasmonic applications. *Chem. Rev.* **2011**, *111*, 3669-3712.
162. Wiley, B.; Sun, Y.; Xia, Y., Synthesis of silver nanostructures with controlled shapes and properties. *Acc. Chem. Res.* **2007**, *40*, 1067-1076.
163. Siekkinen, A. R.; McLellan, J. M.; Chen, J.; Xia, Y., Rapid synthesis of small silver nanocubes by mediating polyol reduction with a trace amount of sodium sulfide or sodium hydrosulfide. *Chemical Physics Letters* **2006**, *432*, 491-496.
164. Skrabalak, S. E.; Au, L.; Li, X.; Xia, Y., Facile synthesis of Ag nanocubes and Au nanocages. *Nature Protocols* **2007**, *2*, 2182-2190.
165. Aslan, K.; Leonenko, Z.; Lakowicz, J. R.; Geddes, C. D., Fast and slow deposition of silver nanorods on planar surfaces: application to metal-enhanced fluorescence. *J. Phys. Chem. B* **2005**, *109*, 3157-3162.
166. Jana, N. R.; Gearheart, L.; Murphy, C. J., Wet chemical synthesis of silver nanorods and nanowires of controllable aspect ratio. *Chem. Commun.* **2001**, 617-618.
167. Wiley, B. J.; Chen, Y.; McLellan, J. M.; Xiong, Y.; Li, S.-Y.; Ginger, D.; Xia, Y., Synthesis and optical properties of silver nanobars and nanorice. *Nano letters* **2007**, *7*, 1032-1036.
168. Yamamoto, T.; Yin, H.; Wada, Y.; Kitamura, T.; Sakata, T.; Mori, H.; Yanagida, S., Morphology-control in microwave assisted synthesis of silver particles in aqueous solutions. *Bull. Chem. Soc. Jpn* **2004**, *77*, 757-761.
169. Aherne, D.; Ledwith, D. M.; Gara, M.; Kelly, J. M., Optical properties and growth aspects of silver nanoprisms produced by a highly reproducible and rapid synthesis at room temperature. *Adv. Func. Mat.* **2008**, *18*, 2005-2016.
170. Rafiuddin, Z. Z., Multi-branched flower-like silver nanoparticles: preparation and characterization. *Colloids and Surfaces A: Physicochem. Eng. Aspects* **2011**, *384*, 427-431.
171. Stober, W.; Fink, A., Controlled growth of monodisperse silica spheres in the micron size range. *J Colloid Interf Sci* **1968**, *26*, 62-69.
172. Lin, S.; Ionescu, C.; Pike, K. J.; Smith, M. E.; Jones, J. R., Nanostructure evolution and calcium distribution in sol-gel derived bioactive glass. *J. Mater. Chem* **2009**, *19*, 1276-1282.
173. Park, S. K.; Kim, K. D.; Kim, H. T., Preparation of silica nanoparticles: determination of the optimal synthesis conditions for small and uniform particles. *Colloids and Surfaces A: Physicochem. Eng. Aspects* **2002**, *197*, 7-17.
174. Attard, G. S.; Glyde, J. C.; Goltner, C. G., Liquid-crystalline phases as templates for the synthesis of mesoporous silica. *Nature* **1995**, *378*, 366-268.
175. Kresge, C. T.; Leonowicz, M. E.; Roth, W. J.; Vartuli, J. C.; Beck, J. S., Ordered mesoporous molecular sieves synthesized by a liquid-crystal template mechanism. *Nature* **1992**, *359*, 710-712.
176. Cai, Q.; Luo, Z.-S.; Pang, W.-Q.; Fan, Y.-W.; Chen, X.-H.; Cui, F.-Z., Dilute solution routes to various controllable morphologies of MCM-41 silica with a basic medium. *Chem. Mater.* **2001**, *13*, 258-263.
177. Wang, F.; Mao, C., Nanotubes connected to a micro-tank: hybrid micro-/nano-silica architectures transcribed from living bacteria as bioreactors. *Chem. Commun.* **2009**, 1222-1224.
178. Wang, F.; Nimmo, S. L.; Cao, B.; Mao, C., Oxide formation on biological nanostructures via a structure-directing agent: towards an understanding of precise structural transcription. *Chem. Sci.* **2012**, *3*, 2639-2645.
179. Ji, Q.; Iwaura, R.; Shimizu, T., Regulation of silica nanotube diameters: Sol-gel transcription using solvent-sensitive morphological change of peptidic lipis nanotubes as templates. *Chem. Mater.* **2007**, *19*, 1329-1334.

180. Savic, S. M.; Vojisavljevic, K.; Pocuca-Nesic, M.; Zivojevic, K.; Mladenovic, M.; Knezevic, N. Z., Hard template synthesis of nanomaterials based on mesoporous silica. *Metall. Mater. Eng.* **2018**, *24*, 224-241.
181. Woo, E.; Ponvel, K. M.; Ahn, I.-S.; Lee, C.-H., Synthesis of magnetic/silica nanoparticles with a core of magnetic clusters and their application for the immobilization of His-tagged enzymes. *J. Mater. Chem* **2009**, *20*, 1511-1515.
182. Fuji, M.; Shin, T.; Watanabe, H.; Takei, T., Shape-controlled hollow silica nanoparticles synthesized by an inorganic particle template method *Advanced Powder Technology* **2012**, *23*, 562-565.
183. Al-Kaysi, R. O.; Dillon, R. J.; Zhu, L.; Bardeen, C. J., Template assisted synthesis of silica-coated molecular crystal nanorods: from hydrophobic to hydrophilic nanorods *J Colloid Interf Sci* **2008**, *327*, 102-107.
184. Liu, W.; Zhu, Z.; Dong, K.; Li, Z.; Zhou, Y.; Qiu, H.; Gao, Y.; Che, S.; Tang, Z., Gold nanorod@chiral mesoporous silica core-shell nanoparticles with unique optical properties. *J. Am. Chem. Soc* **2013**, *135*, 9659-9664.
185. Wang, Y.; Su, X.; Ding, P.; Lu, S.; Yu, H., Shape-controlled synthesis of hollow silica colloids. *Langmuir* **2013**, *29*, 11575-11581.
186. Yang, X.; He, D.; Wang, K.; Tang, J.; Zou, Z.; He, X.; Xiong, J.; Li, L.; Shangguan, J., Synthesis of hollow mesoporous silica nanorods with controllable aspect ratios for drug release in cancer cells. *ACS Appl. Mater. Interfaces* **2016**, *8*, 20558-20569.
187. Zhao, M.; Kang, W.; Zheng, L.; Gao, Y., Synthesis of silica nanoboxes via a simple hard-template method and their application in controlled release. *Materials Letters* **2010**, *64*, 990-992.
188. Lou, X. W.; Yuan, C.; Archer, L. y. A., Double-walled SnO₂ nano-cacoons with movable magnetic cores. *Adv. Mater.* **2007**, *19*, 3328-3332.
189. Yang, S.; Feng, X.; Wang, L.; Tang, K.; Maier, J.; Mullen, K., Graphene-based Nanosheets with a sandwich structure. *Angew. Chem. Int. Ed.* **2010**, *49*, 4795-4799.
190. Hsu, S.-C.; Liu, S.-Y.; Wang, H.-J.; Huang, M. H., Facet-dependent surface plasmon resonance properties of AU-Cu₂O Core-Shell Nanocubes, octahedra and rhombic dodecahedra. *Small* **2015**, *11*, 195-201.
191. Sumper, M.; Brunner, E., Learning from diatoms: Nature's tool for the production of nanostructured silica *Adv. Func. Mat.* **2006**, *16*, 17-26.
192. Cai, X.; Zhu, G.; Zhang, W.; Zhao, H.; Wang, C.; Qiu, S.; Wei, Y., Diatom-templated synthesis of ordered meso/macroporous hierarchical materials. *Eur. J. Inorg. Chem.* **2006**, 3641-3645.
193. Aw, M. S.; Simovic, S.; Addai-Mensah, J.; Losic, D., Silica microcapsules from diatoms as new carrier for delivery of therapeutics. *Nanomedicine* **2011**, *6*, 1159-1173.
194. Bariana, M.; Aw, M. S.; Kurkuri, M.; Losic, D., Tuning drug loading and release properties of diatom silica microparticles by surface modifications. *Int. J. Pharm.* **2013**, *443*, 230-241.
195. Fessi, H.; Puisieux, F.; Devissaguet, J. P.; Ammourey, N.; Benita, S., Nanocapsule formation by interfacial polymer deposition following solvent displacement. *Int. J. Pharm.* **1989**, *55*, 1-4.
196. Beck, L. R.; Cowsar, D. R.; Lewis, D. H.; Cosgrove, R. J.; Riddle, C. T.; Lowry, S. L.; Epperly, T., A new long-acting injectable microcapsule system for the administration of progesterone. *Fertility and Sterility* **1979**, *31*, 545-551.
197. Kwon, H.-Y.; Lee, J.-Y.; Choi, S.-W.; Jang, Y.; Kim, J.-H., Preparation of PLGA nanoparticles containing estrogen by emulsification diffusion-method. *Colloids and Surfaces A: Physicochem. Eng. Aspects* **2001**, *182*, 123-130.
198. Zweers, M. L. T.; Grijpma, D. W.; Engbers, G. H. M.; Feijen, H., The preparation of monodisperse biodegradable polyester nanoparticles with a controlled size. *J. Biomed. Mater. Res. B: Appl. Biomater.* **2003**, *15*, 559-566.
199. Liu, M.; Zhou, Z.; Wang, X.; Xu, J.; Yang, K.; Cui, Q.; Chen, X.; Cao, M.; Weng, J.; Zhang, Q., Formation of poly(L,D-lactide) spheres with controlled size by direct dialysis. *Polymer* **2007**, *48*, 5767-5779.

200. Broadhead, J.; Rouan, S. K. E.; Rhodes, C. T., The spray drying of pharmaceuticals. *Drug development and industrial pharmacy* **1992**, *18*, 1169-1206.
201. Mao, H.-Q.; Roy, K.; Troung-Le, V. L.; Janes, K. A.; Lin, K. Y.; Wang, Y.; August, J. T., Chitosan-DNA nanoparticles as gene carriers: synthesis, characterisation and transfection efficiency. *J. Control. Release* **2001**, *70*, 399-421.
202. Rokhade, A. P.; Agnihotri, S. A.; Patil, S. A.; Mallikarjuna, N. N.; Kulkarni, P. V., Semi-interpenetrating polymer network microspheres of gelatin and sodium carboxymethyl cellulose for controlled release of ketorolac tromethamine. *Carbohydrate Polymers* **2006**, *65*, 243-252.
203. Sarmento, B.; Ribeiro, A.; Veiga, F.; Sampaio, P.; Neufeld, R.; Ferreira, D., Alginate/chitosan nanoparticles are effective for oral insulin delivery. *Pharm Res* **2007**, *24*, 2198-2206.
204. Cheng, J.; Teply, B. A.; Sherifi, I.; Sung, J.; Luther, G.; Gu, F. X.; Levy-Nissenbaum, E.; Radovic-Moreno, A. F.; Langer, R.; Farokhzad, O. C., Formulation of functionalised PLGA-PEG nanoparticles for in vivo targeted drug delivery. *Biomaterials* **2007**, *28*, 869-876.
205. Kim, J. K.; Yang, S. Y.; Lee, Y.; Kim, Y., Functional nanomaterials based on block copolymer self-assembly. *Progress in Polymer Science* **2010**, *35*, 1325-1349.
206. Choucair, A.; Eisenberg, A., Control of amphiphilic block copolymer morphologies using solution conditions. *Eur. Phys. J. E* **2003**, *10*, 37-44.
207. Li, Z.; Chen, Z.; Cui, H.; Hales, K.; Qi, K.; Wooley, K. L.; Pochan, D. J., Disk morphology and disk-to-cylinder tunability of poly(acrylic acid)-b-poly(methyl acrylate)-b-polystyrene triblock copolymer solution-state assemblies. *Langmuir* **2005**, *21*, 7533-7539.
208. Yu, H.; Jiang, W., Effect of shear flow on the formation of ring-shaped ABA amphiphilic triblock copolymer micelles. *Macromolecules* **2009**, *42*, 3399-3404.
209. Han, K.; Zhang, J.; Zhang, W.; Wang, S.; Xu, L.; Zhang, C.; Zhang, X.; Han, H., Tumor-triggered geometrical shape switch of chimeric peptide for enhanced in vivo tumor internalisation and photodynamic therapy. *ACS Nano* **2017**, *11*, 3178-3188.
210. Nagy, M.; Keller, A., Ellipsoidal polymer particles with predesigned axial ratio. *Polymer Commun.* **1989**, *30*, 133.
211. Ho, C. C.; Keller, A.; Odell, J. A.; Ottewill, R. H., Monodisperse ellipsoidal polystyrene latex particles: preparation and characterisation. *Polymer International* **1992**, *30*, 207-211.
212. Champion, J.; Katare, Y. K.; Mitragotri, S., Making polymeric micro- and nanoparticles of complex shapes. *PNAS* **2007**, *104*, 11901-11904.
213. Meyer, R. A.; Meyer, R. S.; Green, J. J., An automated multidimensional thin film stretching device for the generation of anisotropic polymeric micro- and nanoparticles. *Journal of Biomedical Materials Research* **2015**, *103*, 2747-2757.
214. Seisyan, R. P., Nanolithography in microelectronics: A review. *Technicol. Physics* **2011**, *56*, 1061-1073.
215. Brock, D. C.; Moore, G. E., *Understanding Moore's Law Four decades of Innovation*. Chemical Heritage Foundation: 2006.
216. Penon, O.; Novo, S.; Duran, S.; Ibanez, E.; Nogues, C.; Samitier, J.; Duch, M.; Plaza, J. A.; Perez-Garcia, L., Efficient Biofunctionalization of polysilicon barcodes for adhesion to the zona pellucida of mouse embryos. *Bioconjugate Chem.* **2012**, *23*, 2392-2402.
217. Ziaie, B.; Baldi, A.; Lei, M.; Gu, Y.; Siegal, R. A., Hard and soft micromachining for BioMEMS: review of techniques and examples of applications in microfluidics and drug delivery. *Adv. Drug Deliv. Rev.* **2004**, *56*, 145-172.
218. Ishihara, T.; Luo, X., Nanophotolithography based on surface plasmon interference. In *Nanoplasmonics: From fundamentals to applications*, Kawata, S.; Masuhara, H., Eds. Elsevier: 2006.
219. Fu, X.; Cai, J.; Zhang, X.; Li, W.-D.; Ge, X.; He, Y., Top-down fabrication of shape-controlled, monodisperse nanoparticles for biomedical applications. *Advanced Drug Delivery Reviews* **2018**, *133*, 169-187.
220. Chiappini, C.; Tasciotti, E.; Fakhoury, J. R.; Fine, D.; Pullan, L.; Wang, Y.-C.; Fu, L.; Liu, X.; Ferrari, M., Tailored porous silicon microparticles: fabrication and properties. *ChemPhysChem* **2010**, *11*, 1029-1035.

221. Fernandez-Rosas, E.; Gomez, R.; Ibanez, E.; Barrios, L.; Duch, M.; Esteve, J.; Nogues, C.; Plaza, J. A., Intracellular polysilicon barcodes for cell tracking. *Small* **2009**, *5*, 2433-2439.
222. Agusil, J. P.; Torras, N.; Duch, M.; Esteve, J.; Perez-Garcia, L.; Samitier, J.; Plaza, J. A., Highly anisotropic suspended planar-array chips with multidimensional sub-micrometric biomolecular patterns. *Adv. Func. Mat.* **2017**, *27*.
223. Jaganathan, H.; Godin, B., Biocompatibility assessment of Si-based nano- and micro-particles. *Adv. Drug Deliv. Rev.* **2012**, *64*, 1800-1819.
224. Li, B.; He, M.; Ramirez, L.; George, J.; Wang, J., Multifunctional hydrogel microparticles by polymer-assisted photolithography. *ACS Appl. Mater. Interfaces* **2016**, *8*, 4158-4164.
225. Haghgooei, R.; Toner, M.; Doyle, P. S., Squishy non-spherical hydrogel microparticles. *Macromol. Rapid Commun.* **2010**, *31*, 128-134.
226. Hernandez, C. J.; Mason, T. G., Colloidal alphabet soup: Monodisperse dispersions of shape-designed lithoparticles. *J. Phys. Chem. C* **2007**, *111*, 4477-4480.
227. Cui, Y.; Lu, J.; Fu, X.; Bian, J.; Yuan, C.; Ge, H.; Chen, Y., Near-zero-residual layer nanoimprint based on hybrid nanoimprint soft lithography. *Appl. Phys. A* **2015**, *121*, 371-375.
228. Rolland, J. P.; Maynor, B. W.; Euliss, L. E.; Exner, A. E.; Denison, G. M.; DeSimone, J. M., Direct Fabrication and harvesting of monodisperse, shape-specific nanobiomaterials *J. Am. Chem. Soc* **2005**, *127*, 10096-10100.
229. Rolland, J. P.; Hagberg, E. C.; Denison, G. M.; Carter, K. R.; Simone, J. M. D., High-resolution soft lithography: Enabling materials for nanotechnologies. *Angew. Chem. Int. Ed.* **2004**, *43*, 5796-5799.
230. Enlow, E. M.; Luft, J. C.; Napier, M. E.; DeSimone, J. M., Potent engineered PLGA nanoparticles by virtue of exceptionally high chemotherapeutic loadings. *Nano letters* **2011**, *11*, 808-813.
231. Reuter, K. G.; Perry, J. L.; Kim, D.; Luft, J. C.; Liu, R.; DeSimone, J. M., Targeted PRINT hydrogels: The role of nanoparticle size and ligand density on cell association, biodistribution, and tumor accumulation. *Nano letters* **2015**, *15*, 6371-6378.
232. Merkel, T. J.; Herlihy, K. P.; Nunes, J.; Orgel, R. M.; Rolland, J. P.; DeSimone, J. M., Scalable, Shape-specific, top-down fabrication methods for the synthesis of engineered colloidal particles. *Langmuir* **2009**, *26*, 13086-13096.
233. Juranova, J., Illuminating the cellular and molecular mechanism of the potential toxicity of methacrylate monomers used in biomaterials. *Drug and Chemical Toxicology* **2018**, *43*, 266-278.
234. Chithrani, B. D.; Chan, W. C. W., Elucidating the mechanism of cellular uptake and removal of protein-coated gold nanoparticles of different sizes and shapes. *Nano lett.* **2007**, *7*, 1542-1550.
235. Qiu, Y.; Liu, Y.; Wang, L.; Xu, L.; Bai, R.; Ji, Y.; Wu, X.; Zhao, Y.; Li, Y.; Chen, C., Surface chemistry and aspect ratio mediated cellular uptake of Au nanorods *Biomaterials* **2010**, *31*, 7606-7619.
236. Yu, T.; Malugin, A.; Ghandehari, H., Impact of silica nanoparticle design on cellular toxicity and hemolytic activity. *ACS Nano* **2011**, *5*, 5717-5728.
237. Herd, H.; Daum, N.; Jones, A. T.; Huwer, H.; Ghandehari, H.; Lehr, C.-M., Nanoparticle geometry and surface orientation influence mode of cellular uptake. *ACS Nano* **2013**, *7*, 1961-1973.
238. Huang, X.; Teng, X.; Chen, D.; Tang, F.; He, J., The effect of the shape of mesoporous silica nanoparticles on cellular uptake and cell function. *Biomaterials* **2010**, *31*, 438-448.
239. Li, Y.; Kroger, M.; Liu, W. K., Shape effect in cellular uptake of PEGylated nanoparticles: comparison between sphere, rod, cube and disk. *Nanoscale* **2015**, *7*, 16631-16646.
240. Champion, J. A.; Mitragotri, S., Role of target geometry in phagocytosis. *PNAS* **2006**, *103*, 4930-4934.
241. Champion, J. A.; Mitragotri, S., Shape induced inhibition of phagocytosis of polymer particles. *Pharm Res* **2009**, *26*, 244-249.

242. Sharma, G.; Valenta, D. T.; Altman, Y.; Harvey, S.; Xie, H.; Mitragotri, S.; Smith, J. W., Polymer particle shape independently influences binding and internalization by macrophages. *J. Control. Release* **2010**, *147*, 408-412.
243. Muro, S.; Garnacho, C.; Champion, J. A.; Leferovich, J.; Gajewski, C.; Schuchman, E. H.; Mitragotri, S.; Muzykantov, V. R., Control of endothelial targeting and intracellular delivery of therapeutic enzymes by modulating the size and shape of ICAM-1-targeted carriers. *Mol. Ther.* **2008**, *16*, 1450-1458.
244. Lu, Z.; Qiao, Y.; Zheng, X. T.; Chan-Park, M. B.; Li, C. M., Effect of particle shape on phagocytosis of CdTe quantum dot-cystine composites. *Med. Chem. Commun* **2010**, *1*, 84-86.
245. Kozlovskaya, V.; Alexander, J. F.; Wang, Y.; Kunczewicz, T.; Liu, X.; Godin, B.; Kharlampieva, E., Internalization of red blood cell-mimicking hydrogel capsules with pH-triggered shape responses. *ACS Nano* **2014**, *8*, 5727-5737.
246. Cooley, M.; Sarode, A.; Hoore, M.; Fedosov, D. A.; Mitragotri, S.; Gupta, A. S., Influence of particle size and shape on their margination and wall-adhesion: implications in drug delivery vehicle design across nano-to-micro scale. *Nanoscale* **2018**, *10*, 15350-15364.
247. Decuzzi, P.; Pasqualini, R.; Arap, W.; Ferrari, M., Intravascular delivery of particulate systems: Does geometry really matter? *Pharm Res* **2009**, *26*, 235-243.
248. Serda, R. E.; Gu, J.; Bhavane, R. C.; Liu, X.; Chiappini, C.; Decuzzi, P.; Ferrari, M., The association of silicon microparticles with endothelial cells in drug delivery to the vasculature. *Biomaterials* **2009**, *30*, 2440-2448.
249. Decuzzi, P.; Godin, B.; Tanaka, T.; Lee, S.-Y.; Chiappini, C.; Liu, X.; Ferrari, M., Size and shape effects in the biodistribution of intravascularly injected particles. *J. Control. Release* **2010**, *141*, 320-327.
250. Heyder, J.; Gebhart, J.; Rudolf, G.; Schiller, C. F.; Stahlhofen, W., Deposition of particles in the human respiratory tract in the size range 0.005-15 μm . *J. Aerosol Sci.* **1986**, *17*, 811-825.
251. Chandel, A.; Goyal, A. K.; Ghosh, G.; Rath, G., Recent advances in aerosolised drug delivery. *Biomed. Pharmacother.* **2019**, *112*, e108601.
252. Chung, K. F.; Jeyasingh, K.; Snashall, P. D., Influence of airway calibre on the intrapulmonary dose and distribution of inhaled aerosol in normal and asthmatic subjects. *Eur. Respir. J.* **1988**, *1*, 890-895.
253. Dolovich, M. B.; Killian, D.; Wolff, R. K.; Obminski, G.; Newhouse, M. T., Pulmonary aerosol deposition in chronic bronchitis: intermittent positive pressure breathing versus quiet breathing. *Am J Respir Crit Care Med* **1977**, *115*, 397-402.
254. Lourenco, R. V.; Cotromanes, E., I. Characterization of aerosols and their diagnostic uses. *Arch. Intern. Med.* **1982**, *142*, 2163-2172.
255. Patton, J. S.; Fishburn, C. S.; Weers, J. G., The lungs as a portal of entry for systemic drug delivery. *Proc. Am. Thorac Soc.* **2004**, *1*, 338-344.
256. Warheit, D. B.; Hartsy, M., Role of alveolar macrophage chemotaxis and phagocytosis in pulmonary clearance responses to inhaled particles: comparisons among rodent species. *Micros. Res. Tech* **1993**, *26*, 412-422.
257. Vlahos, R.; Bozinovski, S., Role of alveolar macrophages in chronic obstructive pulmonary disease. *Front Immunol* **2014**, *5*, 1-7.
258. Patel, B.; Gupta, N.; Ahsan, F., Particle engineering to enhance or lessen particle uptake by alveolar macrophages and to influence the therapeutic outcome. *Eur. J. Pharm. Biopharm.* **2015**, *89*, 163-174.
259. Edwards, D. A.; Hanes, J.; Caponetti, G.; Hrkach, J.; Ben-Jebria, A.; Eskew, M. L.; Mintez, J.; Deaver, D.; Lotan, N.; Langer, R., Large porous particles for pulmonary drug delivery. *Science* **1997**, *276*, 1868-1871.
260. Gratton, S. E.; Williams, S. S.; Napier, M. E.; Pohlhaus, P. D.; Zhou, Z.; Wiles, K. B.; Maynor, B. W.; Shen, C.; Olafsen, T.; Samulski, E. T.; Desimone, J. M., The pursuit of a scalable nanofabrication platform for use in material and life science applications. *Acc. Chem. Res.* **2008**, *41*, 1685-1695.

261. Taciak, B.; Bialasek, M.; Braniewska, A.; Sas, Z.; Sawicka, P.; Kiraga, L.; Rygiel, T.; Krol, M., Evaluation of phenotypic and functional stability of RAW 264.7 cell line through serial passages. *PLOS one* **2018**, *13*, 1-13.
262. Gallud, A.; Bondarenko, I.; Feliu, N.; Kupferschmidt, N.; Atluri, R.; Garcia-Bennett, A.; Fadeel, B., Macrophage activation status determines the internalization of mesoporous silica particles of different sizes: Exploring the role of different pattern recognition receptors. *Biomaterials* **2017**, *121*, 28-40.
263. Zhao, Y.; Trewyn, B. G.; Slowing, I. I.; Lin, V. S.-Y., Mesoporous silica nanoparticle-based double drug delivery system for glucose responsive controlled release of insulin and cyclic AMP. *J. Am. Chem. Soc* **2009**, *131*, 8398-8400.
264. Shi, H.; He, X.; Wang, K.; Yuan, Y.; Deng, K.; Chen, J.; Tan, W., Rhodamine B isothiocyanate doped silica-coated fluorescent nanoparticles (RBITC-DSFNPs)-based biprobes conjugated to annexin V for apoptosis detection and imaging. *Nanomedicine-Nanotechnol.* **2007**, *3*, 266-272.
265. Cabanas, M. V.; Lozano, D.; Torres-Pardo, A.; Sobrino, C.; Gonzalez-Calbet, J.; Arcos, D.; Vallet-Regi, M., Features of aminopropyl modified mesoporous silica nanoparticles. Implications on the active targeting capability. *Mater. Chem. Phys.* **2018**, *220*, 260-269.
266. Milgroom, A.; Intrator, M.; Madhavan, K.; Mazzaro, L.; Shandas, R.; Liu, B.; Park, D., Mesoporous silica nanoparticles as a breast-cancer targeting ultrasound contrast agent. *Colloid Surface B* **2014**, *116*, 652-657.
267. Rampazzo, E.; Bonacchi, S.; Juris, R.; Montalti, M.; Genovese, D.; Zaccheroni, N.; Prodi, L.; Rambaldi, D. C.; Zattoni, A.; Reschiglian, P., Energy transfer from silica core-surfactant shell nanoparticles to hosted molecular fluorophores. *J. Phys. Chem. B* **2010**, *114*, 14605-14613.
268. Auger, A.; Samuel, J.; Poncelet, O.; Raccourt, O., A comparative study of non-covalent encapsulation methods for organic dyes into silica particles. *Nanoscale Res Lett* **2011**, *6*, 1-12.
269. Abdelwahab, W. M.; Phillips, E.; Patonay, G., Preparation of fluorescently labeled silica nanoparticles using an amino acid-catalysed seeds regrowth technique: Application to latent fingerprints detection and hemocompatibility studies. *J Colloid Interf Sci* **2018**, *512*, 801-811.
270. Elsaesser, A.; Taylor, A.; Yanes, G. S. d.; Mckerr, G.; Kim, E.-M.; O'Hare, E.; Howard, C. V., Quantification of nanoparticle uptake by cells using microscopical and analytical techniques. *Nanomedicine* **2010**, *5*, 1447-1457.
271. Lee, J.-Y.; Kitaoka, M., A beginner's guide to rigor and reproducibility in fluorescence imaging experiments. *Mol. Biol. Cell* **2018**, *29*, 1519-1525.
272. Ashraf, S.; Said, A. H.; Hartmann, R.; Assmann, M.-A.; Feliu, N.; Lenz, P.; Parak, W. J., Quantitative uptake by cells as analysed by different methods. *Angew. Chem. Int. Ed.* **2020**, *59*, 5438-5453.
273. Fei, C.; Lillico, D. M. E.; Hall, B.; Rieger, A. M.; Stafford, J. L., Connected component masking accurately identifies the ratio of phagocytosed and cell-bound particles in individual cells by imaging flow cytometry. *Cytom Part A* **2017**, *91A*, 372-381.
274. Vranic, S.; Boggetto, N.; Contremoulins, V.; Mornet, S.; Reinhardt, N.; Marano, F.; Baeza-Squiban, A.; Boland, S., Deciphering the mechanisms of cellular uptake of engineered nanoparticles by accurate evaluation of internalization using imaging flow cytometry. *Part Fibre Toxicol* **2013**, *10*, 1-16.
275. Schimmelpfeng, J.; Drossolmeyer, E.; Hofheinz, V.; Seidel, A., Influence of surfactant components and exposure geometry on the effects of quartz and asbestos on alveolar macrophages. *Environ. Health Persp.* **1992**, *97*, 225-231.
276. Fenoglio, I.; Croce, A.; Renzo, F. D.; Tiozzo, R.; Fubini, B., Pure-silica zeolites (porosils) as model solids for the evaluation of the physicochemical features determining silica toxicity to macrophages. *Chem. Res. Toxicol.* **2000**, *13*, 489-500.
277. Hart, G.; Hesterberg, T., In vitro toxicity of respirable-size particles of diatomaceous earth and crystalline silica compared with asbestos and titanium dioxide. *Occup. Environ. Med.* **1998**, *40*, 29-42.

278. Trewyn, B. G.; Nieweg, J. A.; Zhao, Y.; Lin, V. S. Y., Biocompatible mesoporous silica nanoparticles with different morphologies for animal cell membrane penetration. *Chem. Eng. J.* **2008**, *137*, 23-29.
279. Meng, H.; Yang, S.; Li, Z.; Xia, T.; Chen, J.; Ji, Z.; Zhang, H.; Wang, X.; Lin, S.; Huang, C.; Zhou, Z. H.; Zink, J. I.; Nel, A. E., Aspect ratio determines the quantity of mesoporous silica nanoparticle uptake by a small GTPase-dependent macropinocytosis mechanism. *ACS Nano* **2011**, *6*, 4434-4447.
280. Hao, N.; Li, L.; Zhang, Q.; Huang, X.; Meng, X.; Zhang, Y.; Chen, D.; Tang, F.; Li, L., The shape effect of PEGylated mesoporous silica nanoparticles on cellular uptake pathway in Hela cells. *Micropor. Mesopor. Mat.* **2012**, *162*, 14-23.
281. Tschernig, T.; Fischer, T.; Grissmer, A.; Beckmann, A.; Meier, C.; Lipp, P.; Schneider, M., Silica nanoparticles of microrods enter lung epithelial cells. *Biomed. Rep.* **2018**, *9*, 156-160.
282. Kurtz-Chalot, A.; Villiers, C.; Pourchez, J.; Boudard, D.; Martini, M.; Marche, P. N.; Cottier, M.; Forest, V., Impact of silica nanoparticle surface chemistry on protein corona formation and consequential interactions with biological cells. *Mater. Sci. Eng. C* **2017**, *75*, 16-24.
283. Karamen, D. S.; Desai, D.; Senthilkumar, R.; Johansson, E. M.; Ratts, N.; Oden, M.; Eriksson, J. E.; Sahlgren, C.; Toivola, D. M.; Rosenholm, J. M., Shape engineering vs organic modification of inorganic nanoparticles as a tool for enhancing cellular internalization. *Nanoscale Res Lett* **2012**, *7*, 1-14.
284. Torras, N.; Aguil, J. P.; Vazquez, P.; Duch, M.; Hernandez-Pinto, A. M.; Samitier, J.; Rosa, E. J. d. I.; Esteve, J.; Suarez, T.; Perez-Garcia, L.; Plaza, J. A., Suspended planar-array chips for molecular multiplexing at the microscale. *Adv. Mater.* **2016**, *28*, 1449-1454.
285. Casal-Dujat, L.; Rodrigues, M.; Yague, A.; Calpena, A. C.; Amabilino, D. B.; Javier Gonzalez-linares; Borrás, M.; Perez-Garcia, L., Gemini imidazolium amphiphiles for the synthesis, stabilization, and drug delivery from gold nanoparticles. *Langmuir* **2011**, *28*, 2368-2381.
286. Reyes, M. E. A. Novel pi-functional components of micro- and nanoparticles for nanomedicine. Universitat de Barcelona Barcelona, 2017.
287. Liberman, A.; Mendez, N.; Trogler, W. C.; Kummel, A. C., Synthesis and surface functionalization of silica nanoparticles for nanomedicine. *Surf. Sci. Rep.* **2014**, *69*, 132-158.
288. Penon, O.; Siapkias, D.; Novo, S.; Duran, S.; Oncins, G.; Errachid, A.; Barrios, L.; Nogues, C.; Duch, M.; Plaza, J. A.; Perez-Garcia, L., Optimized immobilization of lectins using self-assembled monolayers on polysilicon encoded materials for cell tagging. *Colloids Surface B* **2014**, *116*, 104-113.
289. Song, K.-C.; Park, J.-K.; Kang, H.-U.; Kim, S.-H., Synthesis of hydrophilic coating solution for polymer substrate using glycidoxypyltrimethoxysilane. *J. Sol-Gel Sci. Technol.* **2003**, *27*, 53-59.
290. Han, Y.; Mayer, D.; Offenhausser, A.; Ingebrandt, S., Surface activation of thin silicon oxides by wet cleaning and silanization. *Thin Solid Films* **2006**, *510*, 175-180.
291. Giraud, L.; Nadarajah, R.; Matar, Y.; Bazin, G.; Sun, J., Amino-functionalized monolayers covalently grafted to silica-based substrates as a robust primer anchorage in aqueous media. *Appl. Surf. Sci.* **2016**, *370*, 476-485.
292. Aragon, P.; Noguera, P.; Banuls, M.-J.; Puchades, R.; Maquieira, A.; Gonzalez-Martinez, M. A., Modulating receptor-ligand binding in biorecognition by setting surface wettability. *Anal. Bioanal. Chem.* **2018**, *410*, 5723-5730.
293. Perera, H. J.; Mortazavian, H.; Blum, F. D., Surface properties of silane-treated diatomaceous earth coatings: Effect of alkyl chain length. *Langmuir* **2017**, *33*, 2799-2809.
294. Information, N. C. f. B. PubChem Compound Summary for CID 6694, Rhodamine B. <https://pubchem.ncbi.nlm.nih.gov/compound/Rhodamine-B>.
295. Yoo, H.; Juliano, R. L., Enhanced delivery of antisense oligonucleotides with fluorophore-conjugated PAMAM dendrimers. *Nucleic Acids Res.* **2000**, *28*, 4225-4231.

296. Yan, X.; Poelstra, K.; Scherphof, G. L.; Kamps, J. A. A. M., A role for scavenger receptor B-I in selective transfer of rhodamine-PE from liposomes to cells. *Biochem. Biophys. Res. Co.* **2004**, 325, 908-914.
297. Shen, Y.; Chen, J.; Liu, Q.; Feng, C.; Gao, X.; Wang, L.; Zhang, Q.; Jiang, X., Effect of wheat germ agglutinin density on cellular uptake and toxicity of wheat germa agglutinin conjugated PEG-PLA nanoparticles in Calu-3 cells. *Int. J. Pharm.* **2011**, 413, 184-193.
298. Thiele, L.; Rothen-Rutishauser, B.; Jilek, S.; Wunderli-Allenspach, H.; Merkle, H. P.; Walter, E., Evaluation of particle uptake in human blood monocyte-derived cells in-vitro. Does phagocytosis activity of dendritic cells measure up with macrophages. *J. Control. Release* **2001**, 76, 59-71.
299. Toyohara, A.; Inaba, K., Transport of phagosomes in mouse peritoneal macrophages. *J. Cell Sci.* **1989**, 94, 143-153.
300. Al-Haddad, A.; Shonn, M. A.; Redlich, B.; Blocker, A.; Burkhardt, J. K.; Yu, H.; III, J. A. H.; Weiss, D. G.; Steffen, W.; Griffiths, G.; Kuznetsov, S. A., Myosin Va Bound to Phagosomes Binds to F-Actin and Delays Microtubule-dependent Motility. *Mol. Biol. Cell* **2001**, 12, 2742-2755.
301. Araki, N., Role of microtubules and myosins in Fc gamma receptor-mediated phagocytosis. *Front. Biosci.* **2006**, 11, 1479-1490.
302. Keller, S.; Berghoff, K.; Kress, H., Phagosomal transport depends strongly on phagosome size. *Sci. rep.* **2017**, 7, 1-15.
303. Desjardins, M., Biogenesis of phagolysosomes: the 'kiss and run' hypothesis. *Trends Cell Biol.* **1995**, 5, 183-186.
304. Hunh, K. K.; Eskelinen, E.-L.; Scott, C. C.; Malevanets, A.; Saftig, P.; Grinstein, S., LAMP proteins are required for fusion of lysosomes with phagosomes. *EMBO J.* **2007**, 26, 313-324.
305. Hewitt, R. E.; Vis, B.; Pele, L. C.; Faria, N.; Powell, J. J., Imaging flow cytometry assays for quantifying pigment grade titanium dioxide particle internalization and interaction with immune cells in whole blood. *Cytom Part A* **2017**, 91A, 1009-1020.
306. Srivatsan, A.; Pera, P.; Joshi, P.; Wang, Y.; Missert, J. R.; Tracy, E. C.; Tabaczynski, W. A.; Yao, R.; Sajjad, M.; Baumann, H.; Pandey, R. K., Effect of chirality on cellular uptake, imaging and photodynamic therapy of photosensitizers derived from chlorophyll-a. *Bioorgan. Med. Chem.* **2015**, 23, 3603-3617.
307. Peterson, P. K.; Verhoef, J.; Quie, P. G., Influence of temperature on opsonization and phagocytosis of staphylococci. *Infect. Immun.* **1977**, 15, 175-179.
308. Kim, E. J.; Lee, M. Y.; Jeon, Y. J., Silymarin inhibits morphological changes in LPS-stimulated macrophages by blocking NF-KB pathway. *Korean J Physiol Pharmacol* **2015**, 19, 211-218.
309. Pi, J.; Li, T.; Liu, J.; Su, X.; Wang, R.; Yang, F.; Bai, H.; Jin, H.; Cai, J., Detection of lipopolysaccharide induced inflammatory responses in RAW264.7 macrophages using atomic force microscopy. *Micron* **2014**, 65, 1-9.
310. Rieger, A. M.; Hall, B. E.; Barreda, D. R., Macrophage activation differentially modulates particle binding, phagocytosis and downstream antimicrobial mechanisms. *Dev. Comp. Immunol.* **2010**, 34, 1144-1159.
311. May, R. C.; Machesky, L. M., Phagocytosis and the actin cytoskeleton. *J. Cell Sci.* **2001**, 114, 1061-1077.
312. Patel, P. C.; Harrison, R. E., Membrane ruffles capture C3bi-opsonized particles in activated macrophages. *Mol. Biol. Cell* **2008**, 19, 4628-4639.
313. Freeman, S. A.; Grinstein, S., Phagocytosis: receptors, signal integration, and the cytoskeleton. *Immunol. Rev.* **2014**, 262, 193-215.
314. Kleveta, G.; Borzecka, K.; Zdioruk, M.; Czerkies, M.; Kuberczyk, H.; Sybirna, N.; Sobota, A.; Kwiatkowska, K., LPS induces phosphorylation of actin-regulatory proteins leading to actin reassembly and macrophage motility. *J. Cell. Biochem.* **2012**, 113, 80-92.
315. Williams, L. M.; Ridley, A. J., Lipopolysaccharide induces actin reorganization and tyrosine phosphorylation of Pyk2 and paxillin in monocytes and macrophages. *J. Immunol.* **2000**, 164, 2028-2036.

316. Doshi, N.; Swiston, A. J.; Gilbert, J. B.; Alcaraz, M. L.; Cohen, R. E.; Rubner, M. F.; Mitragotri, S., Cell-based drug delivery devices using phagocytosis resistant backpacks. *Adv. Mater.* **2011**, 23, H105-H109.
317. Fernandez-Rosas, E.; Gomez, R.; Ibanez, E.; Barrios, L.; Duch, M.; Esteve, J.; Plaza, J. A.; Nogues, C., Internalization and cytotoxicity analysis of silicon-based microparticles in macrophages and embryos. *Biomed Microdevices* **2010**, 12, 371-379.
318. Novo, S.; Barrios, L.; Santalo, J.; Gomez-Martinez, R.; Duch, M.; Esteve, J.; Plaza, J. A.; Nogues, C.; Ibanez, E., A novel embryo identification system by direct tagging of mouse embryos using silicon-based bar codes. *Human Reproduction* **2011**, 26, 96-105.
319. Novo, S.; Penon, O.; Barrios, L.; Nogues, C.; Santalo, J.; Duran, S.; Gomez-Martinez, R.; Samitier, J.; Plaza, J. A.; Perez-Garcia, L.; Ibanez, E., Direct embryo tagging and identification system by attachment of biofunctionalized polysilicon barcodes to the zona pellucida of mouse embryos. *Human Reproduction* **2013**, 28, 1519-1527.
320. Gomez-Martinez, R.; Hernandez-Pinto, A. M.; Duch, M.; Vazquez, P.; Zinoviev, K.; Rosa, E. J. d. I.; Esteve, J.; Suarez, T.; Plaza, J. A., Silicon chips detect intracellular pressure changes in living cells. *Nature Nanotechnology* **2013**, 8, 517-521.
321. Novo, S.; Mora-Espi, I.; Gomez-Martinez, R.; Barrios, L.; Ibanez, E.; Such, X.; Duch, M.; Mora, X.; Plaza, J. A.; Nogues, C., Traceability of human sperm samples by direct tagging with polysilicon microbarcodes. *Reproductive BioMedicine Online* **2015**, 31, 162-170.
322. Duch, M.; Torras, N.; Asami, M.; Suzuki, T.; Arjona, M. I.; Gomez-Martinez, R.; VerMilyea, M. D.; Castilla, R.; Plaza, J. A.; Perry, A. C. F., Tracking intracellular forces and mechanical property changes in mouse one-cell embryo development *Nature Materials* **2020**.
323. Duran, S.; Duch, M.; Gomez-Martinez, R.; Fernandez-Regulez, M.; Agusil, J. P.; Reina, M.; Muller, C.; Paulo, A. S.; Esteve, J.; Castel, S.; Plaza, J. A., Internalisation and viability studies of suspended nanowire silicon chips in HeLa Cells. *Nanomaterials* **2020**, 10, 1-14.
324. Tanaka, T.; Mangala, L. S.; Vivas-Mejia, P. E.; Nieves-Alicea, R.; Mann, A. P.; Mora, E.; Han, H.-D.; Shahzad, M. M. K.; Liu, X.; Bhavane, R.; Gu, J.; Fakhoury, J. R.; Chiappini, C.; Lu, C.; Matsuo, K.; Godin, B.; Stone, R. L.; Nick, A. M.; Lopez-Berestein, G.; Sood, A. K.; Ferrari, M., Sustained small interfering RNA delivery by mesoporous silicon particles. *Cancer Res.* **2010**, 70, 3697-3696.
325. Yokoi, K.; Godin, B.; Oborn, C. J.; Alexander, J. F.; Liu, X.; Fidler, I. J.; Ferrari, M., Porous silicon nanocarriers for dual targeting tumor associated endothelial cells and macrophages in stroma of orthotopic human pancreatic cancers. *Cancer Lett.* **2013**, 334, 319-327.
326. Shen, J.; Xu, R.; Mai, J.; Kim, H.-C.; Guo, X.; Qin, G.; Yang, Y.; Wolfram, J.; Mu, C.; Xia, X.; Gu, J.; Liu, X.; Mao, Z.-W.; Ferrari, M.; Shen, H., High capacity nanoporous silicon carrier for systemic delivery of gene silencing therapeutics. *ACS Nano* **2013**, 7, 9867-9880.
327. Ven, A. L. v. d.; Kim, P.; Haley, O. H.; Fakhoury, J. R.; Adriani, G.; Schmulen, J.; Moloney, P.; Hussain, F.; Ferrari, M.; Liu, X.; Yun, S.-H.; Decuzzi, P., Rapid tumorigenic accumulation of systemically injected plateloid particles and their biodistribution. *J. Control. Release* **2012**, 158, 148-155.
328. Telko, M. J.; Hickey, A. J., Dry powder inhaler formulation. *Respir. Care* **2005**, 50, 1209-1227.
329. Pudasaini, N.; Upadhyay, P. P.; Parker, C. R.; Hagen, S. U.; Bond, A. D.; Rantanen, J., Downstream processability of crystal habit-modified active pharmaceutical ingredient *Org. Process Res. Dev.* **2017**, 21, 571-577.
330. Gomez-Martinez, R.; Vazquez, P.; Duch, M.; Muriano, A.; Pinacho, D.; Sanvicens, N.; Sanchez-Baeza, F.; Boya, P.; Rosa, E. J. d. I.; Esteve, J.; Suarez, T.; Plaza, J. A., Intracellular Silicon chips in living cells. *Small* **2009**, 6, 499-502.
331. Kern, W., The evolution of silicon wafer cleaning technology. *J. Electrochem. Soc.* **1990**, 137, 1887-1892.
332. Kim, J.; Seidler, P.; Wan, L. S.; Fill, C., Formation, structure, and reactivity of amino-terminated organic films on silicon substrates. *J. Colloid Interface Sci.* **2009**, 329, 114-119.

333. Lu, X.; Cui, W.; Huang, Y.; Zhao, Y.; Wang, Z., Surface modification on silicon with chitosan and biological research. *Biomed. Mater* **2009**, *4*, 1-5.
334. Tanaka, M.; Sawaguchi, T.; Kuwahara, M.; Niwa, O., Surface modification of silicon oxide with trialkoxysilanes toward close-packed monolayer formation. *Langmuir* **2013**, *29*, 6361-6368.
335. Shircliff, R. A.; Stradins, P.; Moutinho, H.; Fennell, J.; Ghirardi, M. L.; Cowley, S. W.; Branz, H. M., Angle-resolved XPS analysis and characterization of monolayer and multilayer silane films for DNA coupling to silica. *Langmuir* **2013**, *29*, 4057-4067.
336. Gunda, N. S. K.; Singh, M.; Norman, L.; Kaur, K.; Mitra, S., Optimization and characterization of biomolecule immobilization on silicon substrates using (3-aminopropyl)triethoxysilane (APTES) and glutaraldehyde linker. *Appl. Surf. Sci.* **2014**, *305*, 522-530.
337. Salzman, G. C., Light scatter: detection and usage. In *Curr Protoc. Cytom*, 2001.
338. Suzuki, H.; Toyooka, T.; Ibuki, Y., Simple and easy method to evaluate uptake potential of nanoparticles in mammalian cells using flow cytometric light scatter analysis. *Environ. Sci. Technol.* **2007**, *41*, 3018-3024.
339. Zucker, R. M.; Massaro, E. J.; Sanders, K. M.; Degn, L. L.; Boyes, W. K., Detection of TiO₂ Nanoparticles in cells by flow cytometry. *Cytom Part A* **2010**, *77A*, 677-685.
340. Toduka, Y.; Toyooka, T.; Ibuki, Y., Flow cytometric evaluation of nanoparticles using side-scattered light and reactive oxygen species-mediated fluorescence-correlation with genotoxicity. *Environ. Sci. Technol.* **2012**, *46*, 7629-7636.
341. Friedrich, R. P.; Janko, C.; Poettler, M.; Tripal, P.; Zaloga, J.; Cicha, I.; Durr, S.; Nowak, J.; Odenbach, S.; Slabu, I.; Liebl, M.; Trahms, L.; Stapf, M.; Hilger, I.; Lyer, S.; Alexiou, C., Flow cytometry for intracellular SPION quantification: specificity and sensitivity in comparison with spectroscopic methods. *International Journal of Nanomedicine* **2015**, *10*, 4185-4201.
342. Cai, D.; Blair, D.; Dufort, F. J.; Gumina, M. R.; Huang, Z.; Hong, G.; Wagner, D.; Canahan, D.; Kempa, K.; Ren, Z. F.; Chiles, T. C., Interaction between carbon nanotubes and mammalian cells: characterization by flow cytometry and application. *Nanotechnology* **2008**, *19*, 1-10.
343. Baldwin, L.; Flanagan, B. F.; Hunt, J. A., Flow cytometric measurement of phagocytosis reveals a role for C3b in metal particle uptake by phagocytes. *Journal of Biomedical Materials Research A* **2004**, *73A*, 80-85.
344. Serda, R. E.; Gu, J.; Burks, J. K.; Ferrari, K.; Ferrari, C.; Ferrari, M., Quantitative mechanics of endothelial phagocytosis of silicon microparticles. *Cytom Part A* **2009**, *75A* (752-760).
345. Donaldson, K.; Murphy, F. A.; Duffin, R.; Poland, C. A., Asbestos, carbon nanotubes and the pleural mesothelium: a review of the hypothesis regarding the role of long fibre retention in the parietal pleura, inflammation and mesothelioma. *Part. Fibre Toxicol.* **2010**, *7*, 1-17.
346. Malich, G.; Markovic, B.; Winder, C., The sensitivity and specificity of the MTS tetrazolium assay for detecting the in vitro cytotoxicity of 20 chemicals using human cell lines. *Toxicology* **1997**, *124*, 179-192.
347. Santini, M. T.; Rainaldi, G.; Ferrante, A.; Romano, R.; Clemente, S.; Motta, A.; Berardis, B. D.; Balduzzi, M.; Paoletti, L.; Indovina, P. L., Environmental fine particulate matter (PM 2.5) activates the RAW 264.7 macrophage cell line even at very low concentrations as revealed by ¹H NMR. *Chem. Res. Toxicol.* **2004**, *17*, 63-74.
348. Romero, S.; Clainche, C. L.; Didry, D.; Egile, C.; Pantaloni, D.; Carlier, M.-F., Formin is a processive motor that requires profilin to accelerate actin assembly and associated ATP hydrolysis. *Cell* **2004**, *119*, 419-429.
349. Waters, K. M.; Masiello, L. M.; Zangar, R. C.; Tarasevich, B. J.; Karin, n. J.; Quesenberry, R. D.; Bandyopadhyay, S.; Teguarden, J. G.; Pounds, J. G.; Thrall, B. D., Macrophage responses to silica nanoparticles are highly conserved across particle sizes. *Toxicol. Sci.* **2009**, *107*, 553-569.

350. Riss, T. L.; Moravec, R. A., Use of multiple assay endpoints to investigate the effects of incubation time, dose of toxin and plating density in cell-based cytotoxicity assays. *Assay Drug Dev Technol* **2004**, *2*, 51-62.
351. Savage, D. T.; Hilt, J. Z.; Dziubla, T. D., In vitro methods for assessing nanoparticle toxicity. In *Nanotoxicity: Methods and Protocols, Methods in Molecular Biology*, Zhang, Q., Ed. Springer Nature: NY, USA, 2019; Vol. 1894.
352. Diakonova, M.; Bokoch, G.; Swanson, J. A., Dynamics of cytoskeletal proteins during Fcg receptor-mediated phagocytosis in macrophages. *Mol. Biol. Cell* **2002**, *13*, 402-411.
353. Viera, O. V.; Botelho, R. J.; Grinstein, S., Phagosome maturation: aging gracefully. *Biochem. J.* **2002**, *366*, 689-704.
354. Czibener, C.; Sherer, N. M.; Becker, S. M.; Pypaert, M.; Hui, E.; Chapman, E. R.; Mothes, W.; Andrews, N. W., Ca²⁺ and synaptotagmin VII-dependent delivery of lysosomal membrane to nascent phagosomes. *J. Cell Biol.* **2006**, *174*, 997-1007.
355. Tapper, H.; Sundler, R., Glucan receptor and zymosan-induced lysosomal enzyme secretion in macrophages. *Biochem. J.* **1995**, *306*, 829-835.
356. Bi, G.-Q.; Alderton, J. M.; Steinherdt, R. A., Calcium-regulated exocytosis is required for membrane resealing. *J. Cell Biol.* **1995**, *131*, 1747-1758.
357. Miyake, K.; McNeil, P. L., Vesicle accumulation and exocytosis at sites of plasma membrane disruption. *J. Cell Biol.* **1995**, *131*, 1737-1745.
358. Weissman, G.; Zurier, R. B.; Spieler, P. J.; Goldstein, I. M., Mechanisms of lysosomal enzyme release from leukocytes exposed to immune complexes and other particles. *JEM* **1971**, *134*, 149-165.
359. Fruijter-Polloth, C., The toxicological mode of action and the safety of synthetic amorphous silica-A nanostructured material. *Toxicology* **2012**, *294*, 61-79.
360. Stone, K. C.; Mercer, R. R.; Gehr, P.; Stocktill, B.; Crapo, J., Allometric relationships of cell numbers and size in the mammalian lung. *Am. J. Respir. Cell Mol. Biol.* **1991**, *6*, 235-243.
361. Blair, W. J., Human respiratory tract model for radiological protection: A revision of the ICRP dosimetric model for the respiratory system. *Health Physics* **1989**, *57*, 249-253.
362. Kim, C. S.; Hu, S. C., Regional deposition of inhaled particles in human lungs: comparison between men and woman. *J. Appl. Physiol.* **1998**, *84*, 1834-1844.
363. Abdelrahim, M. E., Emitted dose and lung deposition of inhaled terbutaline from turbobhaler at different conditions. *Resp. Med.* **2009**, *104*, 682-689.
364. Martin, G. P.; MacRitchie, H. B.; Marriot, C.; Zeng, X.-M., Characterization of a carrier-free dry powder aerosol formulation using inertial impaction and laser diffraction. *Pharm Res* **2006**, *23*, 2210-2219.
365. Labiris, N. R.; Dolovich, M. B., Pulmonary drug delivery. Part I: Physiological factors affecting therapeutic effectiveness of aerosolized medications. *J. Clin. Pharmacol.* **2003**, *56*, 588-599.
366. Albrecht, C.; Hohr, D.; Haberzettl, P.; Becker, A., Surface-dependent quartz uptake by macrophages: potential role in pulmonary inflammation and lung clearance. *Inhal. Toxicol.* **2007**, *19*, 39-48.
367. Landuyt, K. L. V.; Cokic, S. M.; Asbach, C.; Hoet, P.; Godderis, L.; Reichl, F. X.; Meerbeek, B. V.; Vennemann, A.; Wiemann, M., Interaction with rat alveolar macrophages with dental composite dust. *Part Fibre Toxicol* **2016**, *13*, 1-13.
368. Constantini, L. M.; Gilberti, R. M.; Knecht, D. A., The phagocytosis and toxicity of amorphous silica. *PLOS one* **2011**, *6*, 1-10.
369. Watanabe, M.; Okada, M.; Kudo, Y.; Tonori, Y.; Niitsuya, M.; Sato, T.; Aizawa, Y.; Kotani, M., Differences in the effects of fibrous and particulate titanium dioxide on alveolar macrophages of fischer 344 rats. *J. Toxicol. Environ. Health Part A* **2002**, *65*, 1047-1060.
370. Jr, R. F. H.; Thakur, S. A.; Holiam, A., Silica binding and toxicity in alveolar macrophages. *Free radic. biol. med.* **2008**, *44*, 1246-1258.
371. Thibodeau, M. S.; Giardina, C.; Knecht, D. A.; Helble, J.; Hubbard, A. K., Silica-induced apoptosis in mouse alveolar macrophages is initiated by lysosomal enzyme activity. *Toxicol. Sci.* **2004**, *80*, 34-48.

372. Thibodeau, M.; Giardina, C.; Hubbard, A. K., Silica-induced caspase activation in mouse alveolar macrophages is dependent upon mitochondrial integrity and aspartic proteolysis. *Toxicol. Sci.* **2003**, *76*, 91-101.
373. Mathaes, R.; Winter, G.; Besheer, A.; Engert, J., Influence of particle geometry and PEGylation on phagocytosis of particulate carriers. *Int. J. Pharm.* **2014**, *465*, 159-164.
374. Key, J.; Palange, A. L.; Gentile, F.; Aryal, S.; Stigliano, C.; Mascolo, D. D.; Rosa, E. D.; Cho, M.; Lee, Y.; Singh, J.; Decuzzi, P., Soft discoidal polymeric nanoconstructs resist macrophage uptake and enhance vascular targeting in tumors. *ACS Nano* **2015**, *9*, 11628-11641.
375. Beningo, K. A.; Wang, Y.-L., Fc-receptor-mediated phagocytosis is regulated by mechanical properties of the target. *J. Cell Sci.* **2001**, *115*, 849-856.
376. Anselmo, A. C.; Zhang, M.; Kumar, S.; Vogus, D. R.; Menegatti, S.; Helgeson, M. E.; Mitragotri, S., Elasticity of nanoparticles influences their blood circulation, phagocytosis, endocytosis, and targeting. *ACS Nano* **2015**, *9*, 3169-3177.
377. Alexander, J. F.; Kozlovskaya, V.; Chen, J.; Kunczewicz, T.; Kharlampieva, E.; Godin, B., Cubical shape enhances the interaction of layer-by-layer polymeric particles with breast cancer cells. *Adv. Healthcare Mater.* **2015**, *4*, 2657-2666.
378. Hopcroft, M. A.; Nix, W. D.; Kenny, T. W., What is the young's modulus of silicon. *J. Microelectromech. Syst.* **2010**, *19*, 229-238.
379. Klyacho, N. L.; Polak, R.; Haney, M. J.; Zhao, Y.; Neto, R. J. G.; Hill, M. C.; Kabanov, A. V.; Cohen, R. E.; Rubner, M. F.; Batrakova, E., Macrophages with cellular backpacks for targeted drug delivery to the brain. *Biomaterials* **2017**, *140*, 79-87.
380. Shields, C. W.; Evans, M. A.; Wang, L. L.-W.; Baugh, N.; Iyer, S.; Wu, D.; Zhao, Z.; Pusuluri, A.; Ukidve, A.; Pan, D. C.; Mitragotri, S., Cellular backpacks for macrophage immunotherapy. *Sci. Adv.* **2020**, *6*, 1-11.
381. Kwiatkowska, K.; Sobota, A., Signalling pathways in phagocytosis. *BioEssays* **1999**, *21*, 422-431.
382. Shao, J.; Ma, J. K. H., Characterization of a mannosylphospholipid liposome system for drug targeting to alveolar macropages. *Drug Deliv.* **1997**, *4*, 43-48.
383. Valencia, P. M.; Hanewich-Hollatz, M. H.; Gao, W.; Karim, F.; Langer, R.; Karnik, R.; Farokhzad, O. C., Effects of ligands with different water solubilities on self-assembly and properties of targeted nanoparticles. *Biomaterials* **2011**, *32*, 6226-6233.
384. Sanchez, L.; Yi, Y.; Yu, Y., Effect of partial PEGylation on particle uptake by macrophages. *Nanoscale* **2017**, *9*, 288-297.
385. Mosqueira, V. C. F.; Lergrand, P.; Gulik, A.; Bourdon, O.; Gref, R.; Labarre, D.; Barratt, G., Relationship between complement activation, cellular uptake and surface physicochemical aspects of novel PEG-modified nanocapsules. *Biomaterials* **2001**, *22*, 2967-2979.
386. Zahr, A. S.; Davis, C. A.; Pishko, M. V., Macrophage uptake of core-shell nanoparticles surface modified with poly(ethylene glycol). *Langmuir* **2006**, *22*, 8178-8185.
387. Fontana, G.; Licciardi, M.; Mansueto, S.; Schillaci, D.; Giammona, G., Amoxicillin-loaded polyethylcyanoacrylate nanoparticles: Influence of PEG coating on the particle size, drug release rate and phagocytic uptake *Biomaterials* **2001**, *22*, 2857-2865.
388. Nguyen, V. H.; Lee, B.-J., Protein corona: a new approach for nanomedicine design. *Int. J. Nanomedicine* **2017**, *12*, 3137-3151.
389. Liu, X.; Jin, Q.; Ji, Y.; Ji, J., Minimizing nonspecific phagocytic uptake of biocompatible gold nanoparticles with mixed charged zwitterionic surface modification. *J. Mater. Chem* **2012**, *22*, 1916-1927.
390. Zhao, J.; Chai, Y.-D.; Zhang, J.; Huang, P.-F.; Nakashima, K.; Gong, Y.-K., Long circulating micelles of an amphiphilic random copolymer bearing cell outer membrane phosphorylcholine zwitterions. *Acta Biomater.* **2015**, *16*, 94-102.
391. Jung, S.; Park, S.; Choi, D.; Hong, J., Efficient drug delivery carrier surface without unwanted adsorption using sulfobetaine zwitterion. *Adv. Mater. Interfaces* **2020**, *7*, 1-11.
392. Encinas, N.; Angulo, M.; Astorga, C.; Colilla, M.; Izquierdo-Barba, I.; Vallet-Regi, M., Mixed-charge pseudo-zwitterionic mesoporous silica nanoparticles with low-fouling and reduced cell uptake properties. *Acta Biomater.* **2019**, *84*, 317-327.

393. Lin, W.; Ma, G.; Wu, J.; Chen, S., Different in vitro and in vivo behaviours between poly(carboxybetaine methacrylate) and poly(sulfobetaine methacrylate). *Colloid Surface B* **2016**, *146*, 888-894.
394. Chacon-Salinas, R.; Serafin-Lopez, J.; Ramos-Payan, R.; Mendez-Aragon, P.; Hernandez-Pando, R.; Soolingen, D. V.; Flores-Romo, L.; Estrada-Parra, S.; Estrada-Garcia, I., Differential pattern of cytokine expression by macrophages infected in vitro with different mycobacterium tuberculosis genotypes. *Clin. Exp. Immunol.* **2005**, *140*, 443-449.
395. Gutierrez, P.; Closa, D.; Piner, R.; Bulbena, O.; Menendez, R.; Torres, A., Macrophage activation in exacerbated COPD with and without community acquired pneumonia. *Eur. Respir. J.* **201**, *36*, 285-291.
396. Gordon, S., Alternative activation of macrophages. *Nat. Rev. Immunol* **2003**, *3*, 23-35.
397. Han, S.; Mallampalli, R. K., The role of surfactant in lung disease and host defense against pulmonary infections. *Annals ATS* **2015**, *12*, 765-774.
398. Wright, J. R.; Clements, J. A., Metabolism and turnover of lung surfactant. *Am Rev Respir Dis* **1987**, *135*, 428-444.
399. Barr, T. L.; Seal, S., Nature of the use of adventitious carbon as a binding energy standard. *J. Vac. Sci* **1995**, *13*, 1239-1246.
400. Shircliff, R. A.; Martin, I. T.; Pankow, J. W.; Fennell, J.; Stradins, P.; Ghirardi, M. L.; Cowley, S. W.; Branz, H. M., High-resolution X-ray photoelectron spectroscopy of mixed silane monolayers for DNA attachment. *ACS Appl. Mater. Interfaces* **2011**, *3*, 3285-3292.
401. Jaska, G.; Stefane, B.; Kovac, J., XPS and AFM characterization of aminosilanes with different numbers of bonding sites on a silicon wafer. *Surf. Interface Anal.* **203**, *45*, 1709-1713.
402. Szezes, A., Effect of the enzymatically modified supported dipalmitoylphosphatidylcholine (DPPC) bilayers on calcium carbonate formation. *Colloid. Polym. Sci* **2016**, *294*, 409-419.
403. Chen, R.; Hunt, J. A.; Fawcett, S.; D'sa, R.; Akhtar, R.; Curran, J. M., The optimization and production of stable homogenous amin enriched surfaces with characterized nanotopographical properties for enhanced osteoinduction of mesenchymal stem cells. *J. Biomed. Mater. Res. A* **2018**, *106*, 1863-1877.
404. Kallury, K. M. R.; Macdonald, P. M.; Thompson, M., Effect of surface water and base catalysis on the silanization of silica by (aminopropyl)alkoxysilanes studied by X-ray photoelectron spectroscopy and ¹³C cross-polarization/magic angle spinning nuclear magnetic resonance. *Langmuir* **1994**, *10*, 492-499.
405. Lin, O. H.; Akil, H. M.; Ishak, Z. A. M., Surface-activated nanosilica treated with silane coupling agents/polypropylene composites: Mechanical, morphological, and thermal studies. *Polym. Compos.* **2011**, *32*, 1568-1583.
406. Pech, W. A. T.; Esparza-Ruiz, A.; Quintana-Owen, P.; Vilchis-Nestor, A. R.; Carrera-Figueiras, C.; Alejandro; Avila-Ortega, Effects of different amounts of APTES on physicochemical and structural properties of amino-functionalized MCM-41-MSNa. *J. Sol-Gel Sci. Technol.* **2016**, *80*, 697-708.
407. Andriyko, L. S.; Zarko, V. I.; Gun'ko, V. M.; Marynin, A. I.; Olishevskiy, V. V.; Skwarek, E.; Janusz, W., Electrical and physical characteristics of silica nanoparticles in aqueous media effected by cations Na⁺, Ba²⁺ and Al³⁺. *Adsorp. Sci. Technol.* **2015**, *33*, 601-607.
408. Junior, J. A. A.; Baldo, J. B., The behaviour of zeta potential of silica suspensions. *NJGC* **2014**, *4*, 29-37.
409. Lowry, G. V.; Hill, R. J.; Harper, S.; Rawle, A. F.; Hendren, C. O.; Klaessig, F.; Nobbmann, U.; Sayre, P.; Rumble, J., Guidance to improve the scientific value of zeta-potential measurements in nanoEHS. *Environ. Sci. Nano* **2016**, *3*, 953-965.
410. Bilalis, P.; Tziveleka, L.-A.; Varlas, S.; Iatrou, H., pH-sensitive nanogates based on poly(L-histidine) for controlled drug release from mesoporous silica nanoparticles. *Polym. Chem.* **2016**, *7*, 1475-1485.
411. Lee, C. H.; Park, S. H.; Chung, W.; Kim, J. Y.; Kim, S. H., Preparation and characterization of surface modified silica nanoparticles with organosilane compounds. *Colloid. Surf. A Physicochem. Eng. Asp.* **2011**, *384*, 318-322.

412. Wu, Z.; Xiang, H.; Kim, T.; Chun, M.-S.; Lee, K., Surface properties of submicrometer silica spheres modified with aminopropyltriethoxysilane. *J. Colloid Interface Sci.* **2006**, *304*, 119-124.
413. Hanim, S. A. M.; Malek, N. A. N. N.; Ibrahim, Z., Amine-functionalized, silver-exchanged zeolite NaY: Preparation, characterization and antibacterial activity. *Appl. Surf. Sci.* **2016**, *360*, 121-130.
414. Hong, S.; Han, D.; Jang, K.-S., Zeta potential-tunable silica abrasives and fluorinated surfactants in chemical mechanical polishing slurries. *Wear* **2021**, *466-467*, e203590.
415. Gun'ko, V. M.; Voronin, E. F.; Pakhlov, E. M.; Zarko, V. I.; Turov, V. V.; Guzenko, N. V.; Leboda, R.; Chibowski, E., Features of fumed silica coverage with silanes having three or two groups reacting with the surface. *Colloid. Surf. A Physicochem. Eng. Asp.* **2000**, *166*, 187-201.
416. Xu, W.; Riikonen, J.; Nissinen, T.; Suvanto, M.; Rilla, K.; Li, B.; Wang, Q.; Deng, F.; Lehto, V.-P., Amine surface modifications and fluorescent labelling of thermally stabilized mesoporous silicon nanoparticles. *J. Phys. Chem. C* **2012**, *116*, 22307-22314.
417. Knowles, B. R.; Yang, D.; Wagner, P.; MacLaughlin, S.; Higgins, M. J.; Molino, P. J., Zwitterion functionalized silica nanoparticle coatings: The effect of particle size on protein, bacteria, and fungal spore adhesion. *Langmuir* **2019**, *35*, 1335-1345.
418. Knowles, B. R.; Wagner, P.; MacLaughlin, S.; Higgins, M. J.; Molino, P. J., Silica Nanoparticles functionalized with zwitterionic sulfobetaine siloxane for application as a versatile antifouling coating system. *ACS Appl. Mater. Interfaces* **2017**, *9*, 18584-18594.
419. Oliveira, J. F. A. d.; Scheffer, F. R.; Landis, R. F.; Neto, E. T.; Rotello, V. M.; Cardoso, M. B., Dual functionalization of nanoparticles for generating corona-free and noncytotoxic silica nanoparticles. *ACS Appl. Mater. Interfaces* **2018**, *10*, 41919-41923.
420. Dong, Z.; Mao, J.; Yang, M.; Wang, D.; Bo, S.; Ji, X., Phase behaviour of poly(sulfobetaine methacrylate)-grafted silica nanoparticles and their stability in protein solutions. *Langmuir* **2011**, *27*, 15282-15291.
421. Guo, S.; Janczewski, D.; Zhu, X.; Qunitana, R.; He, T.; Neoh, K. G., Surface charge control for zwitterionic polymer brushes: tailoring surface properties to antifouling applications. *J. Colloid Interface Sci.* **2015**, *452*, 43-53.
422. Starck, P.; Mosse, W. K. J.; Nicholas, N. J.; Spiniello, M.; Tyrell, J.; Nelson, A.; Qiao, G. G.; Ducker, W. A., Surface chemistry and rheology of polysulfobetaine-coated silica. *Langmuir* **2007**, *23*, 7587-7593.
423. Chiao, Y.-H.; Chen, S.-t.; Sivakumar, M.; Ang, M. B. M. Y.; Patra, T.; Almodovar, J.; Wickramasinghe, S. R.; Hung, W.-S.; Lai, J.-Y., Zwitterionic polymer brush grafted on polyvinylidene difluoride membrane promoting enhanced ultrafiltration performance with augmented antifouling property. *Polymers* **2020**, *12*, e1303.
424. Bhattacharjee, S., DLS and zeta potential - What they are and what they are not? *J. Control. Release* **2016**, *235*, 337-351.
425. Wang, W.; Lu, Y.; Yue, Z.; Liu, W.; Cao, Z., Ultrastable core-shell structured nanoparticles directly made from zwitterionic polymers. *Chem. Commun.* **2014**, *50*, 15030-15033.
426. Estephan, Z. G.; Jaber, J. A.; Schlenoff, J. B., Zwitterion-stabilized silica nanoparticles: toward nonstick nano. *Langmuir* **2010**, *26*, 16884-16889.
427. Kulkarni, S. A.; Ogale, S. B.; Vijayamohanan, K. P., Tuning the hydrophobic properties of silica particles by surface silanization using mixed self-assembled monolayers. *J. Colloid Interface Sci.* **2008**, *318*, 372-379.
428. Wu, C.-J.; Huang, C.-J.; Jiang, S.; Sheng, Y.-J.; Tsao, H.-K., Superhydrophilicity and spontaneous spreading on zwitterionic surfaces: carboxybetaine and sulfobetaine. *RSC Adv.* **2016**, *6*, 24827-24834.
429. Singh, V.; Huang, C.-J.; Sheng, Y.-J.; Tsao, H.-K., Smart zwitterionic sulfobetaine silane surfaces with switchable wettability for aqueous/nonaqueous drops. *J. Mater. Chem. A* **2018**, *6*, 2279-2288.

430. Hoppstadter, J.; Seif, M.; Dembek, A.; Cavelius, C.; Huwer, H.; Kraegeloh, A.; Kiemer, A. K., M2 polarization enhances silica nanoparticle uptake by macrophages. *Front. Pharmacol.* **2015**, *6*, 1-12.
431. Wallace, W. E.; Keane, M. J.; Murray, D. K.; Chisholm, W. P.; Maynard, A. D.; Ong, T.-m., Phospholipid lung surfactant and nanoparticle surface toxicity: lessons from diesel soots and silicate dusts. *J. Nanopart. Res.* **2007**, *9*, 23-38.
432. Herzog, E.; Byrne, H. J.; Casey, A.; Davoren, M.; Lenz, A.-G.; Maier, K. L.; Duschl, A.; Oostingh, G. J., SWCNT suppress inflammatory mediator responses in human lung epithelium in vitro. *Toxicol. Appl. Pharmacol.* **2009**, *234*, 378-390.
433. Vranic, S.; Garcia-Verdugo, I.; Darnis, C.; Sallenave, J.-M.; Boggetto, N.; Marano, F.; Boland, S.; Baeza-Squiban, A., Internalization of SiO₂ nanoparticles by alveolar macrophages and lung epithelial cells and its modulation by the lung surfactant substitute Curosurf *Environ. Sci. Pollut. Res.* **2013**, *20*, 2761-2770.
434. Camner, P.; Lundborg, M.; Lastbom, L.; Gerde, P.; Gross, N.; Jarstrand, C., Experimental and calculated parameters on particle phagocytosis. *J. Appl. Physiol.* **2002**, *92*, 2608-2616.
435. Khanbeigi, R. A.; Kumar, A.; Sadouki, F.; Lorenz, C.; Forbes, B.; Dailey, L. A.; Collins, H., The delivered dose: Applying pharmacokinetics to in vitro investigations of nanoparticles internalization by macrophages. *J. Control. Release* **2012**, *162*, 259-266.
436. Roser, M.; Fischer, D.; Kissel, T., Surface-modified biodegradable albumin nano- and microspheres. II: effect of surface charges on in vitro phagocytosis and biodistribution in rats. *Eur. J. Pharm. Biopharm.* **1998**, *46*, 255-263.
437. Sharma, P.; Sen, D.; Neelakantan, V.; Shankar, V.; Jhunjhunwala, S., Disparate effects of PEG or albumin based surface modification on the uptake of nano and microparticles. *Biomater. Sci.* **2019**, *7*, 1411-1421.
438. Simon-Yarza, T.; Formiga, F. R.; Tamayo, E.; Pelacho, B.; Prosper, F.; Blanco-Prieto, M. J., PEGylated-PLGA microparticles containing VEGF for long term drug delivery. *Int. J. Pharm.* **2013**, *440*, 13-18.
439. Gonzalez, C. M.; Pizarro-Guerra, G.; Droguett, F.; Sarabia, M., Artificial biomembrane based on DPPC - Investigation into phase transition and thermal behaviour through ellipsometric techniques. *Biochim. Biophys. Acta* **2015**, *1848*, 2295-2307.
440. Castro, C. E. d.; Ribeiro, C. A. S.; Alavarse, A. C.; Albuquerque, L. J. C.; Silva, M. C. C. d.; Jager, E.; Surman, F.; Schmidt, V.; Giacomelli, C.; Giacomelli, F. C., Nanoparticle-Cell interaction: Surface chemistry effects on the cellular uptake of biocompatible block copolymer assemblies. *Langmuir* **2018**, *34*, 2180-2188.
441. Garcia, K. P.; Zarschler, K.; Barbaro, L.; Barreto, J. A.; O'Malley, W.; Spiccia, L.; Steohan, H.; Graham, B., Zwitterionic-coated "stealth" nanoparticles for biomedical applications: Recent advances in countering biomolecular corona formation and uptake by the mononuclear phagocyte system. *Small* **2014**, *10*, 2516-2529.
442. Barbe, C.; Bartlett, J.; Kong, L.; Finnie, K.; Lin, H. Q.; Larkin, M.; Calleja, S.; Bush, A.; Calleja, G., Silica particles: A novel drug-delivery system. *Adv. Mater.* **2004**, *16*, 1-8.
443. Kulkarni, S. A.; Feng, S.-S., Effects of particle size and surface modification on cellular uptake and biodistribution of polymeric nanoparticles for drug delivery. *Pharm. Res.* **2013**, *30*, 2512-2522.
444. Copenhaver, A. M.; Casson, C. N.; Nguyen, H. T.; Fung, T. C.; Duda, M. M.; Roy, C. R., Alveolar macrophages and neutrophils are the primary reservoirs for legionella pneumophila and mediate cytosolic surveillance of type IV secretion. *Infect. Immun.* **2014**, *82*, 4325-4336.
445. Wong, M. E.; Jaworowski, A.; Hearps, A. C., The HIV reservoir in monocytes and macrophages. *Front. Immunol.* **2019**, *10*, 1-16.
446. Guirado, E.; Schlesinger, L. S.; Kaplan, G., Macrophages in tuberculosis: friend or foe. *Semin. Immunopathol.* **2013**, *35*, 563-583.
447. Mischler, S. E.; Cauda, E. G.; Giuseppe, M. D.; McWilliams, L. J.; Croix, C. S.; Sun, M.; Franks, J.; Ortiz, L., Differential activation of RAW 264.7 macrophages by size-segregated crystalline silica. *J. Occup. Med. Toxicol.* **2016**, *11*, 1-14.

448. Veranth, J. M.; Cutler, N. S.; Kaser, E. G.; Reilly, C. A.; Yost, G. S., Effects of cell type and culture media on interleukin-6 secretion in response to environmental particles. *Toxicol. in vitro* **2008**, *22*, 498-509.
449. Salonen, R. O.; Halinen, A. I.; Pennanen, A. S.; Hirvonen, M.-R.; Sillanpaa, M.; Hillamo, R.; Shi, T.; Borm, P.; Sandell, E.; Koskentalo, T.; Aarnio, P., Chemical and in vitro toxicologic characterization of wintertime and springtime urban-air particles with an aerodynamic diameter below 10 μ m in Helsinki. *Scand. J. Environ. Health* **2004**, *30*, 80-90.
450. Arnida; Janat-Amsbury, M. M.; Ray, A.; Peterson, C. M.; Ghandehari, H., Geometry and surface characteristics of gold nanoparticles influence their biodistribution and uptake by macrophages. *Eur. J. Pharm. Biopharm.* **2011**, *77*, 417-423.
451. Hed, J.; Hallden, G.; Johansson, S. G. O.; Larson, P., The use of fluorescence quenching in flow cytometry to measure the attachment and ingestion phases in phagocytosis in peripheral blood without prior cell separation. *Journal of Immunological methods* **1987**, *101*, 119-125.
452. Illien, F.; Rodriguez, N.; AMoura, M.; Joliot, A.; Pallerla, M.; Cribier, S.; Burlina, F.; Sagan, S., Quantitative fluorescence spectroscopy and flow cytometry analyses of cell-penetrating peptides internalization pathways: optimization, pitfalls, comparison with mass spectrometry quantification. *Sci. rep.* **2016**, *6*, 36938.
453. Nuutila, J.; Lilius, E.-M., FLOW cytometric quantitative determination of ingestion by phagocytes needs the distinguishing of overlapping populations of binding and ingesting cells. *Cytom Part A* **2004**, *65A*, 93-102.
454. Thiele, L.; Merkle, H. P.; Walter, E., Phagocytosis and phagosomal fate of surface-modified microparticles in dendritic cells and macrophages. *Pharm. Res.* **2003**, *20*, 221-228.
455. Patino, T.; Soriano, J.; Barrios, L.; Ibanez, E.; Nogues, C., Surface modification of microparticles cause different uptake responses in normal and tumoral human breast epithelial cells. *Scientific reports* **2015**, *5*, e11371.
456. Lu, J.; Liong, M.; Zink, J. I.; Tamanoi, F., Mesoporous silica nanoparticles as a delivery system for hydrophobic anti cancer drugs. *Small* **2007**, *3*, 1341-1346.
457. Manju, S.; Sreenivasan, K., Enhanced drug loading on magnetic nanoparticles by layer-by-layer assembly using drug conjugates: Blood compatibility evaluation and targeted drug delivery in cancer cells. *Langmuir* **2011**, *27*, 14489-12296.
458. Rodrigues, M.; Calpena, A. C.; Amabilino, D. B.; Ramos-Lopez, D.; Lapuente, J. d.; Perez-Garcia, L., Water-soluble gold nanoparticles based on imidazolium gemini amphiphiles incorporating piroxicam. *RSC Adv.* **2014**, *4*, 9279-9287.
459. Almanza-Workman, A. M.; Raghavan, S.; Deymier, P.; Monk, D. J.; Roop, R., Aqueous silane-surfactant co-dispersions for deposition of hydrophobic coatings onto pre-oxidised polysilicon. *Colloid. Surf. A Physicochem. Eng. Asp.* **2004**, *232*, 67-75.
460. Almanza-Workman, A. M.; Raghavan, S.; Petrovic, S.; Gogoi, B.; Deymier, P.; Monk, D. J.; Roop, R., Characterization of highly hydrophobic coatings deposited onto pre-oxidized silicon from water dispersible organosilanes. *Thin Solid Films* **2003**, *423*, 77-87.
461. Fadeev, A. Y.; McCarthy, T. J., Self-assembly is not the only reaction possible between alkyltrichlorosilanes and surfaces: Monomolecular and oligomeric covalently attached layers of dichloro- and trichloroalkylsilanes on silicon. *Langmuir* **2000**, *16*, 7268-7274.
462. Bunker, B. C.; Carpick, R. W.; Assink, R. A.; Thomas, M. L.; Hankins, M. G.; Voigt, J. A.; Sipola, D.; Boer, M. P. d.; Gulley, G. L., The impact of solution agglomeration on the deposition of self-assembled monolayers. *Langmuir* **2000**, *16*, 7742-7751.
463. Tollis, S.; Dart, A. E.; Tzircotis, G.; Endres, R. G., The zipper mechanism in phagocytosis: energetic requirements and variability in phagocytic cup shape. *BMC Syst. Biol.* **2010**, *4*, 1-17.
464. Moller, J.; Luehmann, T.; Hall, H.; Vogel, V., The race to the pole: How high-aspect ratio shape and heterogeneous environments limit phagocytosis of filamentous escherichia coli bacteria by macrophages. *Nano lett.* **2012**, *12*, 2901-2905.
465. Doshi, N.; Mitragotri, S., Macrophages recognize size and shape of their targets. *PLOS one* **2010**, *5*, 1-6.

466. Ye, J.; Shi, X.; Jones, W.; Rojanasakul, Y.; Cheng, N.; Schwegler-Berry, D.; Baron, P.; Deye, G. J.; Li, C.; Castranova, V., Critical role of glass fiber length in TNF-alpha production and transcription factor activation in macrophages. *Am. J. Physiol. Lung Cell Mol. Physiol.* **1999**, 276, L426-L434.
467. Schinwald, A.; Donaldson, K., Use of back-scatter electron signals to visualise cell/nanowires interactions in vitro and in vivo; frustrated phagocytosis of long fibres in macrophages and compartmentalisation in mesothelial cells in vivo. *Part. Fibre Toxicol.* **2012**, 9, 1-13.
468. Hirota, K.; Hsegawa, T.; Hinata, H.; Ito, F.; Inagawa, H.; Kochi, C.; Soma, G.-I.; Makino, K.; Terada, H., Optimum conditions for efficient phagocytosis of rifampicin-loaded PLGA microspheres by alveolar macrophages. *J. Control. Release* **2007**, 119, 69-76.
469. Pacheco, P.; White, D.; Sulchek, T., Effects of microparticle size and Fc density on macrophage phagocytosis. *PLOS one* **2013**, 8, e60989.
470. Schleh, C.; Hohlfeld, J. M., Interaction of nanoparticles with the pulmonary surfactant system. *Inhal. Toxicol.* **2009**, 21, 97-103.

Appendix I – Supporting information from chapter 3

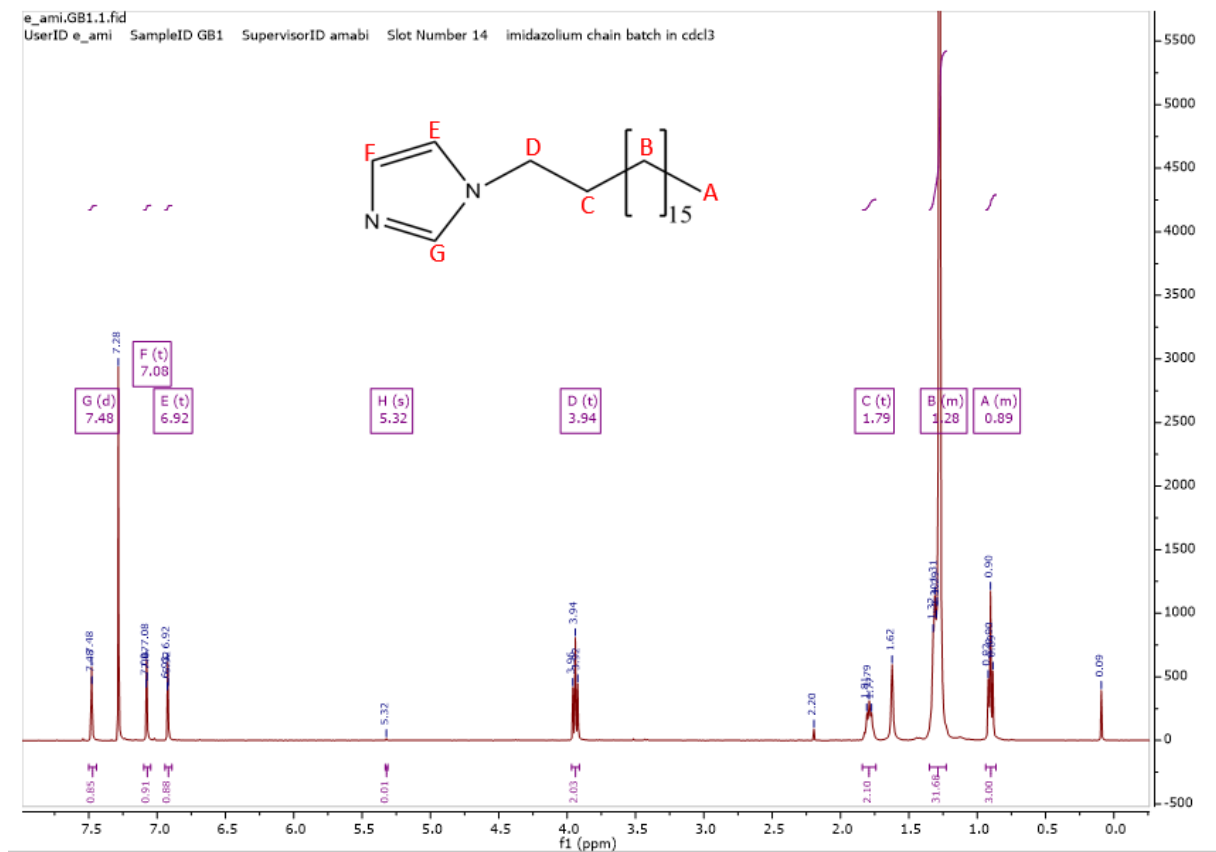


Figure S3.1: ^1H NMR of 1-Octadecyl 1H Imidazole

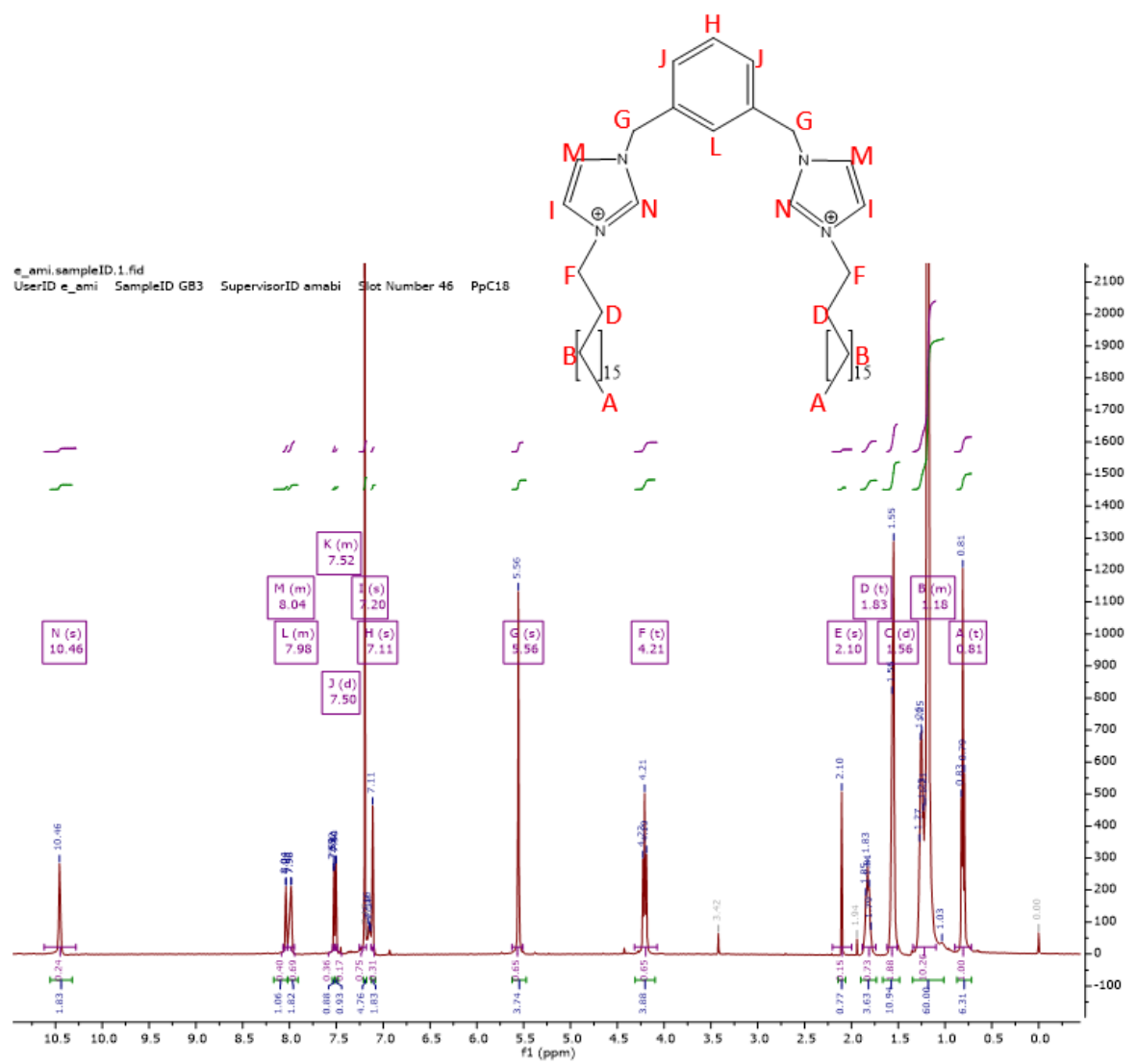


Figure S3.2: ^1H NMR of 1.2Br

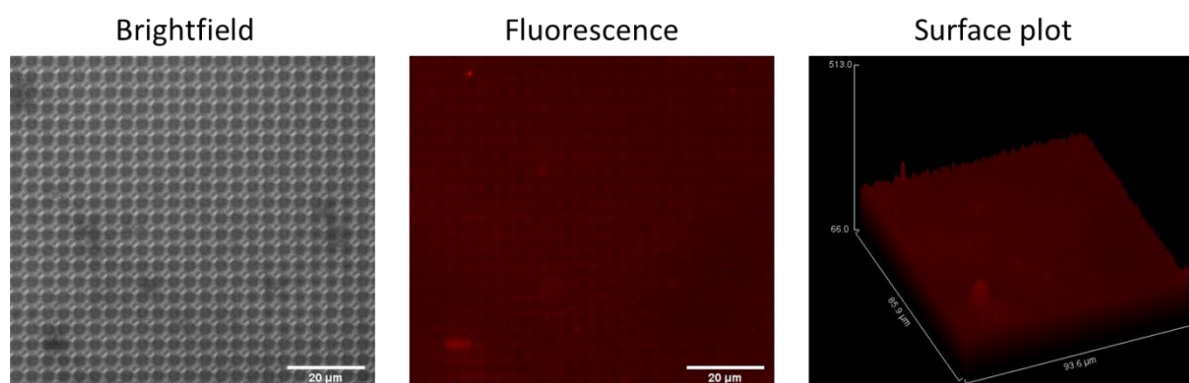


Figure S3.3: Brightfield, fluorescence, and surface plots of surfaces washed with water instead of DMSO after imidazolium treatment in DMSO

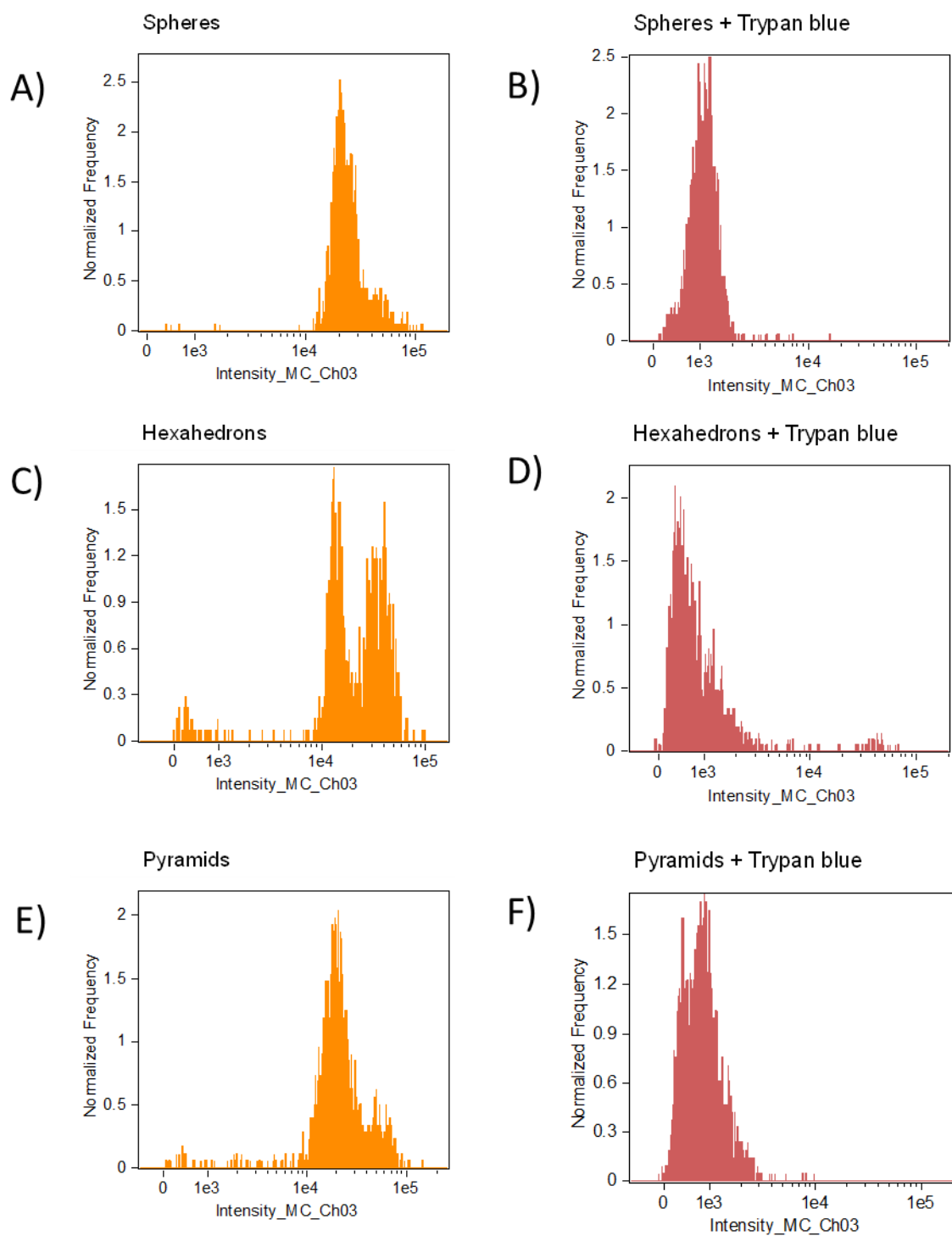


Figure S3.4: Fluorescence intensity histograms of RBITC labelled particles before and after trypan blue quenching.

A) Spheres B) Spheres + trypan blue C) Hexahedrons D) Hexahedrons + trypan blue E) Pyramids F) Pyramids + trypan blue

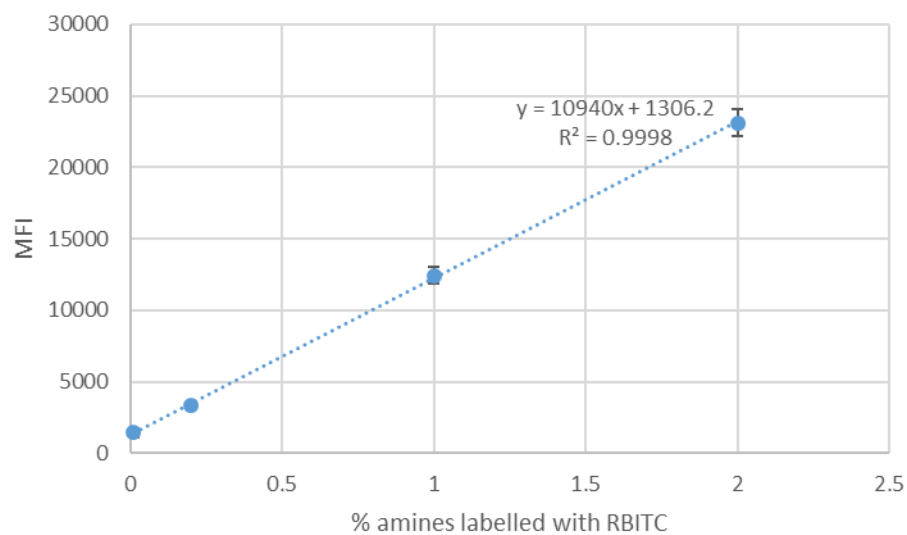


Figure S3.5: Calibration of particle labelling. 3 μm silicon oxide spheres were modified using AUTES pre-labelled with different concentrations of RBITC so that the percentage of surface labelling was known. MFI was then measured using flow cytometry to compare with silicon oxide shapes labelled using AUTES then RBITC sequentially.

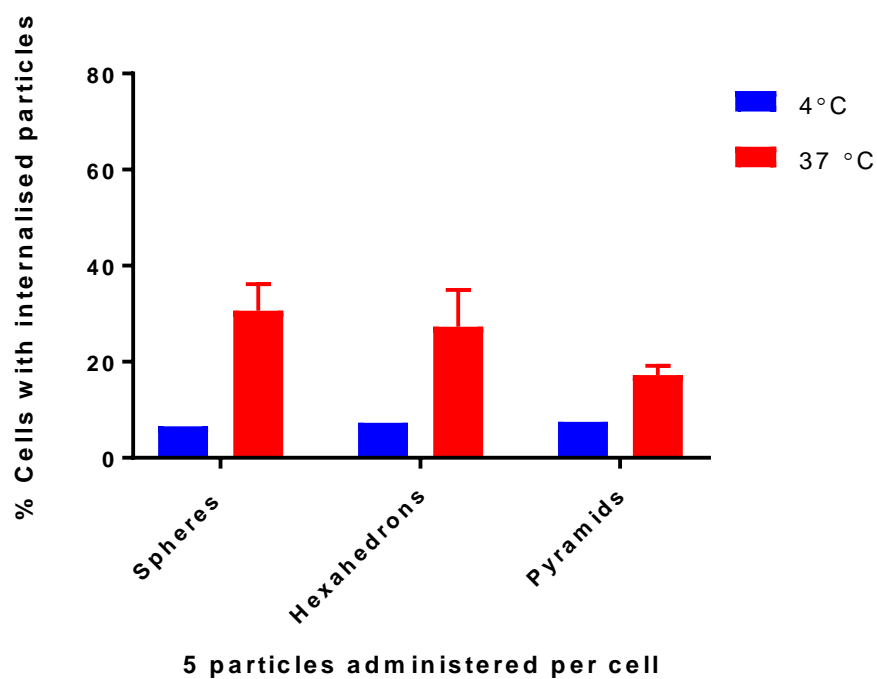


Figure S3.6: Effect of temperature on phagocytosis. Cells were incubated at 4°C for 30 minutes before administration of pre-chilled particles and for the duration of the experiment (4 hours). Cellular uptake was determined by image analysis.

Quantification of particle internalisation by Image analysis

Single cell populations were determined by plotting cell area against cell aspect ratio as shown in figure S3.7. Each dot on the scatter plot is linked with an image and so gating can be checked visually and different populations distinguished to remove unwanted images from the analysis. The population of single cells is then analysed to select a population of cells that are in focus. This is done by creating a histogram using the gradient RMS feature as shown in figure S3.8. This feature ranks images based on their focus, images that have higher scores are more in-focus. By visually checking cells in each bin a minimum focus can be designated (GRMS >50) which is then used for all further analyses.

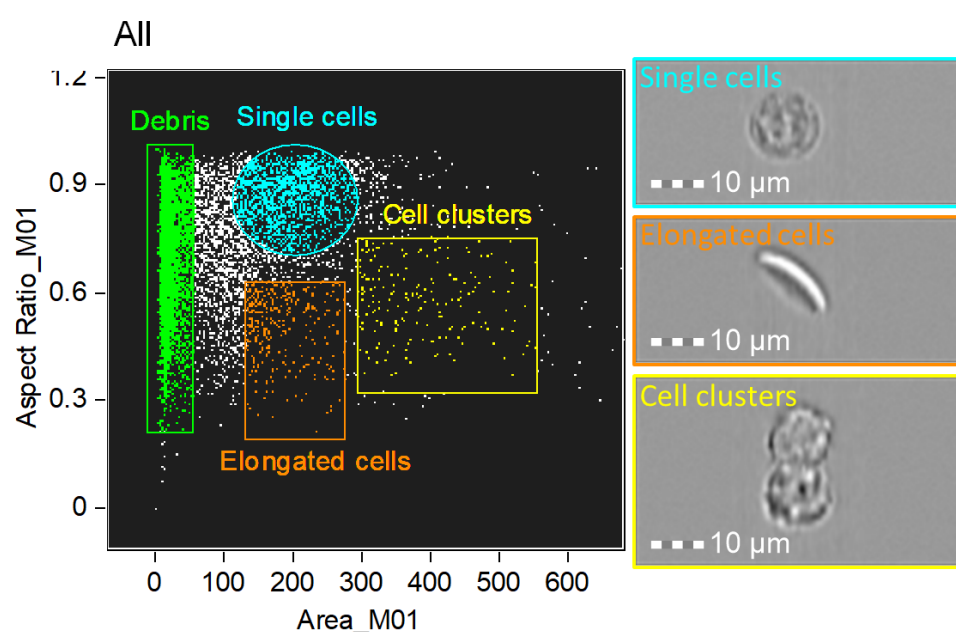


Figure S3.7: Gating of single cell population

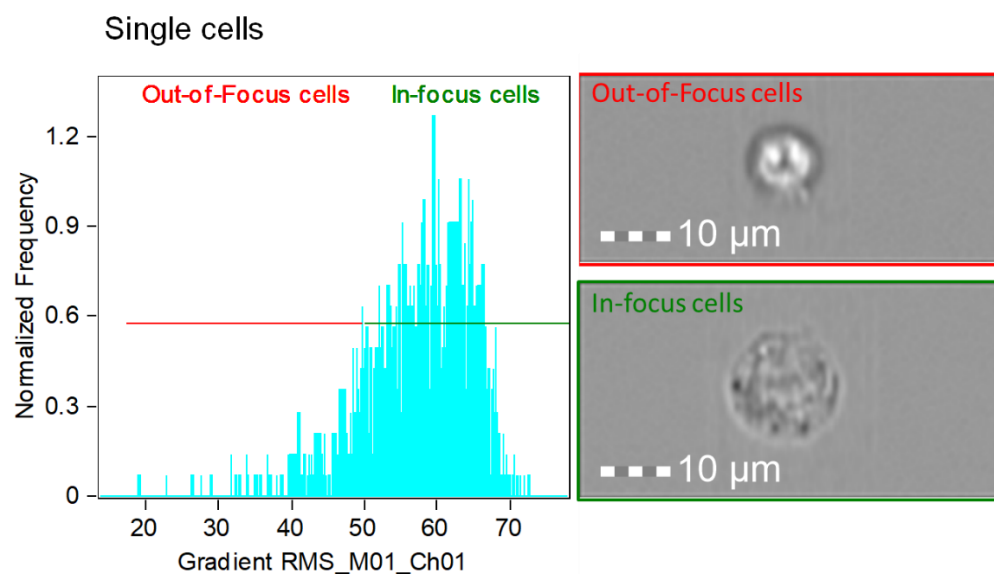


Figure S3.8 Gating of in-focus cell population

In order to quantify particle uptake using image analysis it was first necessary to distinguish populations of cells which were associated with particles. This was achieved by plotting a histogram of fluorescence intensity as shown in figure S3.9. In order to adequately distinguish populations, a control sample of cells that had not been exposed to particles was analysed and a region spanning the fluorescence range of these cells designated as non-associated cells (figure S3.9A). A region with a fluorescence intensity above this gate was then designated as being associated with particles. By analysing a sample of cells which had been exposed to fluorescent particles it was demonstrated that a distinct population appears within the associated region (figure S3.9B). Further confirmation of the cells association with particles was performed by selecting images from each of the regions examples of which are shown in figure S3.9C. Particle fluorescence can be seen in Ch03 and is present only in associated cells.

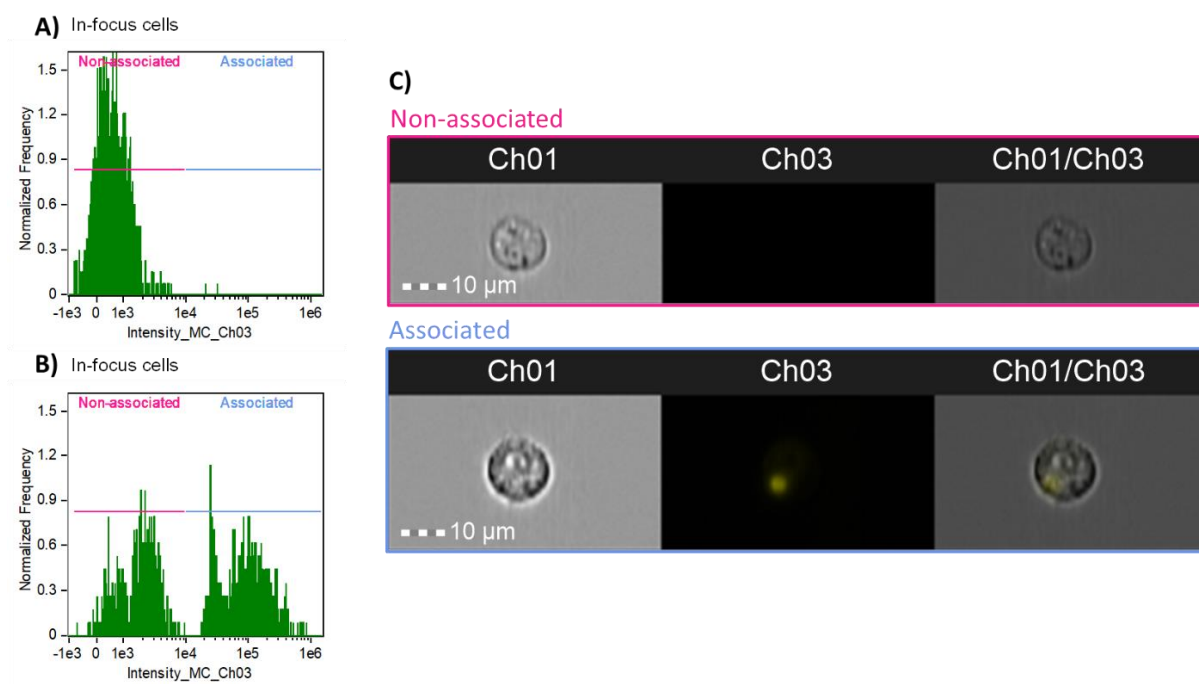


Figure S3.9: Gating of cells associated with particles. A) Histogram of untreated cells B) Histogram of cells treated with RBITC-labelled silicon oxide spheres C) Images of cells from non-associated and associated populations

In order to distinguish surface bound particles from internalised particles a cell mask was created as shown in figure S3.10A (blue region). This mask was eroded to exclude the cell membrane using the adaptive erode feature with an adaptive erode coefficient of 80 as shown in figure S3.10B. This defines an area specific to each cell outside of which particles are considered surface bound by considering the ratio of fluorescence intensity inside the mask to the intensity of the entire cell. This analysis gives each image an internalisation score where a positive score indicates the particle is inside the cell and a negative score indicates the particle is surface bound. A histogram displaying the internalisation scores is produced and regions defined as “cells with external particles” and “cells with internal particles” (figure S3.11).

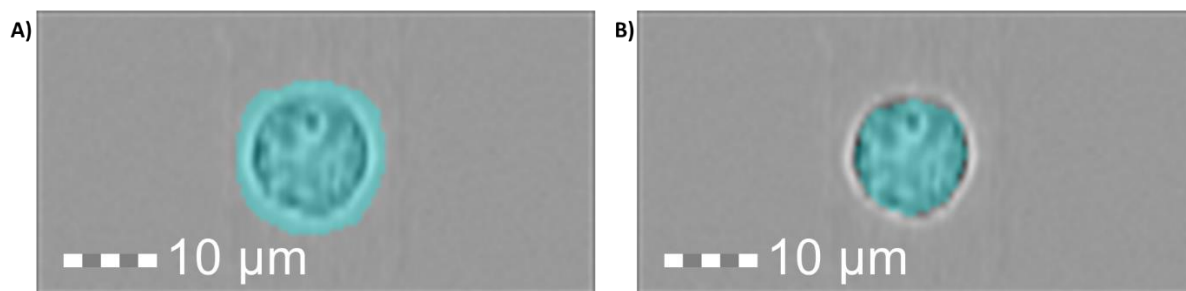


Figure S3.10: Cell masks used to identify cells with internal and surface-bound particles. A) General cell mask B) Eroded cell mask

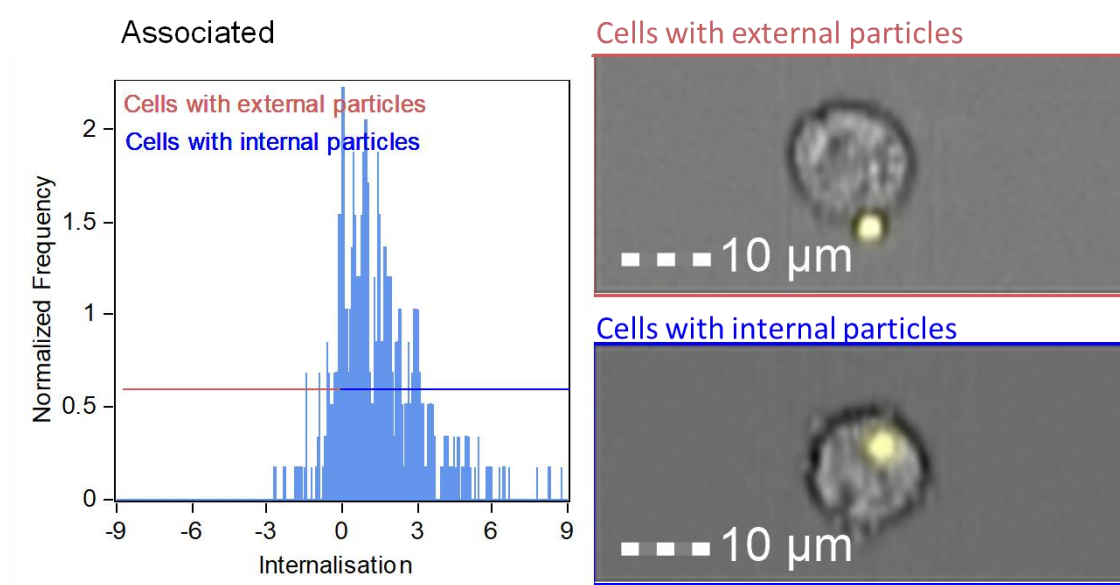


Figure S3.11: Histogram of internalisation score defining whether particles are internalised or surface-bound

Quantification of particle internalisation by trypan blue quenching

The trypan blue quenching method distinguishes internalised particles from those which are surface bound by quenching the fluorescence of the surface-bound particles. Trypan blue is a cell-impermeable dye that only enters the cell when the membrane is damaged and is therefore normally used to distinguish live and dead cells. Trypan blue has an absorption maximum at 580 nm which is the same wavelength of the emission of rhodamine B and so it

quenches fluorescence when in close contact with the fluorophore by absorbing emitted light. As such, only those particles which it can come into close contact with i.e. surface bound particles are quenched.

After following the initial analysis step to isolate single cell populations as in figure S3.7, a plot of intensity in brightfield channel-Ch09 (X-axis) against intensity of fluorescence channel-Ch03 (Y-axis) is used to distinguish cell populations. The brightfield channel intensity relates to the degree of trypan blue staining, dead cells appear darker and so this can be used to distinguish live from dead cells (figure 3.12).

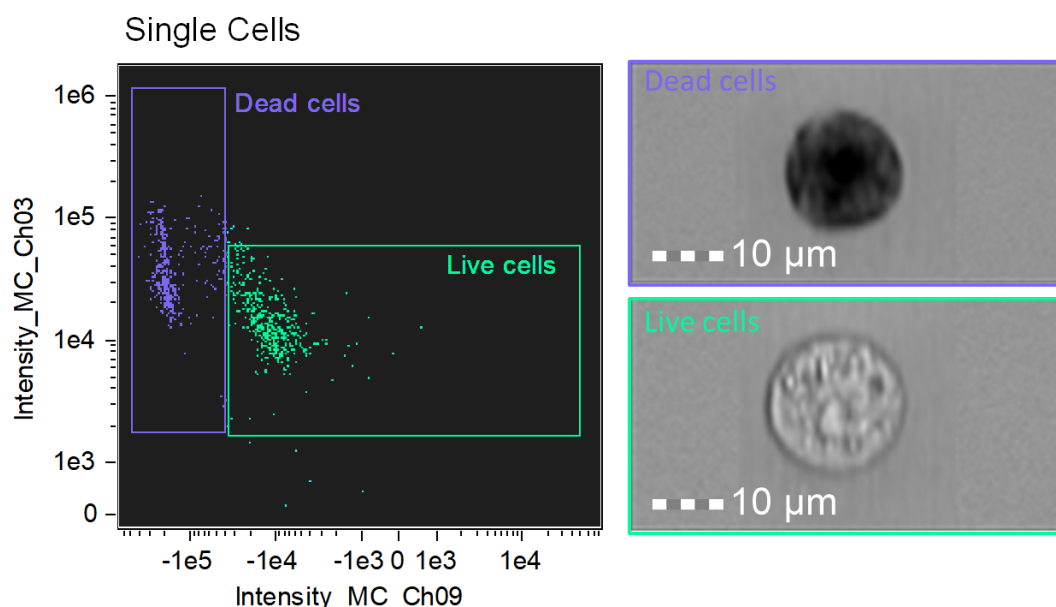


Figure S3.12: Distinction between trypan blue stained and unstained cells

When particles are applied to the cells, a third population that contains live cells that have internalised particles is present (figure S3.13A). This population contains cells which have internal particles (figure S3.13B) and cells that have both internal and external particles, however external particles are no longer fluorescent (figure S3.13C). Cells that have external particles and no internal particles are present in the live cells only region (figure S3.13D) as the fluorescence from their particles has been quenched. The number of live cells with internal

particles is divided by the number of live cells + the number of live cells with internal particles to give the percentage of cells with internal particles.

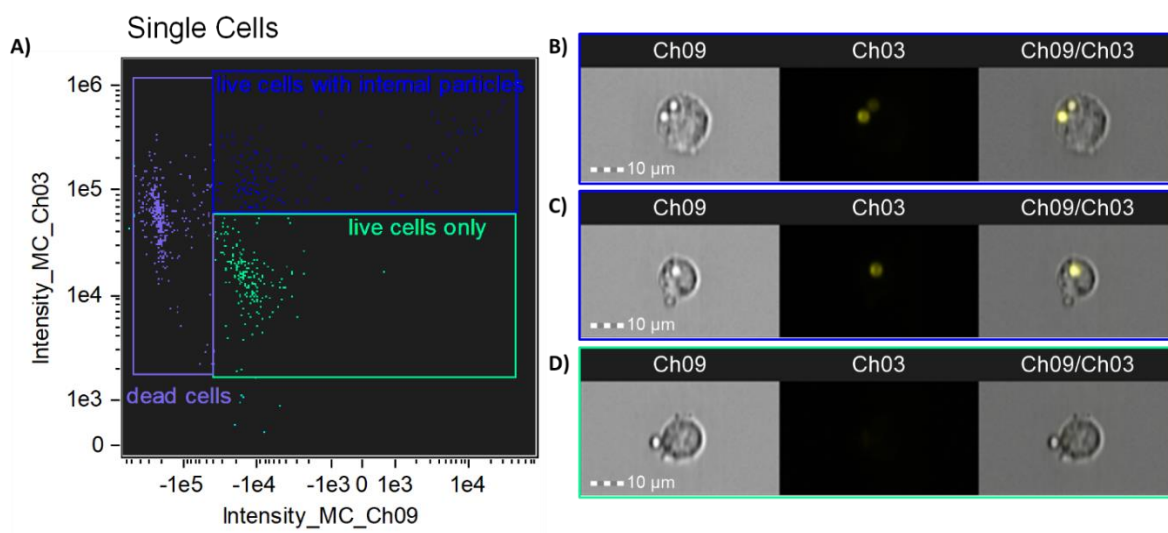


Figure S3.13: Distinction between cells with surface-bound and internalised particles using the trypan blue quenching method. A) B) Brightfield and fluorescence images of a live cell with internal particles only C) Brightfield and fluorescence images of a live cell with both an internal and external particle D) Brightfield and fluorescence images of a live cell with a quenched surface-bound particle

Using spot count analysis to calculate the number of particles per cell

Populations of cells with internal particles (as determined using both the image analysis method and the trypan blue quenching method) were subsequently analysed using the IDEAS analysis software spot count feature to determine the number of particles per cell.

Appendix II - Supporting information for chapter 4

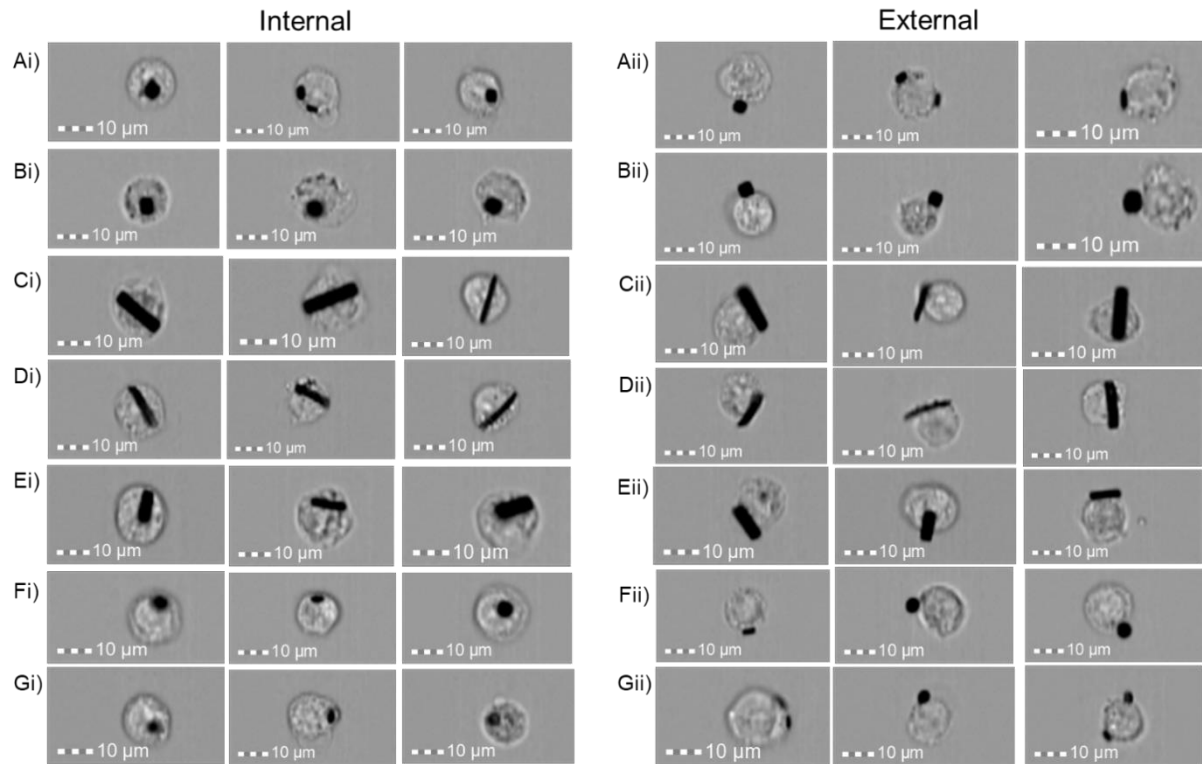


Figure S4.1: Cell images from imaging flow cytometry of cells with internal and external particles. A) Hexahedrons ($3 \times 3 \times 0.5 \mu\text{m}$), B) Cubes ($3 \times 3 \times 3 \mu\text{m}$), C) Bars ($3 \times 15 \times 0.5 \mu\text{m}$), D) Bars ($3 \times 15 \times 0.05 \mu\text{m}$), E) Bars ($3 \times 10 \times 0.5 \mu\text{m}$), F) Circular disks ($d=4 \mu\text{m}$ $h=0.5 \mu\text{m}$), G) Circular disks ($d=3 \mu\text{m}$ $h=0.5 \mu\text{m}$).

Appendix III – Supporting information for chapter 5

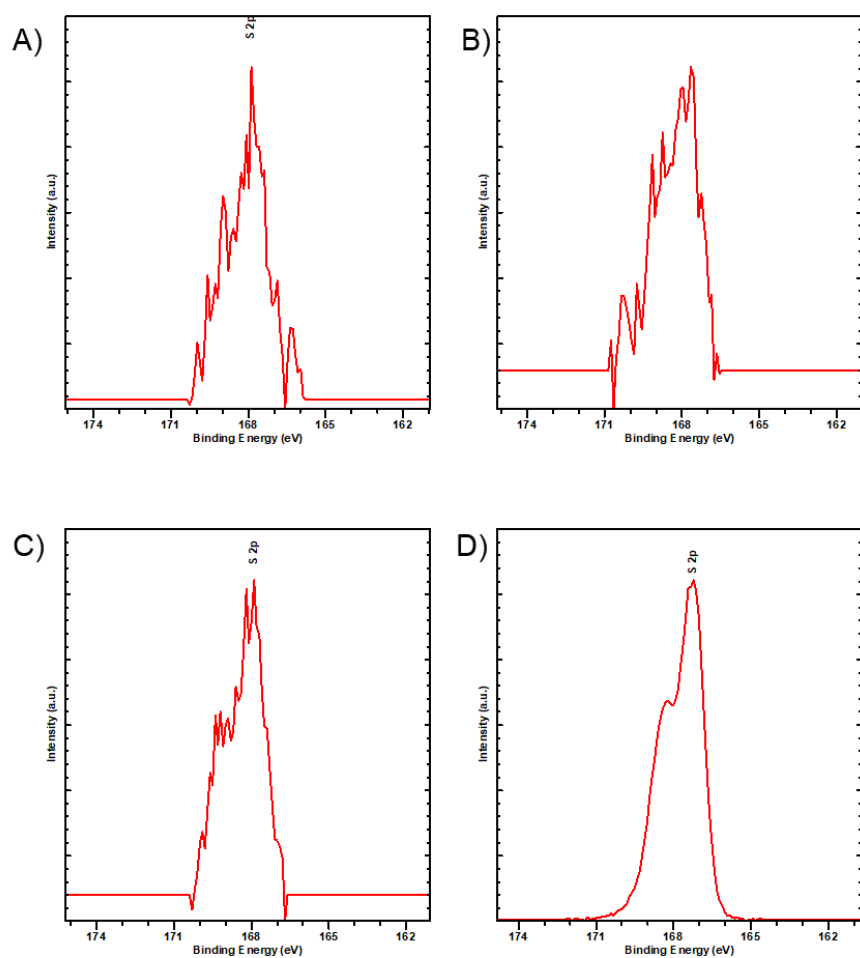


Figure S5.1: High resolution XPS spectra of S peaks from MDSA modified particles. A) 0.5 μm , B) 1 μm , C) 3 μm , D) MDSA powder

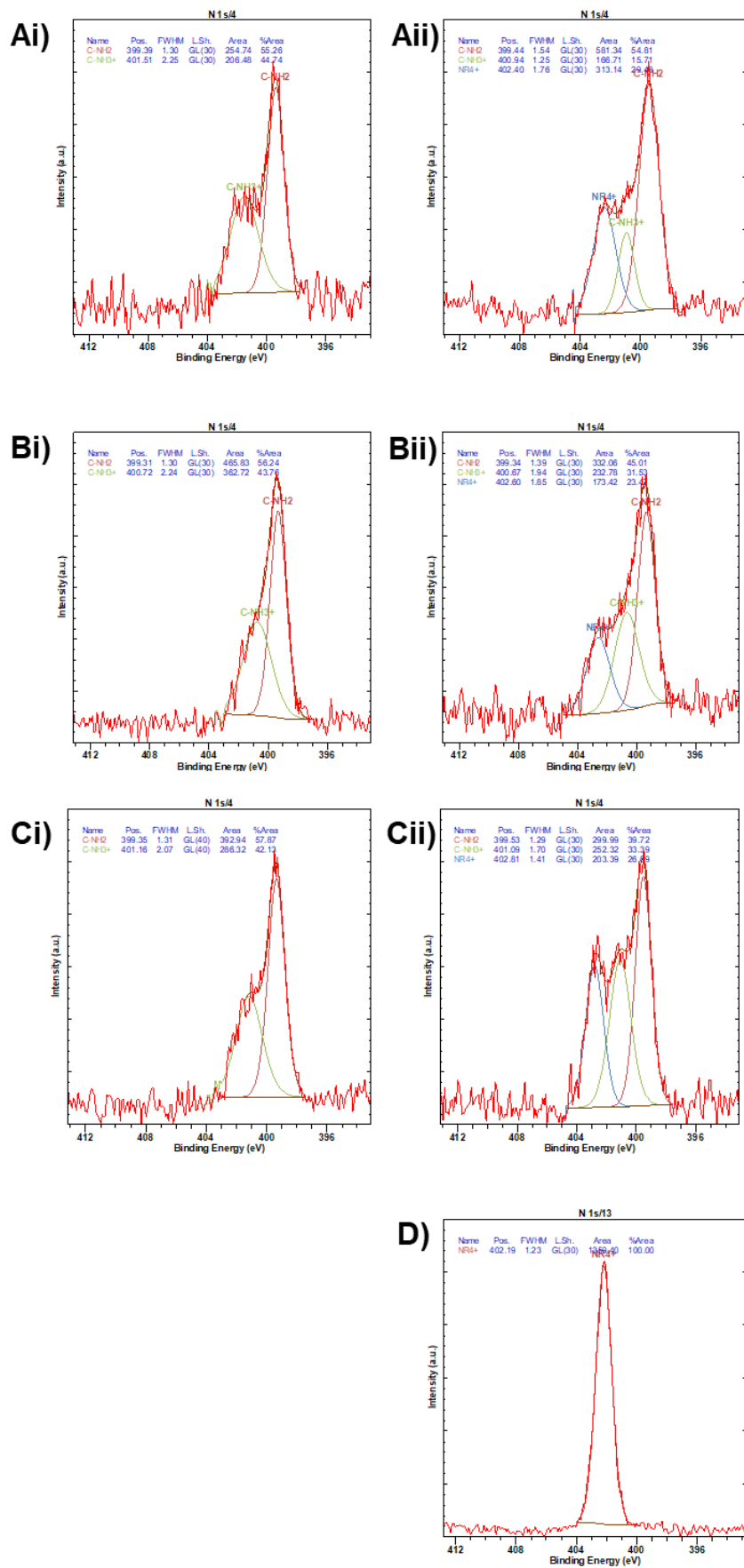


Figure S5.2: High resolution XPS spectra of Nitrogen peaks for silicon oxide particles. A) 0.5 μ m, B) 1 μ m, C) 3 μ m D) MDSA powder. i) Particles modified with AUTES ii) Particles modified with AUTES and MDSA.